UNIVERSITAT POLITÈCNICA DE VALÈNCIA

Department of Electronic Engineering

Area: Biomedical Engineering

Novel cardiac mapping approaches and multimodal techniques to unravel multidomain dynamics of complex arrhythmias towards a framework for translational mechanistic-based therapeutic strategies

Conrado Javier Calvo Saiz

Dissertation submitted in partial fulfillment of the requirements for the degree of

Philosophiæ Doctor (Ph.D.)

Supervisors:

José Millet Roig

Univesitat Politècnica de València, Valencia, Spain

Valencia, march 2022, Spain

UNIVERSITAT POLITÈCNICA DE VALÈNCIA

Department of Electronic Engineering

Area: Biomedical Engineering

Novel cardiac mapping approaches and multimodal techniques to unravel multidomain dynamics of complex arrhythmias towards a framework for translational mechanistic-based therapeutic strategies

Conrado Javier Calvo Saiz

Dissertation submitted in partial fulfillment of the requirements for the degree of

Philosophiæ Doctor (Ph.D.)

in Biomedical Electronics Engineering

Supervisors:

José Millet Roig

Univesitat Politècnica de València, Valencia, Spain

Valencia, march 2022, Spain

The research described in this thesis was partially carried out at Universitat Politècnica de València (Valencia, Spain), the Center for Arrhythmia Research at the University of Michigan, the Spanish National Center for Cardiovascular Research in Madrid, and the Department of Physiology at the Faculty of Medicine at Universitat de València–Estudi General, in partial collaboration with associated clinical partners from the National Research Network in Cardiovascular Disease (CIBERcv, IIS Carlos III). The work and projects presented here were financially supported in part by national and international competitive research grants.

To my dear and beloved ones, to family and friends; to anyone who has contributed to any the studies and results presented in this thesis.

Science never gives up searching for truth,
since it never claims to have achieved it.
Authority in science exists to be questioned,
since heresy is the spring from which new ideas flow.
John C. Polanyi

I'm interested in everything involving work and will; I'm interested in everyone who has an ideal and strives to achieve it.
V. Blasco-Ibañez

Acknowledgements

First and foremost, I would like to thank friends and family for their inconditional support all the way; it has been instrumental in completing this thesis. Thank you to anyone who has contributed to the studies and results presented in this thesis.

Notewithstanding, during several years I've had the opportunity to interact with top class scientists to grow interest in research and look up to.

I would like to express my grattitude to all members at the Center for Arrhythmia Research at the University of Michigan, with whom I started this road and shared many good moments and discussions. Special thanks to the National Center for Cardiovascular Research' Advanced Development in Arrhythmia Mechanisms and Therapy team for many long-run experiments and wonderful discussions together. Special thanks to Peter Lee and Christian Bollensdorf for so many long days and great discussions and advices all the way.

Finally, I would like to thank the group on Experimental Cardiac Electrophysilogy at the Medical School of the University of Valencia – Estudi General, for welcoming new ideas and discussions.

Abstract

Cardiac arrhythmias are a major problem for health systems in the developed world due to their high incidence and prevalence as the population ages, as well as their clinical repercussions, including increasing risk for comorbidities, such as stroke, and overall cardiovascular disease. Atrial fibrillation (AF) and ventricular fibrillation (VF), are amongst the most complex arrhythmias seen in the clinical practice. Clinical consequences of such arrhythmic disturbances include developing complex cardio-embolic events in AF, and dramatic repercussions due to sustained life-threatening fibrillatory processes with subsequent neurological damage under VF, leading to cardiac arrest and sudden cardiac death (SCD). However, despite the technological advances in the last decades, their intrinsic mechanisms are incompletely understood, and, to date, therapeutic strategies lack of sufficient mechanistic basis and have low success rates.

Most of the progress for developing optimal biomarkers and novel therapeutic strategies in this field has come from valuable techniques in the research of arrhythmia mechanisms. Amongst the mechanisms involved in the induction and perpetuation of cardiac arrhythmias such AF, dynamic high-frequency re-entrant and focal sources, in its different modalities, are thought to be the primary sources underlying the arrhythmia. However, little is known about the attractors and spatiotemporal dynamics of such fibrillatory primary sources, specifically dominant rotational or focal sources maintaining the arrhythmia. Therefore a computational platform for understanding active, passive and structural determinants, and modulators of such dynamics was developed using parallel grid computing and GPU acceleration, for unravelling their mechanisms in presence of ionic, passive or geometrical gradients, their relevant biomarkers and major role in the arrhythmia maintenance. This allowed stablishing a framework for understanding the complex multidomain dynamics of rotors with enphasis in their deterministic properties to develop mechanistic approaches for diagnostic aid and therapy.

Understanding fibrillatory processes is key to develop physiologically and clinically relevant scores and tools for early diagnostic aid. Specifically, spectral and time-frequency properties of fibrillatory processes have shown to highlight major

deterministic behaviour of intrinsic mechanisms underlying the arrhythmias and the impact of such arrhythmic events. This is critically relevant in determining early prognosis of comatose survivors after cardiac arrest due to ventricular fibrillation (VF), which is unreliable, especially in patients undergoing mild hypothermia. Using prior knowledge, signal processing, machine learning techniques and data analytics, we aimed at developing a reliable mechanistic risk-score to enable early prediction of cerebral performance and survival, based on VF multi-domain properties and spectral biomarkers. This allowed developing a mechanistic model that reliably correlated time-dependent VF spectral changes with acute cerebral injury in comatose survivors undergoing mild hypothermia after cardiac arrest.

Cardiac optical mapping and electrophysiological mapping techniques have shown to be unvaluable resources to shape new hypotheses and develop novel mechanistic approaches and therapeutic strategies. This technology has allowed for many years testing new pharmacological or ablative therapeutic strategies, and developing multidomain methods to accurately track arrhymia dynamics identigying dominant sources and attractors. Even though, panoramic mapping is the primary method for simultaneously tracking electrophysiological parameters, its adoption by the multidisciplinary cardiovascular research community is limited mainly due to the cost of the technology. Taking advantage of recent technological advances, we focus on developing and validating low-cost optical mapping systems for panoramic imaging using clinically relevant models for basic research and bioengineering.

Resum

Les arítmies cardíaques són un problema important per als sistemes de salut del món desenvolupat a causa de la seva alta incidència i prevalença a mesura que la població envelleix, així com de les seves repercussions clíniques, incloent un augment del risc de comorbiditats, com l'ictus, i les malalties cardiovasculars en general. La fibril·lació auricular (FA) i la fibril·lació ventricular (FV), es troben entre les arítmies més complexes observades a la pràctica clínica. Les conseqüències clíniques d'aquests trastorns arítmics inclouen el desenvolupament d'esdeveniments cardioembòlics complexos en FA i repercussions dramàtiques a causa de processos fibril·latoris sostinguts que posen en perill la vida amb danys neurològics posteriors a la FV, que condueixen a una aturada cardíaca i a la mort cardíaca sobtada (SCD). Tanmateix, malgrat els avanços tecnològics de les darreres dècades, els seus mecanismes intrínsecs s'entenen de forma incompleta i, fins a la data, les estratègies terapèutiques no tenen una base mecanicista suficient i tenen baixes taxes d'èxit.

La majoria dels avenços en el desenvolupament de biomarcadors òptims i noves estratègies terapèutiques en aquest camp provenen de tècniques valuoses en la investigació de mecanismes d'arítmia. Entre els mecanismes implicats en la inducció i perpetuació de les arítmies cardíaques, es creu que les fonts primàries subjacents a l'arítmia són les fonts focals reingressants d'alta freqüència dinàmica i AF, en les seves diferents modalitats. Tot i això, se sap poc sobre els atractors i la dinàmica espaciotemporal d'aquestes fonts primàries fibril·ladores, específicament les fonts rotacionals o focals dominants que mantenen l'arítmia. Per tant, s'ha desenvolupat una plataforma computacional per entendre determinants actius, passius, estructurals i moduladors d'aquestes dinàmiques mitjançant computació en quadrícula paral·lela i acceleració GPU, per desvelar els seus mecanismes en presència de gradients iònics, passius o geomètrics, els seus biomarcadors rellevants i el paper principal de manteniment de l'arítmia. Això va permetre establir un marc per entendre la complexa dinàmica multidomini dels rotors amb ènfasi en les seves propietats deterministes per desenvolupar enfocaments mecanicistes per a l'ajuda i la teràpia diagnòstiques.

La comprensió dels processos fibril·latoris és clau per desenvolupar puntuacions i eines rellevants fisiològicament i clínicament per ajudar al diagnòstic precoç. Concretament, les propietats espectrals i de temps-freqüència dels processos fibril·latoris han demostrat destacar un comportament determinista important dels mecanismes intrínsecs subjacents a les arítmies i l'impacte d'aquests esdeveniments

arítmics. Això és críticament rellevant per determinar el pronòstic precoç dels supervivents en comata després d'una aturada cardíaca a causa de la fibril·lació ventricular (FV), que no és fiable, especialment en pacients sotmesos a hipotèrmia lleu. Mitjançant coneixements previs, processament de senyals, tècniques d'aprenentatge automàtic i anàlisi de dades, ens vam proposar desenvolupar una puntuació de risc mecanicista fiable per permetre la predicció primerenca del rendiment cerebral i la supervivència, basant-nos en propietats multidomini de la FV i biomarcadors espectrals. Això va permetre desenvolupar un model mecanicista que correlacionés de manera fiable els canvis espectrals de FV dependents del temps amb lesions cerebrals agudes en supervivents en comata que estaven sotmesos a hipotèrmia lleu després d'una aturada cardíaca.

Les tècniques de cartografia òptica cardíaca i electrofisiològica han demostrat ser recursos inestimables per donar forma a noves hipòtesis i desenvolupar nous enfocaments mecanicistes i estratègies terapèutiques. Aquesta tecnologia ha permès durant molts anys provar noves estratègies terapèutiques farmacològiques o ablatives i desenvolupar mètodes multidominis per fer un seguiment precís de la dinàmica d'arrímies que identifica fonts i atractors dominants. Tot i que el mapatge panoràmic és el mètode principal per al seguiment simultani de paràmetres electrofisiològics, la seva adopció per part de la comunitat multidisciplinària d'investigació cardiovascular està limitada principalment pel cost de la tecnologia. Aprofitant els avenços tecnològics recents, ens centrem en el desenvolupament i la validació de sistemes de mapes òptics de baix cost per a imatges panoràmiques mitjançant models clínicament rellevants per a la investigació bàsica i la bioenginyeria.

Resumen

Las arritmias cardíacas son un problema importante para los sistemas de salud en el mundo desarrollado debido a su alta incidencia y prevalencia a medida que la población envejece. También lo son sus repercusiones clínicas, incluido el aumento del riesgo de comorbilidades, como el ictus y la enfermedad cardiovascular en general. La fibrilación auricular (FA) y la fibrilación ventricular (FV) se encuentran entre las arritmias más complejas observadas en la práctica clínica. Las consecuencias clínicas de tales alteraciones arrítmicas incluyen el desarrollo de eventos cardioembólicos complejos en la FA, y repercusiones dramáticas debido a procesos fibrilatorios sostenidos que amenazan la vida infringiendo daño neurológico tras paro cardíaco por FV, y que pueden provocar la muerte súbita cardíaca (MSC). Sin embargo, a pesar de los avances tecnológicos de las últimas décadas, sus mecanismos intrínsecos se comprenden de forma incompleta y, hasta la fecha, las estrategias terapéuticas carecen de una base mecanicista suficiente y poseen bajas tasas de éxito. La mayor parte del progreso para el desarrollo de biomarcadores óptimos y estrategias terapéuticas novedosas en este campo ha sido resultado del desarrollo de tecnología y técnicas valiosas en la investigación básica y clínica para el estudio de los mecanismos de arritmia.

Entre los mecanismos implicados en la inducción y perpetuación de arritmias cardíacas, como la FA, se cree que las dinámicas de las fuentes focales y reentrantes de alta frecuencia, en sus diferentes modalidades, son las *fuentes primarias* que mantienen la arritmia. Sin embargo, se sabe poco sobre los atractores, así como, de la dinámica espacio-temporal de tales fuentes fibrilatorias primarias, específicamente, las fuentes focales o rotacionales dominantes que mantienen la arritmia. Por ello, se ha desarrollado una plataforma computacional, para comprender los factores (activos, pasivos y estructurales) determinantes, y moduladores de dicha dinámica, utilizando computación paralela sobre sistemas de altas prestaciones y la aceleración mediante GPU, para desentrañar sus mecanismos en presencia de gradientes iónicos, pasivos o geométricos, así como los biomarcadores relevantes asociados, y su papel principal en el mantenimiento de las arritmias. Esto permitió establecer un marco para comprender la compleja dinámica de los rotores con énfasis en sus propiedades deterministas para desarrollar herramientas basadas en los mecanismos para ayuda diagnóstica y terapéutica.

Comprender los procesos fibrilatorios es clave para desarrollar marcadores y herramientas fisiológica- y clínicamente relevantes para la ayuda de

diagnóstico temprano. Específicamente, las propiedades espectrales y de tiempo-frecuencia de los procesos fibrilatorios han demostrado resaltar el comportamiento determinista principal de los mecanismos intrínsecos subyacentes a las arritmias y el impacto de tales eventos arrítmicos. Esto es especialmente relevante para determinar el pronóstico temprano de los supervivientes comatosos después de un paro cardíaco debido a fibrilación ventricular (FV), cuyo pronóstico no es preciso. Utilizando conocimientos previos, procesado y técnicas de aprendizaje automático y análisis de datos, nuestro objetivo fue desarrollar un marcador y modelo de riesgo mecanicista confiable para permitir la predicción temprana del rendimiento cerebral y la supervivencia, apoyado en biomarcadores espectrales y multidominio de la FV. Esto permitió desarrollar un modelo mecanicista que correlaciona de manera confiable los cambios espectrales de FV dependientes del tiempo con la lesión cerebral aguda en supervivientes comatosos que experimentaban hipotermia leve después de un paro cardíaco.

Las técnicas de mapeo electrofisiológico, el mapeo eléctrico y óptico cardíaco, han demostrado ser recursos muy valiosos para dar forma a nuevas hipótesis y desarrollar nuevos enfoques mecanicistas y estrategias terapéuticas mejoradas. Esta tecnología permite además el trabajo multidisciplinar entre clínicos y bioingenieros, para el desarrollo y validación de dispositivos y metodologías para identificar biomarcadores multi-dominio que permitan rastrear con precisión la dinámica de las arritmias identificando fuentes dominantes y atractores con alta precisión para ser dianas de estrategias terapeúticas innovadoras. Es por ello que uno de los objetivos fundamentales ha sido la implantación y validación de nuevos sistemas de mapeo en distintas configuraciones que sirvan de plataforma de desarrollo de nuevas estrategias terapeúticas. Aunque el mapeo panorámico es el método principal y más completo para rastrear simultáneamente biomarcadores electrofisiológicos, su adopción por la comunidad científica es limitada principalmente debido al coste elevado de la tecnología. Aprovechando los avances tecnológicos recientes, nos hemos enfocado en desarrollar, y validar, sistemas de mapeo óptico de alta resolución para registro panorámico cardíaco, utilizando modelos clínicamente relevantes para la investigación básica y la bioingeniería.

Abbreviations and Acronyms

A&A	Description
AF	Atrial Fibrillation
AP	Action Potential
APD_{XX}	Action Potential Duration at XX% Repolarization Level
G_X	Maximal conductance ionic channel family X
BCL	Basic Cycle Length
ECG	Electrocardiogram
CFAE	Complex Fractionated Atrial Electrograms
CRN	Model Courtemanche-Ramirez-Nattel
CRN-K	Model Courtemanche-Ramirez-Nattel-Kneller
I_{K1}	Inward rectifier potassium ionic current
I_{KACh}	Corriente Rectificadora de Entrada de Potasio Modulada por ACh
I_{Kr}/g_{Kr}	Rapid repolarizing potassium ionic current / conductance
I_{Ks}/g_{Ks}	Slow repolarizing potassium ionic current / conductance
I_{to}/g_{to}	Transient outward potassium ionic current / conductance
I_{CaL}/g_{CaL}	L-type calcium current ionic current / conductance
I_{Na}/g_{Na}	Fast sodium ionic current / conductance.
ACh / ACo	Acetilcholine
h·j	Fraction of sodium channels available
$h \cdot j_{peak}$	Maximal fraction of sodium channels available in a cycle
DF	Dominant Frequency
ERP	Effective Refractory Period
LIPV o VPII	Left inferior pulmonary vein
RSPV o VPSD	Right superior pulmonary vein
PVLAJ	Pulmonary Vein Left Atrial Junction
LA o AI	Left Atrium
RV	Right Ventricle
PV o VP (s)	Pulmonary Veins
WL_{XX}	WaveLength (at XX%)
CI	Coupling interval
RF	Radiofrequency
dV/dt_{max}	Maximal depolarization velocity
VC o CV	Conduction velocity
CI	Intervalo de Acoplamiento
CICR	Calcium induced calcium released
FEM	Finite element method
FVM	Finite Volume Method
ODE	Ordinary Differential Equation
VW	Vulnerable Window
C-I	‘ALL’ Ionic currents vary spatially, all gradients condition.
C-II	‘ALL BUT I_{K1}’ Ionic currents vary spatially but I_{K1}

C-III	‘ONLY I_{K1}’ Only I_{K1} ionic gradient in tissue, rest homogenous
V_m	Membrane potential
SP	Singularity point
S1,S2	S1S2 protocol reentry induction
TSP	Spatiotemporal representation
I-V	Current-voltage relationship ionic channel
MDP	Minimum Diastolic Potential

List of figures

Chapter 1

Introduction

Cardiac arrhythmias are a major problem for health systems in the developed world due to their high incidence and prevalence as the population ages, as well as their clinical repercussions, including increasing risk for comorbidities, such as stroke, and overall cardiovascular disease. Atrial fibrillation (AF) and ventricular fibrillation (VF), are amongst the most complex arrhythmias seen in the clinical practice. Clinical consequences of such arrhythmic disturbances include developing complex cardio-embolic events in AF, and dramatic repercussions due to sustained life-threatening fibrillatory processes with subsequent neurological damage under VF, leading to cardiac arrest and sudden cardiac death (SCD). However, despite the technological advances in the last decades, their intrinsic mechanisms are incompletely understood, and, to date, therapeutic strategies lack of sufficient mechanistic basis and have low success rates.

Amongst the mechanisms involved in the induction and maintenance of fibrillatory processes are focal activity and re-entry in its different modalities. Triggering activity mediated by focal sources may be associated in arrhythmogenesis involving post-potentials and maintenance of the arrhythmia. When the initiating factors interact on a suitable substrate, they generate re-entrant activations that exacerbate the arrhythmia. Substrates in

which the refractoriness, conduction velocity and wavelength are shortened, in presence of regional functional heterogeneities, or in presence of structural alterations or geometrical constraints, inhomogeneous conduction patterns may favor the appearance and perpetuation of fibrillatory processes. Various modulating factors, such as the autonomic nervous system, or myocardial stretching, modify the electrophysiological properties of myocytes. How focal and re-entrant sources are affected dynamically by regional heterogeneities, substrate and other modulating factors, and their consequences, are still under profound study.

Most of the progress for developing optimal biomarkers and novel therapeutic strategies in this field has come from valuable techniques in the research of arrhythmia mechanisms. Despite current advances for understanding fibrillatory processes, such those found in AF, little is known about the attractors and dynamics of fibrillatory primary sources, specifically dominant rotational or focal sources maintaining the arrhythmia. Maintenance of AF by fast rotors in the left atrium (LA) or at the pulmonary veins (PVs) is not fully understood. To gain insight into this dynamic and complex process, we developed a computational platform and studied the role of the heterogeneous distribution of transmembrane currents in the PVs and LA junction (PV-LAJ) in the localization of rotors in the PVs. Further research was carried to test whether simple pacing protocols could be used to predict rotor drift in the PV-LAJ using experimentally observed heterogeneities in IK1, IKs, IKr, Ito, and ICaL, and human atrial kinetics to simulate various conditions with the major purpose of investigating rotor drifting mechanisms and their spatiotemporal dynamics. This allowed stablishing a framework for understanding the complex multidomain dynamics of rotors with emphasis in their deterministic properties to develop mechanistic approaches for diagnostic aid and therapy.

Understanding fibrillatory processes is key to develop physiologically and clinically relevant scores and tools for early diagnostic aid. Specifically, spectral and time-frequency properties of fibrillatory processes have shown to highlight major deterministic behaviour of intrinsic mechanisms underlying the arrhythmias and the impact of such arrhythmic events. This is critically relevant in determining early prognosis of comatose survivors after cardiac arrest due to ventricular fibrillation (VF), which is unreliable, especially in patients undergoing mild hypothermia. Using prior knowledge, signal processing, machine learning techniques and data analytics, we aimed at developing a reliable mechanistic risk-score to enable early prediction of cerebral performance and survival, based on VF multi-domain properties and spectral biomarkers. This allowed developing a mechanistic model that reliably correlated time-dependent VF spectral changes with acute cerebral injury in comatose survivors undergoing mild hypothermia after cardiac arrest. However, it has been shown that spontaneous VF dynamics may differ from induced VF under controlled conditions in the clinical electrophysiology laboratory. Therefore it is necessary to develop the appropriate technology and tools to stablish a link from the mechanisms under realistic spontaneous fibrillatory conditions to the development of effective therapeutic strategies in the clinical setting.

Cardiac optical mapping and electrophysiological mapping techniques have shown to be unvaluable resources to shape new hypotheses and develop novel mechanistic approaches and therapeutic strategies. This technology has allowed for many years testing new pharmacological or ablative therapeutic strategies, and developing multidomain methods to accurately track arrhythmia dynamics identifying dominant sources and localizing attractors. Even though, panoramic mapping is the primary method for

simultaneously tracking electrophysiological parameters, its adoption by the multidisciplinary cardiovascular research community is limited mainly due to the complexity and cost of the technology. Taking advantage of recent technological advances, we focus on developing and validating low-cost optical mapping systems for panoramic imaging using clinically relevant models for basic research studies and bioengineering applications.

1.1. Objectives

The main goal of this thesis is **to develop techniques, computational tools and technology for understanding intrinsic mechanisms of primary and dominant drivers of complex arrhythmias as well as serve as a platform for developing advanced diagnosic & therapeutic strategies.** Specifically, **this thesis is aiming for** i) setting up a computational platform to study spiral drift dynamics of primary rotors, ii) determining major VF features for neurological damage prediction after cardiac arrest, and, iii) developing a platform for scalable low cost panoramic optical mapping configurations for studying high-throughput drug-testing, cardiac arrhythmia drivers' dynamics and other biomedical engineering applications.

For this purpose, the following secondary objectives were proposed:

Aim1: *To develop a computational platform for simulation of cardiac electrophysiological tissue and geometrical models to determine functional and structural determinants of primary and dominant driver dynamics with interest in the role of major ionic repolarizing currents.*

Aim2. *To study the mechanisms of wavebreak and spiral drift under regional heterogeneity with interest in the pulmonary veins left atrial junction transition.*

Aim 3. *To develop a mechanistic-based score for cerebral performance and survival after cardiac arrest due to VF impact.*

Aim 4. *To set-up new technologies and multimodal techniques for multiparametric and panoramic electrophysiological optical mapping for the study of cardiac arrhythmias in translational animal models.*

Aim 5. *To validate different low-cost high-resolution optical mapping configurations for the study of cardiac fibrillation.*

1.2. Structure of the thesis

In order to achieve the objectives presented, this dissertation is structured in the following chapters:

Chapter 2: State of the art. In this chapter, clinical, experimental and technical background knowledge is presented.

Chapter 3: Mechanisms of rotor drifting dynamics and sink-to-source attractors of primary reentrant sources in cardiac arrhythmias. In this chapter, we test a computational platform for the study of cardiac arrhythmia mechanisms. We focus on unraveling the major role of rectifying and repolarizing currents on rotor drifting dynamics, as well as passive and geometrical determinants, which are addressed in detail. Both spatiotemporal and spectral dynamics of fibrillatory processes are quatified to determine

rotor drift dynamics and predicting tissue attractors of dominant drivers of complex fibrillatory processes under AF.

Chapter 4: Spectral-based risk-score for early prediction of mortality in patients suffering from cardiac arrest. In this chapter, the main aim is to develop a mechanistic-based multivariate model and risk score that reliably predicts cerebral performance and survival, on admission of comatose survivors undergoing therapeutic hypothermia for ventricular fibrillation taking into account biomarkers representing deterministic features of the arrhythmia mechanisms.

Chapter 5: High-resolution optical mapping systems for panoramic imaging of complex arrhythmias and drug-action in translational animal models. In this chapter we aim to overcome the limitations of traditional optical mapping by introducing, implementing and validating novel low-cost optical mapping configurations for panoramic and multiparametric imaging.

Chapter 6: Conclusions. In this chapter the main findings already discussed in previous chapters are listed raising the major conclusions regarding each of the objectives of the thesis.

Chapter 7: Contributions related to this thesis. In this chapter the main contributions associated with this thesis as well as those derived and closely related are presented.

.

Chapter 2

Background

In this chapter a summarized review on clinical and technical background regarding the different research fields dealt within this thesis is addressed.

2.1. Introduction to cardiac electrophysiology

The heart is the main engine of our body and weighs between 200 and 450 grams. The cardiac organ is a pump responsible for blood circulation in the body, a closed system, at constant pressure. At the end of a life it has expanded and contracted more than 3.5 million times. In terms of fluid pumped it is comparable to emptying 48 Olympic swimming pools (3125 m^3). This extraordinary organ beats approximately 100,000 times on average and pumps about 2,000 gallons (7.6 m^3) of blood. On average, the body contains between 5 and 7 liters of blood that continuously circulate through the circulatory system ***(Martini 2014)***.

The heart has its own electrical system. The maintenance of cardiac flow is the result of the contractibility of the cardiac muscle fibers that allow their rhythmic functioning, the result of a synchronized contraction of all the cells,

which are electrically coupled. The heart works as a functional syncytium that has specialized cells that are capable under physiological conditions of generating electrical impulses, responsible for the rhythmic and organized contraction of the heart muscle. These impulses are conducted through a system of specialized fibers, whose mission is to distribute and vehicle these signals into the heart muscle.

The electrical activity of the heart results from the cumulative electrical potential generated by myocardial cells due to differences in ionic composition between intracellular and extracellular media, as well as, the semipermeable nature of the cell membrane which containes voltage-gated ionic channels. The ionic balance between the inside and the outside of the cell, according to the concentration and the electrical charge, is responsible for the electrical activity of the excitable cells, such as the cardiac myocytes.

In clinical practice, the electrocardiogram (ECG), whose importance for clinical diagnosis is essential, is the result of extracellular measurement of cardiac electrical activity in the human torso. These records, comprised by characteristic waves and patters, offer valuable information about the cardiac rhythm regarding cardiac pathologies and electrophysiological disorders.

Like any other complex machinery, the heart is subject to alterations in its orchestrated activity. Therefore, it is capable to adapt to different physiological conditions such as performing exercise. On the other hand, when the normal mechanism fail, the heart undergoes a pathological remodelling leading to cardiac disease. Cardiovascular diseases are the leading cause of death in most developed countries ***(Amini M 2021),*** and arrhythmic phenomena, results from failures in its orchestrated mechanism.

2.1.1. The heart: Cardiac Anatomy and Physiology

The heart is the main organ of the circulatory system, a muscular and conical organ located in the thoracic cavity, in the mediastinum (the space between the lungs), the sternum, the spinal column and inferiorly limited by the diaphragm. The latter works as a double pulsatile biological pump, that is, the right side moves the blood flow towards the lungs (pulmonary circulation) and the left side moves it towards the rest of the body (systemic circulation), thus establishing a double circuit, called the cardiovascular system. Therefore it is in charge of propelling the blood inside the body through the blood vessels at the appropriate pressure and with the necessary flow at all times. In this way the heart distributes oxygenated blood to the organs, while oxygen-poor blood is pumped into the lungs for oxygenation.

Oriented obliquely, the upper end of the heart, to which various veins and arteries connect, is known as the base. The lower pointed end of the heart is the apex. A typical adult human heart measures approximately 12.5 cm from base to apex ***(Martini 2014).*** It is divided into four cavities or chambers: two upper (called atria), which receive blood from the venous system, and two lower (called ventricles), where the arterial circulation is connected. The cardiac chambers are connected two by two by the atrio-ventricular valves. These heart valves are the structure that separates them from each other, preventing a retrograde reflux. There are four valves: the tricuspid valve that separates the right atrium from the right ventricle, the mitral or bicuspid valve that separates the left atrium from the left ventricle, the pulmonary valve that separates the right ventricle from the pulmonary artery, and the aortic valve that separates the left ventricle from the aorta artery.

Anatomically (Figure 2.1), we can see both the different chambers of the heart and the main arteries and veins responsible for distributing the blood flow entering or leaving the heart.

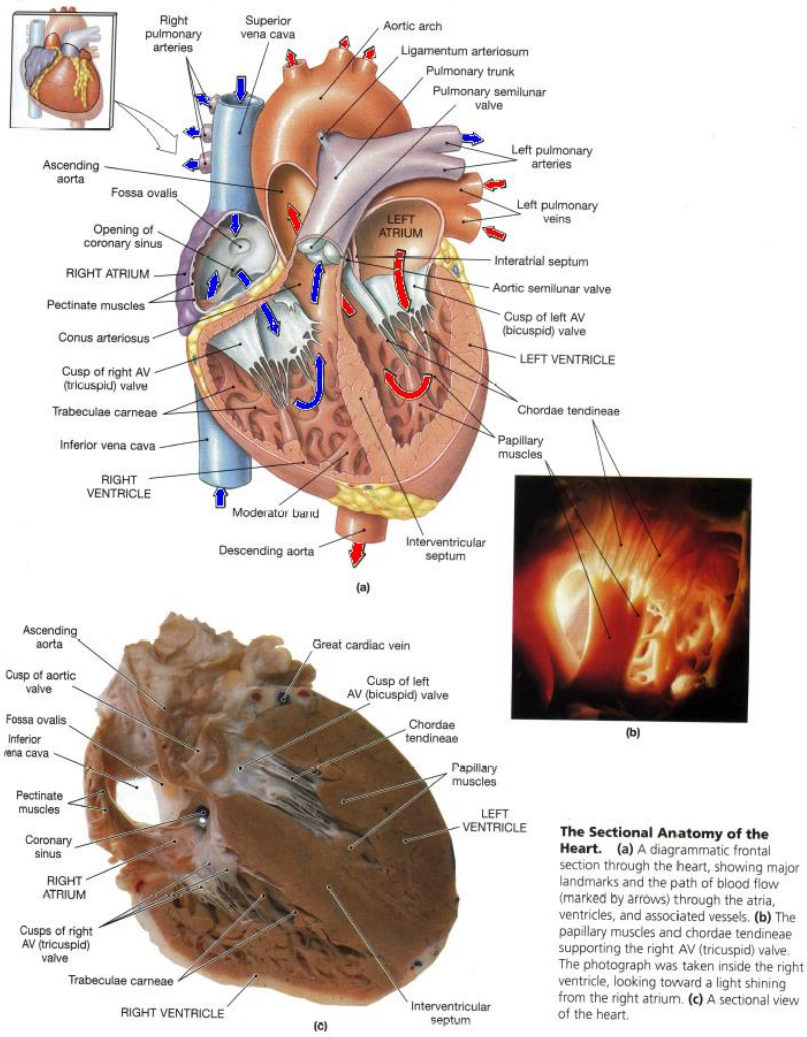

Figura 2.1. Cardiac anatomy. *Mod. Fundamentals of Anatomy and Physiology, F.H. Martini (Martini 2014).*

As can be seen, the four chambers of the heart are communicated two by two, as if they were independent pumps. The right atrium and the right ventricle

form what is classically called the right heart. It receives the blood that comes from the whole body, which empties into the right atrium through the superior and inferior vena cavae. This blood, low in oxygen, reaches the right ventricle, from where it is sent to the pulmonary circulation by the pulmonary artery. Since the resistance of the pulmonary circulation is less than the systemic one, the force (pressure) that the ventricle must exert is less, which is why its muscle size is considerably smaller. The left atrium and the left ventricle form the so-called left heart. It receives blood from the pulmonary circulation, which flows through the four pulmonary veins to the upper portion of the left atrium. This blood is oxygenated and comes from the lungs. The left ventricle sends it through the aorta to distribute it throughout the body and thus supply the tissues with oxygen and nutrients.

The tissue that separates the right heart from the left is called the interventricular septum, which we can be functionally distinguished into two non-separated areas: the upper or interatrial septum, and the lower or interventricular septum, especially important, since the bundle of His, which allows the impulse to be carried travels through the lower parts of the heart.

A muscular sac known as the pericardium loosely surrounds the heart. The cavity between the surface of the heart and the pericardium is known as the pericardial cavity that contains pericardial fluid that acts as a lubricant, reducing friction between opposing surfaces when the heart is beating. The two atria have relatively thin muscular walls and are highly flexible. The expandable part (wrinkled end when there is no blood) of the ear cavity is known as an atrial appendage. The wall of the heart is made up of three different layers. The epicardium is the visceral pericardium that forms the outer surface of the heart. The myocardium is the muscular wall of the heart

that forms both the atria and the ventricles. This layer consists of concentric layers of heart muscle tissue, blood vessels, and nerves. The inner surface of the heart is known as the endocardium. This layer covers the heart valves and is made up of endothelial tissues continuous with blood vessels. The heart is essentially made up of muscle tissue (myocardium) and, to a lesser extent, of connective and fibrous tissue (supporting tissue, valves, and specialized conduction tissue).

The muscles of the heart form bundles of long fibers. To maintain the circulating flow, the heart contracts rhythmically, giving rise to the cardiac cycle, thanks to the contractibility of the cardiac fibers. The contraction of the different chambers, in particular that of the ventricles, is efficient thanks to the spiral orientation of these fibers. The atrial fibers are arranged in concentric circles that wrap around the atria in a figure-eight shape. These fibers pass through the interatrial septum. The ventricular muscles are longer, and form a thick sheath around the ventricles in order to provide the force for strong contractions. The fibers can be seen originating from the base and running towards the apex before turning back again. The fact that cardiac muscle cells are oriented more tangentially than radially and that muscle resistivity is lower in the direction of the fibers is of particular importance in electrocardiography and magnetocardiography ***(Plonsey 1995)***.

Cardiac phenomena that occur from the beginning of one beat to the next comprises the cardiac cycle. Figure 2.2. (a) has arrows indicating the direction of blood flow during a single cardiac cycle ***(Guyton 2011)***. The cardiac cycle begins with a phase called diastole. In this phase, the atrioventricular valves open, allowing blood to flow into the ventricles thanks to the pressure difference between them and the atria. Once the

ventricles are nearly full, blood still flows to the heart entering directly from the veins during this stage called diastasis (middle stage of diastole, passive). The last stage of diastole is atrial systole, in which the atria contract so that the blood that still remains in them passes to the ventricles actively, allowing a 30% increase in blood volume in the ventricles. The second phase of the cardiac cycle is systole, where there is an isometric contraction of the ventricles, in which there is still no volume variation, causing the atrioventricular valves to close. Faced with this increase in intraventricular pressure, the aortic and pulmonary arterial valves open, which is when emptying begins, a stage that lasts almost three-quarters of systole. Once the pressure has dropped, the blood continues to flow out by ventricular contraction during this stage called early diastole. Finally, an isometric relaxation occurs, in which the ventricular fibers relax. Consequently, we have a reduction in interventricular pressure, causing the closure of the semilunar valves of the arteries and the subsequent opening of the atrioventricular valves, thus ending the cardiac cycle. The following illustration summarizes the process (Figure 2.2).

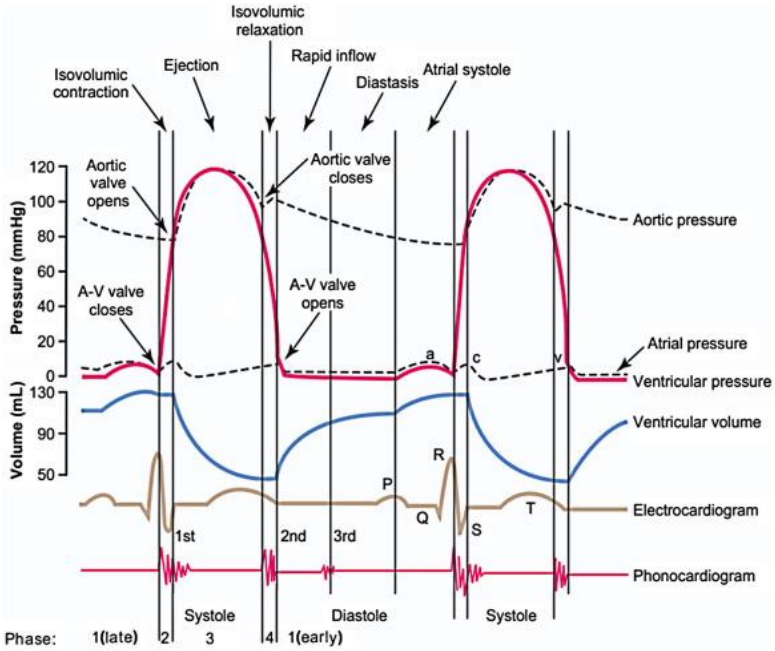

Figure 2.2. The Cardiac Cycle.. *Events during the cardiac cycle (changes in pressure in the chambers, volume as well as their correspondence with the characteristic cardiac waves). Source: Physiology Treaty A.C. Guyton*

The characteristic rhythmic noise that we can hear due to this process is due to the sudden closure of the cardiac valves. First, due to the sudden closure of the AV valves and second, due to the closure of the semilunar or sigmoid valves, actually being the result of the propagation of reverberation from the adjacent blood and the vibration of the walls of the heart and close vessels.

2.1.2. Cardiac Physiology: The Specialized Conduction System

The cardiac cycle causes the heart to alternate between contraction and relaxation approximately 75 times per minute, that is, the cardiac cycle lasts

about 0.8 seconds. The ability of the heart to act as a pump depends on a specialized system to: 1) rhythmically generate impulses that cause rhythmic and synchronized contraction of the myocardium and 2) conduct these impulses quickly, and in an orderly manner to the entire myocardium, to the fibers cardiac muscle. To produce the rhythmic contraction of the heart, the presence of specialized fibers is also required in the conduction of electrical impulses (action potentials) from the area where they originate automatically to the muscular area. This specialized conduction tissue is responsible for the origin and conduction of the electrical stimuli that cause cardiac contractions. The delays between the electrical impulses of the different fibers of the conduction system are adequate and optimal, so that the contraction of all the fibers is organized and practically simultaneous. Furthermore, the magnitudes of the refractory periods (the time interval from when a tissue depolarizes until it regains its excitability), both of the conduction systems and of the fibers themselves, guarantee the absence of unwanted returns of electrical impulses and, of the associated contractions.

The myocardium has four fundamental properties. These properties are automaticity, conductivity, excitability and contractibility. The first one, automaticity, allows you to produce its own stimuli in a rhythmic way. This property is highly developed in the sinoatrial node. Regarding conductivity, it is the ability of myocardial tissue to efficiently receive and transmit electrical stimuli. This capacity is closely related to the refractory period of the cell. Excitability is the ability of myocardial tissue to react to certain stimuli by producing electrical signals (AP), it is also closely linked to the refractory period. Finally, contractibility is the property by which the fiber contracts when it receives an impulse or stimulus, and relaxes in the absence of it ***(Hernán 2002)***.

The heart muscle contracts in the absence of neural and hormonal stimulation (automaticity). The heart's conduction system consists of a synchronous network of specialized cells that initiate and distribute electrical impulses that cause mechanical contraction of the heart muscles. The cardiac cycle begins with the synchronized activity of the cells of the sinus node ***(Guyton 2011)***. The sino-atrial or sinus node (SAN) is embedded in the posterior wall of the right atrium (Figure 2.3, Above). The SAN region contains pacemaker cells that initiate the heartbeat, therefore it is also known as the cardiac pacemaker. The fibers of this node connect directly with the fibers of the atria, so that any stimulus that begins in this node immediately propagates through the internodal or preferential pathways (anterior, middle and posterior, thicker fibers that cause contraction in atrial systole) towards the left atrium (LA) by the Bachmann bundle and towards the lower part of the heart, towards the atrioventricular node (AV node), which introduces the delay necessary for the time lag required between the atrial and ventricular systoles. Thus the ventricles do not contract until the atria have been completely emptied ***(Katz 2000)***. This delay introduced by the AV node is important because it also serves as a filter when activity in the atria is turbulent.

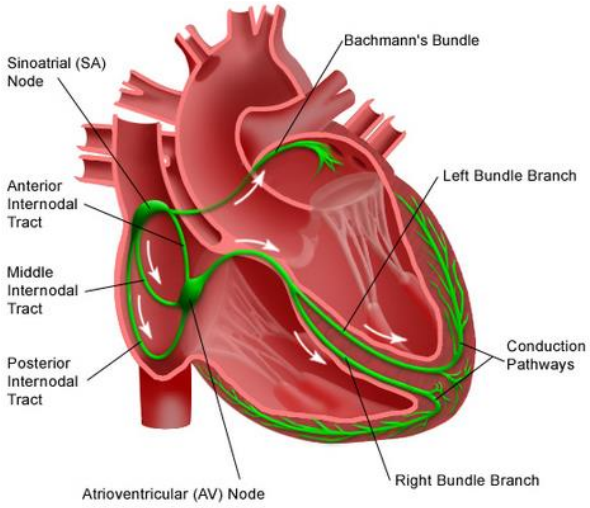

Figura 2.3. Cardiac electrical system. *The specialized driving system.*

The specialized conduction fibers of the common bundle, called the Bundle of His, allow the propagation of the impulse from the AV node. The Bundle of His is now divided into two main branches that run along the walls of the septum (the left branch divides into two sub-branches, anterior and posterior) ***(Katz 2000)***. Finally, from these branches arise some other branches, the Purkinje fibers, thick fibers of rapid propagation (functionally similar to neuronal axons) that diverge invading the myocardium in successive branches through the interior of the ventricular wall, where there are numerous activation points (junctions very similar to neuromuscular junctions) with muscle fibers that cause the formation of a wave front that propagates through the ventricular wall, eventually causing the heart to contract ***(Ferrero-Corral 1994)***. This process is the result of cell-to-cell activation in the ventricular wall. Under normal conditions, the depolarizing wavefront (the electrical impulse) propagates from the upper part of the heart (base) to the lower part (apex) and from the endocardium to the epicardium, although its repolarization occurs in the opposite direction due to heterogeneity intrinsic of the ventricular wall.

The SAN node is the one that intrinsically imposes the heart rate, setting the activation frequency of the whole heart. However, it is known that all the cells of the conduction system of the heart, and of the muscle itself are actually capable, by themselves, of generating impulses autonomously (Figure 2.3, Below). What happens, is that if any of these cells is fired (excited) at a higher frequency, it is forced to follow that rhythm and that is why the SAN node sets the activation frequency of the whole heart in a natural way (considered approximately 1Hz). This is why it is called the heart's natural pacemaker. If the connection between the SA node and the AV node fails, the AV node imposes its own pace. Therefore, if electrical conduction is interrupted at some point (blockage), other cells take over from the SAN node, becoming ectopic foci and generating impulses with less frequency than normal, which may become insufficient.

Additionally, the heart rate can be adjusted according to physical demands, stress or hormonal factors. For example, it is considered that it beats slower at night and faster during exercise. The stimulation of the heart, the cardiac rhythm, is coordinated by the autonomic nervous system, both by the sympathetic nervous system (increasing the rhythm and force of contraction) and by the parasympathetic (reducing the rhythm and force of contraction). The transmission of these electrical stimuli produces action potentials that are recorded on the surface of the skin using electrodes by the electrocardiogram (ECG).

2.1.3. From Ionic Channel to Cardiac Action Potential

To perform their various functions, some systems in the human body generate their own signals: bioelectric potentials from excitable cells. Each

excitable cell of the conduction system of the heart exhibits a particular and orchestrated evolution of its bioelectric potential. Any bioelectric signal observable on the surface of the body (by ECG, EEG, etc.) originates in the membranes of the cells of the nervous system with which it is related (specialized cells and myocardial cells of the heart, neurons in the brain, etc.) . Ultimately, the signal captured is the result of the electrochemical activity of the cells, according to the difference in concentration and the electrical charge, which occurs through ion channels and other active transport mechanisms. Charge carriers in organic fluids are fundamentally ions in solution that move in response to certain events, both mechanical (diffusion or entrainment by osmosis) or electrical (potential gradient). The intrinsic electrochemical gradient is due to the fact that the number of ions (charged molecules) in the extracellular medium is very different from that found inside the cell. In the extracellular environment, the most important ions are Na^+ and Cl^-, while K^+ and anionic phosphates predominate inside the cell. The movement of the ions will be that of their chemical gradient and against the electric one in search of equilibrium.

An ion channel (Figure 2.4), is a protein or set of homologous proteins, with a central aqueous pore and the properties of selectivity (family of ions that can cross it) and 'opening and closing' (regulated by gates that define channel operating states), which mediate its activity. Generally, the characteristic curves of the gates openings/closings fit to Boltzmann-type exponential equations, whose main characteristics are the slope (coperability) and the midpoint (energy, saturation point).

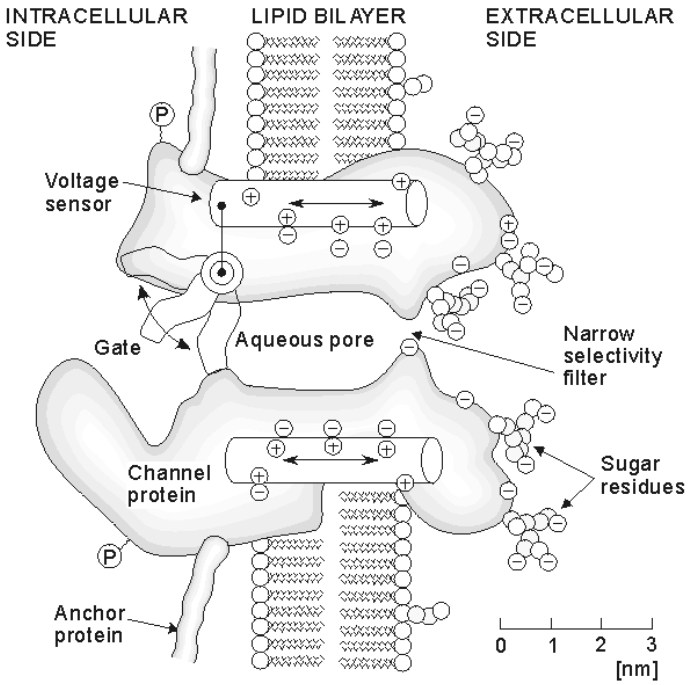

Figura 2.4. Ionic channel. *Working hypothesis, the ionic channel is drawn as a macromolecule with a pore through the center (Plonsey and Malmivuo 1985)*

Within the channels, we can distinguish passive (independent of time or potential) and active channels (voltage-dependent) in terms of their functionality. Ion channels are classified into three groups: 1) voltage-dependent, 2) regulated by extracellular ligand and 3) regulated by intracellular ligand ***(Mohrman 2006)***, in addition to the less studied mechano-sensitive (they translate a mechanical or physical change into a signal by varying its conductance). Among those activated by ligand, there are those that require the binding of a substance to the channel itself to regulate the passage of ions and those that require second messengers. In any case, the voltage-dependent channels are the ones that will attract our interest, they allow the passage of ions depending on the transmembrane voltage (Figure 2.4). Within these, depending on the mechanism of

conduction through the membrane, it requires energy or takes advantage of differences in concentration and gradient, we find electrogenic pumps, ion exchangers and ion channels. Channels are grouped into families based on the ion to which they are permeable. But each family contains channel subtypes that differ in their electrical, pharmacological, and physiological role. Ion channels, characterized by their selectivity and operating states, are not randomly distributed in the membrane but rather are concentrated in specific areas according to their specific function, being common to group them in specialized areas.

The current-voltage (I-V) relationship of an ion channel gives us a lot of important information about its characteristics:

- ➢ If it passes through the origin, this implies that the channels are not selective for only a specific ion or that there is no effective gradient.
- ➢ When the number of open channels changes, due to changes in conductance, it results in a change in the slope of the I-V curve.
- ➢ The value at which the I-V curve crosses zero, the equilibrium potential, is very informative about the selectivity of the channel.
- ➢ Level of rectification. The conductance of the membrane can change with voltage, a phenomenon known as rectification in electrical circuits theory (the channels of biological membranes are open only at certain voltages and closed to others: Normal or 'out': closed at negative voltages, Anomalous or 'in': open at negative voltages).

Therefore, the electrical activity in cardiac cells is the result of differences in ionic composition between the extra and intracellular media, a complex process orchestrated by different types of channels, pumps and exchangers present in it, which gives rise to the action potential.

When the membranes of certain excitable cells, such as cardiac muscle cells, are depolarized by an electrical stimulus, they respond with an impulse. There is a trigger threshold, which depends on each cell type, which is the critical potential level (approximately -60 mV) that must be exceeded for the all or non phenomenon to occur. The mechanism occurs because the intracellular potential that was at rest, that is, polarized (negative with respect to the outside, polarized), undergoes a drastic change in polarity, with a transiently positive potential that rises above + 20 mV (depolarized cell), and later returning (re-polarization), more slowly, to its equilibrium state or resting potential (-80 to -90 mV). This transient variation in potential is called the action potential (AP), and it evolves independently of the presence of a stimulus and has a similar morphology for each cell type (Figure 2.5). The normal action potential is characterized by several phases, which are characterized by the activation of different currents, changes in the conductance of one or more specific ions. During the resting phase (stable and polarized cell) the intracellular potential is similar to the equilibrium potential of potassium ions (since during this phase the permeability to the potassium ion is much higher than the permeabilities of the other ions) and is the current anomalous potassium rectifier (IK1) which remains active during this period, since it presents a high conductance at negative potentials. The reverse rectification property causes it to deactivate during the plateau phase and progressively reactivate during repolarization of the cell. Furthermore, in this phase, the ATPase activity of the Na+K+ pump helps to

maintain equilibrium, which is the basic mechanism in establishing the resting potential. Whereas, the Na+ Ca2+ exchanger (NCX) is the main mechanism of calcium extraction from cardiac cells.

During the depolarization of the membrane (phase 0), of approximate duration 1ms (very fast response), the main current that intervenes is the fast or fast transient sodium current (INa). This is produced by a massive influx of Na+ ions into the interior through the opening of sodium channels (voltage-dependent) ***(Bers 2002)*** characteristic of muscle fibers and the conduction system. The current INa has a high peak value (due to the high conductance of these channels at these voltage levels) and causes a strong upward slope of the action potential, making the interior (intracellular space) more positive. This current remains inactive in the other phases of the action potential. In parallel, and after the activation of INa, a secondary current of calcium entry is activated in some species, which collaborates in the depolarization of the membrane. In phase 1, as a response to such rapid depolarization, while sodium channels are slowly being inactivated, an early repolarization occurs fundamentally mediated by the transient outflow current associated with potassium ***(Hoffman 2000)***, much more important in the epicardium than in the endocardium, and that makes the cell interior a little less positive. Although its activation and inactivation is independent of Calcium, it directly affects the duration of the potential since it controls the time course of other voltage-dependent conductances ***(Hoffman 2000)***. Another component of the transient outflow current associated with this phase is associated with chloride and dependent on calcium has been reported, the presence of which has been shown to be especially smaller ***(Spear 1982)***, faster and expressed only in the atrium. The importance of a

slow sodium current has been reported, whose activity is prolonged during the plateau.

Later in phase 2, the plateau of the action potential depends on a delicate balance between the input currents (depolarizing) and the output currents (repolarizing). It is characterized by a high resistance to ions, the potential remains almost constant slightly above 0 mV, since the exit of potassium ions (in greater quantity inside) is compensated by the entrance of calcium (in greater amount outside), achieving approximately an equilibrium before the entrance of positive charge. On the one hand, the calcium ions enter through the L-type channels (ICaL), and on the other hand, the potassium ions leave thanks to a sustained current of potassium formed by the delayed rectifier current, composed of two components: a fast one (IKr) and a slow one (IKs) ***(Sanguinetti 1990, Liu 1995)*** and a potassium plateau (IKp) ***(Yue 1988)***. The NaCa exchanger, whose current direction depends on the electrochemical gradients of the Na+ and K+ ions, also actively participates in this phase, which during the plateau change as a function of both voltage and intracellular calcium. Towards the second half of the action potential plateau, when Ca2+ has already accumulated inside, as a result of its entry through L-type channels ('long lasting'), the exchanger works directly with the introduction of Na + and, therefore, helping to maintain depolarization for a longer time lengthening the plateau phase ***(Weber 2002)***. A current called the non-selective calcium-activated (Ins) current has also been identified in some species ***(Ehara1988)***. Finally, a current that has been identified in humans, and it is of great importance in the case of early depolarizations, is the slow component of sodium channels ***(Maltsev 1998)*** which presents a slow decay.

The progressive decay of the Calcium current (inactivation of Calcium channels) together with the increase of the delayed or late rectification potassium current (IKr and IKs) at the end of phase 2, gives rise to a gradual decrease in potential. This produces the repolarization of the cell potential, or phase 3, in which the rectifying voltage-dependent potassium currents reach a large value ***(Rudy 2000)***. Furthermore, at the end of phase 3, the potassium current IK1 (incoming anomalous rectifier) appears, which progressively increases and helps to modulate the resting potential. This efflux of potassium ions removes the positive charge from the cell ***(Snyders 2000)***. Finally, returning to phase 4, the activity of both the NaK pump and the exchanger is evident. The Na^+-K^+ (INaK) pump and the Na^+-Ca_2^+ (INaCa) exchanger are the main active mechanisms used by the cell to keep the concentrations of the main ions stable, therefore essential for excitability ***(Fozzard 1994, MA 2000)*** . For their part, atrial cells have an action potential with a shorter duration, they have a large ICa^{2+}-L current, while the IK1 current is smaller than in ventricles, which explains why they have a less negative membrane potential and a slow phase 3 (repolarization). In some species, the presence of an ultra-fast late rectifier current (IKur) that participates in the repolarization of this action potential has also been identified. In the case of self-excitable cells (SAN node or AV node), where the phases are not so delimited, they are characterized by having in phase 4 the so-called pacemaker current (If). This current is the result of the entry of sodium ions accompanied by a lower permeability for potassium, which facilitates reaching the threshold value and causing the potential to be triggered again.

As can be seen in Figure 2.5., the atrial and ventricular action potentials are different due to the differences in the ion channels present, as well as the relative expression of these ion channels.

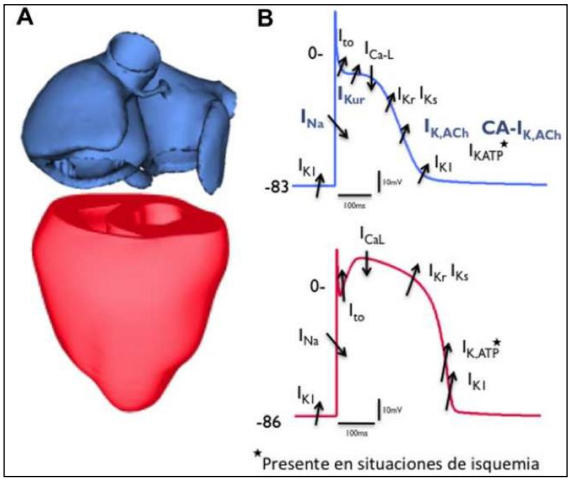

Figura 2.5. Action potentials from atria and ventricles including the major ionic currents.

Under normal conditions, the generation of the ECG depends on four electrophysiological processes: the formation of the electrical impulse in the main pacemaker of the heart, the transmission of this impulse through the fibers specialized in conduction, activation (depolarization) and recovery (repolarization) of the myocardium. In Figure 2.5, the different typical membrane action potentials for atrial and ventricular muscle, and conduction system, are observed.

In the ECG registration, the first wave is the P wave, this is a consequence of the electrical activity that precedes the contraction of the fibers of the atria during atrial systole (its small amplitude is due to the fact that the atrial fibers exist in a comparatively much lower number than the fibers of the myocardium responsible for the rest of the waves) and usually lasts

approximately 100 ms. The period between the end of atrial repolarization and ventricular depolarization is reflected in the PR segment, considered practically isoelectric (without activity) since it refers to the conduction of impulses through the His bundle towards the Purkinje fibers, and the cells involved are few (advanced averaging techniques and specific amplifiers are needed to capture them). Subsequently, contraction of the ventricular fibers produces three waves, known as the QRS complex, lasting approximately 70 ms. The time between two R waves is what defines the heartbeat. The dispersion in ventricular repolarization is what leads to the inscription of the T wave ***(Plonsey 1995, Mohrman 2006)***.

2.1.4. The Electromechanical Function. Excitation-contraction Coupling.

Excitation-contraction coupling (EC or ECC) in cardiac tissue is the process that communicates the electrical excitation of the myocyte - individual cardiac cell - (action potential) with the mechanical contraction of the cardiac muscles ***(Bers 2002)***. A synchronized mechanical contraction is necessary to propel the blood out at a sustained pressure. ECC involves the dynamics of Ca2+ ions, which are the direct activator of myofilaments.

The cells of the cardiac muscle have the following basic structures involved in this process: (1) an extensive myofibrillar structure composed of myofilaments arranged in serial units called sarcomeres, which are responsible for the mechanical processes of shortening and tension development; (2) an internal compartment of the cytoplasm called the sarcoplasmic reticulum (SR), which stores calcium during the diastolic interval with the help of a calcium-storage protein; (3) extensive invaginations of the cell membrane (sarcolemma), called T tubules that

accumulate most of the cell's L-type calcium channels and (4) large numbers of mitochondria that provide ATP to meet the demanding metabolic needs of muscle cardiac. The following Figure 2.6. shows the whole process:

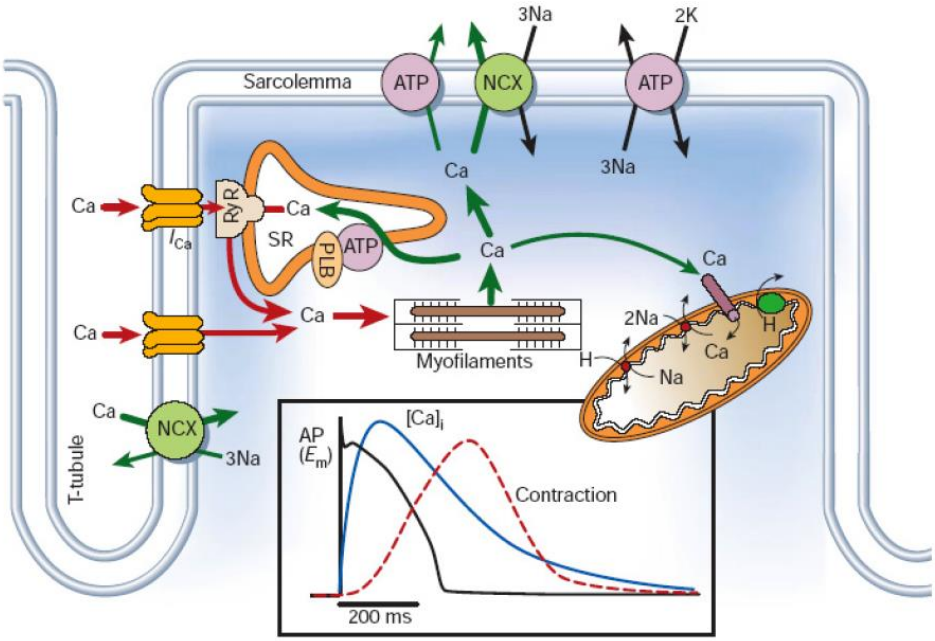

Figura 2.6. The process of Excitation-Contraction Coupling and its relationship with the dynamics of intracellular Ca2 + in cardiac cells. *The time evolution of a typical AP is shown, as well as the dynamics of [Cai]$^{2+}$ ions and mechanical contraction, measured at 37º in rabbit myocytes.* ***(Bers 2002)***

In the cytoplasm there are structures capable of actively storing calcium, such as the cisternae of the endoplasmic reticulum (ER) or the sarcoplasmic reticulum (SR) in muscle cells, so that the cell has an intracellular store of calcium which it can have for its activity (for example, when they are excited) essential in the triggering of the contractile process. In skeletal muscle, the EC process involves a direct protein-protein interaction between two different classes of ion channels: the ryanodine receptor (RyR1) ***(Franzini-Armstrong 1997, Williams AJ 1997)*** which is present in the

sarcoplasmic reticulum (SR) and the dihydropyridine receptor (DHPR) on L-type calcium ion channels of the sarcolemma. Calmodulin is an intracellular regulatory protein that acts as a calcium receptor and that, apart from influencing the interaction of the two previous proteins, plays an important role in the Calcium-dependent inactivation of L-type Calcium channels through DHPR. The channels associated with the RyR1s receptors are ligand-operated calcium channels, and are responsible for releasing calcium from the SR, being the main mediators of this process. These channels are either associated with specific channels or are activated through second messengers.

In response to an electrical depolarization of the sarcolemma, at which time the process begins and the calcium concentration increases in the space near the L-type calcium channels and second messengers concentrated in greater density in the T-tubules, the voltage of the DHPRs (L-type channels and their conductance) is activated and moves (at a certain threshold), at the same time that the calcium channels are opened (potential phase 2, process activating current). This injection of calcium, together with the initial abnormal operation of the exchanger (reverse mode, introducing calcium, facilitated by the high degree of depolarization of the membrane at this stage and the high concentration of sodium) increase the concentration of calcium near the SR receptors, promoting the opening of the RyR1s receptor channels due to a conformational change and adherence of calcium ions in these, and inducing a rapid release of calcium from the SR into the cell intracellular space. This process is known by the name of Calcium Induced Calcium Released ***(Bers 2002)***: it is a positive feedback mechanism, a small amount of Calcium in the cytosol near the receptor causes the release of even more quantity. Each sarcolemmal voltage-gated calcium channel controls a series

of sarcolemmal receptors (this is mediated by proximity). This release of calcium into the T-tubules has a direct relationship both with the duration of the action potential and with the increase in free calcium in the intracellular medium.

The contractile machinery is represented by the myofibrils composed of contractile units called sarcomeres, where some filaments can be distinguished: fine actin filament (containing an elastic protein that recovers the length of the myofibril after contraction) and the thick filament formed by myosin . This drastic increase in intracellular calcium levels will interact with the proteins of the contractile machinery, binding to the troponin-C protein (part of the troponin complex of actin filaments that has an affinity for calcium), producing a conformational change (hydrolyzing ATP in this process and adding a new molecule), interacting actin and myosin, which causes muscle shortening (shortening of the sarcomere), contraction. The process then depends on three basic factors: the amount of calcium released by the ICRC, the intracellular stores of ATP, and the number of conformational changes that take place per unit of time. This cycle continues until intracellular calcium levels are reduced. The relaxation process involves the release of calcium from the intracellular environment. The greatest contribution in this regard is that of calcium-dependent ATPases, both from the sarcolemmal membrane and the SR reticulum. Calcium ions enter the SR through the Ca2 + ATPase pump (also called SERCA, from the English Sarco Endoplasmic Reticulum Calcium ATPase), which represent more than 90% of the protein structures of the SR membrane, from which their importance in relaxation (brings back about 80% calcium). This protein for each mole of hydrolyzed ATP returns 2 molecules of calcium to the interior of the reticulum, helping to empty the cell of calcium in relaxation.

It is regulated by the phosphate receptor protein, phospholamban, which inhibits it when it is not phosphorylated. The calcium incorporated into the SR through these pumps is stored bound to the calsequestrin protein that is found in the part closest to the T-tubules, already available for the release process, completing the cycle ***(Rudy, 2000)***.

This reduces the level of intracellular calcium, preventing it from continuing to bind to Toponin C. But other mechanisms such as the activity of the exchanger (mainly NaCa, which depends on both the membrane potential and the concentrations of both ions on both sides of the membrane), and constantly the mitochondria (although to a lesser extent). As can be deduced, intracellular increases in calcium can be buffered or stabilized by calcium-binding proteins (such as calmodulin, calsequestrin or troponin) to mediate different calcium-dependent processes. These proteins, while the calcium concentration values cease, contribute to trigger compensatory mechanisms that restore them.

2.1.5. Normal and Abnormal Impulse Propagation

It has been seen that under normal physiological conditions, the Sino-Atrial node (SAN) is the natural pacemaker of the heart, it depolarizes spontaneously and continuously (normal sinus rhythm). The excitation wave is routed through the chambers of the heart, channeled through the atria through the AV node, and into the ventricles through the conduction system. This causes the activation of intracellular calcium processes, developing in a precise and coordinated way the excitation-contraction cycle, which allows the heart to pump oxygenated and clean blood (with nutrients, immune cells and regulatory molecules) to the body's organs. The normal cardiac cycle, atrial contractions followed by ventricular contractions in a synchronized

manner, allows blood to be effectively pumped out of the heart. But this automatism, like any other complex machinery, can be subject to problems in its electrical system (that feeds it), alteration of the automatism or, that of the conduction system, and therefore interfere with the effective pumping of blood.

The propagation of PA occurs through the conduction system until it reaches the myocardium, where it spreads cell by cell, through special channels located in the intercalary discs (between myocytes in the axial direction). This is how what are known as 'gap junctions' are formed, by means of connexin proteins that promote intercellular propagation of the cardiac impulse and that allow neighboring cells to develop their AP.

The speed at which the action potential propagates is not constant (neither uniform nor continuous), but depends on the properties (both active and passive) of the medium (anisotropy) and the frequency of stimulation. In general, the factors that can affect the propagation of electrical activity in the myocardium are ***(Garny 2008)***:

- Excitability: ease with which a cell reaches its threshold for the generation of the action potential before a current stimulus.
- Refractoriness: the fact that to ensure that a reactivation does not take place in the same cycle, the cell cannot be re-excited immediately after having generated the action potential, it needs to have reached the equilibrium potential in order to develop a new potential. In the absolute refractory period (PRA), the membrane does not respond at all, since the sodium channels are already open or closed and deactivated. As of the effective refractory period (PRE

or ERP), the membrane is already responsive. These are responsible for temporary conduction blockages during unusual electrical conductions.

- Restitution or recovery: dependence of the duration of the AP on its recovery time (if the time between two potentials is too short it will cause the next AP to have a shorter duration).
- Dispersion: dependence of the wavefront with the recovery time. The wave will slow down if it travels through recently recovered tissue.

For this reason, the dependence on the stimulation frequency (both on the electrical properties of the cells, and consequently on the conduction speed) is known as restitution of the electrical characteristics of the cells. To study this phenomenon, the electrical restitution curve (ERC or APDR) is used, this curve being of great importance in the field of arrhythmogenesis. This curve is defined as the variation of the duration of the action potential with respect to the previous diastolic interval (DI, diastolic interval) ***(Franz 2003)***, where DI is the time that elapses from the end of the repolarization of the previous AP to the beginning of the generated AP by the next stimulus. The characteristics of the mechanisms for reducing the conduction velocity, blocking and generation of reentrant arrhythmias depend on the characteristics that are associated with both the source and the loading of the tissue. In general, the factors that affect the source include the maximum depolarization speed, the maximum amplitude that it can generate, and in some cases, also the duration of the potential. Of course, the passive properties of the tissue can also influence and modulate the amount of current that a source is capable of delivering. Among the factors that affect the properties of the loading tissue are the intrinsic membrane

resistance/capacity, the threshold level of excitation of these cells and the difference between the threshold level and the membrane potential at a given time.

Now, if the conductive pathways are damaged, the normal rhythm of the heart is disturbed. Such abnormal patterns of cardiac electrical activity are known as arrhythmias. To understand the subsequent processes that trigger these rhythmic alterations, it is necessary to clarify basic concepts associated with the propagation of the impulse from the conduction system to the myocardium, as well as between different regions of the heart muscle.

As stated above, the propagation in the myocardium is not uniform and continuous, it depends on the properties of the environment in which it is propagated. It is important to know that the source-sink relationships are changing in different regions of the myocardium. When an ionic current is applied to a cell (for example, the entrance of the Purkinje network to the myocardium), a voltage gradient is generated between it and neighboring cells. The electric current therefore travels in that direction. Under these conditions, the depolarizing input current (which travels in the direction of the gradient from the active cell), is called a 'source' of electrical charge to neighboring cells, which act as 'sinks' of said current. Immediately neighboring cells ('receptors') begin to depolarize due to the arrival of positive charges. On the other hand, for distant cells, the electric potential they reach is subthreshold, and their amplitude decays exponentially with distance. There is, therefore, a phenomenon of 'charge effect' that is imposed by the cells in the direction of propagation on the activated cell, that is, they attract charges away from the membrane (capacitor) of the local cell in the process of activation and therefore they contribute to prevent their depolarization. Therefore, even in physiological situations, due to the

structural distributions of the surrounding tissue (environment), the local heterogeneity of its active properties, or aggravated by pathological remodeling, source-sink mismatches can cause discontinuities in propagation ***(Hoffman 2000)***.

This introduces the concept of 'minimum length or area' and 'security in propagation'. According to the first, the success or failure in propagation will be determined according to whether the density of the source depolarizing current (represented by the current INa) can exceed the repolarizing current density in the direction of propagation (represented by the current IK1) – Figure 2.7.-. Therefore, the sinks in the direction of propagation are not passive, but active, (because the repolarizing currents are still active at all points), they dynamically oppose the depolarization of the fibers ***(Hoffman 2000)***.

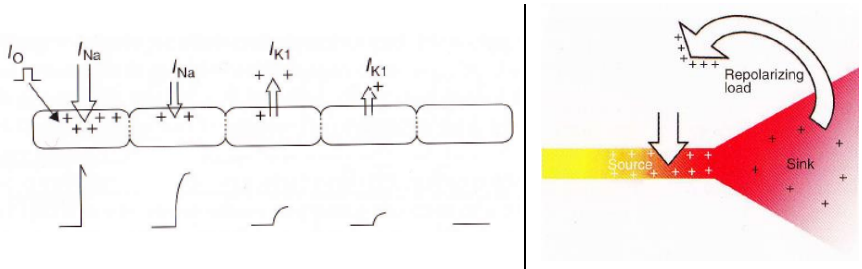

Figura 2.7. Propagation of impulse, 'source-sink' relationships. *Left Local propagation from source (activated cell) to sink (cells at rest in the direction of propagation). Right. Source-sink mismatch due to changes in geometry in the direction of propagation.*

The propagation safety factor is a way of quantifying the continuity of electrical propagation in cardiac tissue. It is about quantifying the excess current that a cell can receive (source or current available to excite) in relation to the amount of current necessary to depolarize it (sink or current

necessary to excite a group of cells) ***(Rudy 1987 1D, Boyle 2010 2D).*** This concept is more complex in tissue than in fiber since the curvature of the wavefront is put into play as well as the conditions of structural heterogeneity and electrical dispersion of the tissue and not only the relations of excess excitatory current and current necessary to be excited. a cell. In tissue, geometric factors, for example, can cause a drop in the safety factor that causes a decrease in the conduction speed, the appearance of repolarization electrotonic current and the possibility of unidirectional blocking and reentry generation, as occurs in the connection points. between Purkinje networks and myocardial tissue. A simple way to explore propagation safety qualitatively, albeit indirectly, is to study the vulnerable window and associated phenomena. For example, the decrease in the conduction velocity, the presence of blockage without re-excitation and the appearance of reentry phenomena in the tissue. Typically this study is done by applying two stimuli that are increasingly close to each other (coupling interval) and classifying the continuity of propagation, allowing a simple qualitative comparison between different groups.

Finally, it is interesting to clarify the concept of vulnerable window. Vulnerability can be defined as the susceptibility of the myocardium to a stimulus that changes abruptly from a normal rhythm (with a synchronous contraction) to one with greater frequency (which is initially synchronous, but eventually switches to an asynchronous one). However, the vulnerable period refers to the time interval during which a premature stimulus is capable of generating a reentry. The duration of this interval depends on the amplitude and duration of the premature stimulus. This needs to exceed the threshold required to generate a propagation of said stimulus. The width of this interval is approximately the same time required for activation (or

recovery) of full propagation through the ventricle. The vulnerable period is easily understood if it is recognized that there is a critical point in the recovery of cellular excitability that separates the state of excitability from the state of refractoriness. In summary, all the factors mentioned that contribute to regulate the spread of AP through cardiac tissues are: physiological, such as the balance of source-sink currents, the level of intercellular communication, the intrinsic heterogeneities of the tissue, etc; as well as pathological, which are critical in determining the degree of discontinuity in propagation, as well as its dependence on frequency.

2.1.6. Basic Mechanisms of Arrhythmia. Reentry.

If the conductive pathways are damaged, the normal rhythm of the heart is disturbed. Such abnormal patterns of cardiac electrical activity are known as arrhythmias.

In Figure 2.8. a traditional general classification is shown, depending on whether it comes from an alteration in the propagation or generation of the impulse.

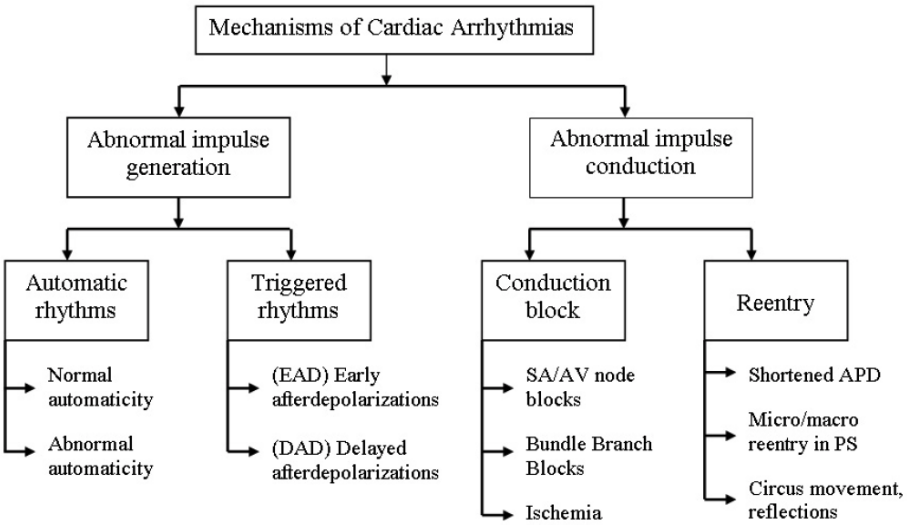

Figura 2.8. Basic Mechanisms of Arrhythmias. Basic general classification

Depending on the criteria chosen, cardiac arrhythmias can be classified in different ways. If this is due to a rhythm disturbance, they can be classified into: bradycardia (slower than the normal heart rate) and tachycardia (faster than the normal heart rate). Any of these prolonged arrhythmias can lead to cardiac fibrillation, which is the complete disruption of the electrical activity of the heart. Additionally, arrhythmias can originate in the atria and ventricles. Those that start in the atria are called atrial or supraventricular arrhythmias (above the ventricles). They include supraventricular tachycardias (paroxysmal supraventricular tachycardia), atrial flutter (AFl), and atrial fibrillation (AF). Generally, atrial arrhythmias are less severe than ventricular arrhythmias, which can be life-threatening. On the other hand, the most common ventricular arrhythmias include premature ventricular contraction (PVC), ventricular tachycardia (VT), and ventricular fibrillation (VF). The latter is the leading cause of sudden cardiac death. According to the above classification, alterations can occur in the generation of impulses

by the pacemaker cells or the impulse conduction system ***(Hoffman 2000, Spear 1982)***.

In summary, cardiac arrhythmias, or rhythm disorders, are conditions in which a failure occurs in the timing and/or coordination of cardiac contraction. Arrhythmias are mainly caused by either the abnormal formation of the excitation wave, a failure or abnormal performance in propagation, or a combination of both. The heart, as a result, may begin to beat excessively fast (tachycardia), too slow (bradycardia), or irregularly (extrasystoles or premature beats). As explained, in normal sinus rhythm, each excitation is generated by a new pacemaker impulse from the SA node. However, in some unusual circumstances the activation wavefront travels around a physical obstacle or a piece of abnormal tissue continuously exciting an area of heart tissue. This phenomenon is called reentry and is believed to be the primary cause of cardiac arrhythmias.

Under normal conditions, a single impulse generated in the SAN activates the atria and ventricles. The impulse propagates, giving rise to an activation wave that depolarizes adjacent excitable tissues and leaves inexcitable tissue behind. When this wave of activation reaches the end of the muscle and is surrounded by inexcitable tissue, it is extinguished. Until a new sinus impulse is generated, the heart will not be activated again. However, in certain circumstances, the activation can persist without extinguishing in an area of the heart, long enough for the neighboring tissue to regain its excitability (thus exceeding its refractory period), with which the same impulse partially re-excites or totally the heart. This stimulus is called a reentrant stimulus, and the mechanism by which it occurs, reentry. Reentry was first properly described by Mayer ***(Mayer1908)*** in 1908, in the jellyfish

ring of nervous tissue. There are two types of reentry: anatomic and functional. This disturbance in the propagation of the potential can be the result of multiple factors, and its importance lies in the fact that it is one of the main mechanisms associated with fibrillation and sudden death. Its spontaneous or sustained presence depends on the simultaneous presence of an arrhythmogenic substrate and a trigger (premature beat), with two essential conditions: the existence of a unidirectional block in the propagation of the impulse, as there are differences in the effective refractory periods in adjacent areas (vulnerable window in the region with the longest refractory period), and the combination of a slow conduction with a short refractory period in the alternative pathway, allowing the reentry of the impulse ***(Henao 2007)***, being therefore highly favored by the intrinsic electrophysiological heterogeneities existing in the re-excited tissue. Therefore, one of the main causes of unidirectional block is regional differences in recovery of excitability. The third pillar that allows the maintenance of reentry is the presence of an autonomic imbalance (arrhythmogenic substrate), which, acting through numerous mechanisms (modulators), completes the elements of the well-known Coummel triangle, in the center of which it should have a special role is myocardial ischemia (local-temporal blockade anemia), since it is the most frequent cause of reentrant phenomena, tachycardia.

The heterogeneity of both functional cardiac tissue, with a different electrical behavior in myocytes, and biochemistry, due to the different ionic concentrations in ischemia, alters the electrical behavior and generates dispersion in the repolarization of the action potential, for which it becomes a functional substrate for the generation of reentrant arrhythmias. In any case, the formation of transmural repolarization gradients between the different

cells of the ventricle does not seem to be sufficient to promote the formation of arrhythmias.

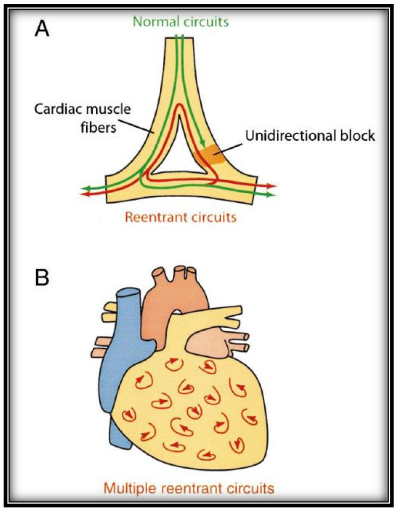

Figura 2.9. Basic scheme functional and anatomical reentry

However, the remodeling of ion channels and/or resistance associated with intercellular spaces in some entities may be sufficient to increase the dispersion of transmural repolarization and, thus, the risk of reentrant arrhythmias. Electrophysiological factors that favor reentry include: a decrease in conduction velocity and a shortening of the refractory period, as well as the dispersion of the action potential duration (APD) and refractoriness. These circumstances, together with the appearance of a premature stimulus, can create a unidirectional blockage in the tissue, and therefore, a reentry. The appearance of this stimulus may be due to the abnormal automaticity of some group of cells. In clinical practice, the enlargement of the heart, drugs that alter refractoriness (and APD), and the existence of areas of ischemic tissue can also facilitate the reentry phenomenon. Excitation can be random or organized: the difference between the two is the way the impulse spreads, either over pathways that continually

change site and location (fibrillation), or through relatively fixed reentry pathways (atrio-ventricular tachycardias by reentry).

2.1.7. Atrial Fibrillation. Epidemiology and Treatment.

Atrial fibrillation (AF) is a supraventricular arrhythmia characterized by uncoordinated activation, a rapid, disorderly and desynchronized atrial rhythm, without the ability to generate effective atrial contractions. It usually begins with one or more very early atrial extrasystoles that fall into the vulnerable atrial period, leading to repeated re-excitation of the atrial fibers. During this arrhythmia, atrial electrical activity is characterized by being formed by a set of rapid and disorganized propagations that vary in amplitude, duration, extension and shape, which is reflected in the electrocardiogram as a rapid and disorderly oscillation of the baseline (F waves, Figure 2.10). Furthermore, the appearance of this type of conduction in the atrium is associated with an abnormally rapid and irregular ventricular response, even though conduction in the atrioventricular node is intact.

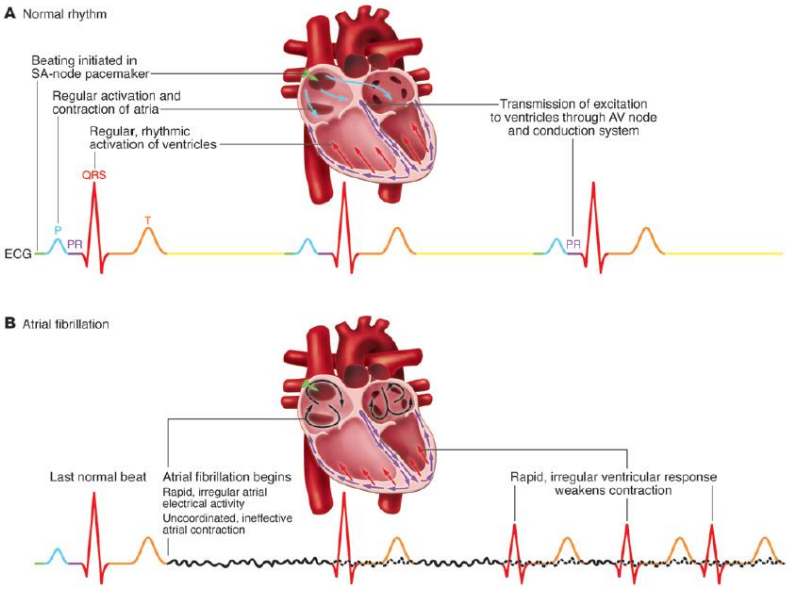

Figura 2.10. ECG V1 records during Sinus Rhythm and Atrial Fibrillation. *[Modified Wakili-Nattel 2011]*

Associated with the risk of stratification in other heart diseases (hypertension, coronary heart disease, etc.), AF is related to an increase in morbidity and mortality. AF negatively affects the quality of life of the patient, as the atrium does not function mechanically, the blood remains stagnant in its compartments, increasing the probability of suffering thromboembolisms in other parts of the circulatory system. About 15% of strokes are the result of AF.

The incidence of AF in the same patient can be variable over time, however, this recurrence is very useful for the clinician when making a diagnosis. The classification based on the most common incidence depends on whether it is self-limited or more episodes appear.

In contrast to other arrhythmias for which effective therapies have been developed, the assignment of a therapy that successfully ends fibrillation

episodes remains of great difficulty, since it is not known with certainty what is the mechanism that causes AF in the vast majority of patients. Due to this lack of knowledge, various therapies are used with greater or lesser success, among them pharmacological treatment, electrical cardioversion and ablation of the areas of the atrium responsible for the arrhythmia. Despite the latest technological advances and the understanding of their mechanisms, derived from experimental models, as well as ablation procedures in patients with AF, anti-arrhythmic drugs continue to be the main strategy for cardioversion and maintenance of sinus rhythm . In those patients in whom the AF is persistent and atrial tissue remodeling has not yet occurred, the arrhythmia usually ends after cardioversion. However, the addition of antiarrhythmic drugs to cardioversion has been shown to decrease recurrence rates. New generations of anti-arrhythmic drugs have reached clinical practice, and others are in the experimental phase. The new drugs act more specifically on atrial ionic currents and at the same time involved in the maintenance of arrhythmia. At the same time, more and more importance is given to the need to act on the atrial arrhythmogenic substrate and the factors that promote it, implicated in the long-term maintenance of the arrhythmia ("up-stream" therapies) ***(Filgueiras-Rama 2012)***. Thus, in addition to rhythm control strategies, these therapies consider the regulation of intracellular Ca2 + homeostasis, the regulation of union channels or 'gap-junctions' or alternatives that attack remodeling through factors and cytokines generated by fibrotic tissue, as well as those that affect the interaction dynamics between fibroblasts and cardiac myocytes to try to control arrhythmias in chronic stages.

The problem of drugs currently accepted for clinical use, due to their minimal toxicity and side effects, lack effectiveness and are limited in terms of efficacy and safety, probably because they are not designed in a 'specific'

way to treat the underlying pathological mechanisms. Advances in basic research technology, with the help of in silico modeling and new signal processing and data mining techniques, have shed light on the mechanisms of AF and proposed new rhythm control strategies. ***(Heijman 2013)***

For those patients in whom the AF is permanent, and the atrial tissue is subjected to remodeling, therapies that seek to restore the normal rhythm in the atrium are abandoned, and thus the is the question of keeping the rthythm control, by pharmacological means, for ventricular protection.

A type of ablation scheme, known as MAZE ***(Calkins 2007)***, is also commonly used in patients in whom the maintenance mechanism of AF is assumed to be of the multiple wave type, usually associated with permanent AF. MAZE ablation (Figure 2.11), consists of a series of standard ablation lesions through the atrium, in order to separate the tissue into smaller areas. With this, it is intended that the area of each separated region is insufficient for the maintenance of the arrhythmia by means of the multiple wave mechanism, since there is not enough space to house the necessary number of wave fronts to maintain fibrillatory propagation. In patients in whom AF is caused by unusual activity in an area of the atrium, may be beneficial electrical isolation of the proarrhythmic tissue of the atrium by ablation of the surrounding tissue (primarily pulmonary vein isolation). This type of mechanism tends to be more common in paroxysmal AF than in the persistent or permanent type, since the proarrhythmic tissue is focused in this region and the rest of the atrium has not yet undergone significant structural remodeling.

In order to improve the ablation procedure in those patients in whom it is assumed that the mechanism of initiation/maintenance of AF is the primary

generator, several authors have focused on the search for proarrhythmic areas by means of recording techniques of atrial electrical activity during AF. In such a way, the location of the area that induces AF allows personalized treatment of each patient based on their specific type of arrhythmia, thereby trying to improve the recurrence rate by minimizing the cauterized tissue.

Spectral analysis and the calculation of the dominant frequency have been proposed to locate these areas of proarrhythmic tissue. Studies in humans with paroxysmal AF have shown that ablation of these sites is highly successful in terminating AF if there are frequency gradients across the atria ***(Sanders 2005, Atienza 2011)***. Success resides in the hypothesis that the maintenance mechanism of these AF is the presence of a high frequency primary generator (ectopic focus or mother rotor) leading to the rest of the atrial tissue, where the area of the posterior wall of the left atrium concentrates the fastest periodic activations. This therapy is not as successful when applied to permanent type AF. Frequency gradients are also found in these patients, although normally the area with the highest dominant frequency does not coincide with the pulmonary veins, and ablation of these regions does not usually end the arrhythmia. On the other hand, other authors defend the possibility of finding these proarrhythmic areas of the atrium by using the local determination of complex fractionated atrial electrograms (CFAEs) ***(Atienza 2011)***. These authors defend that CFAEs are formed in the areas of less conduction and / or pivot points where the wave fronts rotate on themselves (Figure 2.11 (d)).

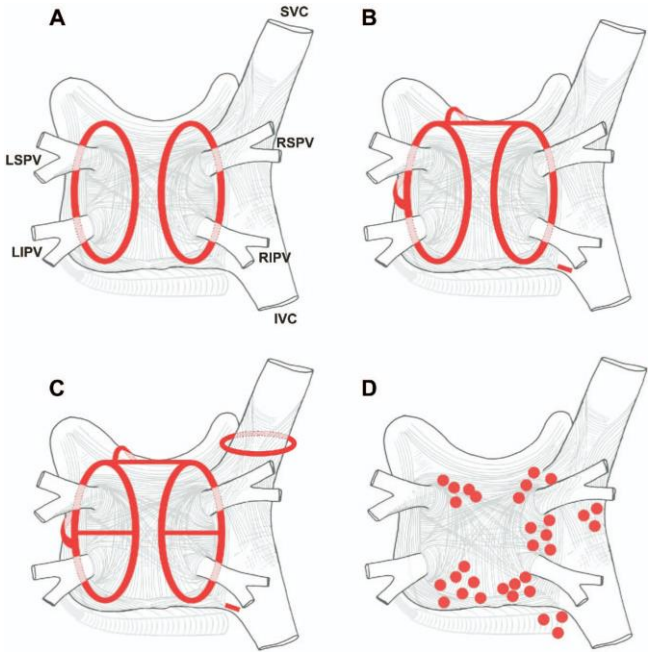

Figura 2.11. Scheme of types of ablation for the treatment of AF*: A) isolation of the pulmonary veins; B) isolation of the pulmonary veins with lines to avoid large reentries; C) similar to B including individual isolation of each pulmonary vein and superior vena cava. D) most common ablation points when CFAE are found*

2.1.8. Theories and mechanisms. Heterogeneity.

The mechanisms underlying AF are very complex, combining spontaneous ectopic activity and fibrillatory activity secondary to reentry and microreentrant phenomena due to high structural and functional heterogeneity of the atrial tissue. At present, the mechanisms that cause the initiation and maintenance of AF are not exactly known. There are various theories that attempt to explain the chaotic behavior of the atrial ***(Jalife 2011)*** (Figure 2.12). The first is the focal theory, in which the disorganization is caused by one or multiple foci, other than the sinus-atrial foci, which are activated spontaneously **(*Mines 1992, Allessie 1995*)**. The second theory is

similar to the first, there is an area of the atrium that causes the entire irregularity of it, but in this case due to a re-entry or re-circulation of the electric wave ***(Jalife 2002, Atienza 2006)***. In contrast to the first two, there is the theory that chaotic electrical activity is self-sustaining due to the existence of multiple waves throughout the entire atrium that collide with each other ***(Allessie 1995).*** While this last theory maintains that the chaotic electrical activity is caused in the whole of the atrium, the other two defend that it is an area of it, either through an ectopic focus, or through a reentry, which dominates the total electrical activity.

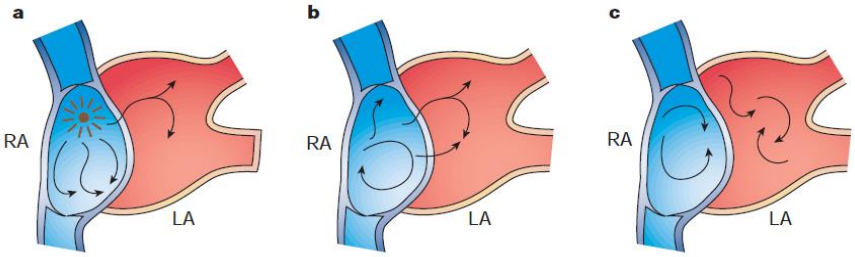

Figura 2.12. Theories of Atrial Fibrillation [Modified Nattel 2002]

Currently, the different theories that try to explain the mechanisms of initiation and maintenance of atrial fibrillation distinguish two lines of general thought, the focal theory, which suggests that AF is caused by the irregularity present in the interactions between the high-frequency wave fronts produced by a primary generator (ectopic focus or reentrant circuit, typically located around large veins or ligaments –VCS, LM, VP PPI, RSPV, LIPV, CS-) and the variable refractoriness properties present in atrial tissue, and the theory of multiple waves or generalized fibrillatory activity, where the irregular activity of the atrium is a consequence of the primary arrhythmogenic mechanism but self-maintenance is guaranteed by the substrate, a high degree of dispersion and heterogeneity in the refractoriness

of the tissue, and the delay and heterogeneity in the driving force. The cardiac myocardium is an especially heterogeneous organ and this condition is favored when the myocardium is remodeled. Although there is clinical evidence that supports both theories, observations in the last decade using techniques that allow recording cardiac electrical activity with high spatiotemporal resolution (in basic research) ***(Jalife 2003)*** and very recently intracavitary recordings with high-resolution multi-electrode catheters (in clinical research), have made the hypothesis of sources of reentry (mother rotor) and generation of fibrillatory activity, the dominant theory to explain the mechanisms of perpetuation of AF ***(Jalife 2011).***

Recent observations on the onset of AF from the pulmonary veins ***(Maltsev 1998)*** and optical mapping studies argue that mother rotors and the fibrillatory conducitons spreadinf produced by them, are the mechanism for AF perpetuation ***(Rudy 2000)***. This suggests that the mechanism underlying AF is complex and may include mechanisms in which ectopic activity, circular reentry, and wavefront fractionation are present, both simultaneously and in different stages of AF.

In addition to these theories in patients with persistent and permanent AF, the specific substrates of the patients are very important. The complexity of the pathophysiology of AF is complicated as it remains sustained longer in the myocardium. These processes are called electrophysiological remodeling. These are alterations in various properties of the atrial tissue as a consequence of AF that further favor the initiation and maintenance of this arrhythmia. Depending on the time that AF is maintained, we can distinguish three basic types of remodeling: electrical (from the first episodes there is progressively a shortening of the PRE), contractile (hypersensitivity and loss

of contraction force persists even after reversion to sinus rhythm) and structural (appears when AF is maintained for long periods of time and is associated with collagen deposition, the appearance of fibrosis, myocardial dilation, and increased activity by non-myocardial species such as fibroblasts; this is associated with chronic AF in patients with persistent and permanent AF, and may not be reversible even when AF is interrupted). Therefore, both with age and in the diseased heart, the atrial wall is remodeled. Age is associated with electrical remodeling with the appearance of regions with delayed conduction, areas of low intensity, and marked changes in electrophysiology. These changes are even more marked in patients with chronic AF. Atrial dilation can result as a consequence of a disorganized contraction, which due to the intrinsic mechanical-electrical feedback of the heart can lead to alterations in the electrophysiological activity of the tissue. The structural remodeling associated with atrial dilation is also commonly associated with a remodeling of the extracellular matrix that results in an increase in the deposition of fibrosis. An area especially sensitive to atrial dilation are the pulmonary veins, which alone can produce an increase in ectopic activity. If these patients also present AF, it has been shown that the myocytes suffer hypertrophy, and are surrounded by even more fibrosis than normal, which contributes to discontinuous spread towards the atrial myocardium of the posterior wall.

2.2. Technical Background

Mathematical models and computer simulation are crucial elements and tools of both Science and Industry. The rapid development of hardware and the drastic improvements in the behavior of numerical algorithms, combined, make the increasingly detailed description of physical and biological phenomena, the basic pillar for the development of precise simulations of

increasing predictive value. Cardiac arrhythmias and sudden cardiac death are among the most common causes of death in industrialized countries, making them one of the most important and established areas of research in recent decades. Despite years of research, its causes and mechanisms are very poorly understood. One of the applications and trends of the theoretical studies of these mechanisms is the computer modeling and simulation of the heart, using anatomically and physiologically detailed and precise models, at different levels of integration, in addition to being a fundamental support tool for many reasons. mainly because the possibilities of clinical and experimental study are very limited at a practical level, apart from the intrinsic ethical and normative issues, especially in the human case. To build a model with these characteristics, a researcher must collect a wide variety of documentation and information from different books and articles published in different areas: biology, physiology, electrophysiology, advanced numerical algorithms, computer programming, etc. Models of cardiac activity based on experimental observations have been developed in parallel with advances in electrophysiology since 1960, since the first models of potassium channel activity and their modeling, employing extensions of the formalisms introduced by Hodgkin and Huxley in 1952 for the squid giant axon (excitable nerve cells). The first models including calcium balance and the importance of sodium channel signaling emerged in the 1980s. Since 1990, these models have been incorporating a greater level of detail or being incorporated into models at higher levels of integration, in addition to becoming more and more specific (cell type and subtype, species type,…).

This development and improvement of the models at their level of realism is a direct result of the continuous interaction between experimental studies and

the development of models for simulation and their learning from the errors of their predecessors. There is currently a great variety of models, differentiated by their level of description, formalities, level of application, experimental data to which they fit, etc; and depending on the type of application and the objectives, one or the other will be more interesting. The current level of development and refinement of the models allows to begin to focus their use on specific applications, such as the development or challenge of drugs and pharmacological agents, saving large amounts of money for pharmaceutical companies and improving the understanding of behavioral mechanisms. and cardiac tissue dynamics. To carry out simulation studies at any of the integration levels (from activity through a specific ion channel, through its contribution to cellular electrical activity, and the phenomena of propagation and electrical conduction in 1D, 2D and 3D , to the complete organ on a large scale), it is necessary to start from a model or mathematical description, which, on the one hand, reproduces detailed properties. For the study in healthy or pathological conditions of said activity in the human ventricle, it is first necessary to build a model at the level of a single cell (0D) that reproduces these properties: main ionic currents that contribute to the potential, dynamics of the main ions (mainly calcium transients), morphology of the action potential and its duration, etc., being at the same time sufficiently efficient computationally according to the level of integration in which it is intended to investigate, according to the objectives, with the work environment and the numerical tools at our disposal.

2.2.1. Registration Techniques

Extensive experimental observations about the electrophysiological properties of cardiac cells have been carried out in the last decades, within

which the creation of techniques such as: voltage clamp, patch clamp, etc. can be highlighted. These results allow the obtaining of precise measurements of the currents that cross the membrane and their properties, allowing to clarify the functioning of the cardiac muscle. Between 1930 and 1940, Hodgkin and Huxley, Cole and Curtis, were able to measure the action potential of a giant squid axon with a micropipette that contained an electrode and that was introduced inside the cell (Figure 2.13). -Only population-based-). The studies carried out at this time laid the basis for the most important concepts of the ionic theory of electrical transmission and gave rise to a new experimental technique that was for more than 50 years the best technique for the study of ion channels: voltage clamp or controlled voltage (potential clamping technique), avoiding the capacitive component of the membrane current. Most of the knowledge on the dynamics of intracellular currents is due to this technique ***(Cole 1955)***. It consists of applying a known voltage across the membrane (fixed, in the form of a pulse, keeping it constant in the study interval) and measuring the current that flows through it to calculate the conductance of the membrane. This technique has been widely used, not only for the characterization of known ion channels, but for the identification of new channels and proteins associated with them.

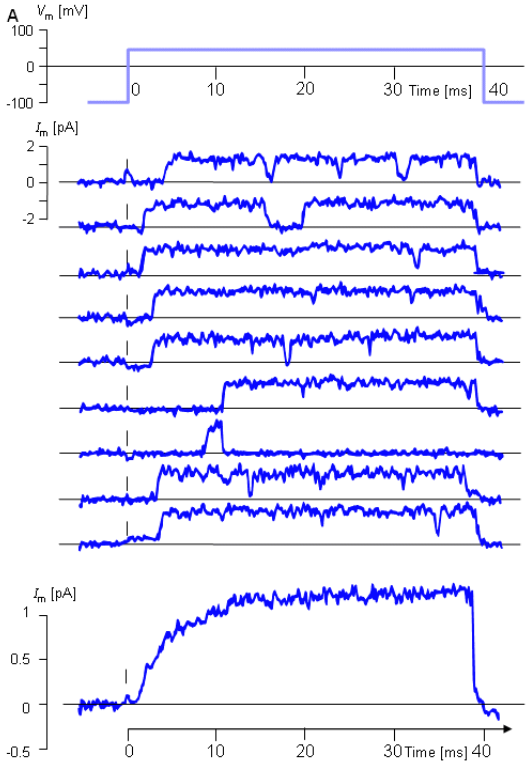

Figura 2.13. Early records of the activity of individual and population ionic currents by voltage clamp.[*Plonsey-Malmuvio 1995]*

These techniques have made it possible to observe the behavior of the channels, which is generally all or nothing at a given moment, the probability of opening or closing them being voltage dependent (voltage sensitive channels). Today, with the improvement of these measures, we know that in reality there are intermediate states or sub-states. The main advantages of these techniques is that they allow us to experimentally determine the VI characteristics of the channels and therefore their characteristic conductance and reversal and equilibrium potential, their opening probabilities and kinematics (activation and inactivation curves) - with a certain probability of error-, refractoriness (if the impulse time is varied) etc. For example, the

current-voltage (I-V) relationship of an ion channel gives us a lot of important information about its characteristics.

2.2.2. Principles of HH

The most widespread (traditional) description for modeling cardiac cell and subcellular activity is based on the formalisms of the Hodgkin-Huxley Nobel awards, pioneers in the development of a mathematical model to describe the action potential of cells of excitable membrane. In their 1952 work, the scientists developed a mathematical theory applicable to nerve fibers capable of simulating the action potentials of isolated neurons ***(Hodgkin Huxley 1952),*** which was a boost in modeling and knowledge about excitable cells and for which they received the Nobel Prize in Physiology and Medicine in 1963. The HH model consists of three first-order linear differential equations that model the behavior of sodium and potassium ion channels, whose coefficients are a function of the membrane potential, in addition to a fourth differential equation that models the electrical behavior of the membrane. Hodgkin and Huxley used their own voltage clamp experiments to fit the coefficients of the equations. Thus, it was the first model to employ a mathematical reconstruction of the experimental observations of the transport, opening and closing kinematics of ion channels instead of complex and abstract equations (Van der Pool and Van der Mark 1928: not based on data physiological), and correctly reproduce the morphologies of action potentials, ionic currents and ionic bases of excitation, impedance changes and conduction velocity (for the squid giant axon).

Despite presenting imperfections (such as the definition of the sense of obtaining the membrane potential), they established the bases of a useful formalism to describe the ionic kinetics of the membrane (cell modeling),

and it has also prevailed over time and has been used as the basis for the development of more complex models of excitable tissues. Considering the current flow through the membrane during activation, they introduced what they called the parallel conductance model, the conceptual basis of the current cell model, defining the membrane capacity (and its capacitive current) in parallel with the cellular currents described. through its resting potential and variable conductances, among which were the main electrotonic currents (sodium and potassium) and a leakage current consisting mainly of chloride ions. The equilibrium potentials were obtained from the Nerst equation, and the conductances per unit area from Ohm's law. In this way, the last equation resulted directly from applying Kirchoff's first law, or what is the same experimentally, the sum of the cellular components of current given an impulse must be zero (open circuit, no re-stimulation, the momentum spreads and disappears). In addition, they introduced the basic properties of ion channels, establishing that the channels were specific to a type of ions, and that their openings and closings were electrically controlled by charged particles (n-particles), which were on the outside or inside (depending on whether the opening or closing mediated) determining states of simple open or closed transitions. In turn, they postulated that the activation state is the process by which channels rapidly open from the closed state during depolarization. Instead, inactivation is the process where channels slowly close during prolonged depolarization. They defined associated transition probabilities, which depended on the current state (transition constants), between the activation of the particles that mediated opening and those that mediated closing. They introduced the equation that allows obtaining the probabilities of transition between states, due to these particles, over time, thus also introducing the need to know an approximation

of the dependence with the steady-state voltage of these particles. This is the basis of the current gate concept.

Thus, they introduced the behavioral equations (channel conductances, description of the operation of the openings and closures, and the general equation of cellular electrical activity), and experimentally adjusted the constants (physical, version potentials, and maximum values of the conductances observed) and the transition probabilities between the steady state opening and closing states. Subsequent to the HH experiments, voltage clamp experiments in myocardial cells and Purkinje fibers, demonstrated that the ionic mechanisms associated with this type of cells were more complex than those of neurons, involving some additional currents but that inherited principles were applicable.

2.2.3. Modelling cellular electrophysiology

The mathematical modeling of physiological systems has gained great importance with the progress of numerical calculation tools and support software in general. These models are made from the prior knowledge of certain characteristics of the functioning of the subsystems and compartments that make up a living organism. Extensive experimental observations about the electrophysiological properties of cardiac cells have been carried out in recent decades, within which we can highlight, among others, the creation of techniques such as: voltage clamp (1940s: Cole 1947, Marmont 1949) ***(Erlich 2003)*** , patch clamp (Sakmann and Neher 1991) ***(Marty 1981),*** etc; These results allow obtaining precise measurements of the currents that cross the membrane, allowing to clarify the functioning of the heart muscle.

The electrical activity, in the case of excitable cardiac cells, is obtained only from the movement of positive charges (especially the K +, Na + and Ca2 + ions are those that influence the membrane potential). The equations that will be shown and discussed below, are compatible or can be derived from basic principles of physics and electrostatics, and are the result of the flow of electrotonic currents through the channels. electrogenic exchangers and pumps. The potential is, therefore, directly proportional to the excess of positive charges inside the cell (Gauss's law for electrical capacity), and is obtained by applying Kirchoff's law to the parallel conductance model inherited from HH formalisms. The equation of Nerst (1888), for the calculation of the reversal or equilibrium potentials, is deduced from the empirical laws of Fick (1855) for the movement of particles by simple diffusion, Ohm (1827) for the movement of charged particles under an electric field and its formal relationship verified by Einstein (1905). Finally, the dynamics of the gates is based on Boltzmann's distribution laws (1868: a particle in thermal equilibrium spends less time in high-energy states than in low-energy states) and Markov's assumptions (1906: the probabilities transition between states in a stochastic system, Markov type, only depend on the current state).

An action potential model (electrically isolated cell) consists of a series of coupled first-order differential equations that describe the behavior of ion channels, in addition to an additional differential equation, which models the electrical behavior of the membrane. to apply Kirchoff's first law to the equivalent electrical circuit of the cell membrane (the total transmembrane current flow at a point must be zero), since at this level the electrical activity results from the flow of current through the ion channels and other

transporters in the cell membrane. These non-linear differential equations provide as a solution the temporal evolution of both the PA and the currents that compose it. In parallel with the inherent capacity of the membrane -per unit area- (and its resulting capacitive current) we have ion channels and transporters. In this scheme the outgoing currents of the cell are positive and the incoming negative.

2.2.4. Reentry dynamics: Functional and structural determinants

The propagation of voltage waves through the myocardium is a non-linear and complex phenomenon, as has been discussed. As discussed in the background, a depolarized cell (source) would have to provide sufficient electrotonic current through junctions to each neighboring cell (sink) in order to bring the membrane potential of that cell above the threshold for activation of the sodium channel (depolarizing current). The process continues as the wave propagates from cell to cell. The process of ion fluxes that occur below the threshold of the membrane potential for the activation of sodium channels is called electrotonic interactions. Now, as we already know in physiological conditions the propagation in the medium is not uniform, but also in pathological conditions, during reentry, the spiral propagation has a marked curvature. Unlike a flat propagation, the cells in the curved wavefront must activate a relatively large number of cells ahead of them, and this results in a decrease in the velocity of conduction (CV). Importantly, if the convexity (positive curvature) of the wavefront exceeds a critical value, then the cells on the wavefront may not be able to provide enough current to excite the cells on the depolarizing wavefront, causing a blockage. of driving. This is a mechanism that can explain the generation of fibrillatory activity in the presence of excitability gradients.

In the case of a spiral wave, the curvature increases with the wave front and the VC decreases towards the center of rotation (Figure 2.14). Near the center (that is, at the tip of the spiral), the curvature is critical and the velocity is zero, forcing the wavefront to pivot around an unexcited but eminently excitable center, the core of the spiral. . Thus, a spiral wave revolves around an area of unexcited cells that are available to be excited once they receive enough current to drive them above the threshold for sodium channel activation. As such, a spiral wave can either be stationary or rotate continuously around the nucleus, as well as it can invade the nucleus, or oscillate generating complex geometric patterns. This is believed to be a consequence of the flow of electrotonic currents between cells in the nucleus and cells at or near the tip of the rotor, therefore it is directly related to the source-sink concept, and the excitation threshold determined by the delicate balance of currents IK1 and INa. Interactions between the tail and the wavefront can also give rise to effects on oscillation or even drift in a homogeneous medium. The spatial extent between the wavefront and the tail is known as the wavelength (WL). The wave front corresponds to depolarization and the wave tail corresponds to repolarization. Therefore, in a plane wave, the WL can be approximated as VC x APD. However, this formula does not generally apply to a spiral wave, as both APD and WL change vary with distance from the center. In the nucleus, cells function as current sinks, shortening the APD of cells in their immediate vicinity, which act as the current source. Therefore, the APD and WL are smaller closer to the nucleus and larger when further away from the nucleus (Figure 2.14).

It has been shown that the frequency at which a spiral wave can rotate around a given nucleus, the size of the nucleus, and the degree of oscillation loops

of the wave depend mainly, but not entirely, on two factors: excitability and APD. If the system is highly excitable, a spiral wave can have a higher critical curvature, since according to the source-sink theory, the minimum excitable area is greater, since the depolarizing current density is greater than that of repolarization. The opposite is true for the reduction of excitability. In such a situation, the curvature of a spiral wave is lower and the propagation of the wavefront also becomes slower, therefore, the critical curvature is lower and there is a greater probability of generation of blockages and front-tail interactions.

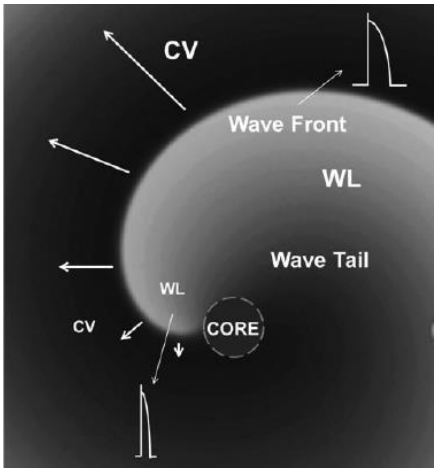

Figura 2.14. Functional properties of spiral propagation [Fuente: JJ Jalife 2011]

If the WL is large close to the nucleus, then there is a high probability that the wavefront collides with its tail, as occurs with blockages of the depolarization current INa, and that over time fibrillation may end or lead to blockages. and local secondary waves. A shorter APD near the core, on the other hand, will result in a smaller WL, which stabilizes the rotation as it minimizes the possibility of oscillation or blocking. Functional wavefront blocks ('wavebreak') occurs in the presence of refractory tissues (discrete or continuous gradients), or when the wavefront (i.e., the source) is too weak to

depolarize cells in front of the wavefront by above the threshold. Functional blocks are critical in rotor formation and the distribution of turbulent activity, also called "fibrillatory conduction."

2.2.5. Ionic gradients and fibrillation dynamics.

While rotors have been recognized as the main mechanism underlying fibrillation for years, the ionic mechanisms responsible for their behavior are still not understood. Previous studies have suggested that the frequency and stability of rotors are largely determined by resting potential (RMP) and VC. These, in turn, are largely controlled by the dynamic interaction between the output component of IK1 and the input component of INa. A recent study has additionally demonstrated that there is a dynamic reciprocity of the isoforms that express these channels, Kir2.1 (IK1) and Nav1.5 (INA), across different species. These results further suggest that the relationship between IK1 and INA plays a central role in the control of membrane properties in the heart. On the other hand, computer simulations first using simplified excitation models and later models that included the kinetics of specific ion channels and millions of electrically coupled cells, predicted that any shortening of APD or increase in excitability should stabilize spiral waves. Furthermore, it was predicted that gradients in APD / excitability should provide a substrate for the generation of conduction blocks ***(Fast 1990)***. Electro-optic recording techniques make it possible to obtain records of the electrical activity of the heart in a considerably wide surface of the heart 'ex vivo' or in cell preparations 'in vitro', with a great spatial and temporal resolution, allowing to record a signal proportional to the potential of membrane.

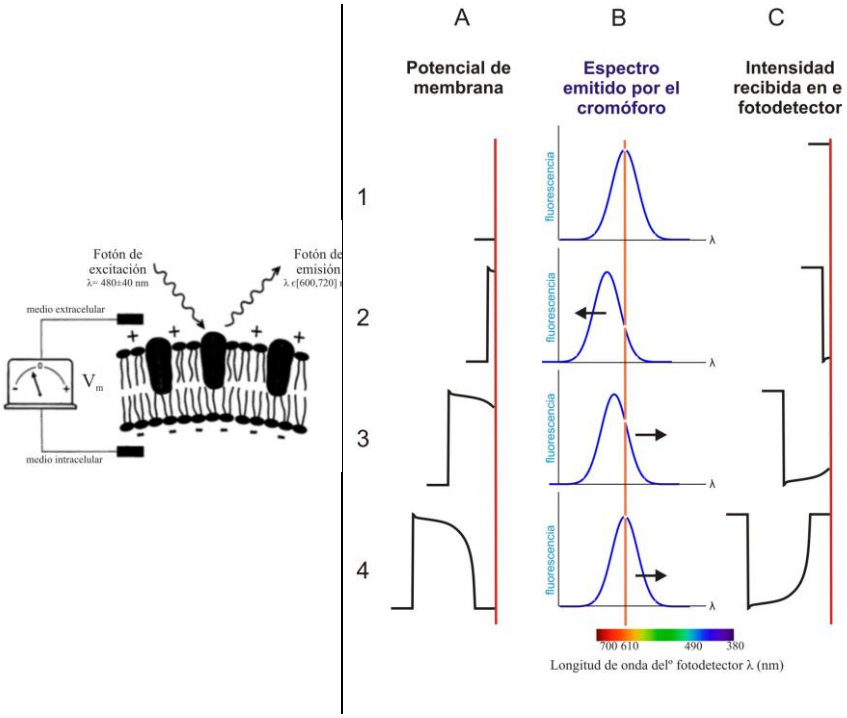

Figure 2.15. Diagram of the fluorescence process that allows the electro-optical recording of cardiac tissue activity.

For this, potentiometric dyes are used, which have the quality of adhering to the cell membrane with great affinity and are responsible for the fluorescence process. The main characteristic of this dye is that while it is linked to the cell membrane, it reflects light with a similar spectrum that varies depending on the electrical potential to which the cell membrane is subjected. This quality turns the potentiometric dye into a highly localized optical action potential transducer, transforming each change in the membrane potential into changes in the spectrum of the emitted light. This operation can be seen in Figure 3.2. To avoid registration problems and to have an electrically functional, but totally mechanically inactive preparation, electromechanical decoupling drugs are used to use this technique. Experiments with isolated hearts ('ex vivo') perfused in the Langendorff system recording ventricular

activity during fibrillation (guinea pig) already demonstrated a decade ago the role of the IK1 current in the generation of frequency gradients during fibrillation (expression of the Kir2.1 isoform is greater in the left ventricle than in the right). Experiments in sheep have also shown that heterogeneity in the expression of isoforms associated with rectifying potassium input channels generates frequency gradients in the atrium and is associated with reentrant arrhythmias ***(Sarmast 2003).*** Experiments in transgenic mice ***(Noujaim 2007)*** successfully associated the overexpression of these channels with an elevation of the RMP and drastic abbreviation of the APD. These data suggest an important role for the IK1 current in controlling the frequency and stability of rotor activity during VF in the heart of mammals. On the other hand, recent experiments with sheep have shown that blocking the sodium channel reduces excitability, which therefore contributes to reducing the speed of propagation and the frequency of the rotors, as a result of oscillations that cause front-tail interactions of the lead sources of reentry ***(Fozzard 1994, Filgueiras 2012)***

In particular, the combination of 'in vitro' and 'in silico' controlled arrimia models has provided a framework to unravel the ionic mechanisms that control fibrillation dynamics, both under homogeneous and heterogeneous conditions. Cultures of myocytes in electrically coupled monolayers have been shown to provide an ideal model for studying how different ion channels affect reentry dynamics under a variety of different conditions (e.g., overexpression / silencing of various proteins, their spatial scattering, models heterocellular coupling of non-myocytes to cardiomyocytes). In addition, the combined use with computational models allows to break down the mechanisms on phenomena observed in these experiments. Among these studies, those that have addressed the study of the effects of the spatial

dispersion of the ionic currents IK1, IKr and IKs (especially the first two) are of special interest, since they are the object of this work and they have also actively participated in those that focus on studying under heterogeneous conditions. In order not to extend this section, the main results are summarized below. The up-regulation of the IKs current, demonstrated in a study with mouse ventricular myocytes -NRVM- that (in contrast to IK1) causes an increase in post-polarization refractoriness. This implies an intrinsic increase in the refractory period beyond the APD, which leads to the generation of conduction blocks and permanent fibrillatory activity in the monolayers. Even so, the frequency of this activity was not significantly increased, probably due to the accumulation of IKs at high frequency.

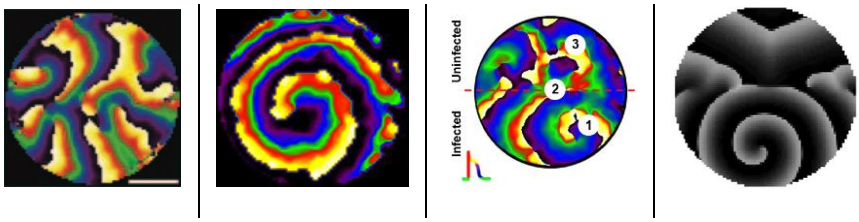

Figure 2.16 Fibrillation dynamics with 'in vitro' models *(a. Overexpressed IKs, b. Overexpressed IKr, c. Gradient in IKr) and 'in silico' (d. Simulation associated with -c-)*

A later study ***(Hou 2010)*** showed that IKr exerts a control over reentry dynamics similar to that of IK1, an overexpression causes an increase in the reentry frequency in addition to a significant reduction in the action potential. Subsequent studies using a regional viral magnetofection technique that allows controlling the regional dispersion of these currents showed that unlike IKr, the dispersion in the IK1 current not only generates gradients in APD in the opposite direction to its up-regulation and is capable of generate high-frequency turbulent activity in the direction of lower APD, but is responsible for a bimodal excitability gradient in the CV ***(Campbell 2012).***

These results have been mechanistically reinforced through the use of numerical and computational techniques. Technical difficulties prevent the simultaneous study of gradients under different conditions, as well as the relative determination of the dispersion in all these currents, 'ex vivo' or 'in vivo', to study the fibrillation mechanisms in detail when gradients and heterogeneities in all ionic currect are present.

2.2.6. Cardiac optical mapping advancements.

Current advancements in cardiac arrhythmia and cardiovascular research have beed fueled by cardiac optical mapping. Nowadays it has undoubtedly proven to be a key technology for comprehensively studying cardiovascular disease growing fast **(*Herron 2012, O'Shea 2020*)** together with technological developments and new generation indicators.

Optical imaging of cardiac tissue uses fluorescent dyes to reconstruct electrical activity of the heart with high spatiotemporal resolution. It has become an invaluable tool for pre-clinical and research laboratories. Furthermore, mapping spatiotemporal dynamics of cardiac excitation and repolarization across extensive areas of the heart has allowed for many years' study arrhythmia mechanisms and/or drug-action for understanding key electrophysiological and pathophysiological processes ***(Efimov 2004).***

Traditional optical mapping setups include the following key components: detectors, illuminating sources, optical filters and lenses, as well as, experimental preparations for studying isolated hearts in Langendorff-perfused preparations, or isolated tissue cultures. However, some of those components are quite expensive preventing its broader use by the scientific

community. Figure 2.17, shows and example of traditional optical mapping reconstruction in a grid of fotodetector.

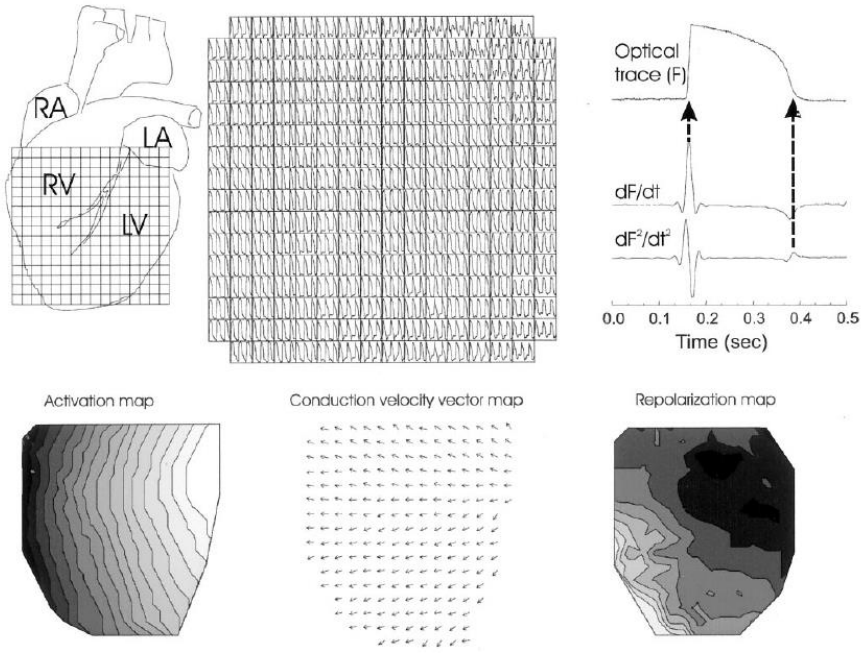

Figure 2.17 Traditional optical mapping of isolated hearts. Sample action potential recordings obtained using traditional optical mapping techniques as well as tradition activation, repolarization and conduction velocity maps derived from reconstructed time series for each detector. *(Efimov 2004)*

Panoramic configurations, either using reflectors, or multiple sensors allow to overcome intrinsic spatinal constraints when studying arrhythmia mechanism. However, such configurations are challenging since need to increase finantial costs, as well as, handling large amounts of data (Kay 2004, Rogers 2007)

Optical mapping studies have bee instrumental enhancing current knowledge of arrhythmia mechanisms. Principles and processing techniques of cardiac action potential have ben extensively addressed before ***(Laughner 2012).***

Spectral dominant frequency analyses, as well as, phase-domain analyses have become increasingly used for characterizing fibrillatory drivers and attractors.

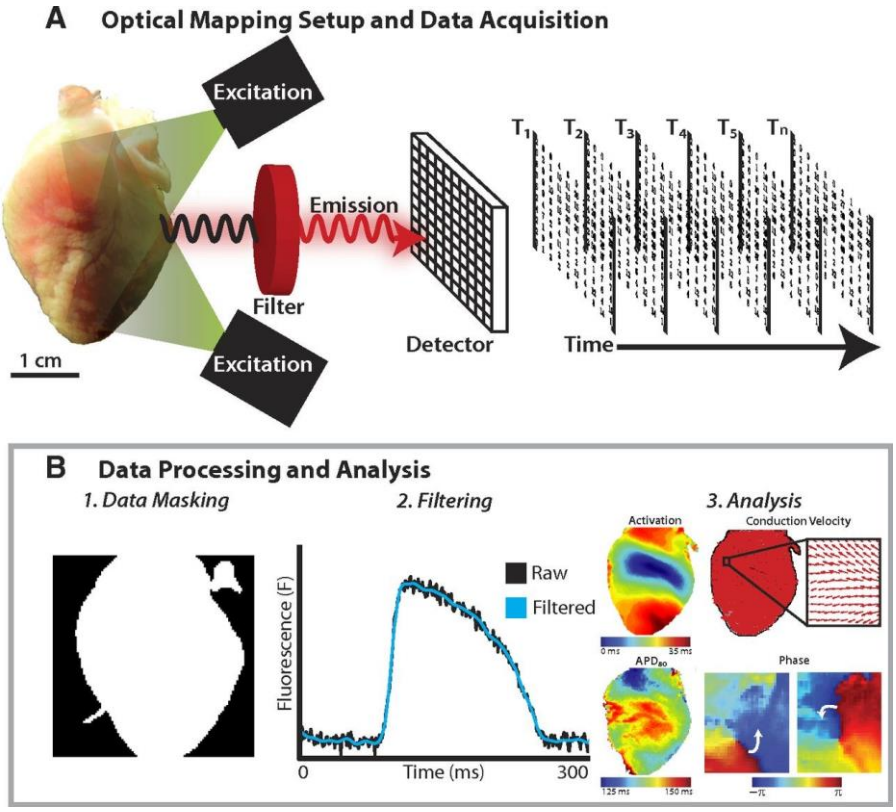

Figure 2.18 Data processing and analyses in reconstructed optical imaging studies. *(Taken from Laughner 2012)*

Traditional optical mapping strategies have evolved in the recent years ***(O'Shea 2009)*** including multiparametric, ratiometric, muti-detector, multimodal, panoramic, endo-epicardial and, more recently, optical mapping of freely beating hearts in-vivo **(*Lee et al 2009*)** thanks to newer generation dyes yet at cost of spatial resolution.

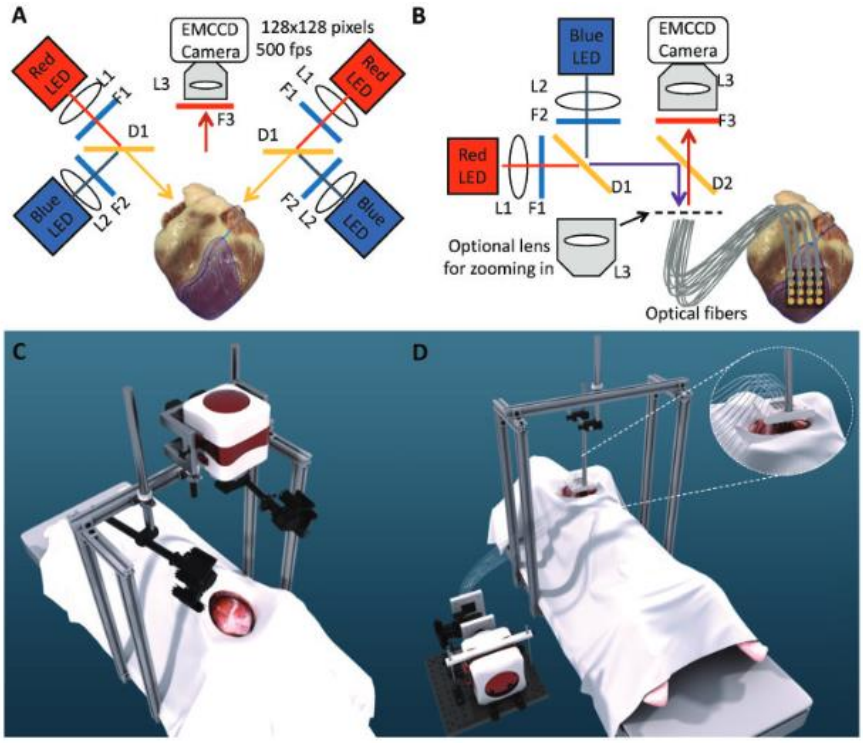

Figure 2.19 Latest optical imaging studies in-vivo. (Lee 2019)

Futhermore, non-simulataneous geometrical acquisition in some studies has allowed for whole heart correlation between anatomy and function using a single- or multiple sensors ***(Gloschat 2018).***

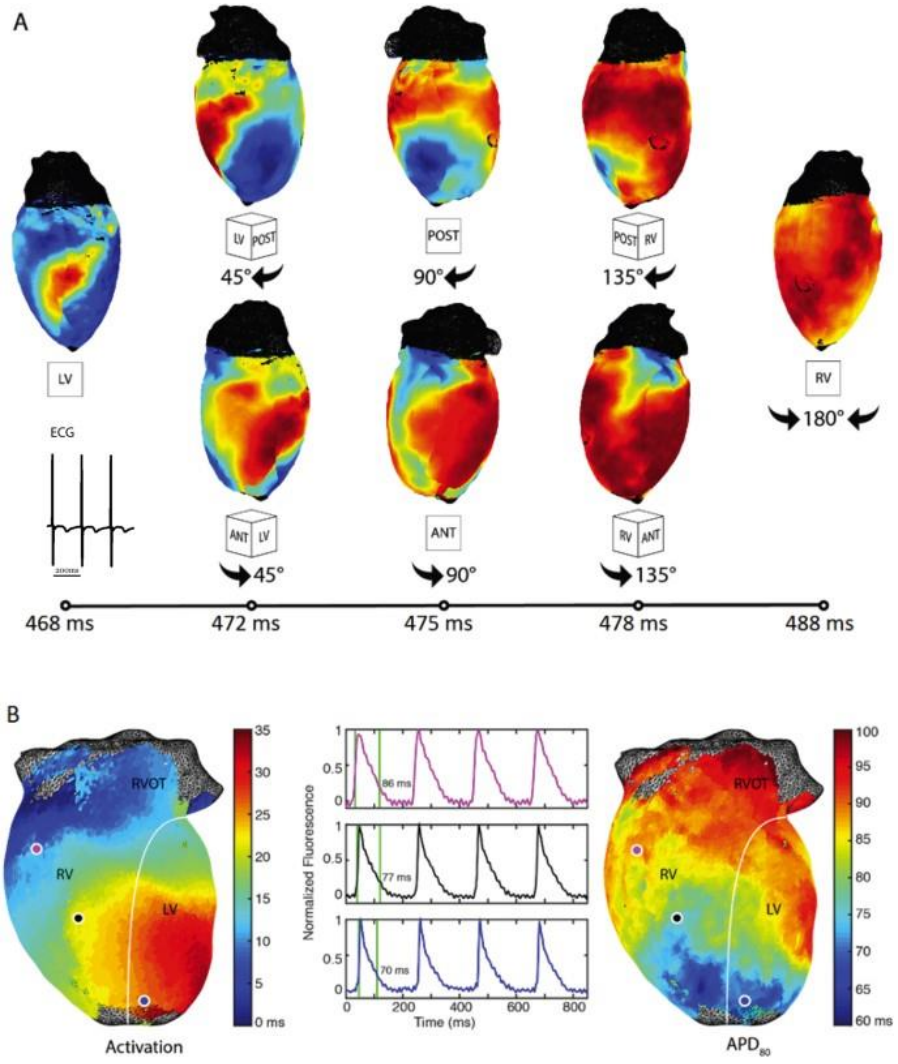

Figure 2.20 Representative panoramic data in small hearts (rat) (Taken fomr Gloschat 2018)

However, despite major breakthroughs, several issues remain, reganding the technological costs of high-resolution panoramic optical mapping configurations, avoiding the use of chemical uncouplers for registration of

extensive areas in freely beating hearts, as well as capturing simultaneously panoramic intrinsic geometrical and functional properties of the heart.

Chapter 3

Mechanisms of rotor drifting dynamics and sink-to-source attractors of primary reentrant sources in cardiac arrhythmias

In this chapter, we test a computational platform for supporting the study of cardiac arrhythmia mechanisms and dynamics. Here, the major role of rectifying and repolarizing currents on rotor drifting dynamics is addressed in detail. Specifically, to address the problem, realistic computational models of cardiac electrophysiology are developed and numerically implemented for testing in high-performance and GPU-based platforms. Under such controlled in-silico conditions, the relative role of active and passive properties of the tissue were studied, specifically a major interest is focused on the relative implication of individual currents to rotor attraction under sink-to-source attractors as well as other passive properties of the tissue.

The results presented in this chapter have been mainly published in (***Calvo CJ 2014***) and other international and national conferences (Chapter 7).

3 Attraction of rotors to the pulmonary veins in Atrial Fibrillation

3.1 Abstract

Maintenance of paroxysmal atrial fibrillation (AF) by fast rotors in the left atrium (LA) or at the pulmonary veins (PVs) is not fully understood. To study the role of the heterogeneous distribution of transmembrane currents in the PVs and LA junction (PV-LAJ) in the localization of rotors in the PVs. We also investigated if simple pacing protocols could be used to predict rotor drift in the PV-LAJ. Experimentally observed heterogeneities in IK1, IKs, IKr, Ito and ICaL in the PV-LAJ were incorporated into 2- and pseudo 3-dimensional models of Courtemanche-Ramirez-Nattel-Kneller human atrial kinetics to simulate various conditions and investigate rotor drifting mechanisms. Spatial gradients in the currents resulted in shorter action potential duration (APD), less negative minimum diastolic potential (MDP), slower upstroke and conduction velocity for rotors in the PV region than in the LA. Rotors under such condition drifted toward the PV and stabilized at the shortest APD and less excitable region, consistent with drift direction under intercellular coupling heterogeneities and regardless of the geometrical constrain in the PVs. Simulations with various IK1 gradient conditions and current-voltage relationships, substantiated its major role in the rotor drift. In our 1:1 pacing protocol, we found that amongst various action potential properties, only the MDP gradient was a rate independent predictor of rotor drift direction. Consistent with experimental and clinical AF studies, simulations in an electrophysiologically heterogeneous model of the PV-LAJ showed rotor attraction toward the PV. Our simulations suggest that IK1 heterogeneity is dominant compared to other currents in determining the drift direction through its impact on the excitability gradient.

These results provide a novel framework for understanding the complex dynamics of rotors in AF (Figure 3.0, reentry in PV-LAJ models).

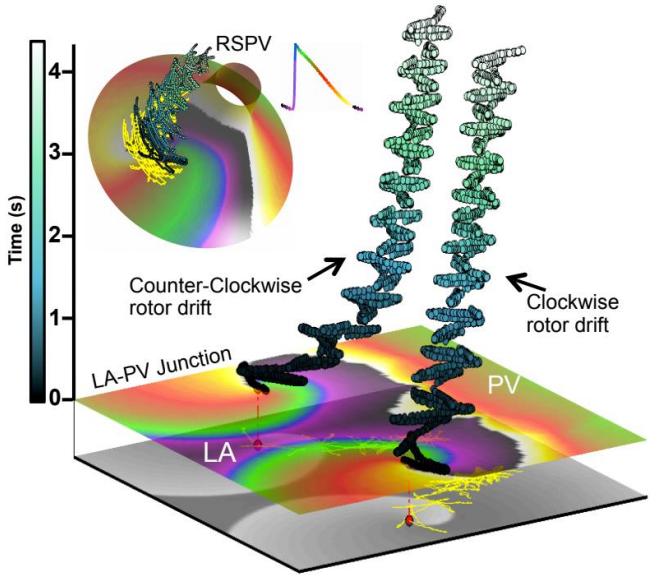

Figure 3.0 *The PV-LAJ models illustrating the intrinsic periodicity of the PVs.*

3.2 Introduction

The mechanisms of atrial fibrillation (AF), the most common cardiac arrhythmia in the clinical practice, are not fully understood. Acute AF in normal isolated sheep hearts has been found to often depend on fast rotors localized mainly to the posterior wall of the left atrium (LA) and the pulmonary veins (PVs) junction (PV-LAJ) with fibrillatory conduction toward the rest of the atria (***Mandapati 2000***). Recent clinical data also points to rotors in various atrial sites as a mechanism driving paroxysmal AF ***(Atienza 2006***, ***Cuculich 2010, Narayan 2012***). Previous simulations have already demonstrated that rotors can occur in the PV-LAJ, provided the PV size is adequate, and non-uniform coupling conditions exist ***(Cherry 2007)***. However, how the rotors form or drift in the PV-LAJ, as well as the underlying ionic mechanisms have not been investigated systematically (***Sanders 2005, Tanaka 2007***).

Earlier studies using simplified cardiac models have shown a causal link between rotor drift, and spatial heterogeneity in the action potential properties ***(Pertsov 1993).*** Rotors drifted toward regions with prolonged action potential duration (APD) or reduced excitability ***(Fast 1990)***, which were inscribed mainly due to heterogeneities in multiple ion channels ***(Nattel 2008)***. In particular, the role of K^+ currents I_{K1} and I_{Kr} may be important, since they are known to be heterogeneously distributed in the heart (***Schram 2002***), and have also been shown to influence rotor dynamics by affecting both the membrane APD and excitability ***(Hou 2010***, ***Noujaim 2007***, ***Pandit 2013***) However the complex heterogeneity in the expression of these channels at the PV-LAJ, such as in dogs, which show a larger current density of I_{Kr} and a smaller density of I_{K1} in the PV compared to LA (***Ehrlich 2003, Cha 2005***), in conjunction with structural discontinuities (narrow PV sleeves compared to the larger LA), precludes a simple prediction of the rotor dynamics at the PV-LAJ.

Our study aims to elucidate ionic mechanisms of rotor drifting at the PV-LAJ. We construct 2- and pseudo 3-dimensional models of the PV-LAJ to investigate the hypothesis that the characteristic heterogeneous dispersion of transmembrane currents during paroxysmal AF, in absence of remodeling, is a determinant of rotor drift. Our numerical simulations demonstrate I_{K1} dominance in conveying a preferential rotor drift direction toward the PVs. We further demonstrate the cycle-by-cycle mechanism by which regions with longer refractoriness and lower excitability tend to attract rotors, and propose a set of measures to confirm our mechanistic proposition linking the ionic properties of the atrial substrate and the predisposition of the PVs, or any other region, to attract or repel rotor activity during AF (***Lemola 2008, Po 2005, Arora 2003***).

3.3 Methods

3.3.1 Numerical models: anatomical descriptions

Numerical simulations were performed on 3 models of the junction between the LA and the PV (Figure 3.1) with increasingly realistic anatomical descriptions:

1. A 50×50 mm^2 regular 2D square mesh model was implemented and subjected to no-flux boundary conditions.
2. A pseudo-3D cylindrical surface model constructed by applying no-flux boundary conditions at the LA and PV edges and periodic boundary conditions on the other two edges of a regular 2D mesh.
3. A pseudo-3D funnel-shaped surface was constructed with near-equilateral triangulated mesh with no-flux boundary conditions on the wide (LA) and narrow (PV) edges. The height of the funnel model was set to 30 mm and its diameter was set to increase exponentially from 10 mm at the PV to 48 mm at the LA edges (see Fig. 3.1) ***(Wozniak-Skowerska 2011)***. Our LA-PVJ funnel model represents a typical right superior PV as described by ***(Wozniak-Skowerska 2011)***. The radii of the PV and LA where selected such that the radius at the ostia location (15 mm from the LA-end) is where the 50% Boltzmann factor was placed. The funnel-like geometry model was generated by circumscribing an exponent function around the central axis of the LA-PVJ. Accordingly we created the shape of the funnel with the radius r as a function of the distance from the PV edge as: r = R + A*exp(z/B), (R, A and B are distance constants) where z, the distance along that axis, was increased with a non-uniform steps that maintained the distance between the rings on the surface of the funnel ($\Delta z^2 + \Delta r^2$) approximately constant. Following, the 3D set of nodes was meshed using the Delaunay triangulation scheme resulting in a

quasi-equilateral triangular connectivity with an average intermodal distance of 0.1 mm and standard deviation of less than 0.01 mm.

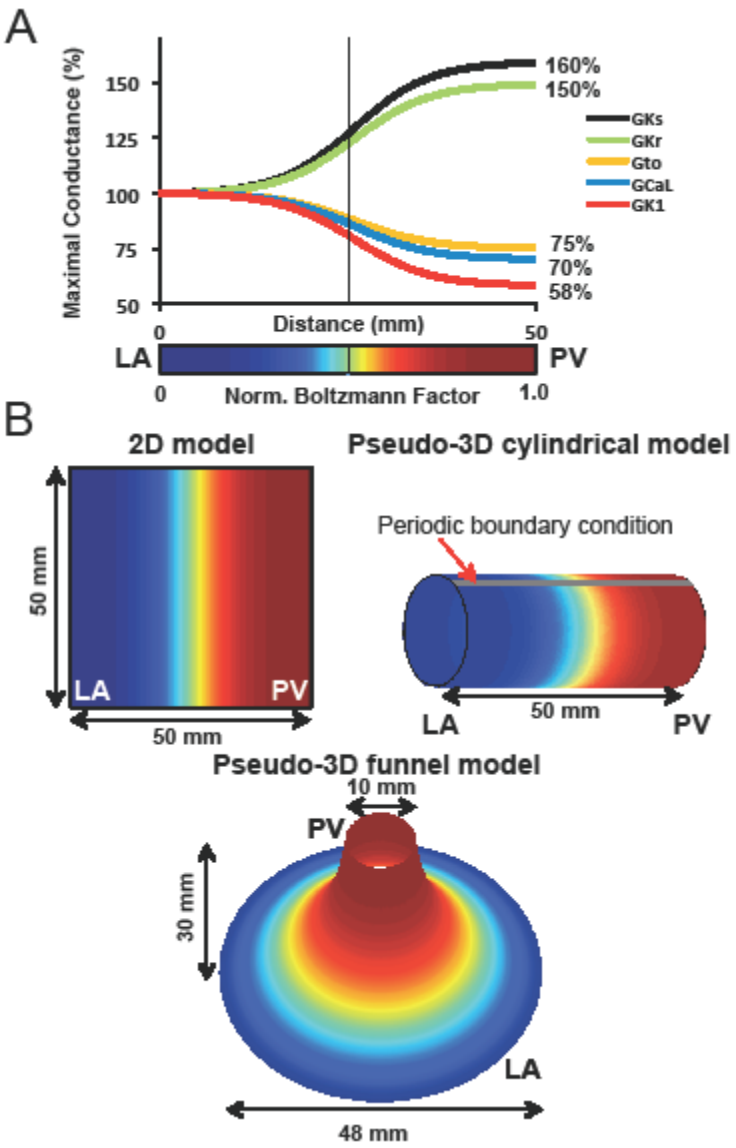

Figure 3.1. *The PV-LAJ models. A. Conductances for I_{CaL}, I_{kr}, I_{ks}, I_{to} and I_{K1} follow a Boltzmann function ($x_{1/2}$=25 mm, vertical dashed line; Δx=5 mm) from LA to PV. Color bar: Normalized Boltzmann factor across the junction. B. Simulat.ions were performed on (i) 2D model of 50×50 mm^2, (ii) cylindrical pseudo 3D model*

generated by a periodic boundary condition in the 2D model and (iii) a funnel-shaped pseudo 3D model. Colors represent the Boltzmann factor values. Cyan-yellow is the steepest gradient region in the PV-LAJ.

3.3.2 Ionic models

The transmembrane potential was based on the Courtemanche-Ramirez-Nattel and Kneller (CRN-K) model of human atrial cell kinetics in the presence of 0.0015 μM Acetylcholine ***(Courtemanche 1998, Kneller 2002, Pandit 2005)***.

I_{KACh} kinetics was based on the formulation by Kneller et al ***(Kneller, 2002)*** with a minimal amount of [ACh]=0.0015 μM to enable rotors in the CRN model of the atria ***(Pandit 2005)***:

$$I_{K,ACh} = \left(\frac{10}{1+\frac{9.12652}{[ACh]^{0.477811}}}\right) \cdot \left(0.013384 + \frac{0.22663}{1+\exp\left(\frac{V+80.253}{50.714}\right)}\right) \cdot (V - E_K) \quad \text{(Eq. 3.1)}$$

where V (mV) is the transmembrane potential and E_K (mV) is the potassium reversal potential. Compatibility of action potentials calculated at 1 Hz pacing between this study and those by Kneller et al ***(Kneller, 2002)*** was confirmed. In the simulations presented in Fig. 3.11, the formulation for I_{K1} based on the Kir2.1 or Kir2.3 isoforms was as reported by Dhamoon et al ***(Dhamoon 2004)*** and differing from the CRN-K model ***(Courtemanche 1998, Kneller, 2002)***:

$$I_{K1} = a_4 + \frac{a_1 \cdot (V - E_K)}{a_2 + \exp[a_3 \cdot (V - E_K)]} \cdot \quad \text{(Eq. 3.2)}$$

Table 3.1 contains values of the a_1-a_4 parameters in Eq. 2 fitted for I_{K1} consisting of either Kir2.1 or Kir2.3 isoforms ***(Dhamoon 2004)***:

Current (isoform)	Coefficient	Value
I_{K1} (Kir2.1)	a_1	0.4719
	a_2	7.1202
	a_3	0.1187
	a_4	0.0
I_{K1} (Kir2.3)	a_1	0.048
	a_2	0.0333
	a_3	0.2227
	a_4	-0.0607

Table 3.1. *Coefficients for data fitted for Kir2.1 and Kir2.3 in the I_{K1} of Eq. 2.* ***(Dhamoon 2004)***

Electrical activity was computed using a mono-domain and numerically stable Euler forward scheme with 100 µm internodal distance, 0.005 ms time step and isotropic diffusion coefficient of 0.062 mm^2/ms adjusted for conduction velocity (CV) of 48 cm/s. Initial conditions were the steady state membrane variables following pacing a single cell at 1 Hz for 10 s.

Additional conditions of heterogeneous intercellular coupling coefficient and distribution of I_{Na} are described and studied in the Supplemental Material. Reentrant excitation patterns were induced by S1-S2 cross-field stimulation protocols and their pivoting points were identified as a singularity point (SP) and tracked in the phase domain (Fig. 3.2).

3.3.3 Simulations and Conditions

Electrical activity was coded in C and MPI and computed on different infraestructures (Flux High Performance Computing -HPC- cluster at the University of Michigan, and using on-premises HPC at UPV) using a mono-domain, finite volume discretization (FVM), Euler forward scheme with 100 µm internodal distance (h), 0.005 ms time step (Δt), and isotropic diffusion coefficient of 0.062 mm^2/ms (D) adjusted for conduction velocity (CV) of 48 cm/s. Numerical stability of the solutions was assured. During

propagation neither irregular (squared, mesh affected) wavefront curvature nor instability of the action potentials, nor any numerical artifacts were observed. Additionally, we verified that our simulations parameters satisfy the 2-dimensional Nyquist stability criterion ***(Clayton 2005)***: $D \cdot \Delta t/h^2 < 1/(2 \cdot \text{dimensions})$ which yields $0.031 < 0.25$. Initial conditions were the steady state membrane variables following pacing a single cell at 1 Hz for 10 s.

Heterogeneous ionic conditions were implemented by assigning a spatial Boltzmann ($x_{1/2} = 25$ mm and $\Delta x = 5$ mm) distribution of conductance for I_{K1}, I_{Ks}, I_{Kr}, I_{to}, and I_{CaL} between the LA and the PV based on data from dogs ***(Cha 2005)*** and described in Figure 3.1-A (maximal conductance for I_{Kr} and I_{ks} where increased by 50% and 60% respectively while I_{K1}, I_{to} and I_{CaL} where diminished by 42%, 25% and 30% respectively). Three conditions of heterogeneity were modeled: 1) all currents varied spatially according their corresponding Boltzmann function (Condition I); 2) all currents, except I_{K1}, varied (Condition II); 3) only I_{K1} varied in space (Condition III). Additional conditions of heterogeneous intercellular coupling coefficient and distribution of I_{Na} were studied.

To investigate the effect of the heterogeneous intercellular coupling in the LA-PV junction ***(Chaldoupi 2009)*** on rotor drift in combination with the ionic heterogeneities additional models were generated with gradients in the isotropic intercellular coupling coefficient. The intercellular coupling in those models was set to vary following a Boltzmann profile (Figure 3.1) between a baseline level at the LA edge of the model (as set in all other conditions) to a 25% smaller value at the PV edge ***(Verhuele 2002).***

3.3.4 Rotors Initiation and Characterization

Rotors were initiated by cross-field stimulations and the instantaneous center of rotation was tracked by its phase singularity point (SP) in the Hilbert-transformed movies ***(Zlochiver Yamazaki 2008, Zlochiver Munoz 2008)*** (see Figure 3.3). In the cylindrical model, two counter-rotating (opposite chirality) rotors were generated and shown to follow a similar drift dynamics. The SP of a rotor was defined as the instantaneous location toward which all the phases in space converged and automatically detected and tracked based on the point-by-point (resolution of about 1 mm) circumferential sum of neighboring phases exhibiting a monotonic progression to approximately 2π. For controls, rotors were initiated in two separated 2D models with either homogeneous LA or PV ionic conductances (in the absence of spatial heterogeneities) and characterized by their rotation frequency, the I_{Na} gating parameters h*j (I_{Na} availability), core size as well as wavefront curvature, action potential duration (APD), wavefront conduction velocity (CV) magnitude and wavelength (WL) of excitation ***(Noujaim 2007, Hou 2010, Campbell 2012)*** determined at 70% amplitude (Figure 3.4). Those parameters are presented for the two simulations as a function of the distance from the SP (Figure 3.4, panel B). The wave front and tail were identified as a continuous isopotential line. During reentry, activation maps were generated at 50% amplitude and used to obtain local CV vector maps. The WL was calculated as the distance between the tail and the front of a wave along the CV vectors (Figure 3.4, Panel B).

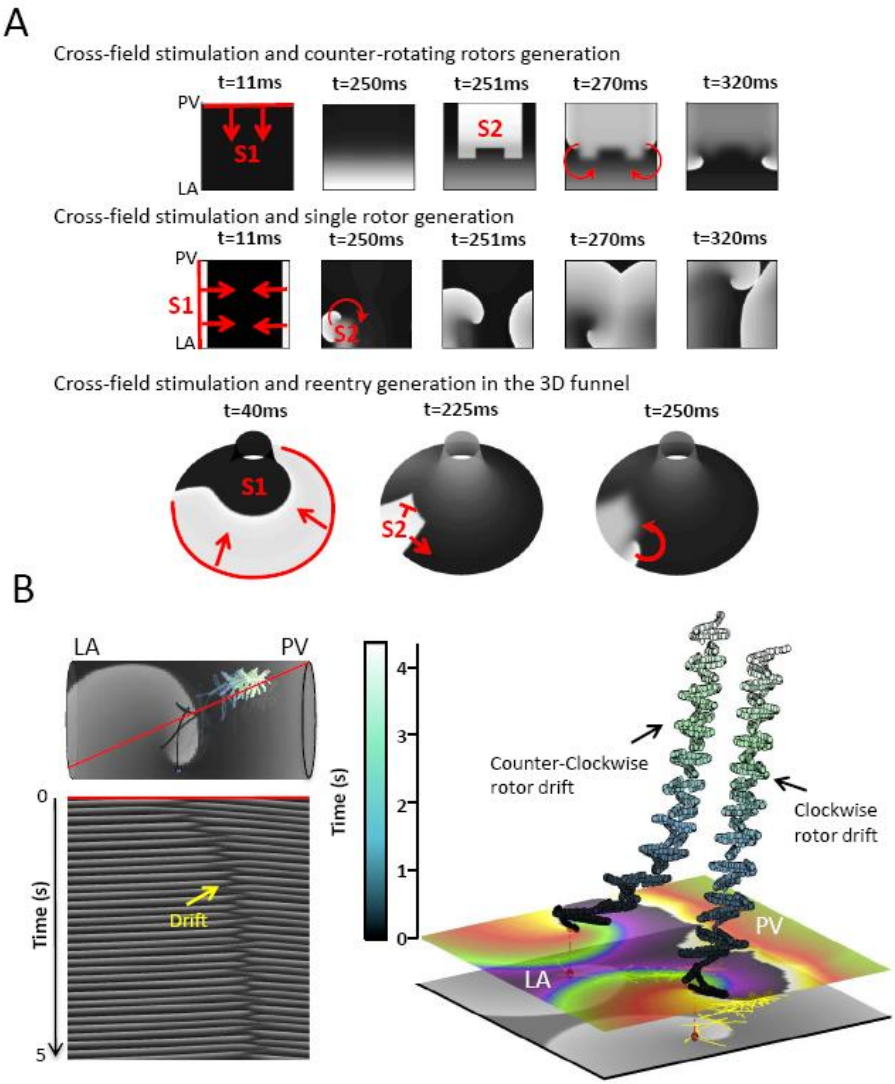

Figure 3.2: Rotors initiation and tracking. *A. Cross-field stimulation leading to two counter rotating or a single rotor in the cylindrical, flat and funnel-like models. Gray-scale corresponds to voltage (black, resting; white excited). Red lines: Location of S1. B. Left: Demonstration of the automatic SP tracking of a drifting rotor as the TSP (bottom) matches the SP trajectory superimposed on the cylinder model (Condition I, top). Right: In a flat model (Condition I), coexisting clockwise and counter-clockwise rotors drift toward the PV, as illustrated by the 3D TSP trajectories whose origin is at the SP in the phase map at t=0.*

3.3.5 Data Analysis

To obtain a measure of effective refractory period (ERP) at a specific stimulation cycle length (CL) we first simulated activity for 10 s to generate steady state conditions at individual cell level and then determined the stimulus strength in the tissue model at ×1.5 the minimum excitation threshold current for a 1 mm virtual pacing electrode. Measurement consisted in 10 S1 stimuli train at CL of 1000, 500 or 140 ms, followed by an S2 premature stimulus at decreasing interval. ERP value was defined as the last (shortest) S2 allowing excitation. Measurements were repeated at 6 locations across the models. Methods used for the parameter measurements from the numerical simulations have been previously described ***(Hou 2010, Campbell 2012)***. Spatial profiles (between the LA and the PV edges) of APD and peak sodium availability $(h*j)_{peak}$ were obtained by averaging those parameters in time for every pixel across the model in the last 2 s of the respective 5 s simulation. Measurements of minimal diastolic potential (MDP) and maximal upstroke velocity $(dV/dt)_{max}$ followed same temporal procedure.

3.3 Results

3.3.1 Ionic gradients and rotor attraction towards the PV

As a demonstration of dependence of rotor drift in the PV-LAJ on the specific ionic current heterogeneity we generated rotors in the 3 conditions implemented in the cylindrical and flat model and tracked the spontaneous trajectory of their SP. Fig. 3.3 demonstrates that the rotor in the heterogeneous PV-LAJ region is unstable and its drift direction is a direct consequence of the particular ionic dispersion.

In condition I, i.e. heterogeneity in the currents I_{K1}, I_{Ks}, I_{Kr}, I_{to}, and I_{CaL} as characterized at the PV-LAJ in dog ***(Cha 2005)***, the drift is toward the PV edge of the model. However, when all the currents except I_{K1} are set to be

heterogeneous, and I_{K1} density is maintained homogenously, and is equal to the LA region value (Condition II), the drift reverses toward the LA (when the I_{K1} is homogeneously equal to the PV region—not shown—the drift is also toward the LA). On the other hand, when all the currents are set uniform (either with the LA or the PV values) and only I_{K1} is set to disperse as in the dog (Condition III), the drift is again toward the PV, but with a faster rate as compared with the drift in Condition I.

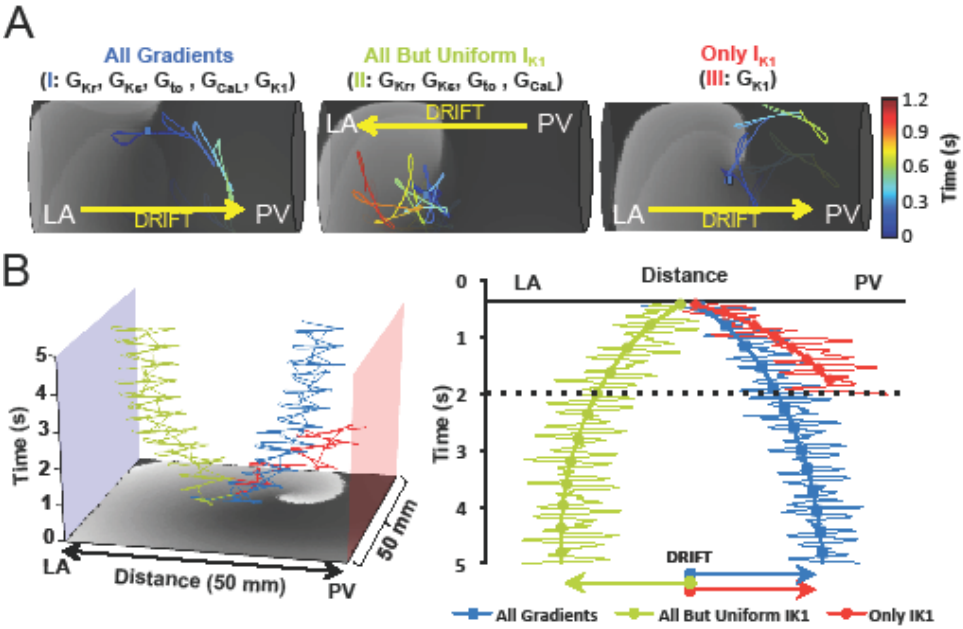

Figure 3.3. *Simulations of rotor drift in the PV-LAJ and I_{K1} role. A. Rotor dynamics on the cylindrical model using the CRN-K kinetics under three conditions: I) all currents varied spatially; II) all currents varied spatially, except I_{K1}; III) only I_{K1} varied spatially. Color-coded traces show the SP trajectory of rotors initiated at the middle of the models (blue dots). Rotors under Conditions I and III drifted towards the PV edge. Drift direction was reversed when I_{K1} heterogeneity was excluded in Condition II. B. Time-space plots and arrows show rotor drift for the 3 conditions in a flat 2D model.*

This set of 3 scenarios in cylindrical as well as in the flat models, shown in Figure 3.3, clearly points to the strong effect of I_{K1} on the direction of the rotor drift in the LA-PV junction area. As controls, we simulated rotors in 2D models with uniform ionic properties of either the LA or the PV that

revealed non-drifting rotors. The rotors in the model with uniform LA properties were slightly faster than those in the model with the uniform PV properties (7.7 vs. 7 Hz, respectively; other properties of the rotors did not vary by more than about 10%; see Figure 3.4).

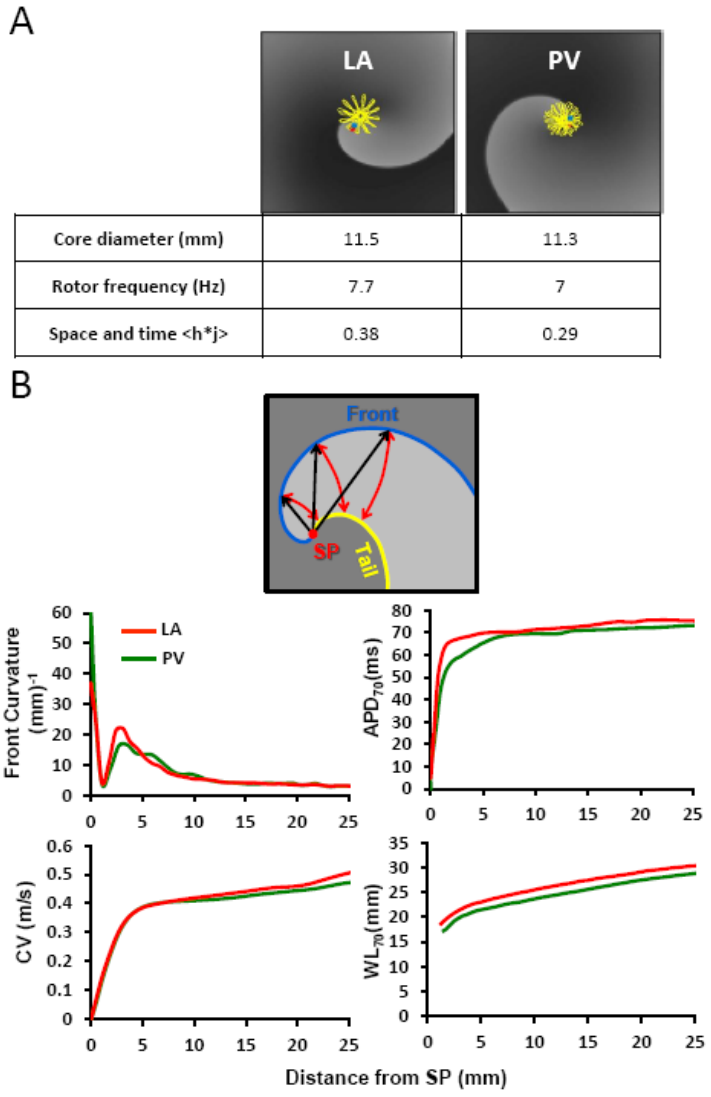

Figure 3.4 Rotors characterization in homogeneous LA and PV models. *The baseline relationship between the substrate and single rotor was studied in separated 2D models with homogeneous ionic conductances of the LA and PV. A. Tracking SP reveals a meandering (yellow traces), without drift, in an area of*

diameters of about 11.4 mm. The LA rotor was slightly faster at 7.7 Hz in comparison with PV rotor at 7 Hz, which was consistent with larger space-time averaged sodium channels availability, h·j, in the LA (0.38) than in the PV (0.29). ***(Pandit 2005)*** *B. Top diagram illustrates the WL (red) as the distance between the isopotentials of front (blue) and tail (yellow) along the CV vectors (not shown) and distance to SP (black). Bottom graphs show rotor properties that qualitatively similar in the LA and PV, but can reach point-wise differences of up to about 20-30%.*

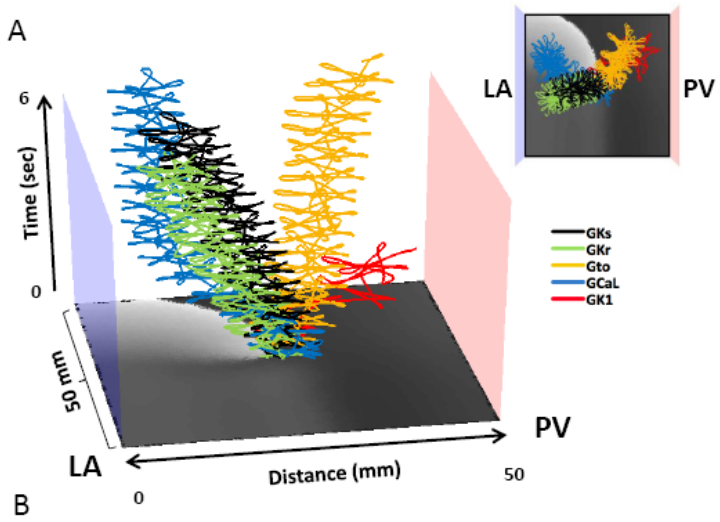

I_{K1}	I_{Kr}	I_{Ks}	I_{to}	I_{CaL}	
PV	PV	PV	PV	PV	I_{K1}
	LA	LA	LA	LA	I_{Kr}
		LA	PV	LA	I_{Ks}
			PV	LA	I_{to}
				LA	I_{CaL}

Figure 3.5 Spatial gradients of individual and paired currents and reentry drift. *A. Effect of spatial gradient for each individual current on rotor drift. 2D PV-LAJ model showing spatio-temporal trajectories of SPs of rotors in gradients of I_{Ks} (black), I_{kr} (green), I_{to} (yellow), I_{CaL} (blue) and I_{K1} (red) as described by the individual Boltzmann distributions in Panel A of Figure 3.1. While I_{to} and I_{K1} cause the rotor to drift toward the PV edge, the gradients in the other currents cause the rotor to drift toward the opposite LA edge. Insert: top view of the trajectories. B. Effect of spatial gradients in paired currents on rotor drift. The table shows the direction of the drift when ionic gradients as indicated in the abscissa and ordinate*

(green cells) were considered. I_{K1} is the only current whose gradient leads to PV attraction (in red fonts) of the rotor regardless of gradient in any other current.

We further tested the effect of all individual and pair-wise currents on drift by switching them from heterogeneous to uniform (Figure 3.5) and concluded again that the I_{K1} heterogeneity is the primary ionic factor that determines the direction of the drift toward the PV. To better understand the mechanisms leading to the attraction of the rotor toward the PV region we quantified electrophysiological properties of the action potential and its propagation across the PV-LAJ.

3.3.2 Heterogeneous excitability and rotor drift in the PV-LAJ

Ionic heterogeneity is imposing non-uniform excitability properties and a rotor drift toward a predictable direction ***(Fast 1990)***. In Fig. 3 we analyze the role of tissue excitability in rotor drifts by quantifying the spatio-temporal distribution of the product of membrane model parameters h and j (h·j) which determines the I_{Na} availability during rotor pivoting ***(Pandit 2005)***. Panel A illustrates the drift trajectory of a rotor in a 2D model under Condition I and shows a time-space plot (TSP) of h·j along the line of the drift. A closer look at the TSP near the pivoting location during a single cycle shows higher values of h·j at the left side (LA) of the drift than at the right side (PV). Thus, a progressive shift of the pivoting point toward the PV is always toward a region with lower h·j values.

Figure 3.6-B shows snapshots of the voltage and h·j at a moment when the wavefront near the rotor tip is propagating toward the LA (top) and a half cycle later, when that wavefront is propagating toward the PV (bottom). The h·j snapshots clearly demonstrate that the wave propagating toward the LA is facing a higher h·j (red) as compared with the wave propagating toward the PV. The h·j gradient during the drift is further confirmed by plotting the time-course of the voltage and h·j at 2 pixels flanking momentarily the SP of

the rotor; one on the LA side and the other on the PV side, 4 mm away from the tip. Those plots show that the peak h·j for each cycle at the LA side is always >0.4 and at the PV side is always <0.4.

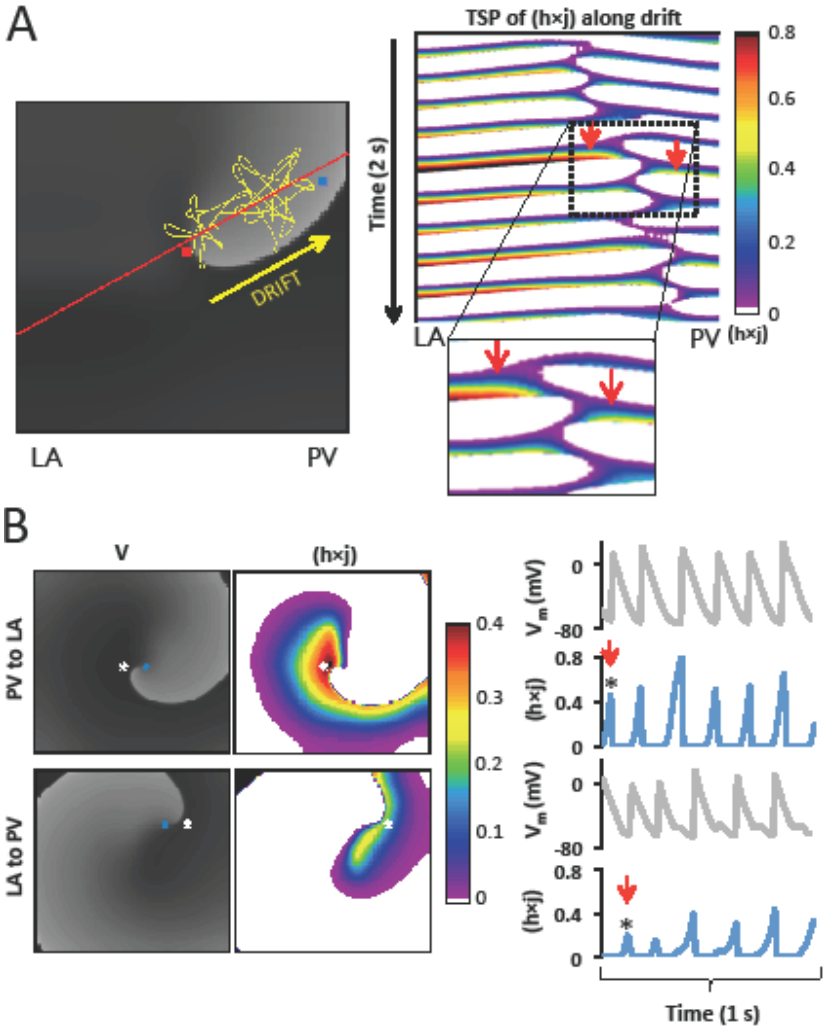

Figure 3.6. *Heterogeneous sodium availability during rotor drift. A. Left. Voltage snapshot (gray scale) with superimposed trajectory of rotor SP (yellow tracing) drifting from the center of the model (red dot) toward its final location at the PV edge (blue dot). Right. Color coded time-space plot for h·j along the rotor drift direction (red solid line in voltage snapshot). Insert is a magnified view showing close to the rotor core h·j is larger on the LA side than on the PV side (red arrows). B. Left. Snapshots of voltage (gray scale) and h·j (color-coded) maps at two instances; when the rotor wave-front near the core is directed from PV to LA (top)*

and about half cycle later, when it is directed from LA to PV (bottom). Blue dots represent the tip of the rotor and white dots are 4 mm from tip, toward LA (top) and toward PV (bottom). Right. Single pixel time-series showing simultaneous voltage and h·j at the white dots. Red arrows indicate the times of the voltage and h·j snapshots on the left side of the panel.

As illustrated in greater detail in Figure 3.7, the alternating SP drift is larger during propagation toward the PV (low h·j) than during its propagation toward the LA (high h·j).

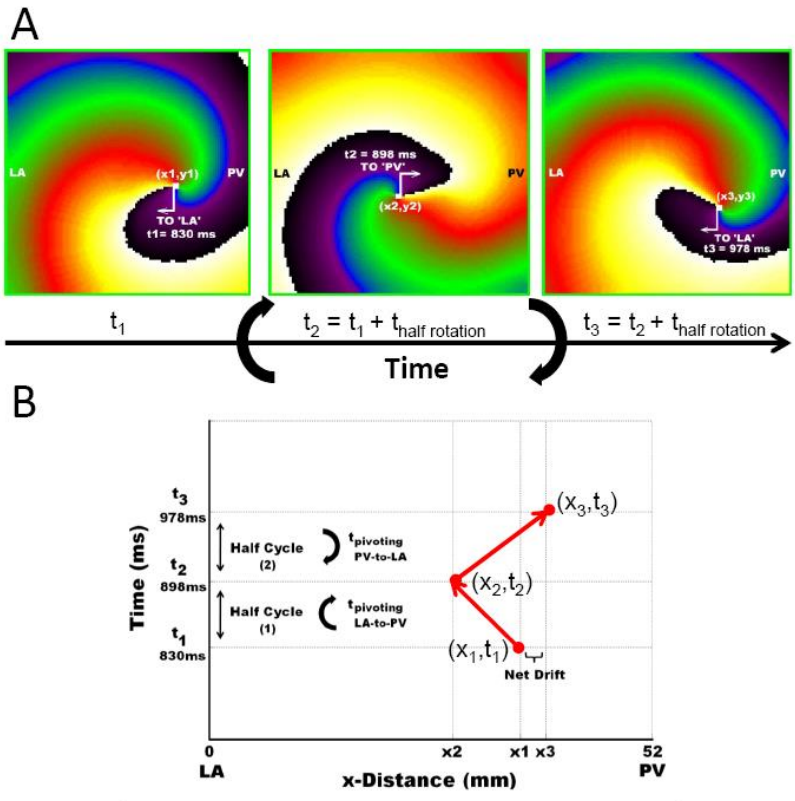

Figure 3.7 Linking rotor pivoting to rotor drift. *The process whereby the region with reduced excitability (h·j) attracts a rotor. A. Snapshots of the rotor at 3 moments: t_1 = 830 ms is a random reference time in which the front near the SP points toward the LA; t_2 = 898 ms is a time half a rotation later in which the front near the SP points toward the PV; t_3 = 978 ms is a time half a rotation later in which the front near the SP points again toward the LA and the rotor has completed a full rotation after t_1. The locations of the SP of the rotor at these 3 times are designated (x_1,y_1), (x_2,y_2) and (x_3,y_3), respectively. B. A time-space plot describing the trajectory*

of the rotor along the x direction (red arrows). The time it takes the rotor to complete its first half rotation is $t_2–t_1$=68 ms is shorter than the time it takes to rotor to complete its second half rotation $t_3–t_2$=78 ms. During that prolonged time the drift toward the PV, ($x_3 – x_2$), is larger than the drift toward the LA, ($x_2 – x_1$), resulting in a net drift, ($x_3 – x_1$), toward the PV once the full rotation is completed.

The result is a net drift toward the lower h·j, i.e., less excitable, region. Importantly, it is noticeable that a presence of heterogeneity at the core area is critical for the rotor drift; in absence of heterogeneity at the core, a rotor may be stable (Figure 3.8).

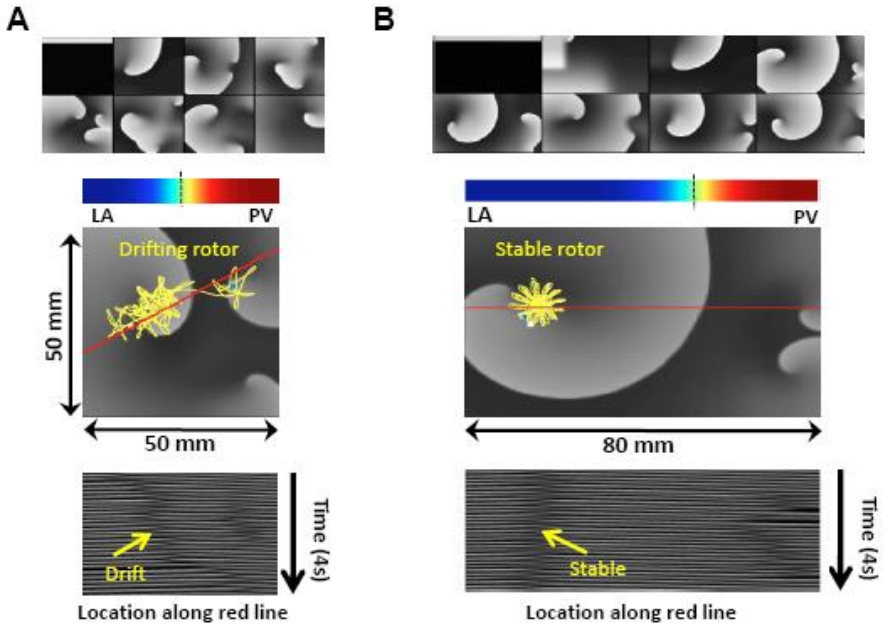

Figure 3.8 Ionic gradient at the core region and rotor drifting. *Here we demonstrate that heterogeneity is required within the core region to induce rotor drift. A. Simulation in a 50×50 mm^2 model of the PV-LAJ whose Boltzmann distribution is varying throughout the model (Condition I). B. Simulation in a 80×50 mm^2 model of the PV-LAJ whose Boltzmann distribution is mostly uniform in the LA portion of the model. Top panels: Sequential voltage snap shots (left to right and top to bottom) of the spontaneous time-course of a rotor initiated in the LA portion of the model. Color bars: The normalized Boltzmann factor variation from the LA (blue, 0) to the PV (red, 1) edges (see Figure 3.1). The dash vertical line illustrates the steepest gradient location. It is appreciated that there is a large area in the LA portion of the model in B that is uniformly zero (blue). The time-space plots (bottom)*

taken along the red lines of the models show that the core size (vertical dark gray band) is smaller than the area with LA uniform conditions in B, but not so in A, enabling a stable rotor in LA region, without a drift, in B but not in A. The appearance of a stable LA rotor in B is consistent with the stable rotor demonstrated recently by Campbell et al ***(Campbell 2012)*** *in a 35-mm wide monolayer of cardiomyocytes with a relatively more step-wise heterogeneity in I_{Kr} expression (Boltzmann ⊿x of about 1 mm compared to 5 mm in the present study)* ***(Noujaim 2007)***

Figure 3.9 summarizes the relationship between rotor drift and spatial distribution of excitability factors during reentry in the three conditions simulated. Panel A shows for illustration purposes a map with the distribution of the time-averaged h·j peak values for the model with greatest excitability gradient (Condition III) and shows that those values are about two-fold larger in the LA edge as compared with those at the PV edge (0.8 and 0.4, respectively). The graph in Panel A presents the spatial profiles of the h·j and the drift direction for the 3 conditions. It is seen that the 2 conditions with lowest density of I_{K1} at the PV edge (blue and red), have profiles with reduced h·j at that edge as well, in contrast to the condition without the I_{K1} gradient, where h·j is maximal at the PV edge. Overall, the directionality of the drift in the 3 conditions as indicated by the superimposed arrows is fully consistent with the rotor attraction by any region with lowest h·j values.

Next, Figure 3.9-B, quantifies metrics associated with the AP measurements of excitability: we focus on the dV/dt_{max} and MDP, which plays a role in determining the availability of I_{Na} during the membrane depolarization. On the left side we present samples of aligned pairs of action potentials recorded in locations (asterisks) near the LA (red) and PV (blue) edges during reentry in the 3 conditions. As can be appreciated, each condition presents a distinct heterogeneity in its action potentials as

quantified on the right side of the panel, but for the 3 conditions the drift direction is toward the regions with lowest excitability as determined by the slowest dV/dt_{max} and most positive MDP ***(Pandit 2005)***.

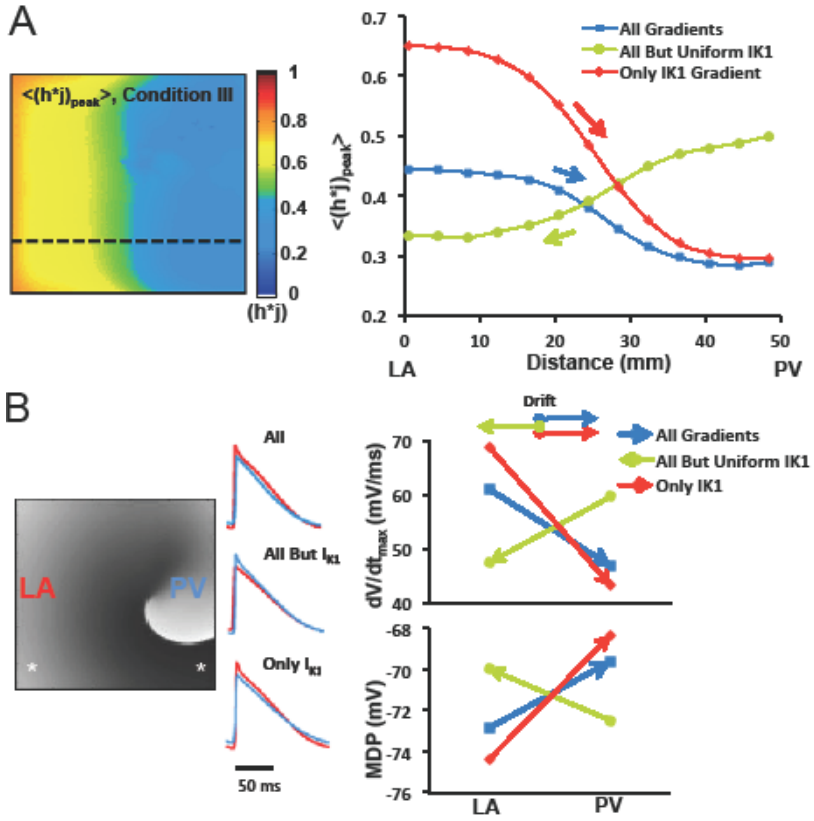

Figure 3.9. *Gradients of sodium availability and AP measurements during rotor drift predict drift direction. A. Left. Map of averaged $(h{\cdot}j)_{peak}$ ($\langle(h{\cdot}j)_{peak}\rangle$) during rotor activity under Condition III (Only I_{K1}) is showing a LA to PV decrease. A. Right. PV-LAJ spatial profiles of $\langle(h{\cdot}j)_{peak}\rangle$ for the 3 conditions modeled. Superimposed arrows indicate direction of rotor drift for each condition, consistently toward the region of lowest $\langle(h{\cdot}j)_{peak}\rangle$ (lowest sodium availability). B. AP measurements of excitability during reentry. Left. A voltage snapshot and APs from the LA (red) and PV (blue) edges (asterisks on map) for the 3 conditions simulated. Right. Upstroke velocity (dV/dt_{max}) and MDP at the LA and PV region with direction of drift (arrows) for the 3 conditions. Drift is consistently toward lowest upstroke velocity and most positive MDP regions.*

3.3.3 Pacing predictors of rotor drift in the PV-LAJ

We investigated pacing protocols that could be used to predict drift direction. In Fig. 3.10, we demonstrate APD profiles consequential of a steady pacing at the center of the junction, where rotors were initiated, and radial propagation. Fig. 3.10-A, illustrates the steady state APD_{80} profiles at 2 Hz pacing for the 3 conditions along with an indication of drift direction. The APD profiles show different gradients for each particular condition of ionic gradients. Correlating the APD profiles with the reentry simulations we find that rotors initiated in Condition I drifted toward the PV (Fig. 3.3-B) and stabilized at the shortest APD region. When the I_{K1} gradient is excluded (Condition II), the APD difference across the transition is maintained, but the drift direction reversed. However, in Condition III, the spatial APD difference is reversed. Yet, the rotor drifts from the LA to the PV and even does it that faster (see Fig. 3.3-B) as there are no ionic effects opposing the I_{K1} effect. Panel B presents ERP and dV/dt_{max} determined at 2 Hz pacing at the LA and PV edges. It is demonstrated that while ERP is, like APD_{80}, inconsistent with drift toward either longer or shorter period, the drift is consistently toward the highest dV/dt_{max} for the 3 conditions.

Noticeably, the LA-PV dV/dt_{max} gradient directions (measured at 2 Hz pacing) in Fig. 3.10-B are contrasting the dV/dt_{max} gradient directions in Fig. 3.9-B (measured during reentry at about 7 Hz), leading us to further assess the dependency of AP properties on pacing frequency. The traces at the top Fig. 3.10-C show that APs in Condition I display distinct variation of duration at different repolarization levels during increasing pacing rate from 2 to 7 Hz; the bar-graph at the bottom of Panel C compares APD values across Condition I for 1000, 500 and 140 ms cycle length (respectively 1, 2 and 7.14 Hz pacing rates) and shows that while at 1 Hz pacing the PV APD is shorter than the LA at all repolarization levels, at 2 Hz and even more so at 7 Hz (close to the rotor frequency), APD_{90} at the PV edge is longer than in the LA. Panel D shows that APD_{80}, dV/dt_{max} and ERP across the model with

Condition I heterogeneity measured only at a cycle lengths of 140 ms (7.14 Hz) resulted in gradient directions consistent with the previous prediction of the drift toward longer APD and lower excitability ***(Fast 1990, Davidenko 1991, Tusscher 2003).***

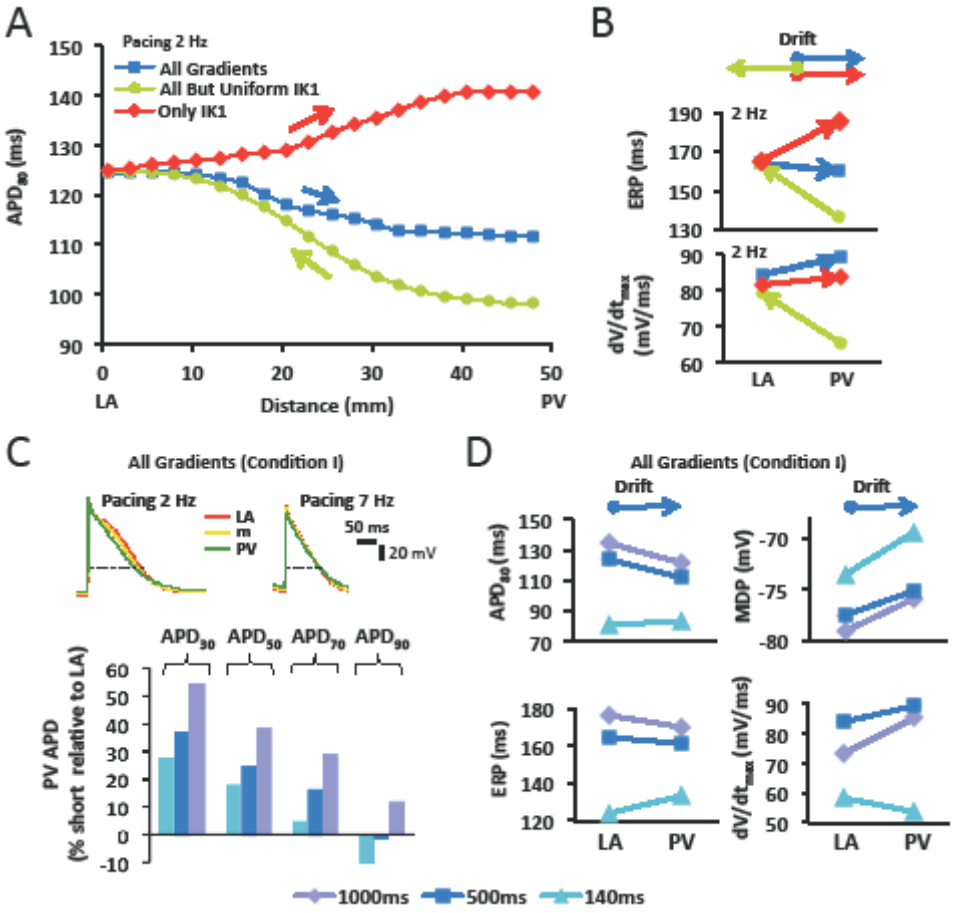

Figure 3.10 *Pacing predictors for drift direction. A. APD_{80} profiles resulting from pacing at 2 Hz in the middle of the model show inconsistent drift (arrows) toward either short or long APD regions for the 3 simulated conditions. B. ERP and dV/dt_{max} measured at LA and PV at 2 Hz pacing for the three conditions show inconsistent drift direction. C. Frequency-dependence of APDs. Top. single pixels APs in 3 locations across the PV-LAJ at 2 and 7 Hz pacing. Bottom, APDs in the PV relative to those in the LA. Notably, at all pacing rates slower than 140 ms, (7.14 Hz - close to the rotation frequencies in the LA and PV; see Fig. 3.2) the APD in the PV is shorter than in the LA (except APD_{90} at 140 and 500 ms). D. APD_{80}, ERP, MDP and*

dV/dt_{max} in the LA and PV as measured at 1000, 500 and 140 ms pacing rate. Drift direction is also indicated (arrows on top).

On the other hand, the LA-PV dispersion of MDP displayed a rate-independent correlation with the drift direction; regardless of the pacing rate, the drift was found consistently toward the region with the most positive MDP (also for Conditions II and III, not shown).

3.3.4 The I_{K1} and rotor drift direction

Figures 3.3 and 3.5 demonstrated the important role of I_{K1} in determining the direction of the rotor drift in the PV-LAJ. Here we study the effect of various relevant current-voltage relationships of I_{K1} on such drift direction. Panel A of Fig. 3.12 shows 4 I-V relationships for different I_{K1} levels, including up- and down-regulation, as well as their corresponding APs showing different APDs and MDPs. The 4 I-V relationships were incorporated in a PV-LAJ model with Condition I and rotor activity as well as AP parameters were tracked. As can be observed from Panel B, increasing or decreasing the $I_{K1,}$ increases or decreases the average rotor frequency, respectively. Panel C demonstrates that h·j profiles across the PV-LAJ vary both in levels and gradient directions as a consequence of altering the I-V relationships. In particular, it is noticeable that rotor drifts toward the PV for a broad range of I_{K1} levels while a reversal in the drift and h·j gradient direction occurs only at a 75% reduction in I_{K1} (a behavior similar to that of a uniform I_{K1} shown under Condition II in Fig. 3.3).

Up- and down-regulation of I_{K1} also hyperpolarize and depolarize MDP as well as increase and decrease upstroke speed, respectively (Panel D), with consistent drifts toward higher MDP and lower upstroke velocity. Overall, the consequences of altering the I-V properties of I_{K1} in the heterogeneous models on h·j, MDP and upstroke velocity shown in panels C and D are complex and suggest a non-monotonic dependency.

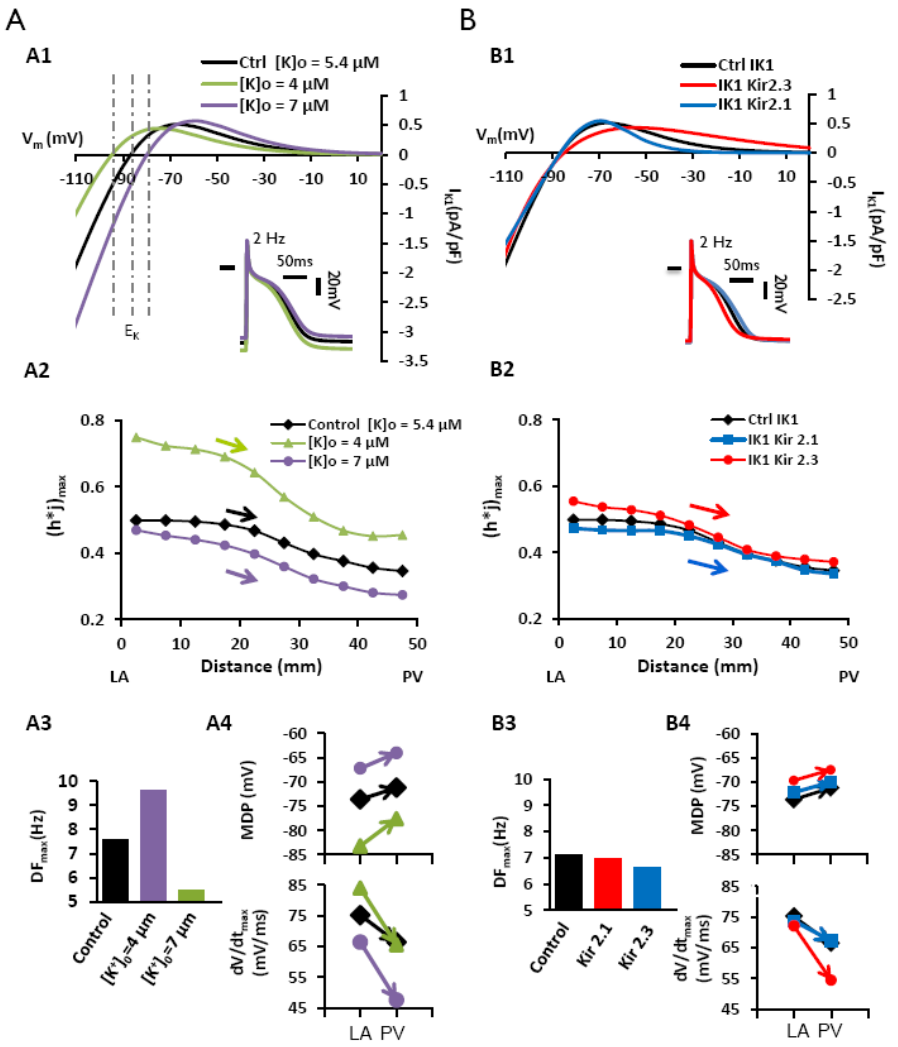

Fig. 3.11. Effect of [K]$_o$ and major I_{K1} isoforms on rotor drift direction. *A. Investigating the effect of [K]$_o$ on rotor drift. A1. I_{K1} I-V curves under conditions of normal, reduced and increased [K]$_o$ demonstrate shifting of the reversal potential and altering slope resistance as well as outward current properties. A2. Rotors drifted toward the excitability sink (lowest h·j) at the PVs for all [K]$_o$ levels. A3. Effect of [K]$_o$ on DF_{max}. A4. Both MDP and dV/dt_{max} measured during rotor activity were consistent predictors of rotor drift for all [K]$_o$ levels. B. Investigating the effect of changes in I-V relationship of I_{K1} resulting from altering its isoforms. B1. I_{K1} I-V profiles for a typical Kir2.1 and Kir2.3 dominant isoforms. B2. As in panel A2, rotor is drifting toward the excitability sink (lowest h·j) in the PV edge for any I-V profile. B3. Effect of the different I-V profiles in B1 on DF_{max} is small. B4. Both MDP and*

dV/dt_{max} measured during rotor activity were consistent predictors of rotor drift for all I-V profiles tested.

Nevertheless, further alterations in extracellular potassium concentration in the range of 4-7 mM, as well as alteration in the I-V profile to resemble closely those of Kir2.1 or Kir2.3 ***(Dhamoon 2004)***, affect excitability and rotation frequency, but do not alter direction of h·j gradients and drift directions toward the PV (Fig. 3.11).

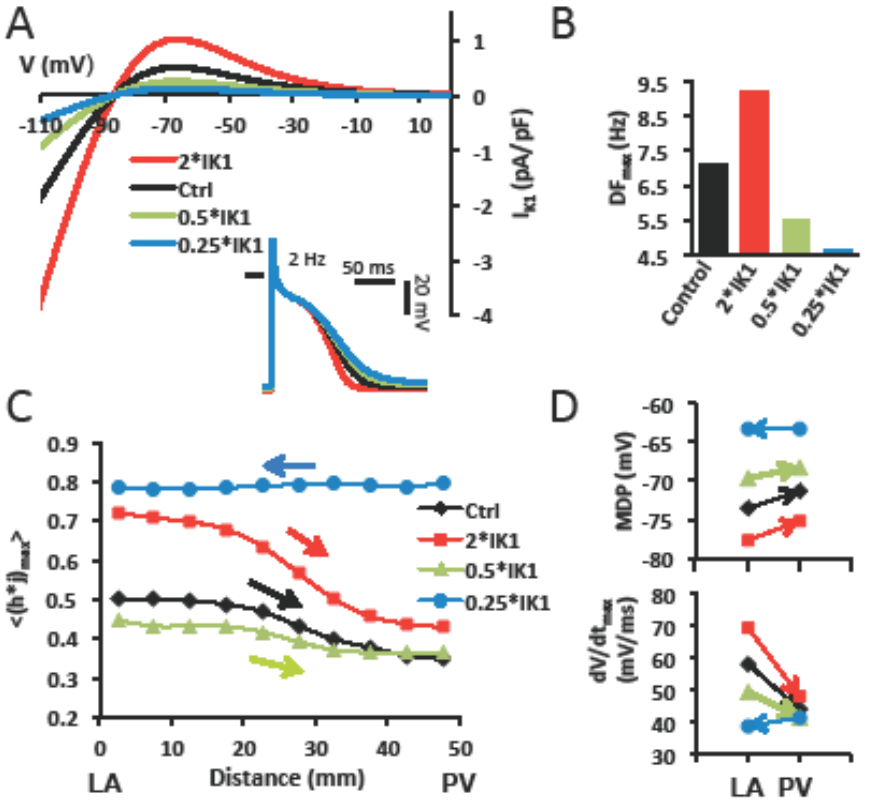

Fig. 3.12 *I_{K1} levels and drift direction. A. I_{K1} I-V curves for normal (control) and other levels of I_{K1} density. Steady state APs induced at 2 Hz are illustrated. B. Rotation frequency in LA homogenous model for each I_{K1} density level. C. Average peak I_{Na} availability profiles show drift towards lower excitability (arrows) in a model with Condition I. D. Analysis of MDP and dV/dt_{max} for each profile at single pixels in the LA and PV (4 mm from boundaries) under Condition I.*

3.3.5 Comparative effects of ionic, passive and geometrical gradients on rotor drift

A gradient in membrane currents is just one of the factors that may affect rotor drift. For example, the PV-LAJ is known to have a heterogeneous intercellular coupling that is also known to affect rotor drifts.

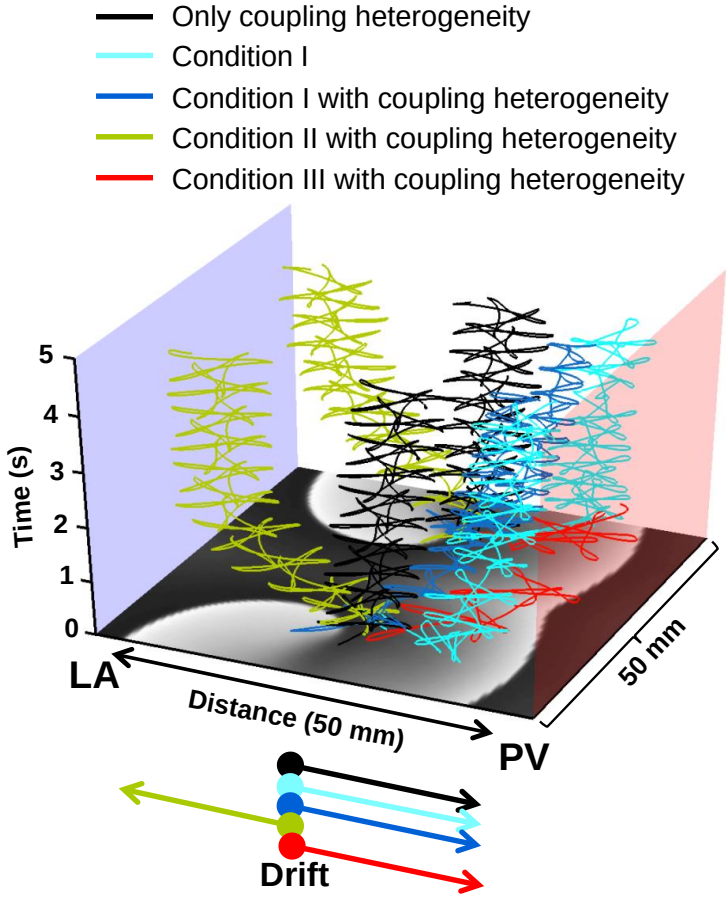

Figure 3.13 Heterogeneous intercellular coupling in the PV-LAJ and rotor drift. *Models were generated with heterogeneous isotropic intercellular coupling following a Boltzmann profile with 25% reduction in the PV vs. the LA edges. The figure shows a TSP and drift directions of counter-rotors at the various conditions indicated. In the presence of only coupling heterogeneity the rotors drift toward the PV (black) less than the drift with all ionic gradients (Cyan, Condition I). The drifts in the models with heterogeneous coupling combined with either Conditions I, II and III did not differ qualitatively from those with a uniform coupling (see Fig. 2)*

suggesting that the presence of the heterogeneous coupling does not alter the major role of I_{K1} in determining the rotor drift direction in the PV-LAJ toward the PV edge, where the coupling coefficient is lowest.

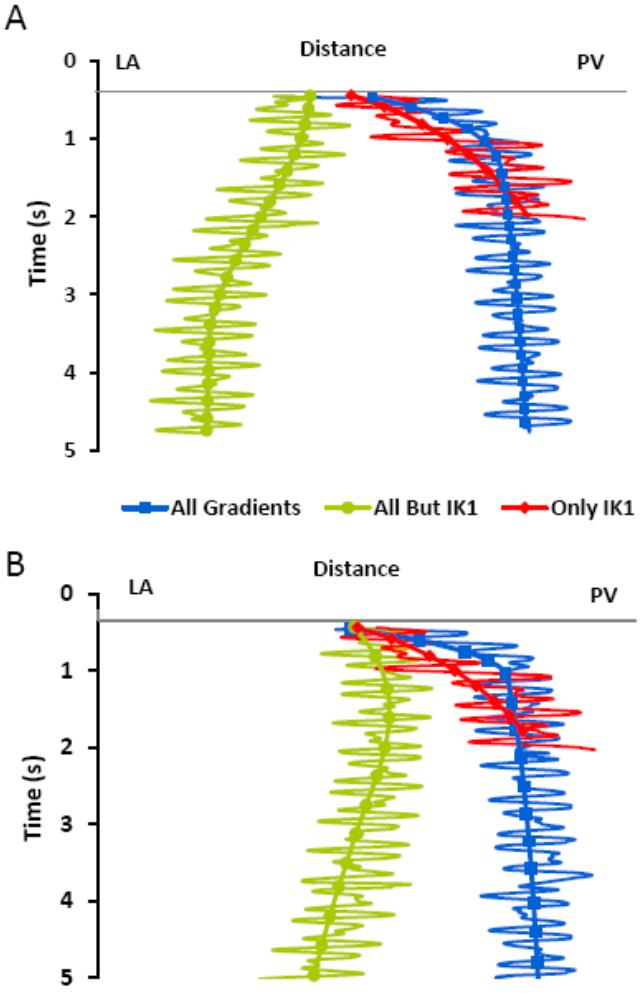

Figure 3.14. Rotor drift in the presence of additional gradient in sodium current. *The presence of I_{Na} gradients in the PV-LAJ is suspected but not yet confirmed. Thus we investigate its role in determining drift direction relative to I_{K1} gradient role. Gradients in I_{Na} whereby the PV conductance was reduced by 20% (panel A) and 40% (panel B) were incorporated in models similar to those used in Fig. 2. The TSPs here show SP trajectory for the 2 conditions of gradients in all currents (All Gradients; Condition I + gradient in I_{Na}; blue traces) and gradients in all currents, but I_{K1} (All but I_{K1}; Condition II + gradient in I_{Na}; green traces), as well a gradient only in I_{K1} (Condition III; Only I_{K1}; red traces). Both panels show evolution of the*

tip trajectories for the rotors similar to those presented in Fig. 2, demonstrating that while I_{Na} contributes to the drift of the rotors in the PV-LAJ, I_{K1} is still the dominant current whose gradient determines drift direction.

Based on a 25% lower density of gap junctions and connexins relative to the rest of the atria ***(Chaldoupi 2009)*** the intercellular coupling in the PVs' region of the LA is speculated to be lower than that of the LA. As expected, the gradient in the passive properties of the tissue ***(Tusscher 2003, Berenfeld 1999)*** attracted the rotor toward the PV, where the coupling coefficient is the lowest (see Fig. 3.13) and in a similar direction as the ionic gradients. Interestingly, our simulations suggest that the I_{K1} heterogeneity is still a major factor determining the drift direction in the presence of the heterogeneous intercellular coupling.

In addition to the ionic heterogeneity, a prominent geometrical feature of the LA-PV junction, namely its funnel-shaped walls, may also affect functional rotor dynamics by spatial confinement in the PV and asymmetric source-sink relationships with the LA ***(Cherry 2007).*** In contrast to the gradient in the coupling, the effect of the geometrical confinement of the PVs on drift is not clear. Accordingly, we constructed a control homogeneous model with a uniform level of ionic currents and another model with heterogeneous distribution of the ionic currents (see Figs 3.1 and 3.3). A single functional rotor was initiated in both models close to the LA edge (Fig. 3.2) and its spontaneous meandering and drift were tracked by the trajectory of its SP. In Fig. 3.15 we show that the ionic gradients play an important role in the drift of a rotor toward the PV even in the presence of a constraint imposed by the narrowing space near the PV. Panel A shows phase snapshots and the trajectory of the rotor superimposed on a homogeneous (left) and heterogeneous (right) funnel models. Panel B is a bull-eye presentation of the rotor trajectory in the homogeneous (left) and heterogeneous (right) funnel models. Panel C of Fig. 3.15 shows that the SP trajectory over a period of 5 sec after onset in the heterogeneous vs. the homogeneous model is

characterized by a drift toward the PV, with gradual shortening of the distance between the pivoting point and the PV edge of the funnel model. Thus we conclude that a generic funnel shape of a realistic dimension of the LA-PV junction does not eliminate the rotor attraction of the PV that is induced by the dispersion of ionic currents across that region.

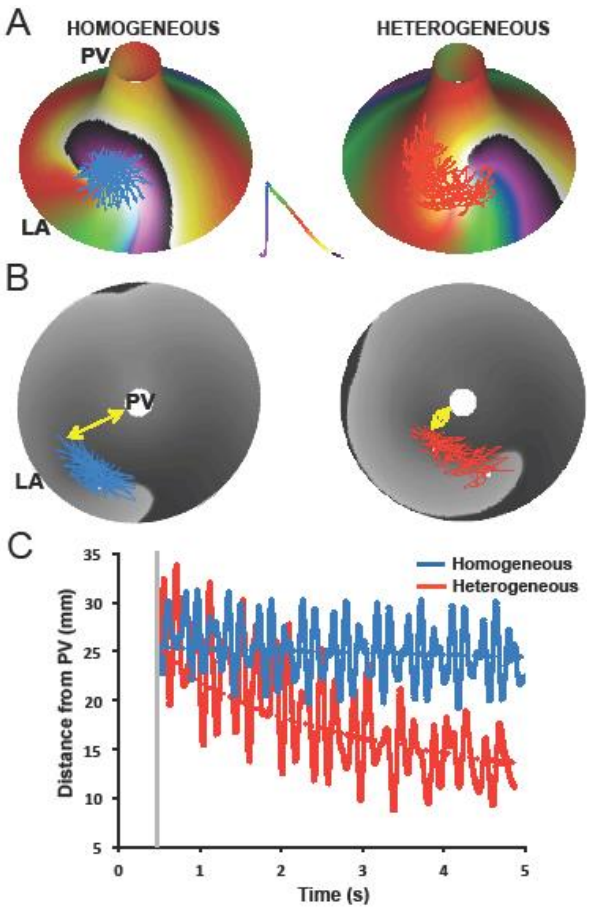

Figure 3.15 *Geometry and drift. A. Funnel-shaped PV-LAJ models with homogeneous (left) and heterogeneous (right, Condition I, see Fig. 3.1). Phase color-coded snapshot activity (see insert) and SP trajectory are superimposed on the model. B. Bull-eye view of the models in A with voltage snapshot (gray levels) and SP trajectories. Yellow arrows indicate a sample distance between the SP and the PV. C. The decreasing distance between the SP and the PV edge demonstrates a PV attraction in the heterogeneous (red) vs. the homogeneous (blue) model.*

3.4 Discussion

3.4.1 Main findings

The main new findings of our study are that: (i) The heterogeneous distribution of transmembrane currents in the PV-LAJ plays a major role in the preferential localization of rotors near or at the PVs, and that the spatial dispersion of I_{K1} is particularly important in determining such attraction. (ii) Rotor drift in the PV-LAJ can be attributed to an excitability (maximum I_{Na} availability) gradient in the vicinity of the rotor pivoting point. (iii) In dissecting tissue properties that can explain rotor drift by conducting simple 1:1 pacing protocols, the MDP variable is a reliable predictor, independent of frequency of pacing (more positive MDP attracts rotors). And finally, (iv) the generic funnel-shaped geometry and the inter-cellular coupling dispersion in the PV-LAJ do not alter the ionic-induced attraction of rotors toward the PV and further suggests that the particular dispersion of transmembrane currents present in the PLA during paroxysmal AF contributes to the important role of the PVs in maintaining the arrhythmia.

4.4.2 Mechanisms of AF and rotor dynamics

Our understanding of AF in individual patients would benefit from knowledge of how driving rotors form and then become stable or unstable, under the conditions of multi-factorial substrate heterogeneity ***(Jalife 2003, Oral 2005)***. Paroxysmal AF in patients and in isolated normal sheep hearts has been found often to depend on fast rotors localized to the posterior wall of the LA and the PVs region with fibrillatory conduction toward the rest of the atria ***(Mandapati 2000, Atienza 2006)***. However, the ionic properties underlying those rotors' formation and drift remain unclear ***(Tanaka 2007, Sarmast 2003)***. Moreover, recent studies have indicated that, in some patients rotors that drive the AF may reside outside of the PV area ***(Narayan 2012)***. Our simulations here demonstrate for the first time that the spatial

distribution of ionic currents found in the canine PV-LAJ are conducive to attracting rotors to the PV region. In addition, we also demonstrate that this attraction toward the LA can be reversed or arrested, if certain ionic currents are altered, which in turn may explain the variability in the location of rotors found in different patients. AF however may involve several co-existing rotors at any given moment. In these cases, in addition to the drift imposed by the underlying substrate, the faster rotors can also exert an overriding influence on the slower rotors ***(Davidenko 1995),*** and the combination of these two factors on rotor dynamics warrants further investigation.

3.4.3 Substrate heterogeneity and rotor drift

In addition to the role of restitution characteristics of cells in rotor stability ***(Kleber 2004)*** simulations with gradient of excitability showed spiral wave drifting in the direction of the region exhibiting lower excitability and velocity, with additional perpendicular component depending on the rotor chirality, ***(Pertsov 1993)*** excitability and repolarization ***(Fast 1990)***, regardless of the details of the initial conditions ***(Wellner 1999).*** Simulations using more biophysically-detailed ionic models found that for a fixed gradient in APD imposed by linearly varying potassium currents, the velocity of the drift of a rotor is a function of the magnitude of the gradient ***(Tusscher 2003)*** and a steep gradient in APD can lead to conduction block of premature beats ***(Sampson 2001)***. Our results here are in agreement with all those previous studies, but refine the previous prediction that rotors would drift toward regions with longer APD ***(Fast 1990, Davidenko 1991, Dhamoon 2004)*** to only >80% repolarization measured at frequencies close to the rotor frequency. Our simulations (Fig. 3.16) also show that drift predictability of various measures of excitability that include ERP, dV/dt_{max} and $h \cdot j$ (I_{Na} availability); only MDP is able to predict drift direction, regardless of the pacing rate at which it is assessed. We also show for the first time that the attraction induced by the ionic heterogeneity is stronger than the constriction

imposed by the small area in the distant PV sleeve produced by the curved geometry (Fig. 3.15). The homogeneous ionic condition simulation in the funnel model of the PV induces a stable, non-drifting rotor, and suggests that the smaller PV vs. LA area increases the safety for propagation toward the PV.

3.4.4 I_{K1}, I_{Kr} and rotor dynamics during fibrillation

I_{K1} and I_{Kr} density gradients in the dog PV-LAJ are found to be opposing each other ***(Cha 2005)***. As recent studies have shown these two currents are important in rotor dynamics and AF ***(Hou 2010, Noujaim 2007, Pandit 2013) (Campbell 2012) (Noujaim 2010, Amit 2010)***, the ionic mechanisms leading to the propensity of the PV region to favor rotor activity ***(Lemola 2008, Po 2005, Aora 2003)*** became complex. We show for the first time a clear propensity of the currents distribution in the PV-LAJ to attract rotors to the PVs and the dominant role for the I_{K1} dispersion over all currents, and in particular I_{Kr}, in determining the localization of a rotor in that area and open the possibility that interplay between I_{K1} and I_{Kr} may be important for the differential localization of rotors in AF.

Ventricular fibrillation in guinea-pigs isolated hearts is driven by stable rotors in the left ventricle (LV) where the outward component of I_{K1} was found to be higher than the right ventricle (RV) ***(Warren 2003, Samie 2001)***. At first, the predictions in the present study suggesting that rotors would stabilize at the lowest I_{K1} region seem to conflict with those previous findings, but a deeper examination reveals that the two studies are complimentary. The present study considers rotors with a core dimension of about 11 mm (Fig. 3.4) that extends over an area that is wider than the distance of about 5 mm in which a gradient of currents was measured in the canine posterior LA (Fig. 3.1) ***(Ehrlich 2003 , Cha 2005)***. Moreover, our simulations here focus on currents heterogeneities that are continuous and

monotonic, and in the absence of any structural heterogeneity. In the guinea-pigs study on the other hand, we have no data on the transition in the density of currents other than I_{K1}, between the LV and RV, which may be present uniformity over areas larger than the core size, thus enabling the rotor's stabilization in the larger I_{K1} zone (Fig. 3.8). Moreover, various anatomical components, such as the papillary bundle, are likely to present additional anchoring factors further stabilizing a driving rotor.

Comparing with other studies, the drift toward low I_{K1} in our study is fully consistent with the simulations by Kneller et al ***(Kneller 2002)*** who studied the effect of artificial heterogeneity in the inward rectifier $I_{K,ACh}$ on AF dynamics. Although not explicitly analyzed, their simulations also suggest that while rotors accelerate their rotation frequency with increasing $I_{K,ACh}$, ***(Sarmast 2003)*** the low $I_{K,ACh}$ regions are the ones that attracts rotors ***(Kneller 2002).*** On the other hand, a recent study by Sekar et al ***(Sekar 2009)*** in circular monolayers with overexpression of I_{K1} either in a central circular island, or in its periphery, showed that rotors stably pivot around the island regardless of the relative level of I_{K1}. In that study the gradient however was very sharp relative to the size of the rotor core, and the preparation was highly symmetrical, which may explain why that study did not show a preferential anchoring of rotors to either low or high inward rectifying K^+ current levels as observed in this and other studies ***(Kneller 2002, Samie 2001)***. Finally, in a prior study in cardiomyocytes monolayers with heterogeneous I_{Kr} expression, stable rotors localized to the region with highest expression of I_{Kr}. ***(Campbell-Calvo 2012)*** Those stable rotors did not drift as in our simulations since they reside in a relatively uniform large region, in accordance with our simulations presented in Figure 3.8.

3.5 Limitations

We study a specific set of membrane kinetic models (CRN-K) with a Boltzmann distribution of the current densities across the PV-LAJ preferred for extensive validation of propagation properties ***(Pandit 2005, Zlochiver 2008)*** over a more recent and detailed model requiring adjustments. ***(Grandi 2001, Deo 2013)*** experimental or clinical data on ionic properties and dispersion in the atria are scarce; we focused on the effect of reported ionic currents data for the dog. However, attraction or repulsion of rotors by the PVs at the PVLAJ, may be affected by factors other than those studied here. For example, the heterogeneity in the intrinsic cellular properties may have different effective heterogeneity in refractory and excitability ***(Wellner 1999)*** depending on structural intercellular coupling, ***(Bub 2005)*** fibrosis ***(Ashihara 2012)*** or the size of the medium ***(Sampson 2001, Viswanathan 1999, Sampson 2002, Sampson 2005).*** Further, the drift of rotors may be further influences by accumulations or intra- or extracellular ions, as has been shown to occur in AF ***(Miyata 2002)***. In our study, we ruled out that PV funnel-like anatomy reverses the ionic-induced attraction to the PVs, however additional anatomical factors such as wall thickness ***(Zhao 2012, Yamazaki 2012),*** the fiber bundles ***(Klos 2008)*** or fibrosis ***(Tanaka 2007)*** may also regulate the drift of rotors; possibly even counteracting the drift trend caused by the ionic gradients. To mitigate these limitations we focused in our study on conditions relevant only to paroxysmal AF, prior to any remodeling and fibrosis, and incorporated various possible I-V relationships to substantiate our conclusions regarding the I_{K1} dominance and drift prediction (see Figs 3.11-3.14). Our study nevertheless should be considered only as a first step in elucidating the concept of heterogeneity-induced drift, and needs to be further tested in future experimental studies.

3.6 Conclusions

Here a computational platform has been validated for studying intrinsic mechanisms, capturing and tracking dynamics and modulating factors of rotor drifting in AF. The author of this thesis has developed all the methodological and analytical results obtained all the results presented.

Regarding the major results, consistent with experimental and clinical studies on paroxysmal AF, simulations in an ionically heterogeneous model of the PV-LAJ showed rotor attraction towards the PVs, consistent with reduced coupling and despite spatial constriction in the PV region. Our simulations suggest that I_{K1} heterogeneity across the PV-LAJ is dominant compared to other currents in conveying drift direction through its effect on refractoriness and excitability. Our simulations also suggest that measuring with high-resolution refractoriness, excitability and diastolic potentials during pacing could provide a mechanistic guidance for the unstable components of rotors that are believed to underlie AF. We have also shown that deterministic spectral and phase-domain properties of rotors may be used for identifying key biomarkers of fibrillatory drivers and their attractors using advanced signal processing techniques which may be used to envision mechanistic-based therapeutic strategies in the clinical setting.

Chapter 4

Spectral-based Risk Score for Early Prediction of Mortality in Patients suffering from Cardiac Arrest

In this chapter, we aim to develop a mechanistic-based multivariate model and risk score that reliably predicts cerebral performance and survival, on admission of comatose survivors undergoing therapeutic hypothermia for ventricular fibrillation taking into account biomarkers representing deterministic features of the arrhythmia. Specifically we test the hypothesis that VF spectral predictors may have a strong significant correlation with survival and neurological performance after cardiac arrest due to VF. Furthermore we test different machine learning approaches finally having a compromise between predictive accuracy and clinical readability of data-driven predictors. Physicians dealing with difficult decisions in comatose survivors after cardiac arrest due to ventricular fibrillation may benefit novel risk scores developed taking into account intrinsic mechanistic considerations to obtain early prognosis information and to optimize the use of intensive-resource care.

4 Spectral Analysis-based Risk Score to Early Predict Mortality and Cerebral Performance in Patients Undergoing Therapeutic Hypothermia for Ventricular Fibrillation and Comatose Status

Here results from the publication *[Filgueiras-Calvo 2015]* are reproduced in author format, together with additional results published in international and national conferences.

4.1. Abstract

Early prognosis in comatose survivors after cardiac arrest due to ventricular fibrillation (VF) is unreliable, especially in patients undergoing mild hypothermia. We aimed at developing a reliable risk-score to enable early prediction of cerebral performance and survival. Sixty-one out of 239 consecutive patients undergoingmild hypothermia after cardiac arrest,with eventual return of spontaneous circulation (ROSC), and comatose status on admission fulfilled the inclusion criteria. Background clinical variables, VF time and frequency domain fundamental variables were considered. The primary and secondary outcomes were a favorable neurological performance (FNP) during hospitalization and survival to hospital discharge, respectively. The predictive modelwas developed in a retrospective cohort (n=32; September 2006–September 2011, 48.5 ± 10.5 months of follow-up) and further validated in a prospective cohort (n = 29; October 2011–July 2013, 5 ± 1.8 months of follow-up). FNPwas present in 16 (50.0%) and 21 patients (72.4%) in the retrospective and prospective cohorts, respectively. Seventeen (53.1%) and 21 patients (72.4%), respectively, survived to hospital discharge. Both outcomes were significantly associated (p b 0.001). Retrospective multivariate analysis provided a prediction model (sensitivity= 0.94, specificity = 1) that included spectral dominant frequency, derived power density and peak ratios between high and low frequency

bands, and the number of shocks delivered before ROSC. Validation on the prospective cohort showed sensitivity = 0.88 and specificity = 0.91. A model-derived risk-score properly predicted 93% of FNP. Testing the model on follow-up showed a c-statistic ≥ 0.89. A spectral analysis-basedmodel reliably correlates time-dependent VF spectral changes with acute cerebral injury in comatose survivors undergoing mild hypothermia after cardiac arrest.

4.2 Introduction

Both in-hospital and out-of-hospital cardiac arrest due to ventricular fibrillation (VF) are associated with high mortality rates and significant cerebral disability.***(Nadkarni 2006, Cobb 2002)*** VF-derived cerebral injury is a very sensitive time-dependent condition with dramatic social and personal consequences. The absence of cerebral blood flow during VF leads to ischemic damage within a few minutes, which increases after reperfusion due to generation of oxygen free radicals, activation of degradative enzymes, together with other mediators.***(Sugawara 2003)*** To date, mild hypothermia is the only therapy that has shown to increase survival rates and functional outcomes in comatose survivors of cardiac arrest due to VF. ***(Bernard 2002, Holzer 2002, Lopez-de-Sa 2012)*** However, the use of sedative and neuromuscular blocking drugs in cooled patients may mask neurological damage and delay examination. Furthermore, early prognostication within the first 72 h after cardiac arrest remains unreliable, which is especially relevant in those patients undergoing highly specialized intensive care who might not have any hopes for recovery.

Reducing the time to DC shock after VF onset is vital to restore spontaneous circulation and minimize cerebral injury.***(Rogove 1995)*** However, the exact time in VF is difficult to determine even after witnessed cardiac arrest. Many VF episodes may initiate as ventricular tachycardia and cerebral blood flow might still

persist until VF develops.***(Bayes de Luna 1989)*** Reliable experimental data from waveform analysis during VF indicate that both spectral dominant frequency (DF) and median frequency decrease after onset of VF.***(Brown, 1989, Stewart 1992)*** In the clinical setting, such a decrease in spectral values correlates with poor defibrillation success and no return of spontaneous circulation (ROSC).***(Strohmenger 1994)*** Moreover, retrospective data in patients with out-of-hospital cardiac arrest and VF have also shown that a 5.61 Hz DF threshold can serve as a good predictor for 1-year survival after discharge.(***Goto 2003***) However, we hypothesize that spectral analysis of VF before a DC shock will accurately reflect the degree of acute cerebral injury as a consequence of time in VF and concomitant myocardial ischemia. Here, we analyzed VF waveform properties before the first DC shock in patients undergoing therapeutic hypothermia due to comatose status after advance life support (ALS) and ROSC. We aimed to identify spectral parameters that in combination with clinical variables may serve to develop a reliable model and risk score to early predict cerebral performance and survival to hospital discharge. We also studied the capacity of the model to predict both outcomes at follow-up.

4.3 Methods

4.3.1 Study Design

The study was performed in a referral center for out-of-hospital cardiac arrest (Hospital Universitario La Paz, Madrid, Spain), in which mild therapeutic hypothermia is routinely used in comatose survivors after the event. The study included consecutive patients who underwent mild hypothermia after cardiac arrest due to VF, eventually with ROSC, and comatose status (Glasgow Coma Scale ≤8) on admission. Patients with witnessed or un-witnessed documented VF were eligible for the study, as long as VF traces before the first DC shock had enough quality and duration (≥3 s) for digitization and analysis of spectral parameters, respectively. We excluded patients with early mortality or hemodynamic instability leading to incomplete 24-h of mild hypothermia, and absence of subsequent

withdrawal of sedation to assess cerebral performance. Other exclusion criteria were age <18 years, Glasgow Coma Scale score after ROSC >8, non-shockable or shockable rhythms other than VF, a terminal illness or cognitive deterioration present before the cardiac arrest, and possible causes of coma other than cardiac arrest. The study was divided in two groups, as follows: Group 1 with eligible patients from September 2006 to September 2011 and retrospective data analysis, and Group 2 with eligible patients from October 2011 to July 2013, in whom we prospectively studied the utility of the predictive algorithm developed in Group 1. All data were collected from a prospective registry. The institutional ethics review committee approved prospective analysis of the patients, in accordance with European Guidelines, the ethical guidelines of the 1975 Declaration of Helsinki and European guidelines for good clinical practice.

4.3.2 Hypothermia protocol in patients

Patients admitted to the acute cardiac care unit underwent routine neurological evaluation before sedation, drug-induced paralysis and initiation of hypothermia protocol as described elsewhere.***(Lopez-de-Sa 2012)*** Briefly, cooling with intravenous cold saline (<8°C) was initiated on admission. This was followed by direct cooling of the blood using the Icy catheter (ZOLL Medical Corporation, Chelmsford, MA) positioned at the inferior vena cava through the femoral vein. Cooling was set at a maximum rate with a target temperature either at 32, 33 or 34°C, which was maintained during 24 hours. Rewarming was controlled at a set rate of 0.1 to 0.3°C per hour to reach 37°C in 12 to 24 hours. Mechanical ventilation was adjusted to ensure mormoxemia and normocapnia. Mean blood pressure was maintained between 85 and 100 mm Hg. Blood glucose level was ensured <180 mg/dL. Limitation of active ALS was considered in patients who remained deeply comatose after 5 days of evolution, as long as it was possible to reach an agreement with their representatives.

4.3.3 VF Spectral Analyses

For each patient, we analyzed VF epochs prior to the first DC shock. All data analyses, extraction and quantifications were done using custom scripts written in MATLAB software (version 7.11.0 R2010b, The MathWorks Inc, Natick, Massachusetts, USA). The scripts were developed using the retrospective cohort. Blinded investigators to clinical outcomes performed waveform and spectral analysis of ventricular fibrillation (VF) traces.

a) Image digitization, signal extraction and interpretation.

Standard ECG tape recordings were used to assess waveform parameters of VF prior to the first documented DC shock in all patients. Lead II traces were extracted unless artifacts were present. A semi-automatic approach was used for digitization using a Matlab-based custom tool. VF recordings were scanned to a digital image (1200 dpi) and stored in a codified digital format. To identify VF traces on the standard ECG-paper, image-processing techniques were applied involving binary thresholding, pixel-to-point conversion and transform techniques. ***(Ravichandran 2013, Kumar 2012)*** When necessary, images were pre-processed to avoid artifacts (contrast, median filtering and interpolation) in the digitization process. Pixel-to-point conversion was applied using the lower waveform envelope. The graphical grid was used as reference for interpretation. Before signal processing, an independent investigator reviewed all digitized traces to ensure accurate extraction of VF deflections.

b) Signal processing.

Digitized signals were post-processed and further analyzed in Matlab. Up to 5-s artifact-free segments prior to the external DC shock were extracted in each patient. Signals with less duration were zero-padded up to 5 s. Only segments of at

least 3 s were eligible for the study (Mean±Std duration 3.91±0.98 s, N=61). All signals were detrended by mean removal. A 4th order polynomial approximation was applied to remove the baseline trend when appropriate. Then, VF tracings were bandpass filtered between 1.5 and 40 Hz using 10th order Butterworth digital filters. Averaged power spectral density (PSD) was obtained at each frequency. We used a non-parametric Welch method for robust Fast Fourier Transform (FFT) estimation with 0.2 Hz spectral resolutions in the 1.5 to 10 Hz band of interest, where at least 90% of the spectral power was concentrated. Spectral information in this band was normalized to the total power for each patient before attempting to extract any spectral variable.

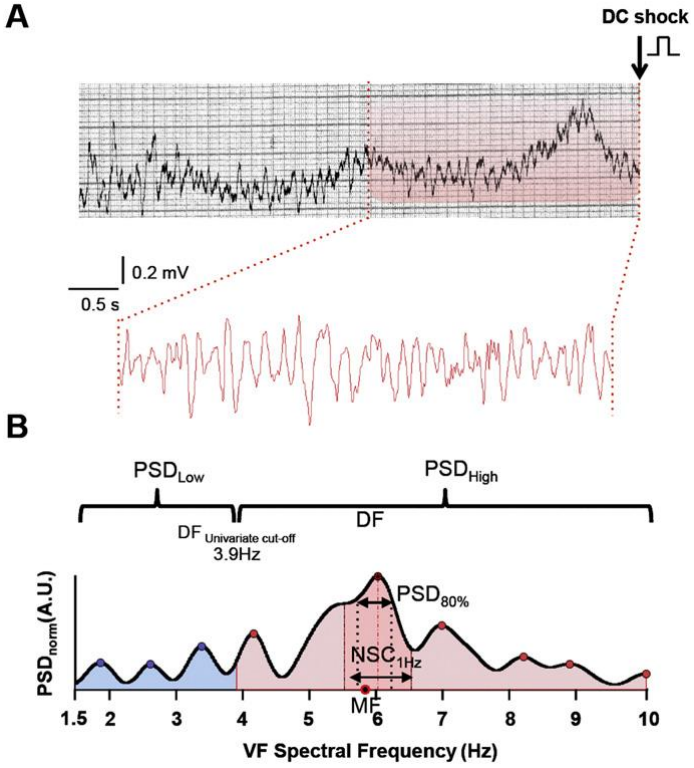

Figure 4.1. Digitization and signal processing of a representative VF trace. *A. Upper panel, single lead VF trace from paper ECG prior to the first DC shock. Lower panel, 5-s VF epoch after digitization, segmentation and codification. B. Representative spectra of the VF trace shown in A. DF,MF, 1-Hz DF spectral concentration and PSD80%, are shown. The univariate cut-off at 3.9 Hz was used*

to define low and high PSD bands. DF = dominant frequency. MF =median frequency. NSC = normalized spectral concentration. PSD = power spectral density.

c) Extracting temporal and spectral variables.

Both time and frequency domain pre-selected variables were extracted and quantified across patients. Fundamental spectral variables for VF were measured and calculated as described elsewhere. ***(Brown 1996, Strohmenger 2001, Eftestol 2000, Reed 2003, Such-Miquel 2013, Kalifa 2006, He 2013)*** Dominant frequency (DF) was defined as the frequency with the highest power in the 1.5 to 10 Hz band of interest. Median frequency (MF) describes the power distribution in the frequency spectrum and it was calculated as the frequency cut-off where 50% of the power in the spectrum was below (and above) in the 1.5-10 Hz band. Normalized spectral concentration at DF, was obtained both at 80% of the maximum PSD ($PSD_{80\%}$) and through all power density contained in the band DF±1Hz (NSC). (***Such-Miquel 2013)*** Spectral regularity index (RI) was defined as the ratio between the power at DF and the power in the 1.5 to 10 Hz band. ***(Kalifa 2006)*** The Amplitude Spectral Area (AMSA) was calculated as the summed product of contributing frequencies weighted by the absolute value of power at that frequency from the PSD Welch spectrum (1.5 to 10 Hz band). (***Schoene P 2014).***

After univariate binary logistic regression analysis on the retrospective cohort, DF offered the best independent prediction accuracy (proportion of true results, both true positives and true negatives, in the population). A cut-off at 3.9 Hz showed the highest sensitivity (0.88) and specificity (0.94) for predicting the primary endpoint in the retrospective cohort. Therefore, we used the 3.9 Hz cut-off to obtain two additional derived ratios of spectral variables as follows (***Sherman LD 2006)***: High-to-Low Power Spectral Density Ratio (HL-PSDR) as the relative power between high (3.9 to 10 Hz) and low (1.5 to 3.9 Hz) bands, and High-to-Low Peak Ratio (HL-pKR) as the relative the number of spectral peaks above and below the 3.9 Hz threshold with power above 40% the frequency with the highest power (DF). We also considered time-domain waveform variables for the study. We

included the mean amplitude over time (A) and the Approximate Entropy Regularity Index (AppEnt), which measures the complexity of a time sequence as the natural logarithm of the relative prevalence of repetitive patterns found within the sequence. ***(Weaver 1985, Ho 1997).***

For multivariate analysis, we selected non-correlated statistically significant variables among all extracted VF fundamental variables. Spearman and Pearson correlations were done to determine monotonic and linear relationships in the retrospective cohort ($p<0.001$). Highly correlated (Rho and $R>0.9$) variables were considered for elimination (Figure 4.2), leaving those with the highest univariate prediction accuracy for the primary outcome.

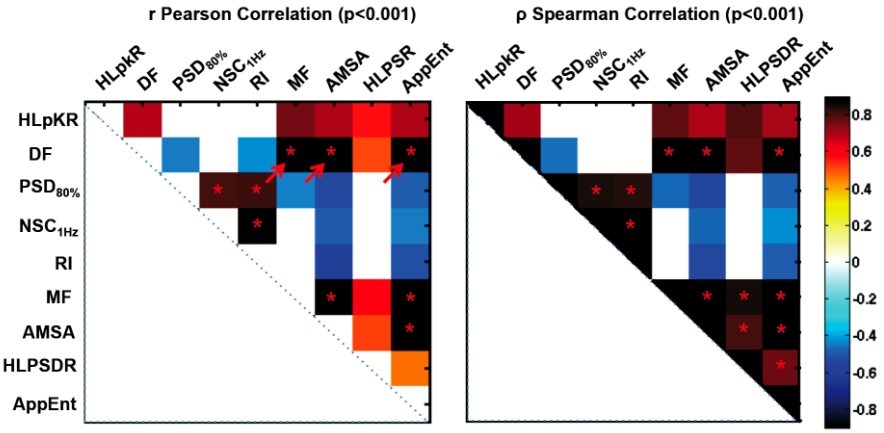

Figure 4.2. *Correlation analysis of spectral variables. Both linear (R Pearson) and monotonic (Rho Spearman) correlation coefficients were calculated among spectral and temporal ventricular fibrillation variables significantly associated to favorable neurological performance. Arrows highlight strong linear and monotonic correlation between DF and MF, AMSA and AppEnt in the retrospective cohort. AMSA= amplitude spectrum area. AppEnt= Approximate Entropy Regularity Index. DF= dominant frequency. HLpKR= High-to-Low peak ratio. HLPSDR= High-to-Low PSD ratio. MF= median frequency. NSC= normalized spectral concentration. PSD= power spectral density. RI= Spectral regularity index.*

4.3.4 Outcomes

The primary outcome was a favorable neurological performance (FNP) during hospitalization. All patients were classified using the Pittsburgh outcome categorization of brain injury as follows: cerebral performance categories (CPC, Table 4.0) 1 and 2 (good and moderate disability, respectively) were considered as FNP, and CPC 3, 4 and 5 (severe disability, vegetative state and brain death, respectively) were considered as a non-FNP. ***(Ho 1997)*** Neurological outcome was established after in-hospital stabilization or before hospital discharge. In patients from group 1, retrospective data were obtained from clinical records during hospitalization. The secondary outcome measure was survival to hospital discharge.

Cerebral Performacnce Categories (CPC)	CPC
1. *Good Cerebral Performance:* Conscious, alert, and able to work and lead a normal life. Might have minor psychological or neurological deficits (mild dysphasia, non-capacitating hemiparesis, or minor cranial nerve abnormalities).	1
2. *Moderate Cerebral Disability:* Conscious. Sufficient cerebral function for part-time work in a sheltered environment or independent activities of daily life (dress, travel by public transportation, food preparation). Such patients may have hemiplegia, seizures, ataxia, dysarthria, dysphasia, or permanent memory or mental changes.	2
3. *Severe Cerebral Disability:* Conscious; patient dependent on others for daily support (in an institution or at home with exceptional family effort) because of impaired brain function. Has at least limited cognition. This category includes a wide range of cerebral abnormalities, from patients who are ambulatory but have severe memory disturbance or dementia precluding independent existence, to those who are paralyzed and can communicate only with their eyes, as in the locked-in syndrome.	3
4. *Coma/vegetative state:* Not conscious, unaware of surroundings, no cognition. No verbal and/or psychological interaction with environment.	4
5. *Brain Death:* Certified brain dead or dead by traditional criteria.	5

Table 4.0: *Glasgow-Pittsburgh Outcome Categorization of Brain Injuty.*

4.3.5 Follow-up

Neurological outcome was prospectively assessed in all survivors after October 2011, either from group 1 or group 2. Specifically, patients from group 2 were evaluated between 3 and 6 months after hospitalization. Neurological outcome was also determined in both groups using the mini-mental state examination as follows: any score ≥24 points (out of 30) indicated a good cognition. Scores <24 indicated cognitive impairment.***(Cole 1991)*** Only patients with both CPC ≤2 and mini-mental state examination score ≥24 were considered to have FNP

at follow-up. Survival after hospitalization was assessed in group 1 after October 2011. In patients from group 2, survival was assessed at 6 months after hospital discharge.

4.3.6 Statistical Analyses

All values are presented as median±SEM (25^{th},75^{th} percentiles) except where noted. The retrospective cohort was used to develop a model for predicting the primary outcome. Each of the clinical, spectral and time domain VF variables underwent univariate analysis to evaluate its association with in-hospital FNP. Normal distribution of variables was assessed with Shapiro-Wilk test. Statistical significance was assessed by the T-test or the Mann-Whitney-Wilcoxon test, as appropriate. If necessary, we used Bonferroni correction for multiple comparisons. Categorical variables and percentile comparisons were compared using a Chi-squared test or the Fisher Exact test, as appropriate. $P<0.05$ was considered statistically significant. Non-correlated variables, amongst statistically significant ones (Figure 4.2), and clinical relevant variables were regressed out against the primary outcome by using a stepwise backward multivariate logistic regression approach. ***(Cole 1991, Adrie 2006)*** All variables were standardized before entering into the multivariate analysis. We considered clinically relevant variables to avoid bias, even though some were non-significant or not associated to the primary outcome. Interestingly, the multivariate analysis resulted in the same prediction model either including all relevant clinical variables or not. Based on the prior correlation results and clinical relevance, all variables considered in the multivariate analyses were the following:

- **Clinical variables:** Atrial fibrillation, heart failure, number of shocks delivered before return of spontaneous circulation (ROSC), time to advance life support (ALS), time performing ALS, age, previous myocardial infarction (MI), previous stroke, chronic renal failure.

- **Fundamental and derived VF variables** with the highest univariate prediction accuracy among highly correlated variables**:** DF, HL-pKR, HL-PSDR, NSC, $PSD_{80\%}$.

Several state-of-the art machine-learning approaches were tested (artificial neural netwoks, support vector machine, bayesian networks, etc), yet given the strong correlation of the major predictors within the study, performace and high-accuracy of the logistic regression analyses, as well as taking into account the importance of having maintaining the interpretability of individual predictors we selected a logistic regression approach.

The multivariate logistic regression was performed using a backward iterative approach to eliminate variables and search for the best performance model, which was determined by the ROC curves obtained for each classification (maximum squared root product of sensitivity and specificity and maximum C-stat). We aimed at predicting the primary outcome (FNP) with the highest sensitivity and specificity achievable using the minimum number of variables that guarantied the best performance and predictive accuracy (ACC, percentage of correctly classified observations). We validated the predictive accuracy of the model in the prospective cohort and we tested the model during follow-up. We also studied in both groups the accuracy of the model in predicting survival. Patients from both groups were categorized according to their risk scores obtained in the multivariate analysis. Goodness of fit was assessed through Pearson residuals and Chi-squared deviance.

To correct for bias, confidence intervals (95%) were found using bias corrected and accelerated bootstrap. ***(DiCiccio 1996)*** Robustness of the correlation between the outcome and expected outcome was challenged using the Jackknife approach to ensure stability beyond individual observations showing that the classification was significantly different from a random classification ($p<0.001$). Finally, patients from both groups were categorized according to their risk scores obtained in the multivariate analysis. Using the best probability threshold obtained

by the prediction model on the retrospective cohort we defined four risk subsets of the population for non-FNP as follows: very low and low risk of non-FNP (expected FNP), high and very high risk of non-FNP (expected non-FNP).

In order to assess the relative contribution of the spectral parameters within the best prediction model (Model I) we evaluated a model built from the spectral predictors alone (Model II) and compared its performance and overall accuracy with: a) a model built using the only clinical variable in our prediction model (Model III), b) a model built from the most associated clinical variables to the primary outcome (FNP) in the retrospective cohort (Model IV), c) a model including both associated clinical variables and the most relevant clinical variables (Model V) (Table 4.10).

Variables included after backward elimination in Model V are described below.

- **Model I** (Best performance model, 4 variables): DF, HL-PSDR, HL-pKR and number of shocks delivered before ROSC.
- **Model II** (3 spectral variables): DF, HL-PSDR and HL-pKR.
- **Model III** (1 clinical variable): number of shocks delivered before ROSC.
- **Model IV** (Best clinical model, 5 variables): number of shocks delivered before ROSC, time to ALS, time performing ALS, heart failure (HF), history of atrial fibrillation (AF).
- **Model V** (Associated and clinical relevant variables, 8 variables): age, number of shocks delivered before ROSC, time performing ALS, HF, history of previous MI, history of AF, history of previous stroke and chronic renal failure. Time to ALS and LVEF after hypothermia were excluded automatically by the backward elimination approach.

All analyses were done using custom Matlab scripts and SSPS v21, for mathematical assistance.

4.4 Results

The workflow of the study is depicted in Figure 4.3. A total of 239 patients undergoing mild hypothermia (n=116, retrospective cohort and n=123, prospective cohort) were assessed for eligibility during the study period.

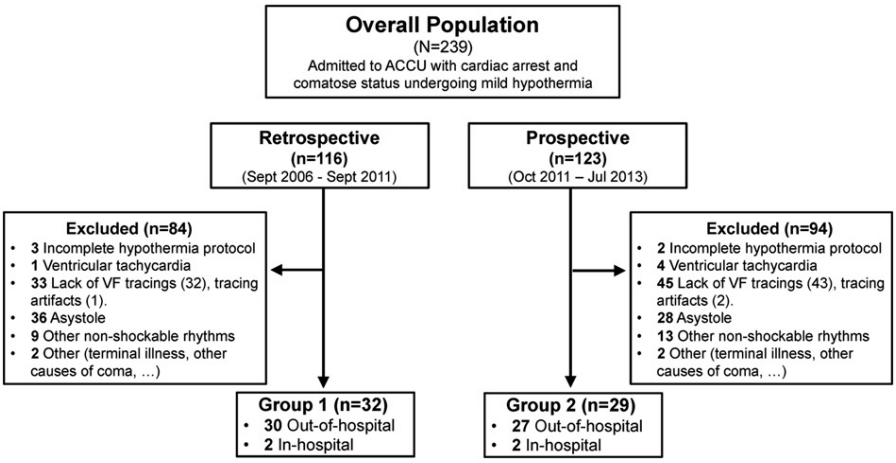

Figure 4.3. Workflow of patients included in group 1 and group 2.

Sixty-one patients (n=31, group 1 and n=29, group 2) fulfilled the inclusion criteria. The vast majority of patients were included after out-ofhospital cardiac arrest (n=57). However, two patients in each group were included after inhospital cardiac arrest due to VF, since comatose status was present after DC shock and ROSC. Baseline clinical characteristics and background treatment of both groups are shown in Table 4.1.

Clinical Characteristics	Retrospective (n=32)	Prospective (n=29)	Overall (n=61)	P
Age(years)	63.5±4.5	55±5.7	55±3.72	0.0409
Male,n(%)	31(96.9)	23(79.4)	54 (88.5)	0.031
Family History of SCD, n(%)	1 (3.57)	8 (40.0)	9 (15.8)	0.009
Hypertension, n(%)	13 (40.6)	15 (51.7)	28 (45.9)	0.385
Dyslipedemia, n(%)	9 (28.1)	13 (44.8)	22 (36.1)	0.174
Diabetes, n(%)	7 (21.9)	3 (10.3)	10 (16.4)	0.224
Smoking Habit, n(%)	12 (37.5)	13 (44.8)	22 (36.1)	0.561
Atrial Fibrillation, n(%)	5 (15.6)	6 (20.7)	11 (18)	0.849
Heart Failure, n(%)	10 (31.3)	6 (20.7)	12 (26.2)	0.234
Previous Myocardial Infarction, n(%)	6 (18.8)	8 (27.6)	14 (22.9)	0.654
Previous Revascularization, n(%)	4 (12.5)	4 (13.8)	6 (13.1)	0.402
Previous Stroke, n(%)	1 (3.1)	1 (3.4)	2 (3.3)	0.943
Chronic Renal Failure, n(%)	2 (6.3)	0 (0)	2 (3.3)	0.271
DCM, n(%)	2 (6.3)	0 (0)	2 (3.3)	0.17
COPD, n(%)	3 (9.4)	5 (17.2)	8 (13.1)	0.363
HCM, n(%)	0 (0)	3 (10.3)	3 (4.9)	0.101
Severe Valvulopathy, n(%)	2 (6.3)	1 (3.4)	3 (4.9)	0.613
Preexcitation, n(%)	0 (0)	1 (3.4)	1 (1.6)	0.289
Time to ALS, (min)	8±2.4	8±2.0	8±1.5	0.887
Time performing ALS, (min)	15±5.9	10±5.3	15±3.9	0.282
Number of shocks delivered before ROSC	3.5±1.6	3±0.87	3±0.9	0.185
Background Treatment				
Aspirin, n(%)	4 (12.5)	5 (17.2)	9 (14.7)	0.602
Thienopyridines, n(%)	1 (3.1)	0 (0)	1 (1.6)	0.524
Betablockers, n(%)	7 (21.9)	9 (31)	16 (26.2)	0.416
Amiodarone, n(%)	2 (6.3)	0 (0)	2 (3.3)	0.271
ACE Inhibitors, n(%)	6 (18.8)	7 (24.1)	13 (21.3)	0.557
ARBs, n(%)	1 (3.1)	3 (10.3)	4 (6.6)	0.239
Statins, n(%)	8 (25)	10 (34.5)	18 (29.5)	0.417
Calcium Antagonists, n(%)	1 (3.1)	2 (6.9)	3 (4.9)	0.496
Diuretics, n(%)	8 (25)	6 (20.7)	14 (22.9)	0.689
Aldosterone Inhibitors, n(%)	1 (3.1)	2 (6.9)	3 (4.9)	0.476
Anticoagulants, n(%)	5 (15.6)	6 (20.7)	12 (19.7)	0.849

ACE= angiotensin-converting enzyme. ALS= advanced life support. ARBs= Angiotensin-receptor blockers. COPD= chronic obstructive pulmonary disease. DCM= Dilated cardiomyopathy. HCM= Hypertrophic cardiomyopathy. ROSC= Return of spontaneous circulation.

Table 4.1: Baseline Characteristics. *Baseline clinical characteristics and background treatment of both groups, retrospective and prospective cohorts.*

Female sex, family history of sudden cardiac death and younger age were more frequent in group 2. Overall, the main cause of VF was coronary heart disease, either acute coronary syndromes (n=27, 45%) or chronic coronary disease (n=14, 23%), followed by idiopathic VF (n=6, 10%) and dilated cardiomyopathy (n=6, 10%) (Fig 4.4).

4.4.1 Outcomes

Primary and secondary outcomes are shown in Table 4.2. Sixteen patients in group 1 (50.0%) and 21 patients in group 2 (72.4%) achieved FNP during hospitalization. Seventeen patients in group 1 (53.1%) and 21 patients in group 2 (72.4%) survived to hospital discharge. After a median follow-up of 48.5±10.5 months (7.0, 68.7) in group 1, 16 patients (50.0%) were still alive, albeit 15 (48.8%) showed FNP. In group 2, 20 patients (68.8%) were alive at 6 months after hospital discharge and 19 (65.5%) showed FNP after 5±1.8 months (3.5, 7.5). Hospitalization outcomes were not statistically different between groups (Table 4.2). No patients were missed during follow-up. Outcomes and follow-up of each individual patient are depicted in Figure 4.4.

Outcome		Retrospective (n=32)	Prospective (n=29)	Overall (n=61)	P(χ2 Test)
Favorable Neurological Performance					
	In-Hospital	16(50.00%)	21(72.41%)	37(60.66%)	0.074
	Follow-Up*	15(46.88%)	19(65.52%)	34(55.74%)	
Survival					
	Hospital discharge	17(53.12%)	21(72.41%)	38(62.30%)	0.121
	Follow-Up*	16(50.00%)	20(68.97%)	36(59.02%)	

*Median±SEM (25th, 75th percenttiles). Retrospective: 48.5±10.5 (27.0,68.7) months. Prospective: 5±1.8 (3.5,7.5) months.

Table 4.2: Primary and secondary outcomes.

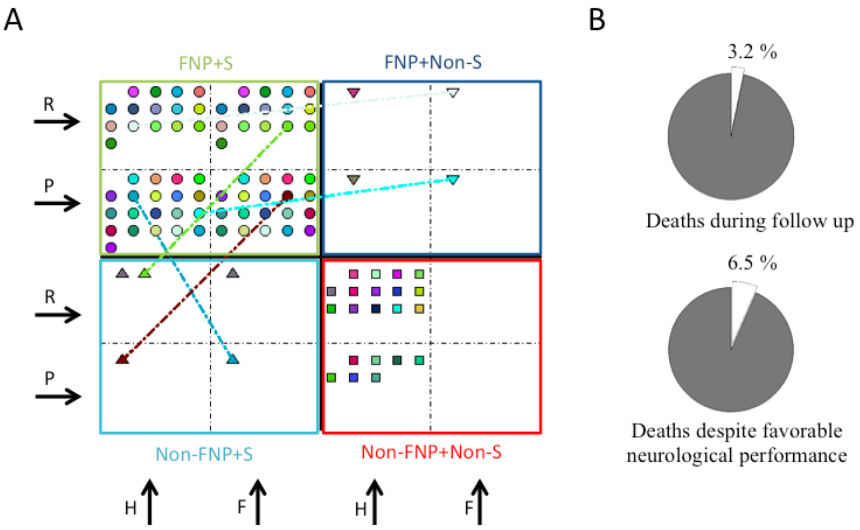

***Figure 4.4**. Individual outcomes and follow-up. **A.** Quadrant-based representation of outcomes and follow-up of each individual patient. Patients are sorted in each quadrant whether they belong to the retrospective (top, R) or prospective (bottom, P) cohorts. Follow-up (F) of patients who survived to hospital discharge (H) is shown on the right for each group. Transitions during follow-up are indicated with a dashed line. Each color represents one patient. Markers represent each quadrant condition (circles; FNP+S, downward triangle; FNP+Non-S, upward triangle; Non-FNP+S and squares; Non-FNP+Non-S). **B.** Pie charts showing deaths at follow-up and deaths despite FNP. FNP= Favorable neurological performance. S= Survival.*

Four patients died (6.5%) despite FNP. There was a statistically significant association between FNP and survival (Table 4.3) in both groups (p<0.001).

		Retrospective (n=32)		**Prospective** (n=29)		**Overall** (n=61)	
		Neurological Performance		**Neurological Performance**		**Neurological Performance**	
		Favorable	Non-Favorable	Favorable	Non-Favorable	Favorable	Non-Favorable
Survival	**Y**	15	2	20	1	35	3
	N	1	14	1	7	2	21
		P(FE)	<0.001	**P(FE)**	<0.001	**P(χ2)**	<0.001

Table 4.3: Significant association between FNP and survival.

4.4.2 Prediction model

In creating the model we only considered the primary endpoint since mortality may occur in patients with FNP due to other causes non directly related with cardiac arrest injury.

	Neurological Performance	Univariate Unadjusted Odds Ratio		
Categories	**P Value**	**OR (CI 95%)**	**Univariate P**	**ACC (CI 95%)***
Clinical Variables				
Age	0.11			
Gender	0.309			
Hypertension	0.281			
Dyslipedemia	0.694			
Diabetes	0.199			
Smoking Habit	0.465			
Atrial Fibrillation	0.07	2.158(0.864 - 5.391)	0.099	0.672(0.506-0.838)
Heart Failure	0.063	1.940(0.945 - 3.986)	0.071	0.655(0.486-0.824)
Previous Myocardial Infarction	0.233			
Previous Revascularization	0.219			
Previous Stroke	0.309			
Chronic Renal Failure	0.516			
DCM	0.144			
COPD	0.544			
HCM	0.565			
Severe Valvulopathy	0.516			
Number of Shocks Delivered before ROSC	0.023	3.025(0.991 - 9.229)	0.052	0.671(0.503-0.837)
Time to ALS	<0.001	10.312(2.044 - 52.032)	0.005	0.689(0.524-0.851)
Time Performing ALS	0.007	2.770(1.046 - 7.336)	0.04	0.676(0.509-0.84)
Background Treatment				
Aspirin	0.285			
Thienopyridines	0.309			
Betablockers	0.669			
Amiodarones	0.144			
ACE Inhibitors	0.365			
ARBs	0.309			
Statins	0.414			
Calcium Antagonists	0.31			
Diuretics	0.314			
Anticoagulants	0.133			
Aldosterone Inhibitors	0.309			
VF Variables				
Spectral Domain				
Fundamental Spectral Variables				
Dominant Frequency	<0.001	0.089(0.020 - 0.403)	0.002	0.884(0.77-0.988)
Median Frequency	<0.001	0.073(0.015 - 0.355)	0.001	0.86(0.741-0.98)
Normalized 80% PSD	0.005	3.121(1.270 - 7.669)	0.013	0.579(0.4-0.75)
1Hz DF Spectral Concentration	0.023	2.198(1.027 - 4.704)	0.042	0.634(0.463-0.805)
Amplitude Spectrum Area (AMSA)	<0.001	0.053(0.008 - 0.362)	0.003	0.85(0.723-0.977)
Spectral Regularity Index	0.07			
Derived Spectral Variables				
High-to-Low Peak Ratio	<0.001	0.073(0.014 - 0.372)	0.002	0.817(0.678-0.954)
High-to-Low PSD Ratio	<0.001	0.034(0.003 - 0.396)	0.007	0.847(0.721-0.969)
Time Domain				
Mean Amplitude	0.11			
Approximate Entropy Regularity Index	<0.001	0.032(0.003 - 0.355)	0.005	0.796(0.652-0.937)

* Univariate predictive accuracy (ACC) averaged for training (Group 1, retrospective) and validation (Group 2, prospective). OR represent univariate odds ratios. AMSA= amplitude spectrum area. PSD= Power spectral density. ROSC= return of spontaneous circulation. Other abbreviations as in Table 1.

Table 4.4. *Univariate analysis and independent predictive accuracy.*

The interval to ALS and total time of ALS reached statistical significance among clinical variables. All fundamental spectral and time domain VF variables, but VF signal amplitude, were significantly associated to the primary endpoint ($p<0.05$) (Table 4.4).

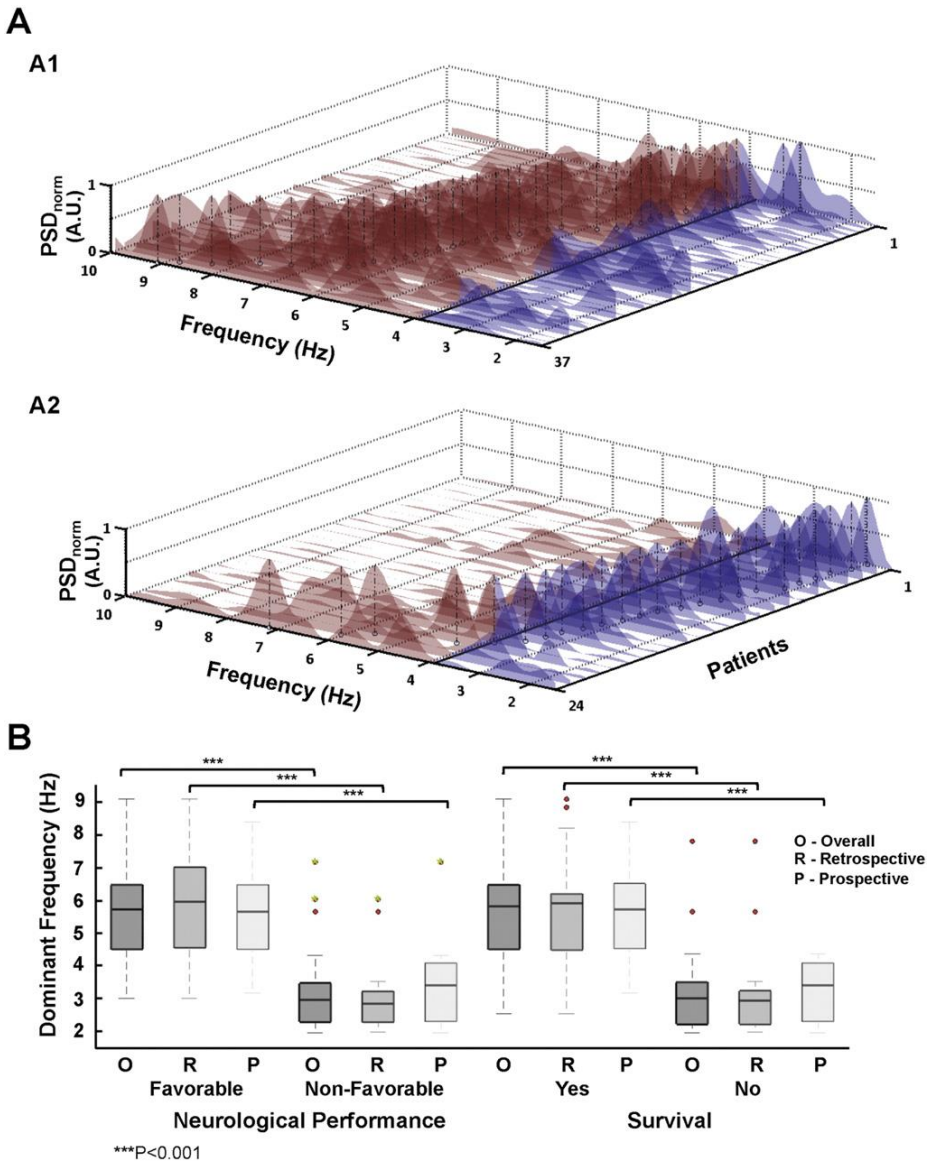

Figure 4.5. Contribution of spectral parameters of VF to the study outcomes. *A. Power spectral density (PSD) of all patients with in-hospital favorable (A1) and non-favorable (A2) neurological performance. The patients are sorted based on their DF values. DF peaks are pointed out for each individual (black vertical dashed-line). The cut-off threshold of 3.9 Hz was chosen for color-coding above (red) and below (blue) the PSD. B. Boxplot representation of DF comparing patients fromboth groups for primary and secondary endpoints. Boxes depictmedian and interquartile range (25–75%). Red dots are outliers at least twice the interquartile range from the*

median. Green dots represent outliers to hospital discharge who improved neurological performance during follow-up.

Interestingly, DF was strongly associated with FNP, which was reflected by the best univariate independent predictive accuracy in the retrospective and prospective cohorts (average 0.884) (Table 4.4).

A cut-off at 3.9 Hz showed the highest sensitivity (0.88) and specificity (0.94) in predicting the primary endpoint in the retrospective cohort. Therefore, we used such a cut-off value to obtain two derived, also significant ($p<0.001$. Table 4.4), spectral variables as follows: high-to-low power spectral density ratio (HL PSDR), as the relative power between high (3.9-10 Hz) and low (1.5 3.9 Hz) bands, and high-to-low peak ratio (HL-pKR), as the relative number of spectral peaks above and below 3.9 Hz with power above 40% of the DF (Figure 4.2).

Graphic representation of individual spectra and DF peaks of the entire population are shown in Figure 4.5A. The vast majority of patients with FNP during hospitalization showed DF values above 3.9 Hz (Figure 4.5A1), unlike those individuals with non-FNP, who had DF values below 3.9 Hz (Figure 4.5A2). Such differences were statistically significant both in the retrospective and prospective cohorts, as well as in the entire population ($p<0.001$. Figure 4.5B). Moreover, DF values also showed significant differences between patients who survived and those who did not survive to hospital discharge ($p<0.001$. Figure 4.5B).

Variable	Multivariate adjusted Odds Ratio	CI 95%
Dominant Frequency	0.252	0.227-0.281
High-to-Low Peak Ratio	0.164	0.145-0.185
High-to-Low PSD Ratio	0.264	0.237-0.295
Number of shocks delivered before ROSC	5.14	4.79-5.51

Table 4.5 Multivariate best performace model including major spectral biomarkers.

Multivariate analysis identified DF, HL-pKR, HL-PSDR and the number of shocks delivered before ROSC as the best performance model to predict in-hospital FNP. Multivariate adjusted odds ratios are shown in Table 4. For the primary endpoint, the model achieved sensitivity=0.94 and specificity=1 (c-statistic=0.98). Validation on the prospective cohort also showed high sensitivity (0.88) and specificity (0.91) (c-statistic=0.89). The multivariate model achieved sensitivity=0.94 and specificity=0.94 to predict in-hospital survival in the retrospective cohort (c-statistic=0.95). For the secondary endpoint, predictive performance was also high in the prospective group (sensitivity=0.88, specificity=0.91, cstatistic= 0.92). ROC curves of the multivariate model are shown in Figure 4.6.

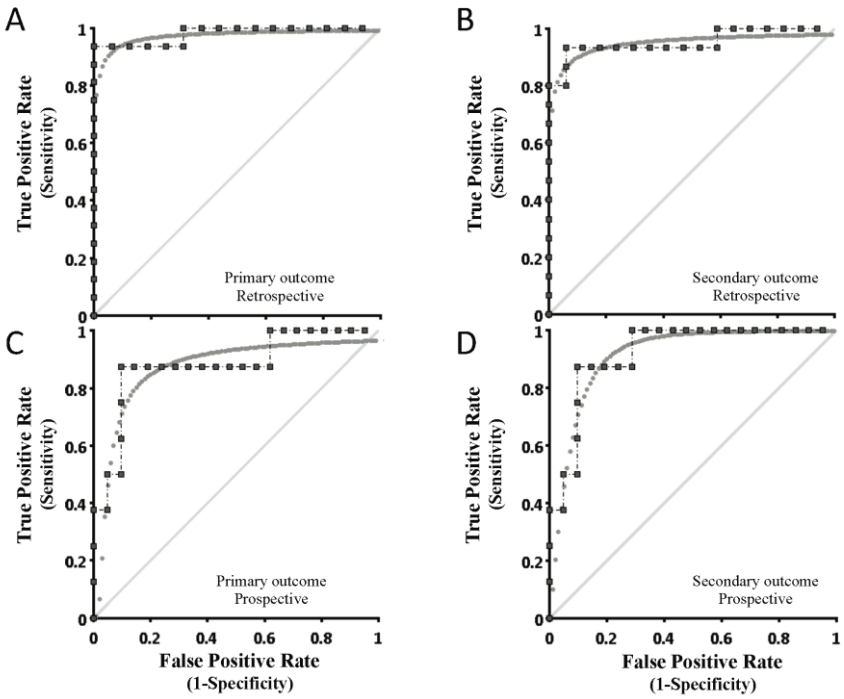

Figure 4.6 ROC curves for the best performance prediction model. A. *ROC curve for in-hospital favorable neurological performance in the retrospective cohort (C-stat= 0.98).* ***B.*** *ROC curve for the secondary end-point (survival) in the retrospective cohort (C-stat= 0.95).* ***C.*** *ROC curve for the primary outcome in the prospective*

cohort. (C-stat= 0.89). ***D.*** *ROC curved for survival to hospital discharge in the prospective cohort (C-stat= 0.92).*

In-hospital performance of the model is shown in Table 4.6.

	Sensitivity	Specificity	C-Stat	ACC
Favorable Neurological Performance				
Retrospective group (Training)	0.94	1	0.98	0.97
Prospective group (Validation)	0.88	0.91	0.89	0.90
Survival Outcome (Test)				
Retrospective group	0.94	0.94	0.95	0.938
Prospective group	0.88	0.91	0.92	0.897

Table 4.6. In-hospital performance of the best multivariate predictive model.

Performance of the model for both outcomes at follow-up also reached high sensitivity, specificity and c-Statistic values (Table 4.7).

	Se	Sp	C-Stat	ACC
Favorable Neurological Performance				
Retrospective group	1	1	1	1
Prospective group	0.88	0.91	0.90	0.90
Survival Outcome (Test)				
Retrospective group	0.88	0.94	0.90	0.90
Prospective group	0.78	0.90	0.89	0.89

Table 4.7. Follow-up performance of the best multivariate predictive model.

4.4.3 Risk score based on the predictive performance model

We used the best performance threshold obtained by the prediction model to define four risk subsets of the population for non-FNP, as follows: very low and low risk of non-FNP (expected FNP), high and very high risk of non-FNP (expected non-FNP). Interquartile ranges of individual variables within each of the risk score groups are shown in Table 4.8.

Risk Score Group	Best Performance Predictors							
	DF(Hz)		HL-pKR (A.U.)		HL-PSDR(A.U.)		Number of shocks before ROSC	
	Median±SEM	Percentiles [p25,p75]	Median±SEM	Percentiles [p25,p75]	Median±SEM	Percentiles [p25,p75]	Median±SEM	Percentiles [p25,p75]
VL	6.35±0.75	[5.42,7.35]	2±0.46	[1,2]	12.3±3.79	[6.65,16.09]	1.5±0.78	[1,3]
L	5.65±0.53	[4.49,6.17]	1±0.45	[1,2]	3.47±1.04	[1.84,5.84]	3±0.67	[2,4]
H	3.12±0.40	[2.5,3.48]	-1±0.39	[-1.5,-0.5]	0.35±0.86	[0.19,1.0]	5±1.58	[2.5,5.5]
VH	2.33±0.28	[2.16,2.64]	-1.5±0.56	[-2,-1]	0.34±0.14	[0.21,0.42]	13±3.62	[10.5,16.5]

DF: Dominant frequency. HL-pKR: High-to-low peak ratio. HL-PSDR: High-to-low power spectral density ratio. Risk score group: L; Low, VL; Very low, H; High and VH; Very high.

Table 4.8 Interquartile ranges of individual variables within each group of risk score for the entire population.

Figure 4.7A shows the observed and predicted probability of inhospital FNP for the entire population. The risk score correctly classifies more than 93% of observations. Only 1 patient in the retrospective cohort was classified as FNP, although the patient was non-FNP during hospitalization (False negative. Figure 4.7B1).

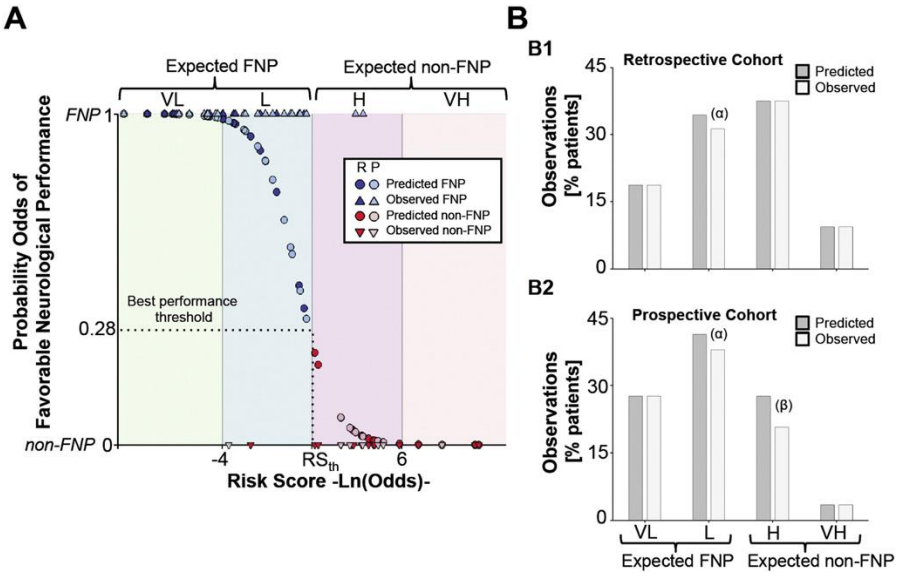

Figure 4.7 Risk score based on the predictive performance of themodel. *A. Observed (triangles) and predicted (circles) probability of FNP for the entire population. Blue and red represent FNP and non-FNP, respectively (dark fill, retrospective; light fill, prospective).We defined four risk groups of non-FNP performance according to their risk scores as follows: expected FNP; very low(VL) and lowrisk (L) and expected non-FNP; high (H) and very high risk (VH). B. Percentage of patients (predicted, dark gray and observed, light gray)who belong to each of the risk score groups in both the retrospective (B1) and prospective cohorts (B2). (α) and (β) represent false negative and false positive individuals, respectively. FNP= favorable neurological performance.*

Three patients in the prospective cohort were identified as false negative and false positives (1 and 2 patients, respectively). The risk score was very reliable in predicting neurological performance in the subgroups of

very low and very high risk of non FNP (Figure 4.7, B1 and B2). Multivariate adjusted logistic regression weights and statistics for each of the four variables included in the risk score are shown in Table 4.9.

Supplemental Table 5. Multivariate adjusted logistic regression weights and statistics for each of the 4 variables of the risk score.

Variables	Multivariate Adjusted Non-standardized LR Weight Values	Statistics			
		Favorable Neurological Performance		Non-Favorable Neurological Performance	
		Median±SEM	Percentiles [p25,p75]	Median±SEM	Percentiles [p25,p75]
Intercept	2.781	-	-	-	-
Dominant Frequency(Hz)	-0.734	5.951±0.475	[4.51,6.47]	2.952±0.417	[2.31,3.48]
High-to-Low Peak Ratio	-1.145	1±0.381	[1,2]	-1±0.451	[-2,-0.5]
High-to-Low PSD Ratio	-0.215	5.061±2.125	[2.05,9.93]	0.335±0.911	[0.19,1.05]
Number of shocks delivered before ROSC	0.445	3±1	[2,4]	5±2	[2.5,7]

Table 4.9 Multivariate adjusted logistic regression weights and statistics for each of the 4 variables of the risk score.

To test the reproducibility of the spectral variables present in the risk score, we quantified changes in the spectral components of VF prior the first reported DC shock using a 3-s sliding window shifted 0.2-s from the DC shock. Interestingly, spontaneous variability of the spectral components a few seconds (maximum available=12 s) before the DC shock did not reflect significant changes in neurological performance prediction and risk score classification for the entire population (Figure 4.8).

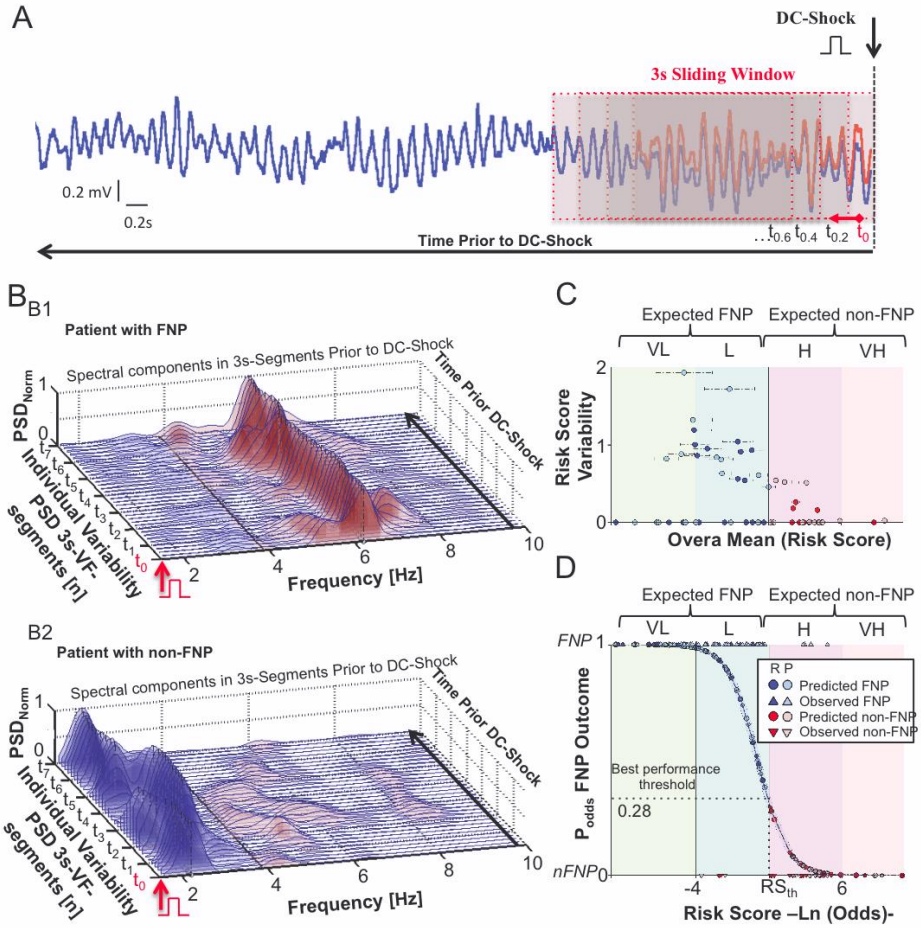

Figure 4.8 *Individual variability of spectral predictors and risk score.* ***A.*** *VF tracing with superimposed 3-s sliding windows that were used to obtain spectral components from the DC shock up to the available signal length (maximum available=12 s). VF spectrum was obtained for each segment and the spectral components were estimated.* ***B.*** *Sequential spectral components along 3-s segments ('t' seconds prior to the DC shock) in a patient with FNP (B1) and a patient with non-FNP (B2). Both patients showed consistent spectral components in time.* ***C.*** *Degree of variability on spectral components assessed by the standard deviation (SD) of the difference on each measure for all segments, over absolute mean of the individual risk score for each patient. Despite the individual variability, all patients were classified within their stratified risk score group.* ***D.*** *Superimposed risk score classification for neurological performance based on the probability assigned by the multivariate model using both the averaged estimation for each predictor and the single up-to-5s segment estimation. Risk score reproducibility was confirmed by*

comparison of the outcome results between both estimations. Both approaches showed the same derived statistics (sensitivity, specificity, C-stat) and best performance threshold for classification. Confidence interval (IC95) is shown in shaded blue for the averaged risk score fitting. VF= ventricular fibrillation. FNP as in Figure 4.4

Further risk score validation in patients without comatose status after DC shock who did not undergo hypothermia (N=11), showed that risk score stratification properly provided FNP values in all cases, as expected (Figure 4.9).

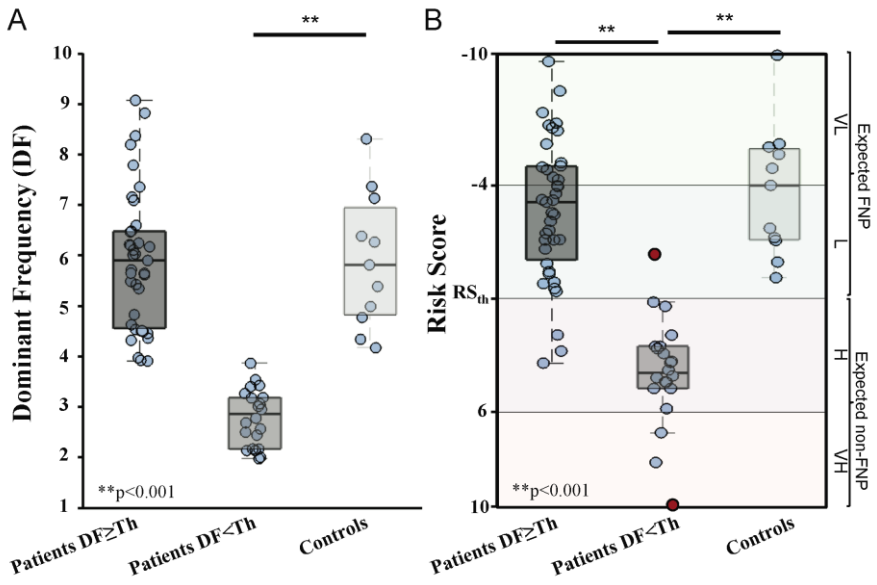

Figure 4.9 *DF and risk score of the study population compared with a control population of VF patients without comatose status after DC shock.* ***A.*** *Boxplot quantification of DF in patients with DF≥Th (n=39), DF<Th (n=22) and Controls (n=11) (Threshold=3.9 Hz). Individual observations (patients) are shown in blue circles spread over the boxplots. Significant differences were found between Controls and patients with DF<Th (p<0.001).* ***B.*** *Risk score classification for all patients from each group. All Controls were properly classified within favorable neurological performance, as expected. Red dots are outliers at least twice the interquartile range (25-75%) from the median. Th=Threshold. VF= ventricular fibrillation.*

4.4.4 Contribution of spectral biomarkers to the predictive performance of the model

The predictive performance of our model was highly dependent on incorporating the spectral variables. Thus, only considering the spectral parameters, the prediction model achieved high sensitivity (0.88) and specificity (0.86) in validation (c-statistic=0.88), compared with sensitivity=0.62 and specificity=0.66 (c statistic=0.67) using the number of shocks delivered before ROSC alone. Moreover, the best clinical prediction model using the most influential clinical factors in the univariate analysis (Table 4.4), we obtained a 5-variable model that achieved sensitivity=0.50 and specificity=0.71 (c-statistic=0.69) in the prospective cohort. The inclusion of additional clinical-relevant variables to achieve better prediction in training resulted in further decrease in the predictive performance of the model in the prospective cohort (c-statistic=0.63). Overall, clinical models did not achieve cstatistic values greater tan 0.69 in the prospective cohort (Table 4.10), which highlights the objective and reliable significance of spectral parameters.

	Test in Retrospective Population			Validation in Prospective Population		
	Se	Sp	C-Stat	Se	Sp	C-Stat
I. Best performance multivariate model (4v)	0.94	1	0.98	0.88	0.91	0.89
Relative contribution of spectral and clinical predictors						
II. Spectral prediction model (3v)	0.88	0.94	0.96	0.88	0.86	0.88
III. Clinical model (1v)	0.68	0.68	0.74	0.62	0.66	0.67
Best clinical models						
IV. Best clinical model with most associated variables (5v)	0.93	0.87	0.93	0.50	0.71	0.69
V. Best clinical model with most associated and relevant variables (8v)	0.87	0.75	0.88	0.87	0.52	0.63

Table 4.10 Contribution of spectral predictors. *Contribution of spectral parameters to the predictive performance of the model and comparisons with the best clinical multivariate models.*

4.5 Discussion

We have introduced a novel practical approach aimed at predicting neurological performance and survival in patients undergoing therapeutic hypothermia after cardiac arrest due to VF and comatose status on admission. In brief, DF before the first DC shock is a strong independent predictor for both FNP and survival using a cut-off value of 3.9 Hz.

To increase the predictive accuracy, multivariate analysis identified DF, HL-pKR, HLPSDR and the number of shocks delivered before ROSC as the best performance model to predict both primary and secondary outcomes. The model showed sensitivity and specificity values above 0.88 and 0.91 in the validation prospective cohort. We also developed a risk score that properly predicted 93% of the in hospital neurological outcome observed in the entire cohort.

Currently, the reliability of early prognosis in comatose survivors after cardiac arrest due to VF is very limited, which severely impairs the ability of physicians to provide accurate information to patients' relatives and to optimize the use of intensive-resource care. Standardization of mild hypothermia delays neurological evaluation and prognostication due to sedation as well as higher rates of misleading biomarker values within the first 24-48 h. ***(Pfeifer 2005)*** Moreover, the large variability of threshold biomarker values used to predict por outcome and different measurement techniques makes it necessary to exert caution and question the prognostic accuracy provided by biochemical markers.

Clinical variables are also inconsistent in their ability to predict both survival and neurological performance, ***(Sandroni 2007)*** as we also showed after developing and validating the best clinical prediction models. Advanced age

seems to be associated with decreased survival after cardiac arrest and resuscitation. ***(Gallagher 1995)*** Interestingly, old age is not associated with non- FNP, ***(Rogove 1995)*** which supports the role of early and appropriate resuscitation to prevent cerebral injury. ***(Abramson 1986)*** However, FNP does not prevent later complications that may lead to in-hospital mortality, especially in old patients. Univariate analysis of our retrospective cohort also showed younger age as significantly associated with survival (data not shown). Conversely, age was not significantly associated with FNP. Likewise, inclusion of clinically relevant variables in the multivariate analysis did not result in age as a variable present in the predictive model.

Time to CPR after collapse has been shown to correlate with functional outcome. ***(Rogove 1995)*** Moreover, when performed properly, CPR improves functional outcome. ***(Abramson 1986)*** However, the quality of CPR administered by a bystander might be extremely variable even if performed by trained personnel, ***(Abramson 1986, Wik 2005)*** which might not add significant improvement in outcome. ***(Bernard 2002)*** The strong predictive value of DF and derived spectral variables may be explained by their ability to provide reliable information of both the time from VF onset and the quality of CPR. Thus, as shown in both humans and animal models, as the VF episode evolves, progressive myocardial ischemia leads to gradual decline in DF values. ***(Brown, 1989, Stewart 1992, Martin 1991, Umapathy 2011)*** Stewart AJ et al. have shown that DF values fall with increased duration of collapse from 5.5 Hz at 3 min to a mean of 2.1 Hz at 20 min. Patients with a mean DF of 3.89±0.25 Hz did not survive longer than 6h after resuscitation, unlike patients with a mean DF of 5.60±0.25 Hz who did survive. ***(Stewart 1992)*** Similar DF values (5.61 Hz) have been reported by Goto Y et al. to predict 1-year survival in a retrospective cohort of patients after out-of hospital cardiac arrest, although data about neurological performance were missed. ***(Goto 2003)*** Our risk score identifies DF of

5.6±0.53 Hz and 6.35±0.75 Hz at low and very low risk of non-FNP, respectively.

The latter does not necessarily correlates with survival, which is reflected by the fact that 2 patients during hospitalization and another 2 patients during follow-up died despite FNP. Previous series have shown that the longer the time between CPR and ROSC the lower the survival rate ***(Nadkarni 2006, Rogove 1995)***, which is similar to what we observed in both cases with FNP and in-hospital mortality after the hypothermia protocol, in whom long CPR (20 and 42 min) and high number of shocks (4 and 5) before ROSC were present. A significantly higher number of shocks delivered before ROSC was also present in patients with DF<3.9 Hz (Figure 4.10), which highlights the difficulties of the heart for acute recovery. Mortality may also occur during the hypothermia protocol before withdrawing sedation.

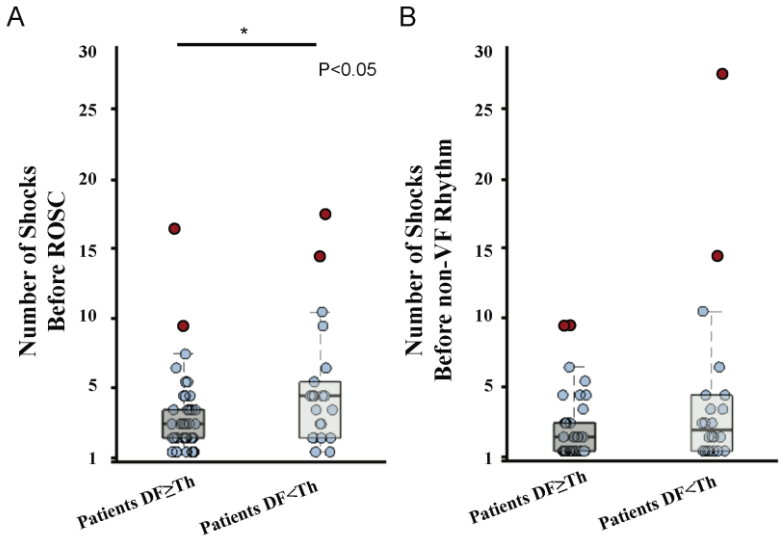

Figure 4.10. *Comparison of the number of shocks delivered during resuscitation between groups with high and low DF.* ***A.*** *A significantly higher number of shocks delivered before ROSC was present in patients with DF values<Threshold (Th) (3.9 Hz). Individual observations (patients) are shown in blue circles spread over the boxplots. Red dots are outliers at least twice the interquartile range (25-75%) from the median.* ***B.*** *No significant differences between groups were found in the number*

of shocks delivered before conversion to non-VF rhythms. DF and VF as in Figures 4.2 and 4.8, respectively.

Thus, data from 4 out of 5 patients, who were excluded due to early mortality and impossibility to assess the primary outcome, showed that risk score stratification would have predicted FNP in 3 out of 4 (Table 4.11). However, early mortality due to other medical circumstances did not allow recovery and neurological assessment.

Excluded patients with Early Mortality	Predictors				Predicted Risk Score (RS)	
	DF (Hz)	HL-pKR (A.U.)	HL-PSD (A.U.)	Number of shocks delivered before ROSC	RS	RS Group
#1	2.16	-1	0.39	10	6.7	VH
#2	4.18	0	1.39	1	-0.14	L
#3	4.47	1	2.77	3	-0.91	L
#4	4.24	0	1.21	1	-0.15	L

Table 4.11 *Risk score prediction for excluded patients (4 out of 5) due to early mortality.*

Interestingly, CPR may increase DF values while coronary blood flow rises, ***(Umapathy 2011, Achleitner 2001)*** which is also associated with increased probability of successful rescue shocks. ***(Strohmenger 1996)*** Increase in DF during resuscitation may explain false positive cases to predict FNP when CPR is delayed after collapse and DF is already low. The latter is supported by recent data by Freese et al. in patients with out-of-hospital cardiac arrest due to VF. ***(Freese 2013)*** The authors showed that a waveform analysis algorithm to decide whether to apply an immediate defibrillatory shock or a CPR interval before the shock, did not improve overall survival to hospital discharge compared with a standard shock-first protocol. In the study, prognosis may have been determined by the spectral values at the beginning of CPR. Yet, an increase in favorable VF waveform parameters during CPR increases the probability of ROSC and survival to admission. ***(Freese 2013)*** DF alone showed the best univariate independent predictive accuracy amongst spectral variables. However, relying on DF alone may not be accurate in some cases; for instance when the DF peak is close to the cut-off

value. Our multivariate model includes 2 additional derived measures (HL-PSDR and HL-pKR) that aided to clarify such cases. The probability of a favorable outcome increases as the relative power of high spectral bands (3.9-10 Hz) and the number of significant spectral peaks above 3.9 Hz also increase (Figure 4.11).

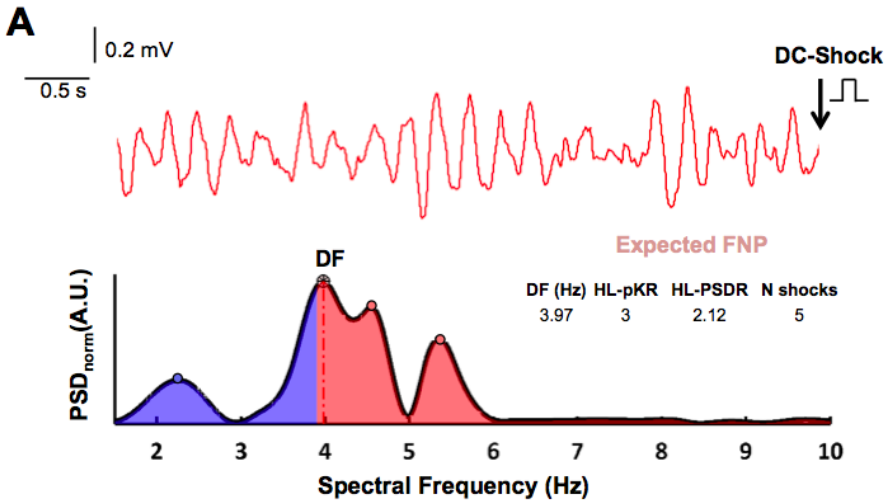

Figure 4.11: *Representative VF recordings with a DF peak close to the cut-off value (3.9 Hz). Upper panel, digitized trace before the first DC shock. Lower panel, representative spectra of the VF signal. Blue color filing shows low spectral bands (1.5 to 3.9 Hz) and red filling shows high spectral bands. Despite a DF peak at 3.97 Hz, both HL-PSDR (2.12) and HL-pKR (3) aided in correctly classifying such a case within low risk of non-favorable neurological performance: Risk score Log (odds); Log (-1.79). DF and VF as in Figures 4.2 and 4.8, respectively.*

Data by Schoene et al. also highlights the role of AMSA over the course of the first 3 shocks during resuscitation in predicting survival and FNP in a large retrospective cohort of patients with out of-hospital cardiac arrest due to VF. ***(Schoene 2014)*** Calculation of AMSA will typically provide higher AMSA values in traces with more highfrequency content, which agrees with our results based on DF. The data is also consistent with However, Schoene et al. did not distinguish between patients with or without comatose status on admission. Moreover, the authors did not provide information about post-

cardiac arrest care using mild hypothermia. Here, we focused on a population with baseline comatose status on admission and mild hypothermia as uniform therapy to minimize postcardiac arrest syndrome.

Finally, data from Nielsen et al prompted us to consider the role of hypothermia after cardiac arrest and whether a target temperate rather tan controlling the body temperature at 36 °C must be pursued. ***(Nielsen 2013)*** We speculate that temperature may have a minimum role in patients with very low risk (i.e., favorable risk score) or very high risk of cerebral injury at baseline (i.e., asystole). However, target temperature may matter in patients with borderline values to minimize post-cardiac arrest syndrome. Altogether, the results support the clinical relevance of the predictive model and risk score to assist physicians and patients´ relatives who deal with difficult decisions after out-of hospital cardiac arrest due to VF.

4.6 Limitations

This was a single center study with a limited number of patients, in which survival rates may be higher than expected. However, our data is consistentwith similar series in dedicated units that included patients after admission to the ACCU, with an initial rhythm reported as VF and using mild hypothermia ***(Nielsen 2013,Broyce 2015).*** Therefore, the study population may be skewed towards patientswith FNP, since patientswho died in transit or survived to hospital admission but died in the emergency department or during the hypothermia protocol, beforewithdrawing sedation, were excluded. Differences between groups regarding age, gender and family history of sudden cardiac death may have occurred due to the study design. However, the highly reliable predictive performance of the spectral-based model compared with clinical models in the validation cohort, suggests

that the model is suitable for clinical practice upon developing appropriate clinical tools. The proposed risk score will nevertheless benefit from further validation in a multicenter study with more patients.

In this study, we selected multivariate logistic regression approaches. Artificial intelligence and maching learning in the field of cardiac electrophysiology has traditionally been selected based on simplicity and understandability. Current advances in deep learning and complex artificial intelligence methodologies are growing together with the rapid growth in computational power for analyzing large population datasets identifying multiple disease states. In our study, we prioritize using the most clinically readable model to ensure its integration in the clinincal setting while maintaining high predictive accuracy and performance. Two critical factors ensured maintaining high performace: first, the strict patient inclusion/exclusion criteria within the study protocols; and more importantly, that our hypothesis that spectral deterministic properties of VF are strongly correlated with the outcomes proved us right. The multivariate logistic regression approach showed high-accuracy performance both within the test and validation databases. Yet, future studies in larger multicentric cohorts should address again a performance comparison with optimized ML methods.

Finally, a significant number of traces were not available on admission, which may raise the concern of selection bias. However, our results are consistent with previous studies, which reduce likelihood for such bias ***(Jennett 1975, Mungas 1991, Pfeifer 2005, Boyce 2014, Schoene 2014).*** In the future, either incorporating the algorithm into external defibrillators or automated signal transferring from defibrillators to portable medical devices, for signal processing and risk score calculation, may avoid such limitation.

The model will also benefit from future studies aiming at direct comparisons of current biochemical and neurological markers to establish the net benefit on early prognosis.

4.7 Conclusion

In this study, we have tested a mechanistic-based strategy for selecting deterministic spectral properties of VF as key predictors of patients' survival and favorable neurological performance. Here, a model for predicting VF implications on cerebral performacnce and suvival was developed taking into account VF deterministic features and complexity. Specifically, a spectral analysis-based model demonstrates high reliability in predicting in-hospital FNP and survival to discharge in patientswith comatose status on admission after cardiac arrest due to VF. These results highlight once again the important link between the study of VF mechanisms as the basis for finding the right biomarkers and methods for diagnosis and therapy.

Chapter 5

High-resolution Optical Mapping Systems for Panoramic Imaging of Complex Arrhythmias and Drug-Action in Translational Animal Models

In this chapter we aim to develop a modular platform for the advanced study of complex arrhythmia mechanims, pharmacological action studies as well as device testing in translational animal models. A major interest is to overcome the limitations of traditional optical mapping by introducing novel low-cost optical mapping configurations for panoramic imaging. We present an overview of results from the transition from single-sensor single-view traditional optical mapping to various panoramic imaging configurations. We also characterize such configurations in terms of feasibility, cost, signal quality and ability to provide enough spatiotemporal high-resolution data to extract valuable biomarkers of the electrophysiological process. Quantitative validation of the different optical mapping configurations is provided as well as tested in several case studies. Finally, we analyse the repolarization pattern

on the overall cardiac surface of the heart and attempt to correlate these findings with the incidence and characteristics of VF in specific conditions. To conclude, we provide a critical overview of current approaches for panoramic optical mapping of the heart, their contributions to the field of cardiac electrophysiology, and future trends from different optical imaging modalities as applied to cardiac physiology at organ and tissue levels.

Introduction

Cardiac arrhythmias remain poorly understood. Current therapeutic strategies have poor success rates and need comprehensive understanding of fibrillatory mechanisms. It is of great interest in order to advance the field in the years to come, to develop new tools and methodologies for individualized therapeutic strategies improving current outcomes and success rates.

Optical mapping has advanced our understanding of cardiac mechanisms transforming pre-clinical cardiac electrophysiology. Procedural, technological and methodological advancements are fuelling novel optical mapping configurations. The development of second and third generation fluorescent dyes, allowed to work with blood perfused preparations in isolated studies ***(Zaitsev 2003),*** and more recently to test its potential in-vivo ***(Lee 2019).*** Recent developments have extended available analytical resources ***(Laughner 2012, Gloschat 2018, O'Shea 2019)*** to facilitate and promote the use of optical mapping.

Amongst major limitations of optical mapping preventing its use from a broader community are the intrinsic dependence on chemical uncouplers and non-FDA approved fluorescent dyes, and, more importantly, the inherent

cost of the technology, even in single camera configurations, usually the most expensive part of any setup.

Performing optical mapping with a single camera sensor may result in missing important electrophysiological phenomena ***(Bray 2000, Kay 2004).*** However, current technological advancements allow for developing optimized configurations towards a low-cost open-source philosophy to expand its use to the broader scientific community ***(Lee-Calvo 2017, Gloschat et al 2018, Rybashlykov D 2021).*** Furthermore, this allows for panoramic optical mapping configurations for comprehensive translational studies. However, further innovation may be needed to study the problems related to the curvature of the heart. In this chapter, we propose different modular configurations, proof-of-concept and case studies, towards developing a platform, trying to lower the financial thresholds while optimizing the reconstruction of cardiac action potentials, which may serve as a link for developing new tools and therapeutic strategies between the wet-lab and the patient in the clinical setting.

The results presented in the different sections within this chapter have been published in journal articles or international conferences (listed in chapter 7), or are currently under review.

5 Low-cost Panoramic Imaging and Mapping of Complex Cardiac Arrhythmias and Drug-Action in Translational Animal Models

In this section, the article [*Lee P-Calvo C et al Nat Sci Rep*] is partially reproduced.

5.1. Abstract

Panoramic optical mapping is the primary method for imaging electrophysiological activity from the entire outer surface of Langendorff-perfused hearts. To date, it is the only method of simultaneously measuring multiple key electrophysiological parameters, such as transmembrane voltage and intracellular free calcium, at high spatial and temporal resolution. Despite the impact it has already had on the fields of cardiac arrhythmias and whole-heart computational modeling, present-day system designs precludes its adoption by the broader cardiovascular research community because of their high costs. Taking advantage of recent technological advances, we developed and validated low-cost optical mapping systems for panoramic imaging using Langendorff-perfused pig hearts, a clinically-relevant model in basic research and bioengineering. By significantly lowering financial thresholds, this powerful cardiac electrophysiology imaging modality may gain wider use in research and, even, teaching laboratories, which we substantiated using the lower-cost Langendorff-perfused rabbit heart model.

5.2 Introduction

Optical mapping is a high-speed fluorescence imaging method that uses fluorescent dyes to measure cardiac and neuronal electrophysiological parameters such as transmembrane voltage, intracellular free calcium and

cell-to-cell communication. In the cardiac electrophysiology field, this method has enabled researchers to study properties of both healthy and diseased heart tissue at high spatial and temporal resolution ***(Boukens 2014, Herron 2012)***. Coupled with the use of drugs to perturb component cell and tissue activity, this method has helped provide mechanistic insights into how life-threatening arrhythmias arise and how they are sustained. Furthermore, whole-heart computer modeling and simulation studies may also be validated with optical mapping data, leading to the design and development of rational antiarrhythmic therapies *in silico* ***(Trayanova 2011)***.

A critical limitation of using optical mapping to study fibrillation on the epicardial surface of a Langendorff-perfused heart is that a camera can only take 2D images from one point-of-view. If one wants to detect ventricular ectopic beats or track spiral waves out of the one field-of-view afforded by a single camera, a panoramic optical mapping system is needed ***(Boukens 2014, Herron 2012)***. Panoramic imaging systems either use multiple cameras, mirrors, or both to simultaneously image the globe-shaped heart from multiple points-of-view. System configurations providing from two to four points-of-view have been developed by several groups ***(Lin 1999, Bray 2000, Kay 2004, Ripplinger 2009)***. Two points-of-view allows one to image the anterior (front) and posterior (back) of the heart while four points-of-view yields overlapping fields-of-view and more complete spatial information. All such systems have enabled the visualization and quantitative analysis of complex arrhythmias.

Despite its impact on the field of cardiac arrhythmias, panoramic optical mapping continues to be a prohibitively expensive procedure, limiting its widespread use. Currently, the highest cost components are the high-speed fluorescence imaging cameras. Considering that the cost of the cameras most

commonly used in the field is ~$40,000 USD each, constructing a panoramic imaging system utilizing four cameras may put the use of this powerful method out of reach to many research programs standing to gain from it. Add to this the cost of the optics, light sources, computer, electronics, mechanical and optomechanical components, it is easy to conceive of the total system cost rising above ~$180,000 USD.

The cameras used for optical mapping must meet certain minimum requirements to generate data of sufficient quality. Using standard fluorescent dyes, the photodetectors of the camera should be capable of recording action potentials and calcium transients with adequately high signal-to-noise ratios (SNRs) under nonfibrillatory and fibrillatory rhythms. Furthermore, these recordings must be achieved at minimal spatial and temporal resolution to capture propagation of the activation front and to describe wave patterns. For pig hearts, studies have shown negligible signal content above 100 Hz in the temporal domain and below 3x3mm in the spatial domain ***(Mironov 2006)***. Hence, a camera with a frame-rate/sampling-frequency of at least 200 Hz and resolution of at least 50x50 pixels will surpass these minimal resolution limits (conservatively assuming heart dimensions of 15x15cm). If the goal of the imaging system is to capture all spatiotemporal phenomena on the epicardial surface of the heart, then the camera must be able to detect the highest frequency events at the requisite spatial resolution. Among the common animal models used for obtaining translational cardiac electrophysiology data (ex. rabbits and pigs), ventricular fibrillation in the rabbit heart represents the highest frequency events, reaching as high as ~30 Hz ***(Chorro 2006, Gray 1998)***. Although a minimum sampling frequency of ~60 Hz is needed, a sampling frequency of at least 300 Hz will preserve the general morphology of action potentials and calcium transients.

In this study, we describe three optical mapping systems built around a collection of four Wide-VGA USB3.0 CMOS cameras (~$600 USD each at the time of writing) and one 2.2 Megapixel USB3.0 CMOS camera (~$1200 USD at the time of writing). Although the imaging systems described here were mainly validated with pig hearts, the systems were designed to be used with animal models ranging in size from the adult rabbit to the adult pig (or human). The most costly system described here is a four-camera optical mapping system providing four overlapping fields-of-view ***(Kay 2006)***. The total cost of this system, including all the optics, light sources, custom-built computer, electronics, mechanical and optomechanical components, was less than the ~$40,000 USD typically spent for one standard optical mapping camera system. Although some applications will certainly require such high-performance cameras, the systems described here represent inexpensive alternatives capable of yielding data of sufficient quality for arrhythmia research.

We now present the design and validation of three optical mapping systems. The first system uses four cameras to image the transmembrane voltage from the entire epicardial surface of the heart from four equally-spaced points-of-view. The second system uses four cameras to simultaneously image transmembrane voltage and intracellular free calcium from the anterior (two cameras) and posterior (two cameras) surface of the heart. Lastly, the third system uses just one high spatial resolution camera and multiple mirrors to image transmembrane voltage from the anterior and posterior surface of the heart. Besides meeting the minimal signal quality and spatiotemporal resolution requirements, we designed the imaging systems to be capable of making continuous long-duration recordings, which is not a common feature of panoramic optical mapping systems but has been proven to be important

in the study of ventricular fibrillation ***(Bayly 1993, Huang 1998)***. In terms of illumination, we built all light-sources around modern high-power light-emitting-diodes (LEDs), driving costs down further ***(Boukens 2014, Herron 2012)***. Besides the custom-machined mechanical components, all other components used are readily obtainable off-the-shelf (see **Materials and Methods**).

5.3 Materials and Methods

5.3.1 Computer system

We built a custom computer to support all three optical mapping systems (**Figure S1**). The computer is composed of the following key components: 1) operating system: Microsoft Windows 7 Professional 64-bit, 2) processor: Intel Core i7-3770 Ivy Bridge Quad-Core 3.4GHz, 3) motherboard: ASUS P8Z77-V LK, 4) memory: G.SKILL 16GB (2 x 8GB) 240-Pin DDR3 SDRAM and 5) three solid state drives (SSDs): SAMSUNG 850 PRO 2.5" 128GB SSD. One SSD is used for the operating system and the other two are used for saving image sequences from the cameras in real time. All computer components were purchased from Newegg (Newegg Canada Inc., Richmond Hill, Canada). In addition, the computer uses a 4-port USB3.0 PCI express card (part #: AL00014; IDS Imaging Development Systems GmbH, Obersulm, Germany) for camera communication and data acquisition. To record the frame exposure start signals from each camera, we use a PC oscilloscope (PicoScope 2205 MSO; Pico Technology Limited, Cambridgeshire, United Kingdom). Time stamps for image frames received by the computer are also recorded by the acquisition software.

5.3.2 Software

Camera configuration, image alignment and focusing are performed using uEye Cockpit, a component of the downloadable IDS Software Suite (IDS Imaging Development Systems GmbH). Custom acquisition software for the cameras was written in the C# programming language using the IDS Software Suite. The light sources are controlled by a microcontroller-based circuit, which can communicate with the computer via the USB interface (**Figure S1**). Custom control and communication software for the microcontroller and computer were written in Spin (Parallax Inc., Rocklin, CA) and MATLAB (The MathWorks Inc., Natick, MA), respectively, and are described elsewhere [42]. Custom software written in MATLAB was used for image processing.

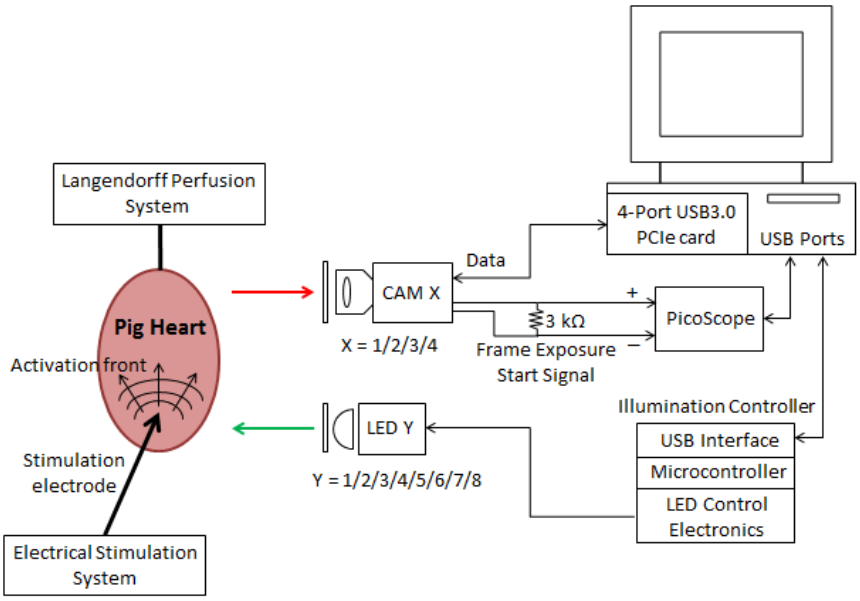

Figure 5.0: Optical Mapping System Layout *System schematic showing the major components of the optical mapping systems (see text for details). The system can support up to four cameras and eight high-power LED light sources.*

5.3.3 Mechanical Framework

The design and machining of the mechanical framework for the optical mapping systems were done in-house. Mechanical and optomechanical components were purchased from McMaster-Carr (Elmhurst, IL) and Thorlabs Inc. (Newton, NJ). Raw metal, such as aluminum bars and rods, were acquired from a local metal distributor (Mr. Metal, Etobicoke, Canada).

5.3.4 Electronics

The major electronic components of the system are outlined in **Figure 5.0**. The custom-built illumination controller, which drives all the LED light sources, is a modification of a system described before, ***(Lee 2011)*** where detailed circuit diagrams and software code are provided. The primary difference is in the total light output power supported by the controller. Because of the large surface area of the heart and the need to drive up to eight high-power LEDs simultaneously, a significantly more powerful controller was designed and built. All electronic components, including the LEDs, can be acquired from major electronic components distributors (Digi-Key Electronics, Thief River Falls, MN; Mouser Electronics Inc., Mansfield, TX).

5.3.5 Optical mapping systems: *Optical Mapping System 1*

As shown in **Figure 5.1**, this system uses four identical CMOS cameras CAM 1 – CAM 4 (part #: UI-3220CP-M-GL; IDS Imaging Development Systems GmbH) to acquire images from four points-of-view spaced 90^{o} apart. Between 500nm – 800nm, the cameras have a quantum efficiency of 40 – 50 % (datasheets available on the company website). Using the uEye Cockpit software, each camera is configured to record 120x160 superpixels (4x4 binning mode; 4x4 pixels per superpixel) at 400 fps. All four cameras are triggered to start image acquisition simultaneously via software, after which they run in freerun mode to achieve maximum frame

rates (i.e. exposure and readout-transfer of the image data are performed in parallel).

Eight green LEDs (part #: CBT-90 Green; Luminus Devices Inc., Woburn, MA) are used to excite di-4-ANEPPS dye-loaded tissue (**Figure 5.1a**). The excitation light from each LED passes through a plano-convex lens L1 (part #: LA1951; Thorlabs Inc.) and excitation filter F1 (part #: FF01-534/20-25; Semrock Inc., Rochester, NY). Fluorescence emission light from the tissue is passed through a custom-made emission filter F2 (part #: ET577.5LP; Chroma Technology Corp, Bellows Falls, VT) and then collected with a camera lens L2 (part #: DO-1795; Navitar Inc., Rochester, NY).

For the 1 kHz recordings shown in **Figure 5.3b**, another CMOS camera was used (part #: UI-3360CP-NIR-GL; IDS Imaging Development Systems GmbH). Between 500nm – 800nm, the camera has a quantum efficiency of 40 – 70 % (datasheets available on the company website). This higher resolution camera was configured to record 160x220 superpixels (4x4 binning mode; 4x4 pixels per superpixel) at 1000 fps. The same emission filter and camera lens were used in this proof-of-principle recording.

5.3.6 Optical mapping systems: Optical Mapping System 2

As shown in **Figure 5.5**, this system uses four identical CMOS cameras CAM 1 – CAM 4 (part #: UI-3220CP-M-GL; IDS Imaging Development Systems GmbH) to acquire images from the anterior and posterior surface of the heart. Each camera is configured the same way as in **Optical Mapping System 1**.

Four green LEDs (part #: CBT-90 Green; Luminus Devices Inc., Woburn, MA) are used to excite RH237 and rhod-2AM dye-loaded tissue (**Figure 5.5a**). The excitation light from each LED passes through a plano-convex

lens L1 (part #: LA1951; Thorlabs Inc.) and excitation filter F1 (part #: FF01-534/20-25; Semrock Inc., Rochester, NY). Fluorescence emission from both dyes are first separated by a dichroic mirror D1 (part #: T685LPXR; Chroma Technology Corp). Separated emission light from rhod-2AM and RH237 then pass through emission filter F2 (part #: ET590/50M; Chroma Technology Corp) and custom emission filter F3 (part #: ET700LP; Chroma Technology Corp), respectively. Both filtered lights are then collected by camera lenses, both labeled L2 (part #: DO-1795; Navitar Inc.). And because of the reflections at the dichroic mirrors, images from CAM 2 and CAM 4 are flipped horizontally during image processing.

5.3.7 Optical mapping systems: Optical Mapping System 3

As shown in **Figure 5.7**, this system uses one CMOS camera CAM (part #: UI-3360CP-NIR-GL; IDS Imaging Development Systems GmbH) and six mirrors to acquire images from the anterior and posterior surface of the heart. Using the uEye Cockpit software, the camera is configured to record 468x1024 superpixels (2x2 binning mode; 2x2 pixels per superpixel) at 350 fps. For both sides of the heart, fluorescence emission is reflected by two 127x178mm flat mirrors, both labeled M1 (part #: 40-043; Edmund Optics Inc., Barrington, NJ, USA), and one 81x100mm flat mirror M2 (part #: 41-621; Edmund Optics Inc.). Reflected emission light from both sides are then collected by a camera lens L1 (part #: DO-5095; Navitar Inc.) and filtered with custom emission filter F1 (part #: ET577.5LP; Chroma Technology Corp). Images are flipped horizontally during image processing because of the mirror reflections.

5.3.7 Validation study in the Langendorff-perfused Rabbit Heart

Female New Zealand White rabbits (body weight ~3 kg, n=4) were used in this supplementary study. The experimental studies were conducted in accordance with institutional guidelines and regulations [National

(ECC/566/2015, RD53/2013) and European (2010/63/EU) guidelines for the care and use of laboratory animals]. All *in vivo* experimental procedures were evaluated and granted by the Institutional Animal Care and Use Committee (IACUC) of CNIC and the Local Competent Authority. Surgical procedures were carried under general anesthesia following premedication with a combination of intramuscular Xylazine (10 mg/kg i.m.) and Midazolam (2 mg/kg i.m.) and induced with a slow intravenous administration of Ketamine (20 mg/kg i.v.). After intubation and venous catheterization through the marginal vein, animals were mechanically ventilated with intermittent positive pressure and anesthesia was maintained by a combination of Fentanyl (0.010 mg/kg/h i.v.) and Sevoflurane (2%). Heparin (300 UI/kg) was administered to avoid coronary blood coagulation and vital signs were monitored during the procedure to control anesthesia status. Excised hearts were then submerged in cold (4 ºC) Tyrode's solution, cleaned and then cannulised through the aorta and connected to a constant-flow Langendorff-perfusion apparatus. Hearts were perfused with oxygenated (95% O_2, 5% CO_2) bicarbonate-buffered solution (composition in mM: NaCl 123, $CaCl_2$ 1.8, KCl 5.4, $MgCl_2$ 1.2, NaH_2PO_4 1.4, $NaHCO_3$ 24, Glucose 10) at a circulating flow rate of 30 mL/min. Ionic pH of the perfusate (7.4) and temperature (36-37ºC) were monitored during the experiment.

Fluorescent dyes were injected at a short distance upstream from the aortic cannula for coronary perfusion. For transmembrane voltage imaging, hearts were loaded with dye by slowly delivering, without recirculation, either 1) a solution containing 20 µL of di-4-ANBDQPQ (27 mmol/L in ethanol, University of Connecticut Health Center, USA) and 2 µL of Pluronic F-127 (20% stock solution in DMSO; part #: 2510; TEFLabs Inc., Austin, TX) or 2) 20 µL of 2.5 mg/mL (in DMSO) RH237 (part #: 61018; Biotium Inc.,

Hayward, CA). For intracellular free calcium imaging, hearts were loaded with dye by slowly delivering 250 µL of 1 mg/mL (in DMSO) rhod-2AM (part #: 50024; Biotium Inc.). During calcium dye loading, the heart underwent a recirculating perfusion of 300 mL of perfusate containing 0.5 mM probenecid (part #: 2522; TEFLabs Inc.) for 30 minutes. After dye loading, the perfusate was replaced with fresh perfusate containing 10µM blebbistatin (part #: 674289-55-5; Cayman Chemical Company, Ann Arbor, MI) to reduce contraction during imaging.

5.3.7 Optical mapping in the rabbit heart

For imaging the voltage dye di-4-ANBDQPQ, two red LEDs (part #: CBT-90 Red; Luminus Devices Inc., Woburn, MA) were used to excite dye-loaded tissue (**Figure 5.9a,b**). The excitation light from each LED was passed through a plano-convex lens (part #: LA1951; Thorlabs Inc., Newton, NJ) and excitation filter (part #: ZET642/20X; Chroma Technology Corp, Bellows Falls, VT). Fluorescence emission light from the tissue was passed through a custom-made emission filter (part #: ET700LP; Chroma Technology Corp) and then collected with a camera lens (part #: DO-1795; Navitar Inc., Rochester, NY). The same emission filter and camera lens were used for both the CMOS and EMCCD camera. For imaging voltage dye RH237 and calcium dye rhod-2AM, the same configuration as **Optical Mapping System 2** was used.

5.3.8 Optical mapping in the pig heart

Six Large White pigs weighing 17-20 kg were used in this proof-of-principle study (n=2 for **Optical Mapping System 1**; n=2 for **Optical Mapping System 2**; n=2 for **Optical Mapping System 3**). The experimental studies were conducted in accordance with institutional guidelines and regulations [National (ECC/566/2015, RD53/2013) and European (2010/63/EU)

guidelines for the care and use of laboratory animals]. All *in vivo* experimental procedures were evaluated and granted by the Institutional Animal Care and Use Committee (IACUC) of CNIC and the Local Competent Authority. Surgical procedures were carried under general anesthesia following premedication with a combination of intramuscular Xylazine (2 mg/kg i.m.) and Midazolam (0.5 mg/kg i.m.) and induced with intravenous Ketamine (20 mg/kg i.v.). After intubation and venous catheterization through the marginal vein, animals were mechanically ventilated with intermittent positive pressure and anesthesia was maintained by a combination of Fentanyl (0.010 mg/kg/h i.v.) and Sevoflurane (2%). Heparin (300 UI/kg) was administered to avoid coronary blood coagulation and vital signs were monitored during the procedure to control anesthesia status. Hearts were exposed via median sternotomy and a 9 VDC battery was used to induce ventricular fibrillation during the extraction. Excised hearts were then submerged in cold (4 ºC) Tyrode's solution, cleaned and then cannulised through the aorta and connected to a constant-flow Langendorff-perfusion apparatus. Hearts were perfused with oxygenated (95% O_2, 5% CO_2) Tyrode's solution (composition in mM: NaCl 130, $NaHCO_3$ 24, NaH_2PO_4 1.2, $MgCl_2$ 1, Glucose 5.6, KCl 4, $CaCl_2$ 1.8 and albumin 0.04g/L) at a circulating flow rate of 200-240 mL/min ***(Quintanilla 2015)***. Ionic pH of the perfusate (7.4), oxygenator status and temperature (36.5-37.5ºC) were monitored during the experiment. Intracavitary volumes in atrial and ventricular chambers were adjusted to resemble physiological stretch in diastole as described elsewhere ***(Filgueiras-Rama 2011)***.

Fluorescent dyes were injected at a short distance upstream from the aortic cannula for coronary perfusion. For transmembrane voltage imaging, hearts were loaded with dye by slowly delivering, without recirculation, 0.250 mL of 2.5 mg/mL (in DMSO) of either di-4-ANNEPS (part #: 61010; Biotium

Inc., Hayward, CA) or RH237 (part #: 61018; Biotium Inc.). For intracellular free calcium imaging, hearts were loaded with dye by slowly delivering 2 mL of 1 mg/mL (in DMSO) rhod-2AM (part #: 50024; Biotium Inc.). During calcium dye loading, the heart underwent a recirculating perfusion of 1.5 L of perfusate containing 0.5 mM probenecid (part #: 2522; TEFLabs Inc., Austin, TX) for 30 minutes. After dye loading, the perfusate was replaced with fresh perfusate containing 10μM blebbistatin (part #: 674289-55-5; Cayman Chemical Company, Ann Arbor, MI) to reduce contraction during imaging. For drug testing, Nifedipine (N7634; Sigma-Aldrich Dorset, UK) from a 20 mM stock solution (dissolved in DMSO) was diluted in the perfusate to 2 μM.

5.4 Results

5.4.1 Optical mapping framework: Optical mapping system 1

The system shown in **Figure 5.1** utilizes four high-speed Wide-VGA USB3.0 CMOS cameras spaced 90^{o} around the isolated heart on the horizontal plane, providing a 360^{o} view of the heart ventricles ***(Kay 2006)***. Although not implemented here, a surface scanner can be used to generate a 3D surface reconstruction of the epicardial surface, enabling the fluorescence signals collected from the four cameras to be mapped onto a geometric model of the heart surface. Each camera (CAM 1 – CAM 4 in **Figure 5.1a**) is configured to record 120x160 superpixels (4x4 binning mode; 4x4 pixels per superpixel) at 400 frames-per-second (fps). All cameras are controlled by a single custom-built computer via USB3.0 interfaces. The frame exposure start signal generated by each camera allows one to record when each camera captures a frame. Although each camera is triggered to start at the same time, the inherent variation between camera hardware clocks can lead to slight timing differences between cameras over long duration recordings. The

recorded sequence of frame exposure start signals from each camera allows one to deal with any such drifts during post-processing of the image sequences. We found the drift of a few milliseconds over tens of seconds of recording to be negligible relative to the electrophysiological phenomena observed in this study.

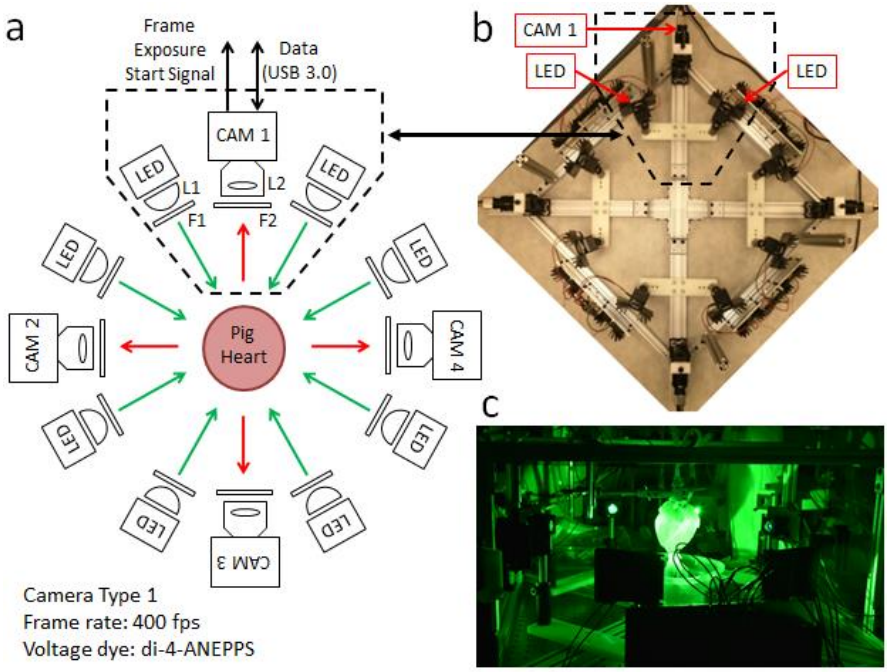

Figure 5.1: Optical Mapping System 1: Layout (Langendorff-Perfused Pig Heart) ***(a)*** *System schematic showing key components (see text for details). One camera and two LED light sources are used to image the heart from each point-of-view (green arrows: excitation light, red arrows: fluorescence emission light).* ***(b)*** *Bird's-eye view of the imaging and illumination subsystems outlined in* ***(a)****.* ***(c)*** *A picture of part of the system during an experimental run. The illuminated pig heart is visible at the center of the picture.*

As shown in **Figure 5.1**, two LED light sources are mounted on the left and right side of each camera. The LEDs are mounted to heat sinks and the emitted light lensed and filtered to provide illumination on all imaged surfaces of the dye-loaded heart. The off-the-shelf potentiometric dye di-4-

ANEPPS was used because of its popularity, ease of loading, brightness and large fractional fluorescence change during cardiac action potentials (***Boukens 2014, Herron 2012, Fluhler 1985, Lee 2001)***.

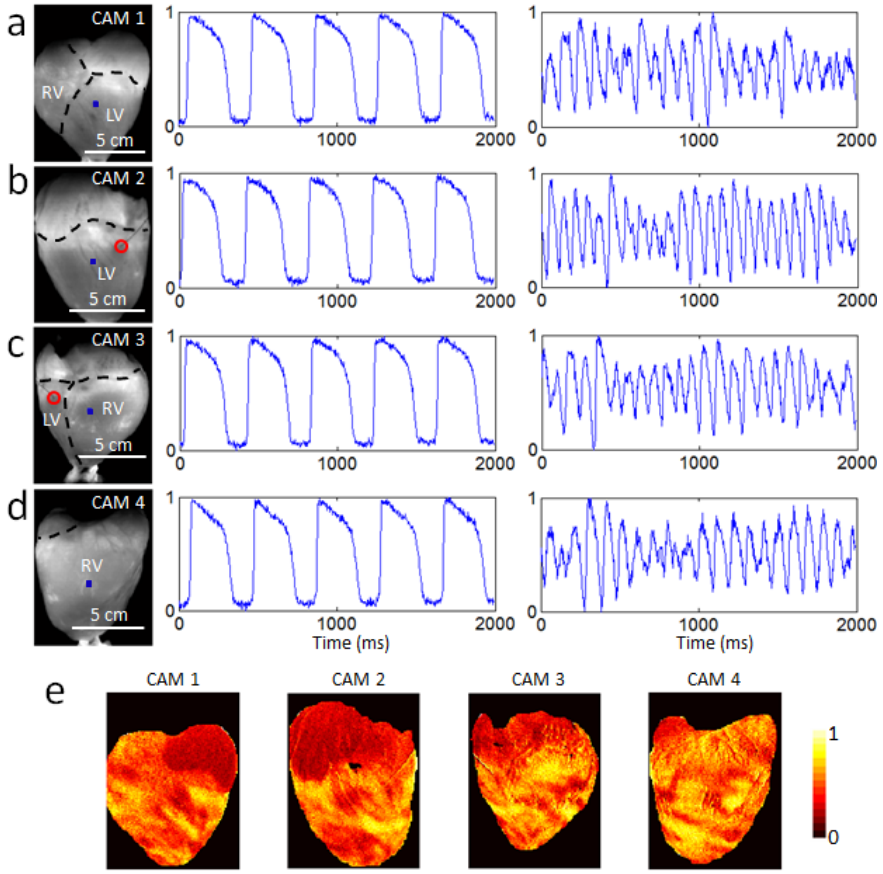

Figure 5.2: Optical Mapping System 1: Sample Data (Langendorff-Perfused Pig Heart) *Normalized fluorescence signals from the* ***(a)*** *anterior,* ***(b)*** *left lateral,* ***(c)*** *posterior and* ***(d)*** *right lateral points-of-view of the heart during electrical pacing (middle panel) and ventricular fibrillation (right panel), taken from the blue-square regions shown (left panel). In the left panels, the right ventricle, left ventricle and atria are demarcated by black dashed lines and the red circle indicates the location of electrical point stimulation. Each of the four cameras can be independently positioned and rotated to adjust and optimize the position of the heart in its field-of-view. The varying scale bars in the left panels reflects these adjustments. Signals are in arbitrary fluorescence units.* ***(e)*** *Normalized fluorescence intensity map (colorbar shown) at one time point during ventricular fibrillation.*

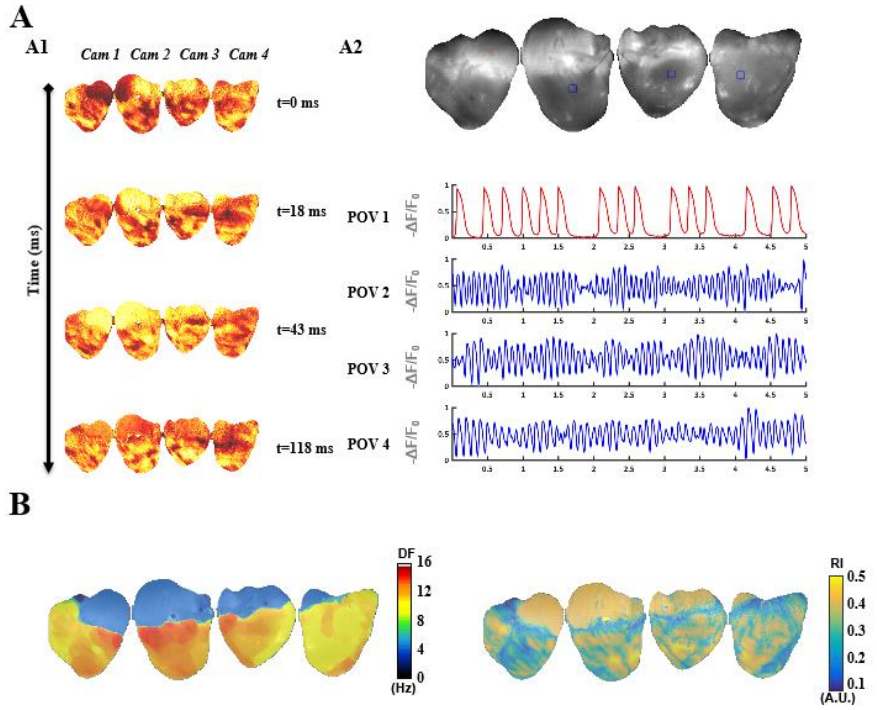

Figure 5.3: Ventricular fibrillation and quantification of spectral-based parameters. A. *Normalized fluorescence intensity maps at several time points during ventricular fibrillation.* ***B.*** *Dominant frequency and regularity index maps.*

Figure 5.2a,b,c,d shows sample raw data, unfiltered in time. The heart was imaged while being electrically paced and during ventricular fibrillation. The SNR was sufficient for quantitative analysis for at least one hour of experimentation. For example, during pacing, the SNRs for CAM 1, CAM 2, CAM 3 and CAM 4 were ~49, ~52, ~50, and ~46, respectively. These sample values were calculated using the signals shown in **Figure 2a,b,c,d** and the formula SNR = (AP Amplitude)/(SD during diastolic intervals), where AP: action potential and SD: standard deviation ***(Evertson 2008)***. **Figure 2e** shows a normalized transmembrane voltage fluorescence intensity maps at one time point during ventricular fibrillation, illustrating irregular electrical activity.

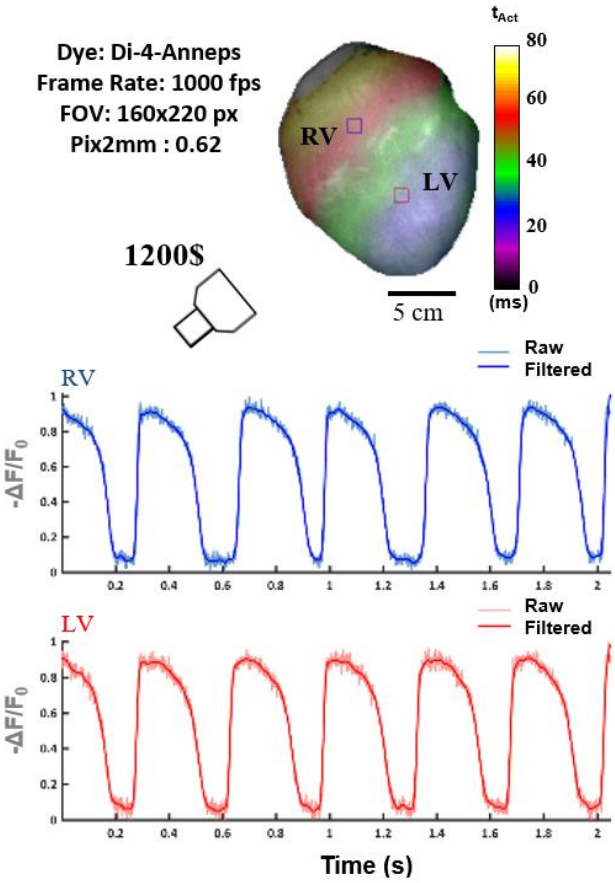

Figure 5.4: Whole-heart ventricular fibrillation mapping quantification of activation times. *Normalized fluorescence intensity signals at one time point are shown during sinus rhythm.*

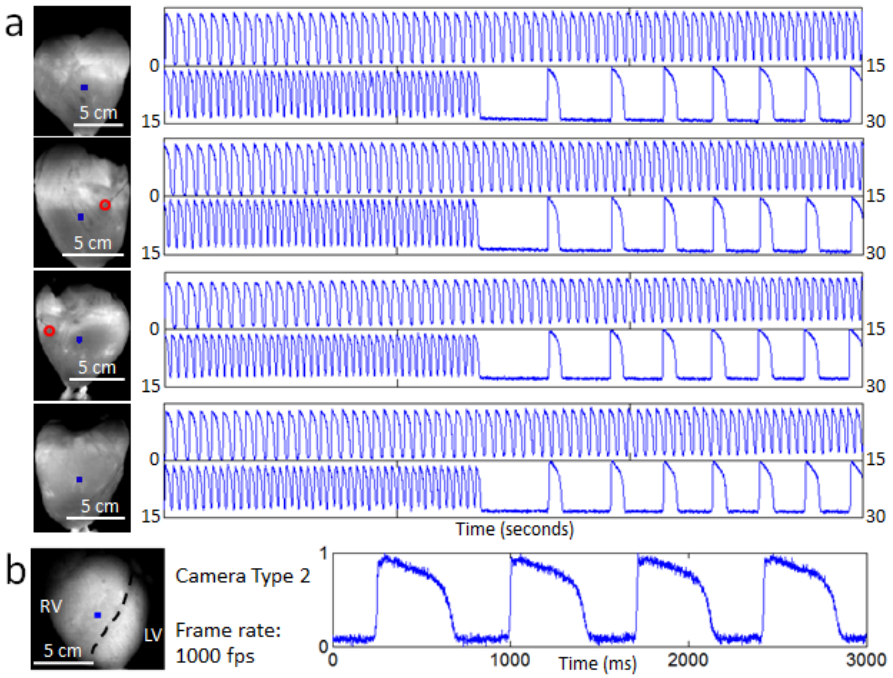

Figure 5.5: Optical Mapping System 1: Long-Duration and 1 kHz Recordings (Langendorff-Perfused Pig Heart) (a) *Samples of long-duration recordings from the same heart shown in Figure 5.2. The 30 second segments show normalized fluorescence signals from the blue-square regions (left panel) at increasing pacing frequency. At ~22 seconds, the pacing was stopped and the heart returned to sinus rhythm. In the left panels, the red circle indicates the location of electrical point stimulation.* ***(b)*** *Normalized fluorescence signals from the blue-square region (left panel) on the surface of another heart taken at higher spatial and temporal resolution. In the left panel, the black dashed line demarcates the right ventricle and left ventricle. Signals are in arbitrary fluorescence units.*

Figure 5.5a presents samples of long-duration recordings that were taken simultaneously from all four cameras. In the 30 second segments shown, the heart was paced at increasing frequency in an attempt to induce ventricular fibrillation (at ~22 seconds, we stopped pacing). In this particular experiment, we failed to induce fibrillation and the heart returned to sinus rhythm. Although most of the proof-of-principle recordings in this study

were 20-30 seconds in duration, we have tested the system's recording capability out to a minimum of 60 seconds.

Although a frame rate of 400 fps is more than adequate to capture the highest frequency components of the action potential signal in the pig epicardium, some applications may require more temporal resolution. As a demonstration, we replaced one of the Wide-VGA USB3.0 CMOS cameras with the 2.2 Megapixel USB3.0 CMOS camera used in **Optical Mapping System 3** (described later). This more expensive camera provides higher spatial and temporal resolution while maintaining similarly sized pixels. Configuring the camera to record 160x220 superpixels (4x4 binning mode; 4x4 pixels per superpixel), a frame rate of 1000 fps can be achieved. As can be seen in **Figure 5.5b**, the SNR remains sufficient at significantly higher frame rates (SNR ~35 for the action potentials shown in **Figure 5.5b**).

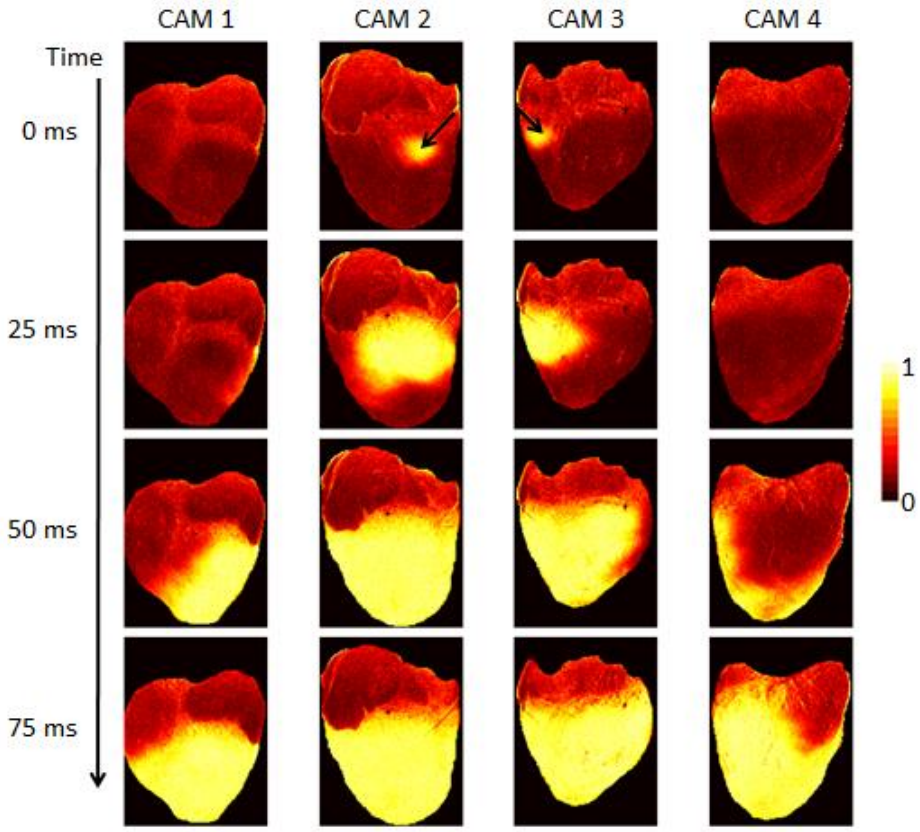

Figure 5.6: Optical Mapping System 1: Propagation Image Sequences (Langendorff-Perfused Pig Heart). *Normalized fluorescence intensity maps (colorbar shown) at progressive time points during electrical pacing (400 ms cycle length). The black arrows indicate the location of electrical point stimulation.*

Figure 5.6 shows a time series of normalized transmembrane voltage fluorescence intensity maps during point electrical pacing (400 ms cycle length). The black arrow shows the stimulation site, which was visible in both CAM 2 and CAM 3 points-of-views. Four frames from a 25 ms interval are shown just after stimulation, illustrating the propagation of the activation front from the stimulation site. Point electrical stimulation was performed to

emphasize the need for panoramic imaging when trying to detect events not visible from only one point-of-view.

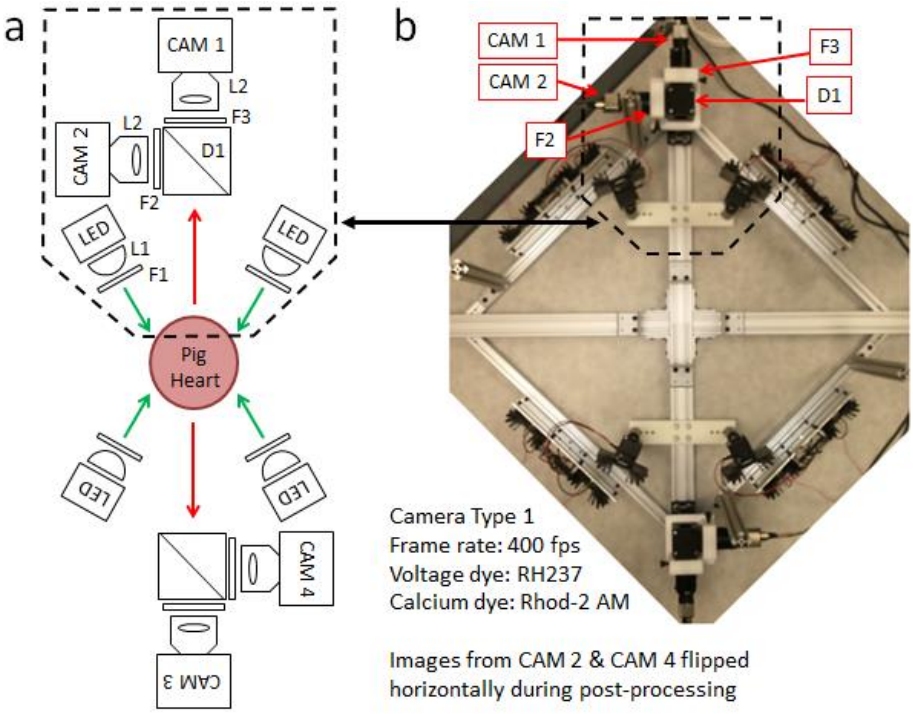

Figure 5.7: Optical Mapping System 2: Layout (Langendorff-Perfused Pig Heart) ***(a)*** *System schematic showing key components (see text for details). Two cameras and two LED light sources are used to image the heart from each point-of-view (green arrows: excitation light, red arrows: fluorescence emission light). One of the two cameras (CAM 1/CAM 3) is used to image transmembrane voltage while the other (CAM 2/CAM 4) is used to image intracellular free calcium.* ***(b)*** *Bird's-eye view of the imaging and illumination subsystems outlined in* ***(a)***.

5.4.2 Optical mapping framework: Optical mapping system 2

In cardiac electrophysiology, transmembrane voltage and intracellular free calcium are two of the most important parameters of interest because of their joint roles in excitation-contraction coupling ***(Bers 2002)***. As such, the simultaneous measurement of both parameters has become the gold standard

in optical mapping. The system shown in **Figure 5.7** uses the same four high-speed Wide-VGA USB3.0 CMOS cameras to simultaneously image transmembrane voltage and intracellular free calcium from the anterior and posterior surface of the heart. For both points-of-view, one camera images action potentials while another images calcium transients. Each camera (CAM 1 – CAM 4 in **Figure 5.7a**) is configured to record 120x160 superpixels (4x4 binning mode; 4x4 pixels per superpixel) at 400 fps.

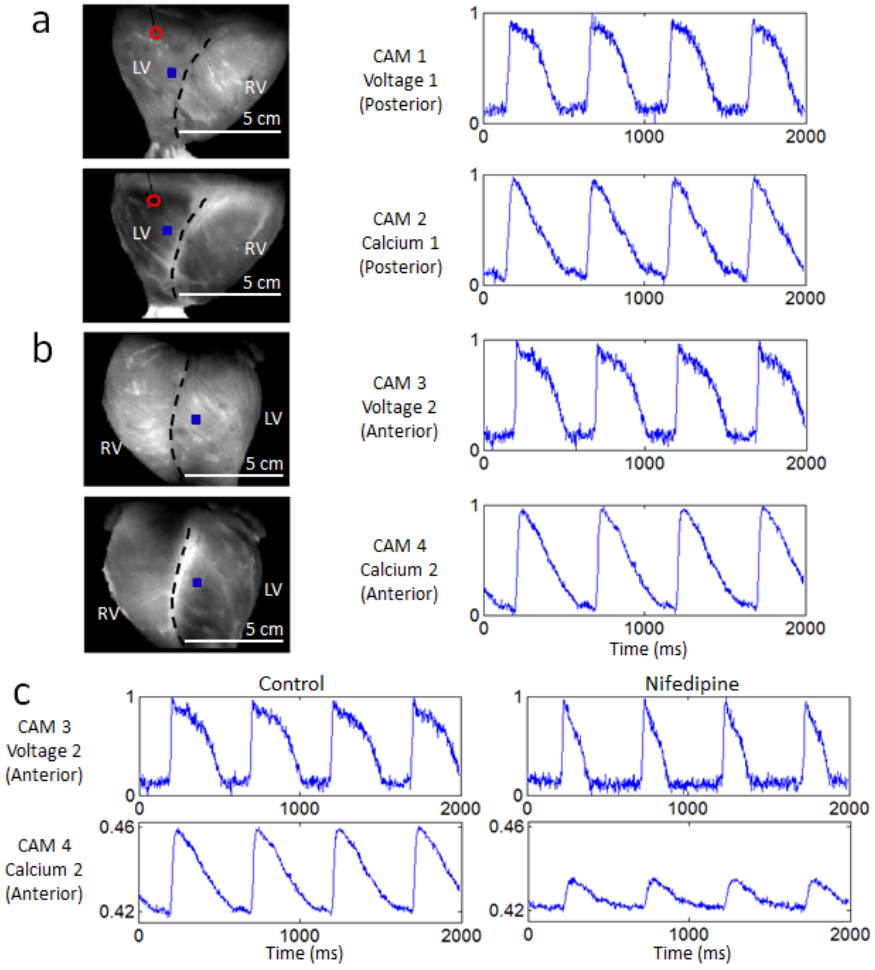

Figure 5.8: Optical Mapping System 2: Sample Data (Langendorff-Perfused Pig Heart) *Normalized fluorescence signals from the (a) posterior and (b) anterior points-of-view of the heart during electrical pacing, taken from the blue-square*

regions shown (left panel). In the left panels, the right ventricle and left ventricle are demarcated by black dashed lines and the red circle indicates the location of electrical point stimulation. The four cameras can be independently positioned and rotated to adjust and optimize the position of the heart in their respective fields-of-view. (c) Control signals and altered signals (after exposure to 2 μM nifedipine) from a region on the anterior surface of the heart during electrical pacing at 2 Hz (same as in (b)). The action potential duration shortened and the calcium transient amplitude decreased. Signals are in arbitrary fluorescence units.

We used RH237 and rhod-2AM to measure transmembrane voltage and intracellular free calcium, respectively ***(Choi 2000, Warren 2007, Visweswaran 2013, Jaimes 2016)***. These off-the-shelf dyes are widely used in combination by the optical mapping community and have the benefit of being excitable by the same light source. As shown in **Figure 5.9**, two LED light sources are mounted on the left and right side of each dual-camera module. They are identical to the ones used in **Optical Mapping System 1**.

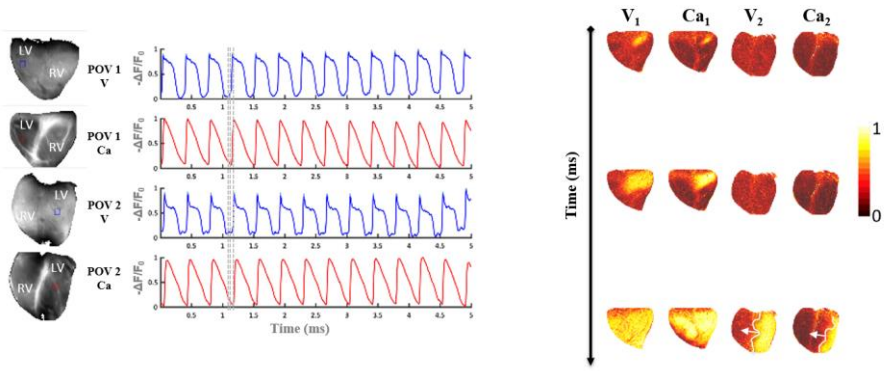

Figure 5.9: Simultaneous voltage and calcium acquisition during pacing. Normalized fluorescence signals (left) and normalized fluorescence maps (right) at different time points.

Figure 5.8 shows sample raw data, again unfiltered in time. The heart was imaged during electrical pacing at a cycle length of 500 ms. Compared to di-4-ANEPPS, we found RH237 and rhod-2AM challenging to load in the pig heart, emphasizing the need to optimize dye-loading protocols for each dye

and species. The SNRs for CAM 1, CAM 2, CAM 3 and CAM 4 were ~24 (voltage), ~34 (calcium), ~26 (voltage), and ~43 (calcium), respectively, calculated using the signals shown in **Figure 5.8a,b**.

As a proof-of-principle application, we measured the effect of nifedipine on the action potential and calcium transient. Nifedipine is a clinically-relevant 1,4-dihydropyridine calcium-channel blocker that reduces the action potential duration ***(Himmel 2012)*** and calcium transient amplitude ***(Levi 1996)***. **Figure 5.8c** shows sample control signals and signals obtained from the same tissue region ~10 minutes after adding nifedipine to the perfusate (2 µM concentration). The calcium transient signals were not normalized to demonstrate the reduction in signal amplitude.

5.4.3 Optical mapping framework: Optical mapping system 3

Recent advances in CMOS camera technologies have made possible high-speed imaging at megapixel spatial resolutions. And with the advent of the high-speed USB3.0 interface, it is possible to continuously record image sequences from cameras directly to the computer's solid-state drives. The system shown in **Figure 5.10** takes advantage of the progress in spatial resolution by performing multi-view optical mapping with a single camera. By using six mirrors, the system can image both the anterior and posterior surface of the heart using just one high resolution camera. This system uses a 2.2 Megapixel USB3.0 CMOS camera configured to record 468x1024 superpixels (2x2 binning mode; 2x2 pixels per superpixel) at 350 fps.

Single-camera panoramic optical mapping systems have been constructed and validated before ***(Lin 1999, Lee 2012)***. These systems used two mirrors placed at the back of the heart to show two reflected images of the posterior surface. This provided three views, spaced ~120^{o} apart, with one direct view

and two reflected. Because of the longer light path, reflected images of the heart were smaller. All three views were roughly in focus because of the small size of the hearts used and the large depth-of-focus of the camera lens. The much larger size of the pig hearts used in this study made challenging this implementation, which led us to the presented configuration, which provides two equal views of the anterior and posterior surface. Though less emission light is collected compared to the more direct view approaches of **Optical Mapping Systems 1 and 2**, sufficient signal quality can be achieved with such high-light Langendorff-perfused heart preparations.

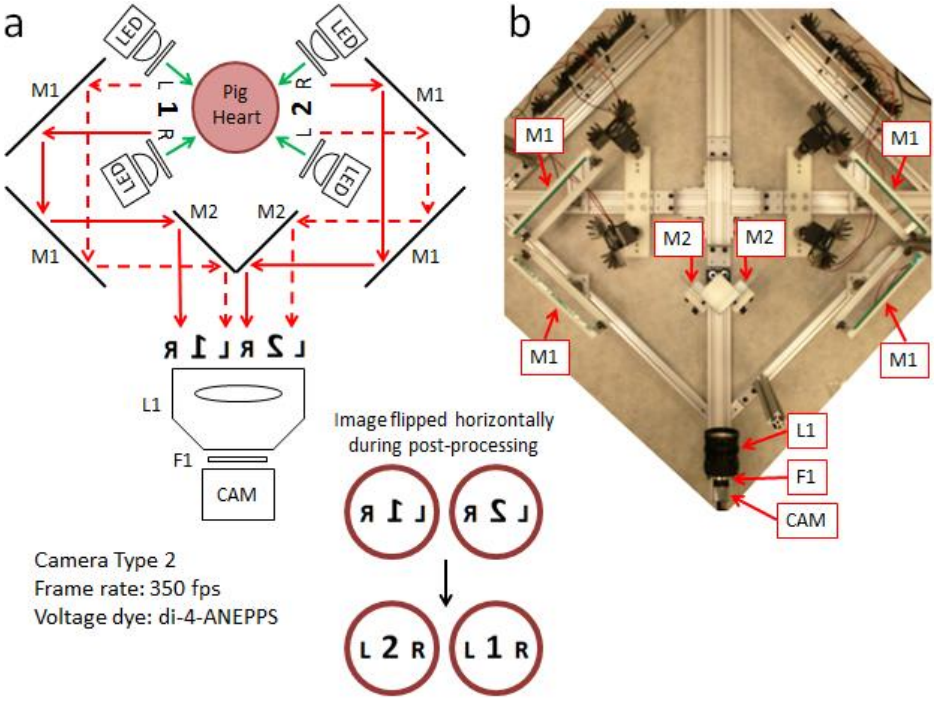

Figure 5.10: Optical Mapping System 3: Layout (Langendorff-Perfused Pig Heart) (a) *System schematic showing key components (see text for details). One high resolution camera, six mirrors and four LED light sources are used to image the heart from the anterior and posterior points-of-view (green arrows: excitation light, red arrows: fluorescence emission light).* ***(b)*** *Bird's-eye view of the imaging and illumination subsystems outlined in* ***(a)***.

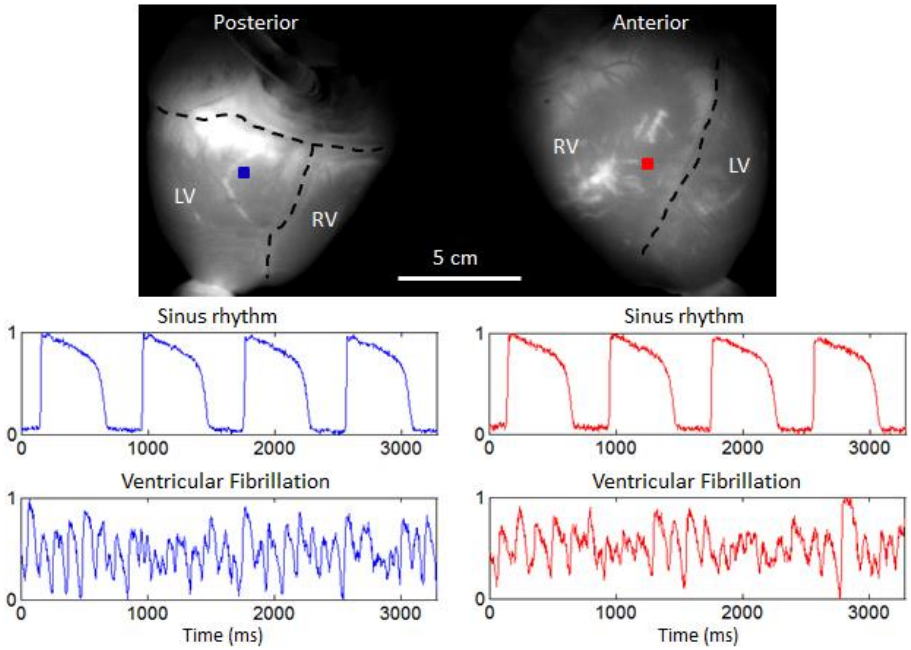

Figure 5.11: Optical Mapping System 3: Sample Data (Langendorff-Perfused Pig Heart) *Normalized fluorescence signals from the posterior and anterior points-of-view of the heart during sinus rhythm and ventricular fibrillation, taken from the blue-square and red-square regions shown, respectively. In the top panel, the right ventricle, left ventricle and atria are demarcated by black dashed lines. Signals are in arbitrary fluorescence units.*

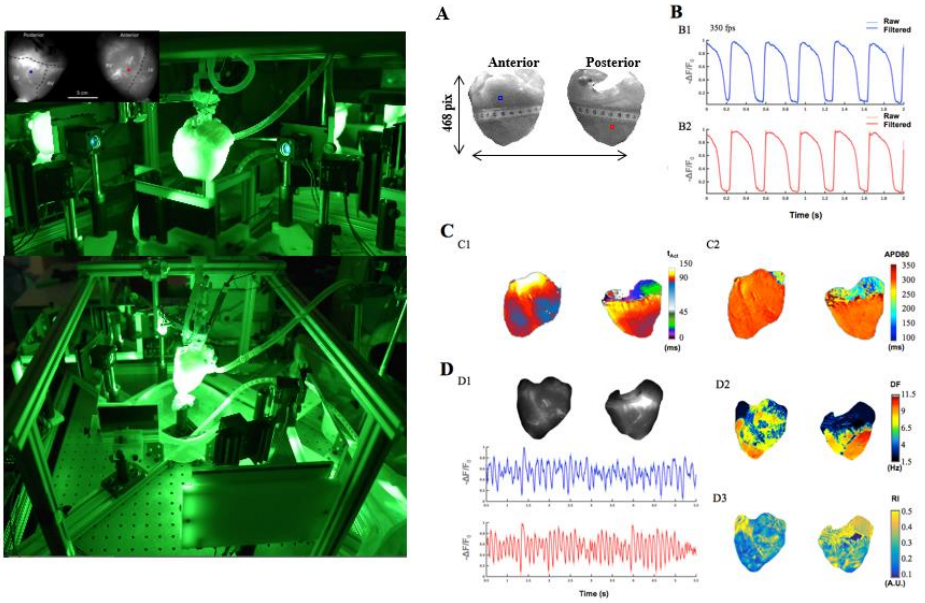

Figure 5.12: Optical Mapping System 3: Experimental set-up and parametric mapping

Figure 5.11 shows sample raw data, unfiltered in time. The heart was imaged during sinus rhythm, electrical pacing and ventricular fibrillation. During sinus rhythm, the SNR from points on the posterior (blue) and anterior (red) surface were ~78 and ~55, respectively, calculated using the action potentials shown in **Figure 5.11**.

5.4.4 Validation study in the Langendorff-Perfused Rabbit Heart

An extensive study using a large animal model may be too costly to pursue for many research groups and would certainly be too expensive to use in a biomedical engineering teaching laboratory, for which these systems were also designed for.

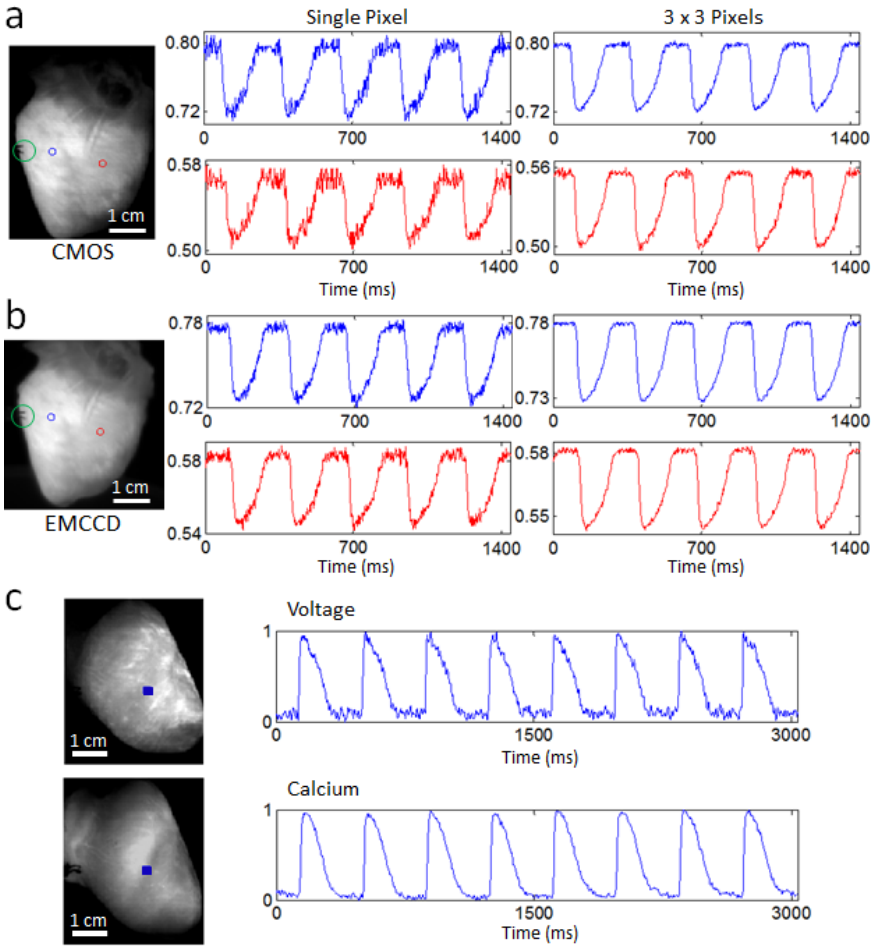

Figure 5.13: Sample Data from Langendorff-Perfused Rabbit Hearts *Fluorescence signals from two points on the ventricles (left panel; centered on the red and blue circles) during electrical pacing (green circle indicates the location of electrical point stimulation) using the (a) CMOS camera and (b) EMCCD camera (see text for details). Single pixel and spatially averaged (3x3 pixels) traces are shown, unfiltered in time. The SNRs were considerably higher for the EMCCD camera. (c) Simultaneous voltage and calcium imaging traces (normalized) taken from the blue-square regions shown (left panel) during sinus rhythm. Signals are in arbitrary fluorescence units.*

An extensive study using a large animal model may be too costly to pursue for many research groups and would certainly be too expensive to use in a biomedical engineering teaching laboratory, for which these systems were also designed for. Therefore, we tested the same CMOS cameras used in

Optical Mapping Systems 1 and 2 in the Langendorff-perfused rabbit heart. Using the uEye Cockpit software, each camera was configured to record 120x160 superpixels at 400 fps. For comparison, images were also taken with another camera typically used in optical mapping systems (Evolve 128 EMCCD camera; 128x128 pixels; Photometrics, AZ, USA).

Figure 5.13a,b shows sample raw data, unfiltered in time. The traces shown were collected during electrical point stimulation at a 280 ms cycle length. **Figure 5.13a** shows data from the CMOS camera while **Figure 5.13b** shows data from the EMCCD camera. The traces were not normalized to illustrate the relative saturation levels. Rabbit hearts were imaged with the CMOS camera while being electrically paced and during ventricular fibrillation. In **Figure 5.13a**, the SNRs for the single-pixel blue and red traces were ~14 and ~9, respectively, while the SNRs for the spatially-averaged (3x3 pixels) blue and red traces were ~40 and ~36, respectively. These sample values were calculated using the signals shown in **Figure 5.13a**. For comparison, the same heart was imaged with the EMCCD camera under the same conditions (frame rate = 400 fps and same illumination intensity). In **Figure 5.13b**, the SNRs for the single-pixel blue and red traces were ~23 and ~19, respectively, while the SNRs for the spatially-averaged (3x3 pixels) blue and red traces were ~59 and ~47, respectively. These sample values were calculated using the signals shown in **Figure 5.13b**. As expected, the EMCCD camera performed considerably better than the low-cost CMOS camera, and the difference in performance would be magnified in low-light level preparations like cardiac monolayers. However, for high-light level preparations, these modern low-cost CMOS cameras represent inexpensive alternatives capable of yielding data of sufficient quality. Furthermore, **Figure 5.13c** shows sample raw data, again unfiltered in time, demonstrating the suitability of

using these CMOS cameras for intracellular calcium imaging in Langendorff-perfused rabbit hearts.

5.5 Discussion

We have described and tested three low-cost optical mapping systems capable of panoramic imaging in a translational heart model. Our most costly implementation has a total system cost less than that of one standard optical mapping camera system, making this method financially viable to more research groups. There are, however, certain limitations with our approach. First, the high-speed CMOS cameras used have lower light sensitivity and more noise compared with the cameras typically used by the optical mapping community (**Figure 5.13a,b**). Thus, using these cameras in low-light level preparations like cardiac monolayers or tissue-engineered constructs may yield unacceptably low SNRs. But for isolated hearts from adult rabbits to adult pigs, we have demonstrated that these low-cost CMOS cameras produce sufficient SNRs to study arrhythmias and drug-action. Second, we used blebbistatin as an excitation-contraction uncoupler to minimize motion 'artifacts' in our fluorescence signals. Though this is currently standard practice in the optical mapping field, recent studies have shown that this compound can have deleterious effects on cardiac tissue ***(Kanlop 2010, Swift 2012)***. Consequently, it would be desirable to develop a low-cost optical analog to the epicardial electrode sock, designed to record epicardial activity in a beating heart ***(Worley 1987)***.

Although the presented systems can be used as is, there is still room for improvement. First, dye loading optimization in large animal models, like the pig, is necessary to improve SNRs and to further reduce costs since larger hearts generally require more dye. The use of newly-developed

potentiometric dyes will also improve SNRs because they have been shown to produce larger fractional changes in fluorescence during action potentials ***(Lee 2012, Matiukas 2007, Yan 2012)***. Second, exploration of other low-cost high-speed cameras is essential as the development of digital industrial cameras has been progressing at a rapid pace. We utilized CMOS cameras made by IDS Imaging Development Systems GmbH because of their cost, performance and programming interface. We are currently exploring newer, and in some cases lower-cost, cameras from the same manufacturer and other manufacturers like Allied Vision Technologies GmbH and Basler AG.

Studying cardiac arrhythmias in animal models has been essential to furthering our understanding of this complex biological phenomenon. However, small animal models like the mouse do not represent a clinically-relevant model for studying either ventricular or atrial fibrillation, especially if the study of arrhythmia dynamics in isolated hearts is complemented with the *in vivo* phenotype. The use of animal models like the goat, sheep or pig permit researchers to obtain *in vivo* phenotypes of arrhythmias similar to those observed in the clinical setting ***(Filgueiras-Rama 2012, Tschabrunn 2016)***. Experiments in such models substantially increase the cost of both *in vivo* and *ex vivo* studies ***(Martins 2014)***. As such, low-cost implementations of powerful experimental methods like panoramic optical mapping will help enable more extensive *in vivo* and *ex vivo* studies in large mammals with complex arrhythmias, a capacity limited to few laboratories. Importantly, the panoramic mapping approach enables one to track rotors on the myocardial surface at a resolution not achievable in current clinical electrophysiology procedures, which are limited to simultaneous multipolar recordings ***(Narayan 2012, Krummen 2014)***.

By lowering the financial threshold for implementing panoramic optical mapping, building a system that combines panoramic optical mapping with electrical mapping may be feasible while maintaining cost containment. For instance, simultaneous panoramic imaging and endocardial mapping using a balloon electrode array would provide both epicardial and endocardial information, respectively, which are both relevant in the study of ventricular arrhythmias ***(Durrer 1970, Downar 1988, Jia 2002)***. Furthermore, doing both of these measurements in a torso-tank fitted with hundreds of body-surface electrodes would simultaneously provide a complete set of electrocardiogram information on the pseudo-torso surface ***(Oster 1997, Ramanathan 2004)***. ECG imaging based on body surface potentials allows clinicians to non-invasively infer the electrical activity in the heart by solving an "inverse problem." Though much progress has been made in reconstructing cardiac electrical activity from these remote electrode measurements, validating these inferences with combined panoramic optical mapping and endocardial mapping should prove useful. Finally, parallel work in the field of whole-heart computational modeling will undoubtedly benefit from such multi-modal validation measurements, leading to a more coherent picture of complex arrhythmias and therapeutic interventions to restore sinus rhythm ***(Trayanova 2011, Baillargeon 2014, Chabiniok 2016).***

5.6 Conclusion

In this sub-study, a novel scalable framework for studying cardiac arrhythmias by means of panoramic optical mapping is presented describing three optimized configurations towards comprehensive electrophysiological studies. Considering current costs for such systems, these alternative approaches will open up new experimental possibilities and offer a significant reduction in the economical threshold as would be needed to gain

wider use by the arrhythmia research community. Panoramic optical mapping, however, only provides information from the epicardial layer of the heart. Endocardial and transmural measurements must be made simultaneously to provide a more coherent picture of complex arrhythmias. Altogether, the designs described in this studies will make this integration more technically and financially viable.

5.7 Novel panoramic whole heart mapping for simultaneous non-overlapped parametric electrophysiological imaging: a platform for drug-testing, modelling and biomedical engineering applications

In this chapter, results are reproduced from the publication [Calvo et al 2017 '*A single-sensor high-resolution panoramic optical mapping configuration for simultaneous non-overlapped complete atrial and parametric imaging*']

Introduction

Nowadays optical mapping (OM) is the primary method for imaging electrophysiologically relevant parameters from the outer surface of Langendorff-perfused hearts. This technique has become essential for comprehensively understanding mechanisms of cardiac propagation during physiological activation, arrhythmia, and therapeutic antiarrhythmic interventions in translational hearts. Panoramic whole heart optical mapping systems, using either multiple cameras, plane mirrors or a combination of both, have been developed to overcome intrinsic visualization limitations to traditional single-sensor designs ***(Lin S 1999, Efimov 2004).*** However current panoramic OM systems are financially challenging for physiology

and engineering research labs since require multiple sensors to completely map wide areas of the surface, which further results on overlapping regions and/or missing areas of interest due to the intrinsic shape of the heart. In this study, we propose and validate a new spatially resolved low-cost single-sensor configuration to simultaneously record atrial and ventricular function in relation to its anatomy without overlapping regions.

Understanding comprehensively the mechanisms of spread of cardiac propagation at the organ level, and thus, characterize the distribution of transmembrane voltage throughout the heart, is one of the major objectives in cardiac electrophysiology. The ability to record with high-resolution simultaneously multiple physiological parameters, as well as, to monitor large-scale phenomena such as fibrillation and/or defibrillation processes, has made OM a solid central technique to dynamically characterize function in relation to anatomy ***(Herron TJ 2012, Boukens B 2013)***

This technique has enabled physiology researchers studying mechanisms of initiation and maintenance of life-threatening arrhythmias and the action of novel therapeutic interventions. Likewise, current therapeutic trends in clinical settings, either by using algorithms to accurately tracking and targeting arrhythmia drivers, and validation of predictive computational models used to test new therapeutic strategies in the clinical settings, have extensively benefited from developments in OM. Despite its widespread application in experimental and pre-clinical cardiac electrophysiology, OM of isolated hearts have been traditionally applied to record localized or constraint areas, missing critical information of the unknown dynamic processes occurring during discontinuous propagation in presence of arrhythmias. This is especially relevant during arrhythmia settings, for example, in presence of regional acute interventions or chronic substrate

alterations, or simply when the interest is to characterize the spatiotemporal large-scale non-linear dynamics of dominant driving mechanisms.The aim of this study was to compare and validate a new high-resolution and spatially-resolved low-cost single-sensor panoramic optical mapping configuration for simultaneous imaging and parametric mapping of atrial and ventricular activation during normal and abnormal activation.

We designed an OM setup for studying whole heart electrophysiology using a single-sensor configuration in combination with a curved mirror with similar exponential curvature to that of the outer shape of the heart. After camera calibration and motion compensation, accurate reconstruction of optical transients and assessment of propagation under different conditions was done to evaluate reconstructed signal-to-noise ratios and overall mapping quality.

Optical mapping system: Layout

We devised a system layout integrated with the perfusion circuit comprising a single-view scientific camera (sensor element), a control system for led illumination, electrical stimulation and simultaneous sensing of physiological variables. A precision near ellipsoidal curved mirror (highly concentrated reflectance in the range 380nm-800nm), with exponential profile and diameter to harbour small to large hearts was used to simultaneously obtain fluorescence from every point in the ventricular and atrial surfaces. A simplified schematic is shown in Figure 1. A four-point illumination array was placed surrounding the reflector element. The heart was perfused using a thin silicon-tube attached to a rigid body. Wired atrial electrodes were placed from a custom cannula unresponsive to light excitation. Tyrode’s perfusion liquid was collected from the bottom keeping

the feedback circuit closed using a custom funnel-shaped cup with integrated electrodes to record a reference pseudo-ecg.

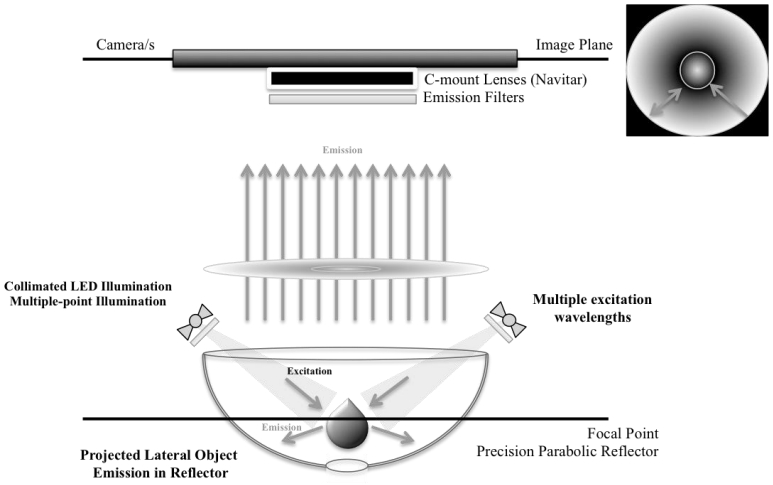

Figure 5.14: Proposed panoramic optical mapping system layout using a single-sensor configuration with a curved-parabolic reflector element.

Tyrode's perfusion liquid was collected from the bottom keeping the feedback circuit closed using a custom funnel-shaped cup with integrated electrodes to record a reference pseudo-ecg.

Experimental models and protocol

Six New Zealand White rabbits and one Large White pig were included in the study. Animal care and the experimental protocols used in the study complied with EU directive 2010/63 on the protection of animals used for scientific purposes, and were approved by the Institutional Animal Care and Use Committee of the University of Valencia (CEEA:A1404746730665). Rabbit hearts were excised through a medial sternal incision after anaesthetic pre-medication (ketamine 35 mg/kg and heparinization) and sodium-pentobarbitone (100 mg/Kg) overdose via injection in the left marginal ear vein. After removal, hearts placed in appropriately adjusted cold Tyrode's

solution were connected into flow and pressure controlled Langendorff systems, respectively for rabbit and pig hearts. Hearts were stabilized and physiological variables monitored for 15-20 min.

After stabilization we used 5-10uM blebbistatin to maintain the heart mechanics uncoupled during the experiment and reduce motion artifacts. High-resolution OM was performed using di-4-ANDBQPQ near-infrared dye. Illumination was collimated and passed through excitation filters fully exciting the whole myocardium. Fluorescence emission was appropriately collected and passed through a long-pass near infrared filter. Acquisition was performed using a EMCCD scientific camera (Evolve128, 1KHz, Photometrics, AZ, USA).

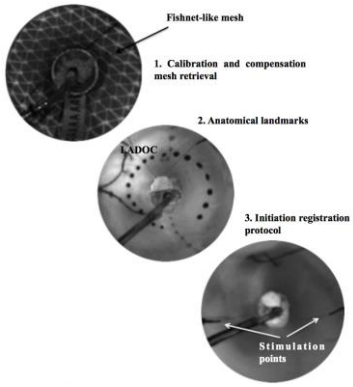

Figure 5.15. Fishnet-like pattern and anatomical landmarks unresponsive to light excitation used during calibration in Heart#02-03.

Electrical signals and optical sequential images, were synchronized through a monostable-based triggering circuit. We characterized signal-to-noise ratios (SNR) of reconstructed action potentials (AP) during sinus rhythm and stimulation in specific anatomical locations. Hearts were stimulated to explore dynamic restitution properties and continued until ventricular

fibrillation (VF) was induced with and without presence of a coronary occlusion in the LAD-artery (LADOC).

Camera calibration and optical mapping reconstruction

Initial camera calibration was done using a fishnet-like pattern to set the heart positioning and subsequent correspondence mapping. Nylon landmarks, as shown in Figure 2, unresponsive to light excitation were used as references to ensure accurate motion compensation using a block-matching cross-correlation strategy. Reconstructed optical maps were evaluated in terms of signal-to-noise ratios after normalization.

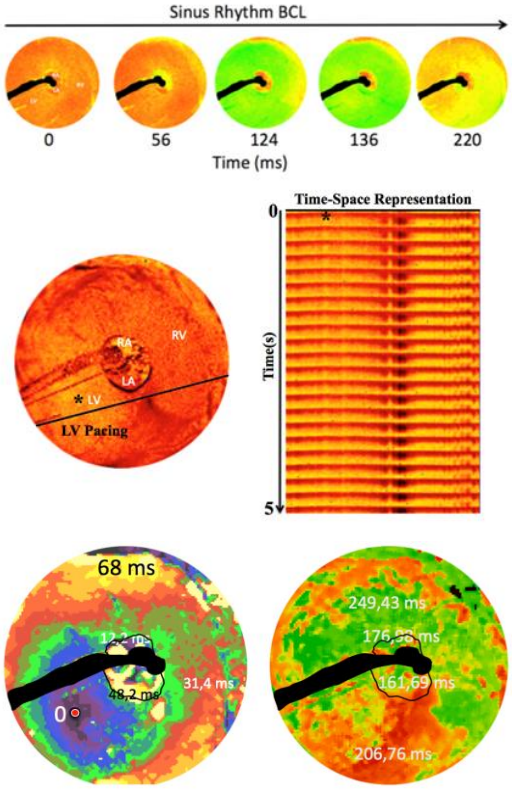

Figure 5.16. Activation process during sinus rhythm and during stimulation in one rabbit heart. *A. Snapshots showing normalized fluorescence (F/Fo) during activation and recovery during sinus rhythm and time-space representation of paced activation. B. Activation map during ventricular pacing and APD80 map are shown.*

Quantitative post-processing

Semi-automatic mask determination was applied using thresholding and connected component analyses for background removal. Labelling of different anatomical regions was done manually and refined using morphological post-processing. After reconstruction, fluorescence signals were detrended by baseline removal, normalized and filtered in time. We obtained parametric maps of the activation and repolarization spread propagation processes using first and second derivatives of the reconstructed signals. Action potential durations were obtained as durations from the activation to 80% of repolarization (Figure 3). Spectral dominant frequency mapping and phase mapping were used for fibrillatory conduction spatiotemporal assessment.

Results

Successful high-resolution OM showed high SNRs in atrial and ventricular surfaces (Figure 1, 28±11 dB). Figure 1, shows activation and recovery processes during sinus (A) and pacing (B), sequentially in the outer surface of each chamber of the heart. A time-space representation is shown during pacing illustrating propagation from the LV to the rest of the heart. Activation maps showed propagation throughout the heart surface. APD in selected locations highlight differences during fixed-point stimulation (APD80, ms) between left and right chambers in transmembrane potential transient durations.

Ventricular fibrillation, induced in the presence of a coronary occlusion, is illustrated in the figure below, together with single pixel recordings in each chamber. Retrograde irregular activation is observed in the recorded atrial responses.

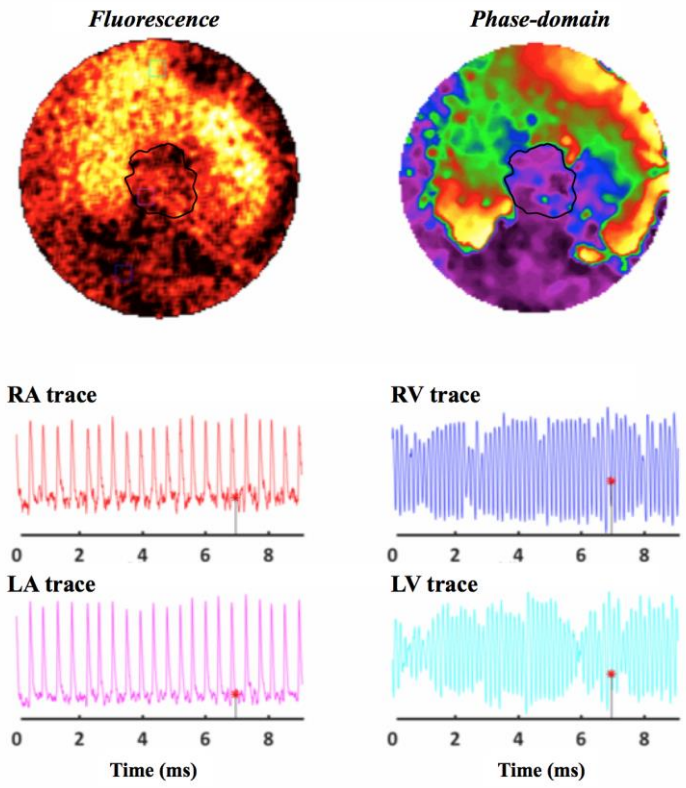

Figure 5.17. Normalized fluorescence maps and single pixel recordings simultaneously in the atrium and ventricles. Snapshots of transmembrane voltage in the time domain (normalized fluorescence, top-left) and phase-domain (normalized Hilbert transform, top-right) during ventricular fibrillation in presence of a LAD coronary occlusion. Bottom. Single-pixel recordings from atrial and ventricular locations.

Characterization of the fibrillatory process in Heart#04 is summarized in Figure 5. Wavebreak was observed near the coronary occlusion. Spatial profiles showed evident differences in dominant frequency and organization from the occlusion elsewhere, and between chambers.

In this example, high activation and rotatory waves were observed surrounding the coronary occlusion. This configuration allowed for spatiotemporal identification of fibrillatory activation throughout the whole heart surface.

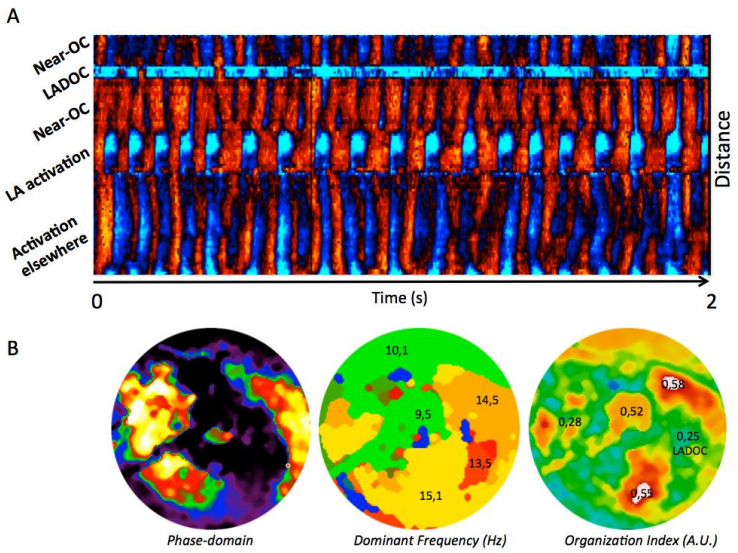

Figure 5.18. Time-Space plot of normalized fluorescence across the occlusion as well as parametric maps of the process. A. Time-space plot representation during fibrillatory activation in each region. B. Reconstructed phase-domain and DF mapping. Shown are high-resolution maps for OI and DF.

In this sub-study we devised a novel configuration to simultaneously map atrial and ventricular physiology without overlapping regions taking advantage of the heart shape. This configuration allowed us to reconstruct action potential transients and the spread propagation with high-resolution. Even though the presented configuration may be useful as it is, it can be further optimized, and even lower its financial costs, as previously described ***(Lee-Calvo 2017)***

Even though the preparation and calibration may be further optimized to improve reconstruction quality and/or reduce preparation times, it is clear that this configuration has proven useful to perform high-quality quantitative physiological studies and retrieve data simultaneously from whole-heart epicardial locations. Additionally, the presented configuration can be easily extended for multi-parametric mapping studies and/or combined with additional compatible techniques to obtain endocardial mapping and/or tank-based pseudo-ecg mapping to correlate activity from different layers. This information can be used to develop detailed mathematical models.

Discussion and conclusions

Studying cardiac arrhythmias in animal models has been essential to furthering our understanding of this complex biological phenomenon. However, small animal models like the mouse do not represent a clinically-relevant model for studying either ventricular or atrial fibrillation, especially if the study of arrhythmia dynamics in isolated hearts is complemented with the in vivo phenotype. The use of animal models like the goat, sheep or pig permit researchers to obtain in vivo phenotypes of arrhythmias similar to those observed in the clinical setting ***(Filgueiras-Rama et al. 2012; Tschabrunn et al. 2016).*** Experiments in such models substantially increase the cost of both in vivo and ex vivo studies ***(Martins et al. 2014).*** As such, low-cost implementations of powerful experimental methods like panoramic optical mapping will help enable more extensive in vivo and ex vivo studies in large mammals with complex arrhythmias, a capacity limited to few laboratories. Importantly, the panoramic mapping approach enables one to track rotors on the myocardial surface at a resolution not achievable in current clinical electrophysiology procedures, which are limited to

simultaneous multipolar recordings ***(Narayan et al. 2012; Krummen et al. 2014).***

By lowering the financial threshold for implementing panoramic optical mapping, building a system that combines panoramic optical mapping with electrical mapping may be feasible while maintaining cost containment. For instance, simultaneous panoramic imaging and endocardial mapping using a balloon electrode array would provide both epicardial and endocardial information, respectively, which are both relevant in the study of ventricular arrhythmias ***(Durrer et al. 1970; Downar et al. 1988; Jia et al. 2002).*** Furthermore, doing both of these measurements in a torso-tank fitted with hundreds of body-surface electrodes would simultaneously provide a complete set of electrocardiogram information on the pseudo-torso surface ***(Oster et al. 1997; Ramanathan et al. 2004).*** Body surface potential mapping, as this approach is known, allows clinicians to non-invasively infer the electrical activity in the heart by solving an "inverse problem." Though much progress has been made in reconstructing cardiac electrical activity from these remote electrode measurements, validating these inferences with combined panoramic optical mapping and endocardial mapping should prove useful. Finally, parallel work in the field of whole-heart computational modeling will undoubtedly benefit from such multi-modal validation measurements, leading to a more coherent picture of complex arrhythmias and therapeutic interventions to restore sinus rhythm ***(Trayanova 2011; Baillargeon et al. 2014; Chabiniok et al. 2016).***

We validated a novel single-sensor configuration for parametric OM of cardiac propagation throughout the whole epicardial surface taking into account the cardiac curvature. Even though further optimization may be necessary to ensure homogeneous focusing, it may represent a new low-cost

framework for physiology and engineering labs working in the fields of cardiac arrhythmias and whole-heart computational modeling.

Chapter 6

Conclusions

In this chapter, global conclusions of the studies carried within this thesis are presented in relation to the objectives stated in Chapter 1.

6.1 Conclusions

Regarding the main objective, '*To develop techniques, computational tools and technology for understanding intrinsic mechanisms of primary and dominant drivers of complex arrhythmias as well as serve as a platform for developing advanced diagnostic & therapeutic strategies*'

A framework for computational simulations running on high performance computing platforms as well as using GPU acceleration have been implemeted for studying major determinants of reentry dynamics in presence of regional heterogeneities and geometrical constraints. Likewise, computational techniques based on signal and image-based spectral and phase analyses have been implemented for localizing and tracking accurately reentrant sources. Spectral properties of ventricular fibrillation have been determinant on unraveling the impact of fibrillatory episodes in cardiac arrest patients. Finally, a low-cost platform for comprehensive panoramic and multiparametric optical mapping of cardiac electrophysiology has been

validated under different use-case scenarios for the study of cardiac arrhythmias and drug testing.

Regarding the secondary aims:

Aim1: *To develop a computational platform for simulation of cardiac electrophysiological tissue and geometrical models to determine functional and structural determinants of primary and dominant driver dynamics with interest in the role of major ionic repolarizing currents.*

A computational framework for simulations of cardiac electrophysiology has been developed for studying cardiac remodeling and arrhythmias. Specifically, geometrical models of the PV-LAJ including realistic gradients on active properties and heterogeneities on passive properties of the tissue have been used to study dynamics of primary reentrant sources on cardiac tissue. Repolarizing currents such IKr or IKs have shown to influence rotor stability and wavebreak formation. Despite that IKr and IK1 gradients have been found in opposite directions in the atrium we showed for the first time a dominant role of IK1 dispersion over all ionic currents determining drifting of primary sources. We observed that a delicate interplay between IK1 and IKr might determine the spatiotemporal differential localization of rotors. These results point out the importance of envisioning mechanistic-based therapeutic strategies targeting preferential localization of primary sources either by selective pharmacological interventions or ablative apporache devising minimal lesions in such locations.

Aim2. *To study the mechanisms of wavebreak and spiral drift under regional heterogeneity with interest in the pulmonary veins left atrial junction transition.*

We have demonstrated the major role of IK1 heterogeneity and excitability gradients as active attractors of spiral waves during fibrillation. Additionally, the multidomain techniques developed, incluing phase- and spectral-analyses allowed us to accurately localize and track dynamically primary reentrant sources. Specifically, in the setting of the PV-LAJ, attraction of reentrant sources to the PVs was consistent with reduced coupling and excitability, despite any geometrical constraints. I_{K1} heterogeneity across the PV-LAJ showed to be dominant compared to other ionic currents in conveying drift direction through its effect on refractoriness and excitability. Therefore measuring with high-resolution refractoriness, excitability and diastolic potentials during pacing protocols may provide a non-invasive or minimally invasive future guidance for determining and localizing dinamically attractors of unstable components of dominant rotors, which are believed to underlie AF.

Aim 3. *To develop a mechanistic-based score for cerebral performance and survival after cardiac arrest due to VF impact.*

A mechanistic-based multivariate model and risk score that reliably predicts cerebral performance and survival, on admission of comatose survivors undergoing therapeutic hypothermia for ventricular fibrillation have been developed taking into account biomarkers (such as dominant frequency, regularity index, high-to-low spectral ratios, etc) representing deterministic and mechanistic features of the arrhythmia. Signal processing, spectral analyses and machine learning tools have been implemented, validated and integrated in the early diagnostic workflow. We prove and conclude that a spectral analysis-based model, reflecting deterministic properties of inherent fibrillatory mechanisms, demonstrates high (>90%) reliability in predicting

in-hospital FNP and survival to discharge in patients with comatose status on admission after cardiac arrest due to VF.

Aim 4. *To validate new technologies and multimodal techniques for multiparametric and panoramic electrophysiological optical mapping for the study of cardiac arrhythmias in translational animal models.*

A modular platform optimized for electrophysiological studies of voltage and calcium simultaneousneusly with a configurable field of view has been validated in small and large hearts. Automatic multidomain analyses of multi-view image sequences can be carried within the platform including advanced analytical tecniques in phase, time-frequency and spectral domains. Computational times have been reduced for data processing and automatic feature extraction in such large datasets by using GPU-based acceleration.

Aim 5. *To validate different low-cost high-resolution optical mapping configurations for the study of cardiac fibrillation mechanisms and drug action.*

A novel scalable framework for studying cardiac arrhythmias by means of panoramic optical mapping is validated describing optimized configurations for comprehensive electrophysiological studies. More interestingly such systems represent alternative approaches that will open up new experimental possibilities and offer a significant reduction in the economical thresholds with coming generation of CMOS sensors compiting with high-end scientific cameras at the organ level. This technique could be combined with simultaneous endocardial measurements to provide more comprehensive understanding of complex arrhythmias being more finantially viable. Additionally, this phylosophy may allow for future educational and device

testing applications. To our knowledge this provides a technically and finantially viable framework for future electrophysiological and pharmacological studies, data-enriched modelling and biomedical engineering applicactions in the cardiovascuar field.

6.2 Future studies

Future studies may employ the tools and techniques developed together with such scalable and modular experimental systems validated during this thesis for further understanding complex arrhythmia mechanisms and, to support testing new therapeutic strategies. Altogether the techniques and technology developed within this thesis will serve as a platform for scalable electrophysiological studies, high-thoughput pharmacological testing, and bioengineering applications. We also foresee their use for a broader research community and even for educational applications using low-cost experimental setups being more finantially accessible. Specific use-case studies derived from these studies have been already submitted and/or prepared for publication.

Chapter 7

Contributions

7.1. Contributions of this thesis

In this section the main and related research publications and contributions of this thesis are listed.

7.1.1. Journal papers

[1]. **Calvo C**, Deo M, Zlochiver,S ,Millet J, Berenfeld O Atraction of rotors to the pulmonary veins in paroxismal atrial fibrillation: a modelling study. *Biophysical Journal 2014;106(8),1811-21* ***Quality metrics. IF-2014: 3,976 Rank:Q1.*** **Editorial New and Notable:** Drifting through the beehive *BiophysJ. 2014,106(8):1555-6.*

[2]. Filgueiras-Rama D.*, **Calvo C***, Salvador-Montañés O, Cádenas R., Ruiz-Cantador J., Armada E, Rey JR, Merino JL, Peinado R, Pérez-Castellano N, Pérez-Villacastín J,. García J., Jiménez S, Castells F, Chorro FJ, López-Sendón JL, Berenfeld O, Jalife J., López de Sá E, Millet J *** Equal Contribution First Authors** Spectral Analysis-Based Risk Score to Early Predict Mortality and Cerebral Performance in Patients Undergoing Therapeutic Hypothermia for Ventricular Fibrillation and Comatose Status. *International Journal of Cardiology 2015;186,250-258* ***Quality metrics: IF2015-2016 6.175 Q1 (Cardiac and cardiovascular systems)***

[3]. Lee P.*****, **Calvo C***, Almazán JM, Quintanilla JG, Chorro FJ, Yan P., Loew L, Filgueiras-Rama D., Millet J. ***Equal Contribution First Authors** Low-Cost Optical Mapping Systems for Panoramic Imaging of Complex Arrhythmias and Drug-Action in Translational Heart Models *Nature Scientific Reports, Nature Publishing Group 7:43217,2017* ***Quality metrics. IF2017: 5.8 Rank:***

Q1 (Multidisciplinary Sciences)

[4]. **Calvo C**, et al. Panoramic whole heart mapping for simultaneous non-overlapped parametric electrophysiological imaging: a platform for drug-testing, modelling and biomedical engineering applications *(Submitted)*

[5]. **Calvo C**, et al. Panoramic imaging reveals differences in septal endocardial and epicardial conduction properties during normal and fibrillatory rhythms. *(Submitted)*

7.1.2. Related journal paper publications

[6]. Campbell K, **Calvo C**, et al Spatial gradients in action potential duration created by regional magnetofection of hERG are a substrate for wavebreak and turbulent propagation in cardiomyocyte monolayers. *Journal of Physiology 2012;15;590(24),6363-79*

[7]. **Calvo C**, et al. Therapeutic Ranolazine Prolongs Ventricular Wavelength at High-rates Preventing Stretch-driven Unstable Components and Spatiotemporal Voltage-Calcium Uncoupling during the Time-Course of Acute Myocardial Mechanoelectric Feedback *(Submitted)*

[8]. Chorro FJ, Canto I, Brines L, Such-Miquel L, **Calvo C**, et al Ranolazine Attenuates the Electrophysiological Effects of Myocardial Stretch in Langendorff-Perfused Rabbit Hearts. *Cardiov. Drugs Ther. 2015;29(3),231-41*

[9]. Filgueiras D, Castrejón S, **Calvo C**, et al Basic mechanisms of the new antiarrhythmic drugs in atrial fibrillation. *Arch. Med. Cardiol 2012;82(3),139-52*

7.1.3. Derived and related international conferences

[1]. **Calvo C**, Guill A, Tormos A, Such-Miquel L, Arias Mutis O., Zarzoso M, Chorro J, Millet J A single-sensor high-resolution panoramic optical mapping configuration for simultaneous non-overlapped complete atrial and parametric imaging IEEE Computing in Cardiology 2018

[2]. **Calvo C,** Tormos A, Zarzoso M, Guill A, Chorro FJ, Millet J A single-sensor panoramic optical mapping system for whole heart parametric imaging Biophysical J Supp TN 18-L-5685-BPS

[3]. **Calvo C**, Tormos A, Roses E, Zarzoso M, Arias O, Cebrían A, Jimenez S, Millet J, Chorro J, Guill A Dual-sided mapping during global stretch using a

custom miniaturized endocardial balloon with multipurpose multichannel acquisition system for preclinical electrophysiological studies IEEE Computing in Cardiology 2017

[4]. **Calvo C,** Tormos A, Roses E, L. Such-Miquel, Zarzoso M, S. Jimenez, Such L, Millet J, Chorro FJ, Guill A Simultaneous electro-optical endocardial and epicardial mapping of mechanoelectric feedback by left ventricular stretch in the isolated rabbit heart. An experimental validation of a custom-made endocardial balloon array with volume control FEPS Acta Physiologica SI 221;713;118-128

[5]. **Calvo C**, Óscar Salvador-Montañés, Antonio Guill, Santiago Jiménez, Alvaro Tormos, Francisco Castells, Francisco J. Chorro, José Millet, David Filgueiras-Rama Spectral Characteristics of Spontaneous VF Prior DC-Shock are Significantly Different from T-Wave Shock-Induced Post-Resucitation Episodes in Out-of-Hospital Cardiac Arrest Survivors Heart Rhythm 2015 12(5),S338-S339

[6]. **Calvo C,** Filgueiras-Rama, D, Jimenez-Serrano S, Castells F, Chorro FJ, Millet J Evaluation of short-term individual variability on the contribution of spectral-based predictors to cardiac arrest neurological performance and survival outcomes *Proceedings Computing in Cardiology 2014*

[7]. Filgueiras-Rama D*, **Calvo C***, Óscar Salvador-Montañés, Rosalía Cádenas, Jose Ruiz-Cantador, Eduardo Armada, Juan Ramón Rey,JL Merino, Rafael Peinado, Nicasio Pérez-Castellano, Julián Pérez-Villacastín, Jorge G. Quintanilla, Santiago Jiménez, Francisco Castells, Francisco J. Chorro, JL López-Sendón, Omer Berenfeld, José Jalife, Esteban López de Sá, José Millet Spectral Analysis-Based Risk Score to Early Predict Mortality and Cerebral Performance in Patients Undergoing Therapeutic Hypothermia for Ventricular Fibrillation and Comatose Status Circulation vol.130 Supp 2 A17810

[8]. **Calvo CJ,** Zarzoso M, Del Canto I, Parra G, Brines L, Roses EJ, Guill A, Alberola A, Millet J, Chorro FJ Therapeutic doses of ranolazine prolong ventricular action potential duration with a frequency-dependent effect without modifying calcium transient duration European Heart Journal Supplement 2014, (35),254-255

[9]. **Calvo CJ,** Zarzoso M, Such-Miquel L, Guill A, Tormos A, Brines L, Yagüe-Mayans J, Roses E, Del Canto I, Such L, Chorro FJ, Millet J Use-dependent prolongation of ventricular wavelength and regularization of beat-to-beat voltaje-calcium correlation by therapeutic doses of ranolazine in the normal heart Acta Physiologica Supplement 698 Volume 212 p. 48

[10]. Yagüé A., Guill A., Zarzoso M., Cebrián A., Chorro FJ, Millet J, **Calvo C** Comparison of Intensity-based B-splines and Point-to-Pixel Tracking Techniques for Motion Reduction in Optical Mapping Experiments IEEE Computing in Cardiology

[11]. Brines Ferrando L, Canto I, Parra G, Such-Miquel L, Zarzoso M, **Calvo C**, Soler C, Millet J, Such-Belenguer L, Chorro FJ Mechanoelectric feedback alterations induced by the benzothiazepine derivative jtv-519 European Heart Journal (2014), 35, Supp1, 254

[12]. **Calvo C**, Deo M, Zlochiver,S ,Millet J, Berenfeld O Frequency Dependent Pacing Determinants of an IK1-mediated Rotor Drift in the Posterior Left Atrial Wall toward the Pulmonary Veins IEEE Computing in Cardiology

[13]. **Calvo C**, Arias-Mutis O, Such-Miquel, Tormos A, Guill A, Such L, Alberola A, Chorro FJ, Zarzoso M. Study of the induction and characteristics of ventricular fibrillation in an experimental model of metabolic syndrome. Cardiovascular Res S80

[14]. **Calvo C**, Arias-Mutis O, Bizy A, Such-Miquel, Tormos A, Guill A, Such L, Alberola A, Chorro FJ, Zarzoso M. Modifications of atrial refractoriness produced in an experimental rabbit model of diet-induced metabolic syndrome. Cardiovascular Res 2018, 114(suppl_1):S80-S81

[15]. Yagüe Mayans, J, Moscardó V, Chorro FJ, Millet J, **Calvo C** Evaluation of Classical Similarity Measures for Motion Tracking in Experimental Cardiac Optical Mapping Studies *IEEE-EMBS Biomedical and Health Informatics 2014*

[16]. **Calvo C**, David Filgueiras-Rama, Francisco J Chorro, Omer Berenfeld and José Millet Predictive Value of Non-linear Characterization of the Spectral Power-Frequency Distribution of Ventricular Fibrillation in cardiac arrest patients IEEE-EMS Medical and Biological Engineering 2014

[17]. **Calvo C,** Manolo Zarzoso, Antonio Guill, Alvaro Tormos, Luis Such-Miquel, Eduardo Roses, Francisco J Chorro and José Millet Blob-based evaluation of Drug-Induced Modifications on Ventricular Fibrillation Complexity during Acute Mechano-electric Feedback using Dual Optical Mapping IEEE-EMS Medical and Biological Engineering 2014

[18]. **Calvo CJ**, Deo M, Berenfeld O A spatial gradient in IK1 density across the pulmonary vein left atrial junction attracts atrial fibrillation drivers to the pulmonary veins Heart Rhythm Journal Supplement, 2010, Vol 7, No 11 Supp, 1716-1717

7.1.4. Derived and related national conferences

[19]. Calvo CJ, Tormos A, Roses E, Millet J, Such-Miquel L, Zarzoso M, Chorro FJ, Guill A Mapeo simultáneo endo-epicárdico durante estiramiento global en corazón aislado revela propiedades de restitución bifásicas responsables del incremento de complejidad durante fibrilación ventricular *Rev Esp Cardiol. 2017;70(Supl.1):659*

[20]. Filgueiras-Rama, D, **Calvo CJ**, Salvado O, Perez-Castellano N, Perez-Villacastín J, García-Quintanilla J, Lopez de Sa E, Millet J Valor del análisis espectral frente a las variables clínicas como modelo predictivo de daño neurológico en pacientes con estado comatosos tras fibrilación ventricular. Sección arritmias Sociedad Española de Cardiología 2014

[21]. Calvo C, Arias O, Bizy A, Guill A, Tormos A, Such.Miquel L, Alberola A, Such L, Chorro FJ, Zarzoso M Modifications of dynamic restitution during induction of ventricular fibrillation in a model of metabolic syndrome *Journal of Physiology and Biochemistry Supplement 1:87 XXXIX Congress of the Spanish Society of Physiological Sciences 2018*

[22]. Piñero M, Guill A, Tormos A, Ontoria I, Zarzoso M, Such L, Chorro FJ, Sepúlveda P, Millet J, **Calvo C** Dose-response calcium transient modifications by ranolazine on restitution and spontaneous reentrant activity using a custom cardiac monolayer optical mapping setup *Journal of Physiology and Biochemistry Supplement 1:87 XXXIX Congress of the Spanish Society of Physiological Sciences 2018*

[23]. Calvo C, Arias-Mutis O, Such-Miquel, Bizy A., Guill A, Tormos A, Alberola A, Such L, Chorro FJ Dynamics of phase singularities during ventricular fibrillation in an experimental model of metabolic syndrome. *Journal of Physiology and Biochemistry Supplement 1:87 XXXIX Congress of the Spanish Society of Physiological Sciences 2018*

[24]. Calvo C, Arias-Mutis OJ, Guill A, Tormos A, Millet J, Alberola A, Such L, Chorro FJ, Zarzoso M Estudio de las características espectrales de la fibrilación ventricular en un modelo experimental de síndrome metabólico *Rev Esp Cardiol 2016:69 Supl 1:570 (6001)*

[25]. Calvo CJ, Arias-Mutis OJ, Such-Miquel L, Guill A, Parra G, Such L, Chorro FJ., Zarzoso M Modificaciones intrínsecas de las características espectrales de la fibrilación ventricular producidas en un modelo experimental de síndrome metabólico en conejo *Rev Esp Cardiol. 2017;70(Supl.1):150*

[26]. **Calvo CJ**, Zarzoso M, Tormos A, Such-Miquel L, Soler C, Such L, Millet J, Chorro FJ La Ranolazina en dosis terapéuticas prolonga la repolarización ventricular sin modificar la duración del transitorio de calcio y regulariza la aparición de alternos a alta frecuencia *Rev Esp Cardiol. (2014),67 Suppl 1 1:1094*

[27]. **Calvo CJ**, Filgueiras-Rama D, Castrejón-Castrejón S, Dionisio-Parra B, Millet J, Castells F, Merino JL, López-Sendón JL Estrategias para la ablación minima con mayor efectividad para detener patrones reentrantes durante fibrilación auricular *REC. (2013),66 Suppl 1 1:493*

[28]. Filgueiras-Rama D, **Calvo CJ**, Millet J, Merino JL, Castells F, Castrejón-Castrejón S, Salvador O, Estrada A, Figueroa J, Ortega M, López-Sendón JL Valor mecanístico y predictive del análisis spectral del ECG de superficie en pacientes con fibrilación auricular paroxística sometidos a cardioversión farmacológica por vernakalant *Rev Esp Cardiol 2013;66 Supl 1:493*

[29]. Simarro E, Julia J, Castells F, Jimenez S, Calvo CJ, Fontenla A, Lopez M, Millet J Evolución de la frecuencia dominante en fibrilación auricular accidental en el tratamiento con vernakalant *Proceedings Congreso Anual de la Sociedad Española de Ingeniería Biomédica 412:415 2014*

[30]. David Filgueiras Rama, **Calvo CJ**, Sergio Castrejón, David Doiny, Alejandro Estrada, Marta Ortega, Jorge Figueroa, José Millet Roig y Jose L. Merino Flutter auricular izquierdo con conducción fibrilatoria al resto de la aurícula *Suplemento reunión anual sección electrofisiología y arritmias 2013*

[31]. Brines-Ferrando L, Canto I, Parra G, Such-Miquel L, Zarzoso, **Calvo CJ**, Soler C, Chorro FJ Modificaciones producidas por el JTV519 sobre la complejidad de la activación de la fibrilación ventricular bajo los efectos del estiramiento agudo miocárdico *Rev Esp Cardiol. (2015),68 Suppl 1 1:539*

[32]. Canto I, Brines-Ferrando L, Such-Miquel L, Soler C, **Calvo CJ**, Zarzoso, Such L, Chorro FJ Efectos de concentraciones crecientes de ranolazina sobre las modificaciones electrofisiológicas del estiramiento agudo ventricular *Rev. Esp. Cardiol. (2015),68 Suppl 1 1:506*

7.1.5. Registered intellectual property and patents

[1]. ***Conrado J Calvo*** *, David Filgueiras-Rama, Esteban López de Sá y Areses, José Millet Roig Method for predicting or pronosticating neurological performance in*

patiente who have suffered a cardiac arrest and optionally comatose status due to ventricular fibrillation P14382456.3-1657, European Patent Office EP/2014/0382456, PCT/EP2015/076893

7.1.6. Editorials and book chapters

[1]. Almazán JM, Marina M, **Calvo C**, Filgueiras-Rama D Electrophysiology and Arrhythmias. Bioelectricity. Editorial CTO ISBN 978.84.16706-02-0

References

(Abramson 1986) *NS Abramson et al. 1986. A randomized clinical study of cardiopulmonary-cerebral resuscitation: design, methods, and patient characteristics. Brain Resuscitation Clinical Trial I Study Group. Am J Emerg Med 1986;4:72-86.*

(Achleitner 2001) *Achleitner U, Wenzel V, Strohmenger HU, et al. The beneficial effect of basic life support on ventricular fibrillation mean frequency and coronary perfusion pressure. Resuscitation 2001;51:151-8.*

(Adrie 2006) *Adrie C, Cariou A, Mourvillier B, Laurent I, Dabbane H, Hantala F, et al. Predicting survival with good neurological recovery at hospital admission after successful resuscitation of out-of-hospital cardiac arrest: the OHCA score. Eur Heart J. 2006;27:2840-5.*

(Allesie 1995) *M. A. Allessie, et al. "Atrial arrhythmias: State of the art, ch. Electrophysiological mechanisms of atrial fibrillation", pp. 155-161. J. P. DiMarco and E. N. Prytowsky, 1995.*

(Amini 2021) *Amini, M., Zayeri, F. & Salehi, M. Trend analysis of cardiovascular disease mortality, incidence, and mortality-to-incidence ratio: results from global burden of disease study 2017. BMC Public Health 21, 401 (2021). https://doi.org/10.1186/s12889-021-10429-0*

(Amit 2010) *Amit, G., K. Kikuchi, I. D. Greener, L. Yang, V. Novack, and J. K. Donahue. 2010. Selective molecular potassium channel blockade prevents atrial fibrillation. Circulation 121: 2263-2270.*

(Arora 2003) *Arora, R., S. Verheule, L. Scott, A. Navarrete, V. Katari, E. Wilson, D. Vaz, and J. E. Olgin. 2003. Arrhythmogenic substrate of the pulmonary veins assessed by high-resolution optical mapping. Circulation 107: 1816-1821.*

(Ashihara 2012) *Ashihara, T., R. Haraguchi, K. Nakazawa, T. Namba, T. Ikeda, Y. Nakazawa, T. Ozawa, M. Ito, M. Horie, and N. A. Trayanova. 2012. The role of fibroblasts in complex fractionated electrograms during persistent/permanent atrial fibrillation: implications for electrogram-based catheter ablation. Circ. Res. 110: 275-284.*

(Atienza 2006) *Atienza F et al. Activation of inward rectifier potassium channels accelerates atrial fibrillation in humans: evidence for a reentrant mechanism. Circulation 2006 December 5;114(23):2434-42.*

(Atienza 2006) *Atienza, F., J. Almendral, J. Moreno, R. Vaidyanathan, A. Talkachou, J. Kalifa, A. Arenal, J. P. Villacastin, E. G. Torrecilla, A. Sanchez, R. Ploutz-Snyder, J. Jalife, and O. Berenfeld. 2006. Activation of inward rectifier potassium channels accelerates atrial fibrillation in humans: evidence for a reentrant mechanism. Circulation 114: 2434-2442.*

(Atienza 2011) *Atienza et al. Mechanisms of fractionated electrograms formation in the posterior left atrium during paroxysmal atrial fibrillation in humans. J Am Coll Cardiol. 2011 Mar 1;57(9):1081-92*

(Baillargeon 2014) *Baillargeon, B., Rebelo, N., Fox, D. D., Taylor, R. L. & Kuhl, E. The living heart project: A robust and integrative simulator for human heart function. Eur. J. Mech. A/Solids* ***48,*** *38–47 (2014).*

(Bayes de Luna 1989) *Bayes de Luna A, Coumel P, Leclercq JF. Ambulatory sudden cardiac death: mechanisms of production of fatal arrhythmia on the basis of data from 157 cases. Am Heart J 1989;117:151-9.*

(Bayly 1993) *Bayly, P. V. et al. A quantitative measurement of spatial order in ventricular fibrillation. J. Cardiovasc. Electrophysiol.* ***4,*** *533–46 (1993).*

(Beeler 1997) *Beeler GW, Reuter H Reconstruction of the action potential of ventricular myocardial fibres. J Physiol 1977 268:177-210*

(Berenfeld 1999) *Berenfeld, O., and A. M. Pertsov. 1999. Dynamics of intramural scroll waves in three-dimensional continuous myocardium with rotational anisotropy. Journal of Theoretical Biology 199: 383-394.*

(Bernard 2002) *Bernard SA, Gray TW, Buist MD, et al. Treatment of comatose survivors of out-of-hospital cardiac arrest with induced hypothermia. N Engl J Med 2002;346:557-63.*

(Bers 1987) *M. Bers, "Cardiac excitation-contraction coupling," NATURE, vol. 415, January, pp. 198–205, 2002. vol. 43, pp. 1049–56, 1987.*

(Bers 2002) *Bers, D. M. Cardiac excitation-contraction coupling. Nature* ***415,*** *198–205 (2002).*

(Boukens 2014) *Boukens, B. J. & Efimov, I. R. A century of optocardiography. IEEE Rev. Biomed. Eng.* ***7,*** *115–125 (2014).*

(Boyce 2014) *Boyce LW, Vliet Vlieland TP, Bosch J, Wolterbeek R, Volker G, van Exel HJ, et al. High survival rate of 43% in out-of-hospital cardiac arrest patients in an optimised chain of survival. Neth Heart J. 2014.*

(Bray 2000) *Bray, M. A., Lin, S. F. & Wikswo Jr, J. P. Three-dimensional surface reconstruction and fluorescent visualization of cardiac activation. IEEE Trans. Biomed. Eng.* ***47,*** *1382–1391 (2000).*

(Brown 1996) *Brown CG, Dzwonczyk R. Signal analysis of the human electrocardiogram during ventricular fibrillation: frequency and amplitude parameters as predictors of successful countershock. Ann Emerg Med. 1996;27:184-8.*

(Brown, 1989) *Brown CG, Dzwonczyk R, Werman HA, Hamlin RL. Estimating the duration of ventricular fibrillation. Ann Emerg Med 1989;18:1181-5.*

(Bub 2005) *Bub, G., A. Shrier, and L. Glass. 2005. Global organization of dynamics in oscillatory heterogeneous excitable media. Phys. Rev. Lett. 94: 028105.*

(Calkins 2007) *Calkins H et al. "HRS/EHRA/ECAS expert consensus statement on catheter and surgical ablation of atrial fibrillation: recommendations for personnel, policy, procedures and follow-up." Europace; vol. 9(6), pp. 335-79. Jun 2007.*

(Campbell 2012) *Campbell, K., C. J. Calvo, S. Mironov, T. Herron, O. Berenfeld, and J. Jalife. 2012. Spatial gradients in action potential duration created by regional magnetofection of hERG are a substrate for wavebreak and turbulent propagation in cardiomyocyte monolayers. J. Physiol 590: 6363-6379.*

(Cha 2005) *Cha TJ, Ehrlich JR, Zhang L, Chartier D, Leung TK, Nattel S. Atrial Tachycardia Remodeling of Pulmonary Vein Cardiomyocytes: Comparison With Left Atrium and Potential Relation to Arrhythmogenesis. Circulation 2005;111(6):728-35.*

(Cha 2005) *Cha, T. J., J. R. Ehrlich, L. Zhang, D. Chartier, T. K. Leung, and S. Nattel. 2005. Atrial Tachycardia Remodeling of Pulmonary Vein Cardiomyocytes: Comparison With Left Atrium and Potential Relation to Arrhythmogenesis. Circulation 111: 728-735.*

(Chabiniok 2016) *Chabiniok, R. et al. Multiphysics and multiscale modelling, data-model fusion and integration of organ physiology in the clinic: ventricular cardiac mechanics. Interface Focus* ***6,*** *20150083 (2016).*

(Chaldoupi 2009) *Chaldoupi, S. M., P. Loh, R. N. Hauer, J. M. de Bakker, and H. V. van Rijen. 2009. The role of connexin40 in atrial fibrillation. Cardiovasc. Res. 84: 15-23.*

(Cherry 2007) *Cherry, E. M., J. R. Ehrlich, S. Nattel, and F. H. Fenton. 2007. Pulmonary vein reentry--properties and size matter: insights from a computational analysis. Heart Rhythm 4: 1553-1562.*

(Choi 2000) *Choi, B. R. & Salama, G. Simultaneous maps of optical action potentials and calcium transients in guinea-pig hearts: mechanisms underlying concordant alternans. J. Physiol.* ***529 Pt 1,*** *171–188 (2000).*

(Chorro 2006) *Chorro, F. J. et al. [Time-frequency analysis of ventricular fibrillation. An experimental study]. Rev. española Cardiol.* ***59,*** *869–78 (2006).*

(Clancy 2002) *Clancy C E and Rudy Y Na+ channel mutation that causes both Brugada and long-QT syndrome phenotype: a simulation study of mechanism Circulation 2002; 105 1208–13*

(Clayton 2005) *Clayton RH, Zhuchkova E.A., Panfilov AV. 2005. Phase singularities and filaments: Simplifyingg complexity in computational models of ventricular fibrillation. Progress in Biophysics and Molecular Biology 90 (2006) 378-398*

(Cobb 2002) *Cobb LA, Fahrenbruch CE, Olsufka M, Copass MK. Changing incidence of out-of-hospital ventricular fibrillation, 1980-2000. JAMA 2002;288:3008-13.*

(Cole 1955) *Cole K.S. Ions, potentials and the nerve impulse. In Shedlovsky, T (ed.) Electrochemistry in biology ad medicine. New York, Wiley. 1955; p 121-140*

(Cole 1991) *Cole TJ. Applied logistic regression. In: Hosmer DW, and Lemeshow S, editors. Statist Med. New York: Wiley; 1991. p. 1162-3.*

(Courtemanche 1998) *Courtemanche, M., R. J. Ramirez, and S. Nattel. 1998. Ionic mechanisms underlying human atrial action potential properties: insights from a mathematical model. American Journal of Physiology-Heart and Circulatory Physiology 44: H301-H321.*

(O'Shea 2020) *Christopher O'Shea, S. Nashitha Kabir, Andrew P. Holmes, Ming Lei, Larissa Fabritz, Kashif Rajpoot, Davor Pavlovic, Cardiac optical mapping – State-of-the-art and future challenges, The International Journal of Biochemistry & Cell Biology, Volume 126, 2020, 105804*

(Cuculich 2010) *Cuculich PS, Wang Y, Lindsay BD, Faddis MN, Schuessler RB, Damiano RJ, Jr., Li L, Rudy Y. Noninvasive characterization of epicardial activation in humans with diverse atrial fibrillation patterns. Circulation 2010 October 5;122(14):1364-72.*

(Cuculich 2010) *Cuculich, P. S., Y. Wang, B. D. Lindsay, M. N. Faddis, R. B. Schuessler, R. J. Damiano, Jr., L. Li, and Y. Rudy. 2010. Noninvasive characterization of epicardial activation in humans with diverse atrial fibrillation patterns. Circulation 122: 1364-1372.*

(Davidenko 1991) *Davidenko, J. M., A. M. Pertsov, R. Salomonsz, W. T. Baxter,*

and J. Jalife. 1991. Stationary and drifting spiral waves of excitation in isolated cardiac muscle. Nature 355: 349-351.

(Davidenko 1995) *Davidenko JM, Salomonsz R, Pertsov AM, Baxter WT, Jalife J. Effects of pacing on stationary reentrant activity. Theoretical and experimental study. Circ Res. 1995 Dec;77(6):1166-79.*

(Deo 2013) *Deo, M., Y. Ruan, S. V. Pandit, K. Shah, O. Berenfeld, A. Blaufox, M. Cerrone, S. F. Noujaim, M. Denegri, J. Jalife, and S. G. Priori. 2013. KCNJ2 mutation in short QT syndrome 3 results in atrial fibrillation and ventricular proarrhythmia. Proc. Natl. Acad. Sci. U. S. A 110: 4291-4296.*

(Dhamoon 2004) *Dhamoon, A. S., S. V. Pandit, F. Sarmast, K. R. Parisian, P. Guha, Y. Li, S. Bagwe, S. M. Taffet, and J. M. Anumonwo. 2004. Unique Kir2.x properties determine regional and species differences in the cardiac inward rectifier K+ current. Circ. Res. 94: 1332-1339.*

(Di Francesco 1985) *Di Francesco D, Noble D A model of cardiac electrical activity incorporating ionic pumps and concentration changes Philos. Trans. R. Soc. Lond. B 1985; 307 353–398*

(DiCiccio 1996) *DiCiccio TJ, Efron B. Bootstrap confidence intervals. Statist Sci. 1996;11:189-212.*

(Downar 1988) *Downar, E., Harris, L., Mickleborough, L. L., Shaikh, N. & Parson, I. D. Endocardial mapping of ventricular tachycardia in the intact human ventricle: Evidence for reentrant mechanisms. J. Am. Coll. Cardiol.* ***11,*** *783–791 (1988).*

(Dumaine 1999) *Dumaine R, Towbin JA, Brugada P, et al. Ionic mechanisms responsible for the electrocardiographic phenotype of the Brugada syndrome are temperature dependent. Circ Res 1999; 85:803–809.*

(Durrer 1970) *Durrer, D. et al. Total excitation of the isolated human heart. Circulation* ***41,*** *899–912 (1970).*

(Ebihara 1980) *Ebihara, L. and Johnson, E. A., "Fast sodium current in cardiac muscle. A quantitative description Conductance and kinetics of delayed rectifier potasium channels in nodal cells of the rabbit heart Tratado de fisiología médica," Biophys.J., 1980; vol. 32, no. 2, pp. 779 3703-790.*

(Eftestol 2000) *Eftestol T, Sunde K, Ole Aase S, Husoy JH, Steen PA. Predicting outcome of defibrillation by spectral characterization and nonparametric classification of ventricular fibrillation in patients with out-of-hospital cardiac arrest. Circulation. 2000;102:1523-9.*

(Ehara 1988) *T. Ehara, A. Noma, K. Ono. "Calcium-activated non-selective cation channel in ventricular cells isolated from adult guinea-pig hearts". J. Physiol. Vol. 403. 1988. pp. 117-133.*

(Ehrlich 2003) *Ehrlich, J. R., T. J. Cha, L. M. Zhang, D. Chartier, P. Melnyk, S. H. Hohnloser, and S. Nattel. 2003. Cellular electrophysiology of canine pulmonary vein cardiomyocytes: action potential and ionic current properties. Journal of Physiology-London 551: 801-813.*

(Erlich 2003) *Ehrlich JR, Cha TJ, Zhang LM, Chartier D, Melnyk P, Hohnloser SH, Nattel S. Cellular electrophysiology of canine pulmonary vein cardiomyocytes: action potential and ionic current properties. Journal of Physiology-London 2003 September 15;551(3):801-13.*

(Evertson 2008) *Evertson, D. W. et al. High-resolution high-speed panoramic cardiac imaging system. IEEE Trans. Biomed. Eng.* ***55,*** *1241–1243 (2008).*

(Faber 2000) *Faber, G.M., Rudy, Y. Action potential and contractility changes in I[Na+] overloaded cardiac myocytes: a simulation study. Biophys. J. 2000; 78, 2392–2404.*

(Fast 1990) *Fast VG, Pertsov AM. Drift of a vortex in the myocardium. Biophysics 1990;35:489-94.*

(Fast 1990) *Fast, V. G., and A. M. Pertsov. 1990. Drift of a vortex in the myocardium. Biophysics 35: 489-494.*

(Ferrero-Corral 1994) *J. M. Ferrero Corral, Ferrero y de Loma-Osorio, José María, J. Saiz Rodríguez and A. Arnau Vives, "Potenciales generados por el corazón," in , Universidad Politécnica de Valencia. Departamento de Ingeniería Electrónica, Ed. Valencia: 1994, pp. 289.*

(Filgueiras-Rama 2011) *Filgueiras-Rama, D. et al. High-Resolution Endocardial and Epicardial Optical Mapping in a Sheep Model of Stretch-Induced Atrial Fibrillation. J. Vis. Exp.* ***53,*** *1–7 (2011).*

(Filgueiras-Rama 2012) *Filgueiras-Rama et al****.*** *Cloroquine terminates stretch induced AF more effectively that flecainide in the sheep heart. Circulation: Arrhythmia and Electrophysiology. 2012;5:561–570*

(Filgueiras-Rama 2012) *Filgueiras-Rama, D. et al. Long-term frequency gradients during persistent atrial fibrillation in sheep are associated with stable sources in the left atrium. Circ. Arrhythmia Electrophysiol.* ***5,*** *1160–1167 (2012).*

(Fluhler 1985) *Fluhler, E., Burnham, V. G. & Loew, L. M. Spectra, membrane binding, and potentiometric responses of new charge shift probes. Biochemistry* ***24,*** *5749–5755 (1985).*

(Fozzard 1994) *Fozzard HA Spooner MM, Brown AM Cardiac electrogenesis and the sodium channel. Ionic Channels in the cardiovascular system, Function and Dysfunction. Future Publishing Company 1994; 81-99.*

(Franz 2003) *Franz, M. R., "The electrical restitution curve revisited: steep or flat slope--which is better?," J.Cardiovasc.Electrophysiol., vol. 14, no. 10 Suppl, pp. S140 S147, Oct.2003.*

(Franzini-Amstrong 1997) *Franzini-Armstrong C, Protasi F. Ryanodine receptors of striated muscles: a complex channel capable of multiple interactions. Physiol Rev 1997;77:699-729.*

(Freese 2013) *Freese JP, Jorgenson DB, Liu PY, et al. Waveform analysis-guided treatment versus a standard shock-first protocol for the treatment of out-of-hospital cardiac arrest presenting in ventricular fibrillation: results of an international randomized, controlled trial. Circulation 2013;128:995-1002.*

(Fuster 2006) *V. Fuster, et al, "Acc/aha/esc 2006 guidelines for the management of patients with atrial fibrillation: ex-ecutive summary. –Joint report for practice guidelines" J Am Coll Card, vol. 48, pp. e149-246, 2006.*

(Gallagher 1995) *Gallagher EJ, Lombardi G, Gennis P. Effectiveness of bystander cardiopulmonary resuscitation and survival following out-of-hospital cardiac arrest. JAMA 1995;274:1922-5.*

(Garny 2008) *Garny Alan, Nickerson DP et al CellML ans associated tools and techniques Phil. Trans.R. Soc. Physiol. A 2008; 366 3017–3043*

(Gloschat 2018) *Gloschat, C., Aras, K., Gupta, S. et al. RHYTHM: An Open Source Imaging Toolkit for Cardiac Panoramic Optical Mapping. Sci Rep 8, 2921 (2018). https://doi.org/10.1038/s41598-018-21333-w*

(Goto 2003) *Goto Y, Suzuki I, Inaba H. Frequency of ventricular fibrillation as predictor of one-year survival from out-of-hospital cardiac arrests. Am J Cardiol 2003;92:457-9.*

(Grandi 2001) *Grandi, E., S. V. Pandit, N. Voigt, A. J. Workman, D. Dobrev, J. Jalife, and D. M. Bers. 2011. Human atrial action potential and Ca2+ model: sinus rhythm and chronic atrial fibrillation. Circ. Res. 109: 1055-1066.*

(Gray 1998) *Gray, R. a, Pertsov, M. & Jalife, J. Spatial and temporal organization during cardiac fibrillation. Nature* ***392,*** *75–78 (1998).*

(Guyton 2011) *Guyton A.C., Hall J.E. 'Testbook of Medical Physiology'. Saunders Elsevier 2011. 11ª Ed*

(He 2013) *Mi He, Chen B, Gong Y, Wang K, Li Y (2013) Prediction of Defibrillation Outcome by Ventricular Fibrillation Waveform Analysis: A Clinical Review. J Clinic Experiment Cardiol S10: 009*

(Heijman 2013) *Heijman et al. New directions in antiarrhythmic rug therapy for atrial fibrillation. Future Cardiol. (2013) 9(1), 71–88*

(Henao 2007) *Henao O,FerreroJM,Ramírez E, Javier Sáiz Cardiac arrhythmias generated by electrophysiological heterogeneity:simulation study. Trabajos libres Rev Colomb Cardiol 2007, 14:185-197.*

(Hernán 2002) *Hernán Vélez A., William Rojas M., Jaime Borrero R. and Jorge Restrepo M., "Repaso de la anatomía y de la fisiología cardíacas" 6th ed., Mario Montoya Toro, Ed. Medellín, Colombia: Corporación para Investigaciones Biológicas, 2002, pp. 1*

(Herron 2012) *Herron, T. J., Lee, P. & Jalife, J. Optical imaging of voltage and calcium in cardiac cells & tissues. Circulation Research* ***110,*** *609–623 (2012).*

(Himmel 2012) *Himmel, H. M. et al. Field and action potential recordings in heart slices: Correlation with established in vitro and in vivo models. Br. J. Pharmacol.* ***166,*** *276–296 (2012).*

(Ho 1997) *Ho KK, Moody GB, Peng CK, Mietus JE, Larson MG, Levy D, et al. Predicting survival in heart failure case and control subjects by use of fully automated methods for deriving nonlinear and conventional indices of heart rate dynamics. Circulation. 1997;96:842-8.*

(Hodgkin 1952) *L. Hodgkin, A. F. Huxley. A quantitative description of membrane current and its application to conduction and excitation in nerve". J. Physiol. 1952; Vol 117. 1952. pp. 500-544.*

(Hoffman 2000) *Hoffman, B.F., Dangman, K.H. Mechanisms for cardiac arrhythmias. Experientia 43, 1049–1056 (1987).*

(Holzer 2002) *Holzer et al. 2002. Mild therapeutic hypothermia to improve the neurologic outcome after cardiac arrest. N Engl J Med 2002;346:549-56.*

(Hou 2010) *Hou L, Deo M, Furspan P, Pandit SV, Mironov S, Auerbach DS, Gong Q, Zhou Z, Berenfeld O, Jalife J. A major role for HERG in determining frequency of reentry in neonatal rat ventricular myocyte monolayer. Circ Res 2010 December 10;107(12):1503-11.*

(Hou 2010) *Hou, L., M. Deo, P. Furspan, S. V. Pandit, S. Mironov, D. S. Auerbach, Q. Gong, Z. Zhou, O. Berenfeld, and J. Jalife. 2010. A major role for HERG in determining frequency of reentry in neonatal rat ventricular myocyte monolayer. Circ. Res. 107: 1503-1511.*

(Huang 1998) *Huang, J. et al. Evolution of the organization of epicardial activation patterns during ventricular fibrillation. J. Cardiovasc. Electrophysiol.* ***9,*** *1291–1304 (1998).*

(Jaimes 2016) *Jaimes, R. 3rd et al. A Technical Review of Optical Mapping of*

Intracellular Calcium within Myocardial Tissue. Am. J. Physiol. Heart Circ. Physiol. ajpheart.00665.2015 (2016).

(Jalife 2002) *J. Jalife, O. Berenfeld, and M. Mansour. "Mother rotors and fibrillatory conduction: a mechanism of atrial fibrillation". Cardiovascular Research, vol. 54(2), pp. 204–216, May 2002.*

(Jalife 2003) *Jalife J. Experimental and clinical AF mechanisms: bridging the divide. J Interv Card Electrophysiol 2003 October;9(2):85-92.*

(Jalife 2003) *Jalife, J. 2003. Experimental and clinical AF mechanisms: bridging the divide. J. Interv. Card Electrophysiol. 9: 85-92.*

(Jalife 2011) *Jalife et al. De´ja` vu in the theories of atrial fibrillation dynamics Cardiovascular Research (2011) 89, 766–775*

(Jennett 1975) *Jennett B, Bond M. Assessment of outcome after severe brain damage. Lancet 1975;1:480-4.*

(Jia 2002) *Jia, P., Punske, B., Taccardi, B. & Rudy, Y. Endocardial mapping of electrophysiologically abnormal substrates and cardiac arrhythmias using a noncontact nonexpandable catheter. J Cardiovasc Electrophysiol* ***13,*** *888–895 (2002).*

(Kalifa 2006) *Kalifa J, Tanaka K, Zaitsev AV, Warren M, Vaidyanathan R, Auerbach D, et al. Mechanisms of wave fractionation at boundaries of high-frequency excitation in the posterior left atrium of the isolated sheep heart during atrial fibrillation. Circulation. 2006;113:626-33.*

(Kanlop 2010) *Kanlop, N. & Sakai, T. Optical mapping study of blebbistatin-induced chaotic electrical activities in isolated rat atrium preparations. J. Physiol. Sci.* ***60,*** *109–117 (2010).*

(Katz 2000) *Katz AM 'Physiology of the heart' New York [Raven Press] 2000 PP. 10-510 3rd Edition*

(Kay 2006) *Kay, M. W. & Rogers, J. M. Epicardial rotors in panoramic optical maps of fibrillating swine ventricles. in Annual International Conference of the IEEE Engineering in Medicine and Biology - Proceedings 2268–2271 (2006).*

(Kay 2004) *Kay, M. W., Amison, P. M. & Rogers, J. M. Three-dimensional surface reconstruction and panoramic optical mapping of large hearts. IEEE Trans. Biomed. Eng.* ***51,*** *1219–1229 (2004).*

(Kleber 2004) *Kleber AG, Rudy Y. Basic mechanisms of cardiac impulse propagation and associated arrhythmias. Physiol Rev 2004 April;84(2):431-88.*

(Kleber 2004) *Kleber, A. G., and Y. Rudy. 2004. Basic mechanisms of cardiac impulse propagation and associated arrhythmias. Physiol Rev. 84: 431-488.*

(Klos 2008) *Klos M, Calvo D, Yamazaki M, Zlochiver S, Mironov S, Cabrera J-A, Sanchez-Quintana D, Jalife J, Berenfeld O, Kalifa J. Atrial septopulmonary bundle of the posterior left atrium provides a substrate for atrial fibrillation initiation in a model of vagally mediated pulmonary vein tachycardia of the structurally normal heart. Circ Arrhythmia Electrophysiol.. 2008;1:175-183.*

(Kneller 2002) *Kneller, J., R. Zou, E. J. Vigmond, Z. Wang, L. J. Leon, and S. Nattel. 2002. Cholinergic atrial fibrillation in a computer model of a two-dimensional sheet of canine atrial cells with realistic ionic properties. Circ. Res. 90: E73-E87.*

(Krummen 2014) *Krummen, D. E. et al. Rotor stability separates sustained ventricular fibrillation from self-terminating episodes in humans. J. Am. Coll. Cardiol.* ***63,*** *2712–2721 (2014).*

(Kumar 2012) *Kumar DG, Thakur D, Sharma S, Bhardwaj S. ECG Paper Records Digitalization through Image Processing Techniques. Int J Comput Appl 2012;48:35-8.*

(Laughner 2012) *Laughner JI, Ng FS, Sulkin MS, Arthur RM, Efimov IR. Processing and analysis of cardiac optical mapping data obtained with potentiometric dyes. Am J Physiol Heart Circ Physiol. 2012 Oct 1;303(7):H753-65. doi: 10.1152/ajpheart.00404.2012*

(Lee 2001) *Lee, M. H. et al. Effects of diacetyl monoxime and cytochalasin D on ventricular fibrillation in swine right ventricles. Am. J. Physiol. Heart Circ. Physiol.* ***280,*** *H2689–H2696 (2001).*

(Lee 2017) Lee P, Calvo CJ, Alfonso-Almazán JM, Quintanilla JG, Chorro FJ, Yan P, Loew LM, Filgueiras-Rama D, Millet J. Low-Cost Optical Mapping Systems for Panoramic Imaging of Complex Arrhythmias and Drug-Action in Translational Heart Models. Sci Rep. 2017 Feb 27;7:43217

(Lee 2011) *Lee, P. et al. Single-sensor system for spatially resolved, continuous, and multiparametric optical mapping of cardiac tissue. Hear. Rhythm* ***8,*** *1482–1491 (2011).*

(Lee 2012) *Lee, P. et al. Simultaneous measurement and modulation of multiple physiological parameters in the isolated heart using optical techniques. Pflugers Arch.* ***464,*** *403–14 (2012).*

(Lee 2019) Lee P, Quintanilla JG, Alfonso-Almazán JM, Galán-Arriola C, Yan P, Sánchez-González J, Pérez-Castellano N, Pérez-Villacastín J, Ibañez B, Loew LM, Filgueiras-Rama D. In vivo ratiometric optical mapping enables high-resolution cardiac electrophysiology in pig models. Cardiovasc Res. 2019 Sep 1;115(11):1659-1671.

(Lemola 2008) *Lemola, K., D. Chartier, Y. H. Yeh, M. Dubuc, R. Cartier, A.*

Armour, M. Ting, M. Sakabe, A. Shiroshita-Takeshita, P. Comtois, and S. Nattel. 2008. Pulmonary vein region ablation in experimental vagal atrial fibrillation: role of pulmonary veins versus autonomic ganglia. Circulation 117: 470-477.

***(Levi 1996)** Levi, a J. & Issberner, J. Effect on the fura-2 transient of rapidly blocking the Ca2+ channel in electrically stimulated rabbit heart cells. J. Physiol. 493 (Pt 1)(Pt 1), 19–37 (1996).*

***(Lin 1999)** Lin, S. F. & Wikswo, J. P. Panoramic optical imaging of electrical propagation in isolated heart. J. Biomed. Opt. **4,** 200–7 (1999).*

***(Liu 1995)** Liu, D. W. and C. Antzelevitch. 'Characteristics of the delayed rectifier current (IKr and IKs) in canine ventricular epicardial, midmyocardial and endocardial myocytes: a weaker IKs contributes to the longer action potential of the M cell'. Circ. Res. 76: 351–365, 1995*

***(Lopez-de-Sa 2012)** Lopez-de-Sa E, Rey JR, Armada E, et al. Hypothermia in comatose survivors from out-of-hospital cardiac arrest: pilot trial comparing 2 levels of target temperature. Circulation 2012;126:2826-33.*

***(Luo 1991)** C. H. Luo, Y. Rudy. A model of the ventricular cardiac action potential. Depolarization, repolarization, and their interaction". Circ. Res. 1991; Vol 68.. pp. 1501-1526.*

***(MA 2000)** AM Physiology of the heart New York [Raven Press]2000 PP. 10-510 3nd Edition*

***(Maltsev 1998)** Maltsev V A, Sabbah H N, Higgins R S D, Silverman N, Lesch M and Undrovinas A I Novel, ultraslow inactivating sodium current in human ventricular myocytes Circulation 1998; 98 2545–52*

***(Mandapati 2000)** Mandapati R, Skanes A, Chen J, Berenfeld O, Jalife J. Stable microreentrant sources as a mechanism of atrial fibrillation in the isolated sheep heart. Circulation 2000 January 18;101(2):194-9.*

***(Mandapati 2000)** Mandapati, R., A. Skanes, J. Chen, O. Berenfeld, and J. Jalife. 2000. Stable microreentrant sources as a mechanism of atrial fibrillation in the isolated sheep heart. Circulation 101: 194-199.*

***(Martin 1991)** Martin DR, Brown CG, Dzwonczyk R. Frequency analysis of the human and swine electrocardiogram during ventricular fibrillation. Resuscitation 1991;22:85-91.*

***(Martini 2014)** F. Martini. 'Fundamentals of Anatomy and Physiology'. 6th ed. Pearson Education Inc., Benjamin Cummings, San Francisco, CA, 2004.*

***(Martins 2014)** Martins, R. P. et al. Dominant frequency increase rate predicts transition from paroxysmal to long-term persistent atrial fibrillation. Circulation **129,** 1472–1482 (2014).*

(Marty 1981) *O.P., Marty, A., Neher, E Improved patch clamp techniques for high-resolution current recording from cell and cell-free membrane patche. Pfluger Arch. 1981; 391:85-100.*

(Matiukas 2007) *Matiukas, A. et al. Near-infrared voltage-sensitive fluorescent dyes optimized for optical mapping in blood-perfused myocardium. Hear. Rhythm* ***4,*** *1441–1451 (2007).*

(Mayer 1908) *A. G. Mayer, "Rhythmical pulsation in scyphomedusae:II," Carnegie Institute Publication, vol. 102, no. VII, pp. 113–31, 1908.*

(McAllister 1975) *McAllister, R. E., Noble, D., and Tsien, R. W., "Reconstruction of the electrical activity of cardiac Purkinje fibres Conductance and kinetics of delayed rectifier potassium channels in nodal cells of the rabbit heart Tratado de fisiología médica," J.Physiol, 1975; vol. 251, no. 1, pp. 1 3703-59*

(Mines 1992) *G. R. Mines, "On dynamic equilibrium in the heart," J Physiol, vol. 71, pp. 1254-1267, 1992.*

(Mironov 2006) *Mironov, S. F., Vetter, F. J. & Pertsov, A. M. Fluorescence imaging of cardiac propagation: spectral properties and filtering of optical action potentials. AJP - Hear. Circ. Physiol.* ***291,*** *H327-335 (2006).*

(Miyata 2002) *Miyata A, Dowell JD, Zipes DP, Rubart M, Rate-dependent $[K^+]_0$ accumulation in canine right atria in vivo: electrophysiological consequences. Am J Physiol Heart Circ Physiol. 2002 Aug;283(2):H506-17*

(Mohrman 2006) *D. E. Mohrman and L. J. Heller, 'Cardiovascular Physiology' 6th ed. Lange Medical Books/McGraw-Hill, New York, 2006*

(Mungas 1991) *Mungas D. In-office mental status testing: a practical guide. Geriatrics 1991;46:54-8, 63, 66.*

(Nadkarni 2006) *Nadkarni VM, Larkin GL, Peberdy MA, et al. First documented rhythm and clinical outcome from in-hospital cardiac arrest among children and adults. JAMA 2006;295:50-7.*

(Narayan 2012) *Narayan SM, Krummen DE, Shivkumar K, Clopton P, Rappel WJ, Miller JM. Treatment of Atrial Fibrillation by the Ablation of Localized Sources: CONFIRM (Conventional Ablation for Atrial Fibrillation With or Without Focal Impulse and Rotor Modulation) Trial. J Am Coll Cardiol 2012 August 14;60(7):628-36.*

(Narayan 2012) *Narayan, S. M. et al. Treatment of atrial fibrillation by the ablation of localized sources: CONFIRM (Conventional Ablation for Atrial Fibrillation with or Without Focal Impulse and Rotor Modulation) trial. J. Am. Coll. Cardiol.* ***60,*** *628–636 (2012).*

(Narayan 2012) *Narayan, S. M., D. E. Krummen, K. Shivkumar, P. Clopton, W. J. Rappel, and J. M. Miller. 2012. Treatment of Atrial Fibrillation by the Ablation of Localized Sources: CONFIRM (Conventional Ablation for Atrial Fibrillation With or Without Focal Impulse and Rotor Modulation) Trial. J. Am. Coll. Cardiol. 60: 628-636.*

(Nattel 2008) *Nattel S, Burstein B, Dobrev D. Atrial remodeling and atrial fibrillation: mechanisms and implications. Circ Arrhythm Electrophysiol 2008 April;1(1):62-73.*

(Nattel 2008) *Nattel, S., B. Burstein, and D. Dobrev. 2008. Atrial remodeling and atrial fibrillation: mechanisms and implications. Circ. Arrhythm. Electrophysiol. 1: 62-73.*

(Nielsen 2004) *L.W. Boyce, T.P. Vliet Vlieland, J. Bosch, R.Wolterbeek, G. Volker, H.J. van Exel, et al., High survival rate of 43% in out-of-hospital cardiac arrest patients in an optimized chain of survival, Neth. Heart J. 23 (2015) 20–25.*

(Nielsen 2006) *N. Nielsen, J. Wetterslev, T. Cronberg, D. Erlinge, Y. Gasche, C. Hassager, et al., Targeted temperature management at 33 °C versus 36 °C after cardiac arrest, N. Engl. J. Med. 369 (2013) 2197–2206.*

(Nielsen 2013) *Nielsen N, Wetterslev J, Cronberg T, et al. Targeted temperature management at 33 degrees C versus 36 degrees C after cardiac arrest. N Engl J Med 2013;369:2197-206.*

(Noujaim 2007) *Noujaim SF, Pandit SV, Berenfeld O, Vikstrom K, Cerrone M, Mironov S, Zugermayr M, Lopatin AN, Jalife J. Up-regulation of the inward rectifier K+ current (I K1) in the mouse heart accelerates and stabilizes rotors. J Physiol 2007 January 1;578(Pt 1):315-26.*

(Noujaim 2007) *Noujaim, S. F., S. V. Pandit, O. Berenfeld, K. Vikstrom, M. Cerrone, S. Mironov, M. Zugermayr, A. N. Lopatin, and J. Jalife. 2007. Up-regulation of the inward rectifier K+ current (I K1) in the mouse heart accelerates and stabilizes rotors. J. Physiol 578: 315-326.*

(Noujaim 2010) *Noujaim, S. F., J. A. Stuckey, D. Ponce-Balbuena, T. Ferrer-Villada, A. Lopez-Izquierdo, S. Pandit, C. J. Calvo, K. R. Grzeda, O. Berenfeld, J. A. Chapula, and J. Jalife. 2010. Specific residues of the cytoplasmic domains of cardiac inward rectifier potassium channels are effective antifibrillatory targets. FASEB J. 24: 4302-4312.*

(Oral 2005) *Oral H. Mechanisms of atrial fibrillation: lessons from studies in patients. Prog Cardiovasc Dis 2005 July;48(1):29-40.*

(Oral 2005) *Oral, H. 2005. Mechanisms of atrial fibrillation: lessons from studies in patients. Prog. Cardiovasc. Dis. 48: 29-40.*

(Oster 1997) *Oster, H. S., Taccardi, B., Lux, R. L., Ershler, P. R. & Rudy, Y. Noninvasive Electrocardiographic Imaging: Reconstruction of Epicardial Potentials, Electrograms, and Isochrones and Localization of Single and Multiple Electrocardiac Events. Circulation* ***96,*** *1012–1024 (1997).*

(Pandit 2005) *Pandit, S. V., O. Berenfeld, J. M. Anumonwo, R. M. Zaritski, J. Kneller, S. Nattel, and J. Jalife. 2005. Ionic determinants of functional reentry in a 2-D model of human atrial cells during simulated chronic atrial fibrillation. Biophys. J. 88: 3806-3821.*

(Pandit 2013) *Pandit SV., Jalife J. 2013 Rotors and the dynamics of cardiac fibrillation. Review. Circ. Res. 1;112(5):831-3*

(Pertsov 1993) *Pertsov AM, Davidenko JM, Salomonsz R, Baxter WT, Jalife J. Spiral waves of excitation underlie reentrant activity in isolated cardiac muscle. Circ Res 1993 March;72(3):631-50.*

(Pertsov 1993) *Pertsov, A. M., J. M. Davidenko, R. Salomonsz, W. T. Baxter, and J. Jalife. 1993. Spiral waves of excitation underlie reentrant activity in isolated cardiac muscle. Circ. Res. 72: 631-650.*

(Pfeifer 2005) *Pfeifer R, Borner A, Krack A, Sigusch HH, Surber R, Figulla HR. Outcome after cardiac arrest: predictive values and limitations of the neuroproteins neuron-specific enolase and protein S-100 and the Glasgow Coma Scale. Resuscitation 2005;65:49-55.*

(Plonsey 1995) *Plonsey R, Malmivuo J. 'BIOELECTROMAGNETISM: Principles and Applications of Bioelectric and Biomagnetic Fields'. Oxford University Press 1995*

(Po 2005) *Po, S. S., Y. Li, D. Tang, H. Liu, N. Geng, W. M. Jackman, B. Scherlag, R. Lazzara, and E. Patterson. 2005. Rapid and stable re-entry within the pulmonary vein as a mechanism initiating paroxysmal atrial fibrillation. J. Am. Coll. Cardiol. 45: 1871-1877.*

(Quintanilla 2015) *Quintanilla, J. G. et al. Increased intraventricular pressures are as harmful as the electrophysiological substrate of heart failure in favoring sustained reentry in the swine heart. Hear. Rhythm* ***12,*** *2172–2183 (2015).*

(Ramanathan 2004) *Ramanathan, C., Ghanem, R. N., Jia, P., Ryu, K. & Rudy, Y. Noninvasive electrocardiographic imaging for cardiac electrophysiology and arrhythmia. Nat. Med.* ***10,*** *422–428 (2004).*

(Ravichandran 2013) *Ravichandran L, Harless C, Shah AJ, Wick CA, McLellan JH, Tridandapani S. Novel Tool for Complete Digitization of Paper Electrocardiography Data. IEEE Journal of Translational Engineering in Health and Medicine. 2013:1800107-.*

(Reed 2003) *Reed MJ, Clegg GR, Robertson CE. Analysing the ventricular fibrillation waveform. Resuscitation. 2003;57:11-20.*

(Ripplinger 2009) *Ripplinger, C. M., Lou, Q., Li, W., Hadley, J. & Efimov, I. R. Panoramic imaging reveals basic mechanisms of induction and termination of ventricular tachycardia in rabbit heart with chronic infarction: Implications for low-voltage cardioversion. Hear. Rhythm* ***6,*** *87–97 (2009).*

(Rogove 1995) *Rogove HJ, Safar P, Sutton-Tyrrell K, Abramson NS. Old age does not negate good cerebral outcome after cardiopulmonary resuscitation: analyses from the brain resuscitation clinical trials. The Brain Resuscitation Clinical Trial I and II Study Groups. Crit Care Med 1995;23:18-25.*

(Rudy 2000) *Rudy Y, Zipes DP, Jalife J Cardiac Electrophysiology: From Cell to Bedside. Ionic mechanism of cardiac electrical activity. Third edition. Saunders Company 2000; 257-265.*

(Samie 2001) *Samie, F. H., O. Berenfeld, J. Anumonwo, S. F. Mironov, S. Udassi, J. Beaumont, S. Taffet, and J. Jalife. 2001. Rectification of the Background Potassium Current: A Determinant of Rotor Dynamics in Ventricular Fibrillation. Circ Res 89: 1216-1223.*

*(****Sampson 2001****) Sampson, K. J., and C. S. Henriquez. 2001. Simulation and prediction of functional block in the presence of structural and ionic heterogeneity. American Journal of Physiology-Heart and Circulatory Physiology 281: H2597-H2603.*

(Sampson 2002) *Sampson, K. J., and C. S. Henriquez. 2002. Interplay of ionic and structural heterogeneity on functional action potential duration gradients: Implications for arrhythmogenesis. Chaos 12: 819-828.*

(Sampson 2005) *Sampson, K. J., and C. S. Henriquez. 2005. Electrotonic influences on action potential duration dispersion in small hearts: a simulation study. Am. J. Physiol Heart Circ. Physiol 289: H350-H360.*

(Sampson) *Sampson KJ, Henriquez CS. Simulation and prediction of functional block in the presence of structural and ionic heterogeneity. American Journal of Physiology-Heart and Circulatory Physiology 2001 December;281(6):H2597-H2603.*

(Sanders 2005) *Sanders, P., O. Berenfeld, M. Hocini, P. Jais, R. Vaidyanathan, L. F. Hsu, S. Garrigue, Y. Takahashi, M. Rotter, F. Sacher, C. Scavee, R. Ploutz-Snyder, J. Jalife, and M. Haissaguerre. 2005. Spectral analysis identifies sites of high-frequency activity maintaining atrial fibrillation in humans. Circulation 112: 789-797.*

(Sanders P 2005) *Sanders P et al. Spectral analysis identifies sites of high-frequency activity maintaining atrial fibrillation in humans. Circulation 2005 August 9;112(6):789-97.*

(Sandroni 2007) *Sandroni C, Nolan J, Cavallaro F, Antonelli M. In-hospital cardiac arrest: incidence, prognosis and possible measures to improve survival. Intensive Care Med 2007;33:237-45.*

(Sanguinetti 1990) *M. C. Sanguinetti, N. K. Jurkiewicz. "Two components of cardiac delayed rectifier K+ current. Differential sensitivity to block by class III antiarrhythmic agents". J. Gen. Physiol. Vol. 96. 1990. pp. 195-215.*

(Sarmast 2003) *Sarmast F, Kolli A, Zaitsev A, Parisian K, Dhamoon AS, Guha PK, Warren M, Anumonwo JMB, Taffet SM, Berenfeld O, Jalife J. Cholinergic atrial fibrillation: I-K,I-ACh gradients determine unequal left/right atrial frequencies and rotor dynamics. Cardiovascular Research 2003 October 1;59(4):863-73.*

(Sarmast 2003) *Sarmast, F., A. Kolli, A. Zaitsev, K. Parisian, A. S. Dhamoon, P. K. Guha, M. Warren, J. M. B. Anumonwo, S. M. Taffet, O. Berenfeld, and J. Jalife. 2003. Cholinergic atrial fibrillation: I-K,I-ACh gradients determine unequal left/right atrial frequencies and rotor dynamics. Cardiovascular Research 59: 863-873.*

(Schoene 2014) *P. Schoene, J. Coult, L. Murphy, C. Fahrenbruch, J. Blackwood, P. Kudenchuk, et al., Course of quantitative ventricular fibrillation waveform measure and outcome following out-of-hospital cardiac arrest, Heart Rhythm. 11 (2014) 230–236.*

(Schoene 2014) *Schoene P, Coult J, Murphy L, et al. Course of quantitative ventricular fibrillation waveform measure and outcome following out-of-hospital cardiac arrest. Heart Rhythm 2014;11:230-6.*

(Schoene 2014) *Schoene P, Coult J, Murphy L, Fahrenbruch C, Blackwood J, Kudenchuk P, et al. Course of quantitative ventricular fibrillation waveform measure and outcome following out-of-hospital cardiac arrest. Heart Rhythm. 2014;11:230-6.*

(Schram 2002) *Schram G., Pourrier M. Melnyk P., Nattel S. 2002 Differential distribution of cardiac ion channel expression as a basis for regional specialization in electrical function. Review. Circ. Res. 17;90(9):939-50*

(Sekar 2009) *Sekar, R. B., E. Kizana, H. C. Cho, J. M. Molitoris, G. G. Hesketh, B. P. Eaton, E. Marban, and L. Tung. 2009. IK1 heterogeneity affects genesis and stability of spiral waves in cardiac myocyte monolayers. Circ. Res. 104: 355-364.*

(Sherman 2006) *Sherman LD. The frequency ratio: an improved method to estimate ventricular fibrillation duration based on Fourier analysis of the*

waveform. Resuscitation. 2006;69:479-86.

(Snyders 2000) *Snyders DJ, Zipes DP, Jalife J. Cardiac Electrophysiology: From Cell to Bedside. Molecular biology of potassium channels. Third edition. Saunders Company 2000; 21-31.*

(Spear 1982) *F. Spear and E. N. Moore, "Mechanisms of cardiac arrhythmias," Ann. Rev. Physiol., vol. 44, pp. 485–97, 1982*

(Stewart 1992) *Stewart AJ, Allen JD, Adgey AA. Frequency analysis of ventricular fibrillation and resuscitation success. Q J Med 1992;85:761-9.*

(Strohmenger 1996) *Strohmenger HU, Lindner KH, Keller A, Lindner IM, Pfenninger EG. Spectral analysis of ventricular fibrillation and closed-chest cardiopulmonary resuscitation. Resuscitation 1996;33:155-61.*

(Strohmenger 1994) *Strohmenger HU, Lindner KH, Lurie KG, Welz A, Georgieff M. Frequency of ventricular fibrillation as a predictor of defibrillation success during cardiac surgery. Anesthesia and analgesia 1994;79:434-8.*

(Strohmenger 2001) *Strohmenger HU, Eftestol T, Sunde K, Wenzel V, Mair M, Ulmer H, et al. The predictive value of ventricular fibrillation electrocardiogram signal frequency and amplitude variables in patients with out-of-hospital cardiac arrest. Anesth Analg. 2001;93:1428-33.*

(Such-Miquel 2013) *Such-Miquel L, Chorro FJ, Guerrero J, Trapero I, Brines L, Zarzoso M, et al. Evaluation of the complexity of myocardial activation during ventricular fibrillation. An experimental study. Rev Esp Cardiol. 2013;66:177-84.*

(Sugawara 2003) *Sugawara T, Chan PH. Reactive oxygen radicals and pathogenesis of neuronal death after cerebral ischemia. Antioxid Redox Signal 2003;5:597-607.*

(Swift 2012) *Swift, L. M. et al. Properties of blebbistatin for cardiac optical mapping and other imaging applications. Pflugers Arch. Eur. J. Physiol.* ***464,*** *503–512 (2012).*

(Tanaka 2007) *Tanaka K, Zlochiver S, Vikstrom KL, Yamazaki M, Moreno J, Klos M, Zaitsev AV, Vaidyanathan R, Auerbach DS, Landas S, Guiraudon G, Jalife J, Berenfeld O, Kalifa J. Spatial distribution of fibrosis governs fibrillation wave dynamics in the posterior left atrium during heart failure. Circ Res 2007 October 12;101(8):839-47.*

(Tanaka 2007) *Tanaka, K., S. Zlochiver, K. L. Vikstrom, M. Yamazaki, J. Moreno, M. Klos, A. V. Zaitsev, R. Vaidyanathan, D. S. Auerbach, S. Landas, G. Guiraudon, J. Jalife, O. Berenfeld, and J. Kalifa. 2007. Spatial distribution of fibrosis governs fibrillation wave dynamics in the posterior left atrium during heart failure. Circ.*

Res. 101: 839-847.

(Ten Tusscher 2006) *Ten Tusscher, K.H., Panfilov, A.V. Cell model for efficient simulation of wave propagation in human ventricular tissue under normal and pathological conditions. Phys. Med. Biol. 2006b; 51, 6141–6156.*

(Trayanova 2011) *Trayanova, N. A. Whole-heart modeling : Applications to cardiac electrophysiology and electromechanics. Circulation Research* ***108,*** *113–128 (2011).*

(Tschabrunn 2016) *Tschabrunn, C. M. et al. A swine model of infarct-related reentrant ventricular tachycardia: Electroanatomic, magnetic resonance, and histopathological characterization. Hear. Rhythm* ***13,*** *262–273 (2016).*

(Tusscher 2003) *ten Tusscher, K. H., and A. V. Panfilov. 2003. Reentry in heterogeneous cardiac tissue described by the Luo-Rudy ventricular action potential model. Am. J. Physiol Heart Circ. Physiol 284: H542-H548.*

(Umapathy 2011) *Umapathy K, Foomany FH, Dorian P, et al. Real-time electrogram analysis for monitoring coronary blood flow during human ventricular fibrillation: implications for CPR. Heart Rhythm 2011;8:740-9.*

(Verhuele 2002) *Verhuele S, Wilson EE, Arora R., Engle SK., Scott LR., Olgin JE 2002. Tissue structure and connexin expression of canine pulmonary veins. Cardiovasc. Res. 55: 727-738.*

(Viswanathan 1999) *Viswanathan, P. C., R. M. Shaw, and Y. Rudy. 1999. Effects of IKr and IKs heterogeneity on action potential duration and its rate dependence: a simulation study. Circulation 99: 2466-2474.*

(Visweswaran 2013) *Visweswaran, R., McIntyre, S. D., Ramkrishnan, K., Zhao, X. & Tolkacheva, E. G. Spatiotemporal evolution and prediction of [Ca2+]i and APD alternans in isolated rabbit hearts. J. Cardiovasc. Electrophysiol.* ***24,*** *1287–1295 (2013).*

(Warren 2003) *Warren, M., P. K. Guha, O. Berenfeld, A. Zaitsev, J. M. B. Anumonwo, A. S. Dhamoon, S. Bagwe, S. M. Taffet, and J. Jalife. 2003. Blockade of the inward rectifying potassium current terminates ventricular fibrillation in the guinea pig heart. J. Cardiovasc. Electrophysiol. 14: 621-631.*

(Warren 2007) *Warren, M., Huizar, J. F., Shvedko, A. G. & Zaitsev, A. V. Spatiotemporal relationship between intracellular Ca2+ dynamics and wave fragmentation during ventricular fibrillation in isolated blood-perfused pig hearts. Circ. Res. 101, (2007);101:e90–e101*

(Weaver 1985) *Weaver WD, Cobb LA, Dennis D, Ray R, Hallstrom AP, Copass MK. Amplitude of ventricular fibrillation waveform and outcome after cardiac arrest. Ann Intern Med. 1985;102:53-5.*

(Weber 2002) *Weber CR, Piacentino V,Ginsburg KS, Houser SRand BersDM Na+ Ca2+ exchange current and submembrane [Ca2+]i during the cardiac action potential Circ. Res. 2002; 90 182–9*

(Wellner 1999) *Wellner, M., A. M. Pertsov, and J. Jalife. 1999. Spiral drift and core properties. Phys. Rev. E. Stat. Phys. Plasmas. Fluids Relat Interdiscip. Topics. 59: 5192-5204.*

(Wik 2005) *Wik L, Kramer-Johansen J, Myklebust H, et al. Quality of cardiopulmonary resuscitation during out-of-hospital cardiac arrest. JAMA 2005;293:299-304.*

(Wilhelms 2013) *Wilhelms Mathias, Hettmann Hanne, Maleckar Mary Margot Catherine, Koivum‰ki Jussi T, Dˆssel Olaf, Seemann Gunnar Benchmarking electrophysiological models of human atrial myocytes Frontiers in Physiology 2013 Jan 4;3:48*

(Williams AJ 1997) *Williams AJ. The functions of two species of calcium channels in cardiac muscle excitation-contraction coupling. Eur Heart J 1997;18:(Suppl A):A27-35*

(Worley 1987) *Worley, S. J. et al. A new sock electrode for recording epicardial activation from the human heart: One size fits all. PACE - Pacing Clin. Electrophysiol.* ***10,*** *21–31 (1987).*

(Wozniak-Skowerska 2011) *Wozniak-Skowerska, I., M. Skowerski, A. Wnuk-Wojnar, A. Hoffmann, S. Nowak, A. Gola, M. Sosnowski, and M. Trusz-Gluza. 2011. Comparison of pulmonary veins anatomy in patients with and without atrial fibrillation: analysis by multislice tomography. Int. J. Cardiol. 146: 181-185.*

(Wyse 2004) *D. G. Wyse and B. J. Gersh. "Atrial fibrillation: a perspective. Thinking inside and outside the box". Circulation, vol. 109, pp. 3089–3095, 2004.*

(Yamazaki 2012) *Masatoshi Yamazaki, Sergey Mironov, Clément Taravant, Julien Brec, Luis M. Vaquero, Krishna Bandaru, Uma Mahesh R Avula, Haruo Honjo, Itsuo Kodama, Omer Berenfeld, and Jérôme Kalifa Heterogeneous atrial wall thickness and stretch promote scroll waves anchoring during atrial fibrillation Cardiovascular Research (2012) 94, 48–57*

(Yan 2012) *Yan, P. et al. Palette of fluorinated voltage-sensitive hemicyanine dyes. Proc. Natl. Acad. Sci.* ***109,*** *20443–20448 (2012).*

(Yue 1988) *D. T. Yue, E. Marban. "A novel cardiac potassium channel that is active and conductive at depolarized potentials." Pflugers Arch. Vol. 413. 1988. pp. 127-133.*

(Zeng 1995) *J. Zeng, K. R. Laurita, D. S. Rosenbaum, Y. Rudy. Two components of the delayed rectifier K+ current in ventricular myocytes of the guinea pig type. Theoretical formulation and their role in repolarization". Circulation Research 1995;77:140-152.*

(Zhao 2012) *Zhao J, Butters TD, Zhang H, Pullan AJ, LeGrice IJ, Sands GB, Smaill BH. 2012 An image-based model of atrial muscular architecture: structural anisotropy and electrical activation. Circ. Arrhythm. Electrophysiol. 5,361 – 370.*

(Zlochiver 2008) *Zlochiver, S., M. Yamazaki, J. Kalifa, and O. Berenfeld. 2008. Rotor meandering contributes to irregularity in electrograms during atrial fibrillation. Heart Rhythm 5: 846-854.*

(Zlochiver 2008) *Zlochiver, S., V. Munoz, K. L. Vikstrom, S. M. Taffet, O. Berenfeld, and J. Jalife. 2008. Electrotonic myofibroblast-to-myocyte coupling increases propensity to reentrant arrhythmias in two-dimensional cardiac monolayers. Biophys. J 95: 4469-4480.*